Nonlinear optics in titanium dioxide: from bulk to integrated optical devices

Nonlinear optics in titanium dioxide: from bulk to integrated optical devices

A thesis presented

by

Christopher Courtney Evans

to

The School of Engineering and Applied Sciences

in partial fulfillment of the requirements

for the degree of

Doctor of Philosophy

in the subject of

Applied Physics

Harvard University

Cambridge, Massachusetts

August 2013

Thesis advisor

Eric Mazur

Author

Christopher Courtney Evans

Nonlinear optics in titanium dioxide: from bulk to integrated optical devices

Abstract

In this thesis, we explore titanium dioxide (TiO_2) for ultrafast, on-chip nonlinear optics by studying it in bulk, thin films, and in integrated nonlinear optical devices. TiO_2's large nonlinear index of refraction (30 times that of silica) and low two-photon absorption can enable all-optical switching, logic, and wavelength conversion across wavelengths spanning the telecommunications octave (800–1600 nm). In addition, its high linear index of refraction can enhance optical confinement down to nano-scale dimensions and facilitate the tight waveguide bends necessary for dense on-chip integration. Throughout this thesis, we develop TiO_2 as a novel on-chip nonlinear optics platform.

We begin by studying nonlinear refraction and multiphoton absorption in bulk rutile TiO_2 using the Z-scan technique. We quantify nonlinear refraction and mixed two- and three-photon absorption near TiO_2's half-bandgap (800 nm). This data shows that we can avoid parasitic two-photon absorption by operating at wavelengths longer than 813 nm.

Planar integrated photonic devices require high-quality thin films that can act as low-loss planar waveguides. We deposit thin films of TiO_2 on oxidized silicon wafers using reactive sputtering of titanium metal in an oxygen environment. Our

optimized amorphous and polycrystalline anatase TiO_2 thin films have high refractive indices from 2.4–2.8 at visible wavelengths and planar waveguiding losses as low as 0.4 dB/cm (826 nm).

Using electron-beam lithography, we structure these films to fabricate waveguides with sub-micron features. We quantify propagation losses at wavelengths from 633 to 1550 nm and observe losses as low as 4 dB/cm. Next, we demonstrate devices including bends, directional couplers, and racetrack resonators that form the basic building-blocks for more advanced photonic devices.

Finally, we observe the first nonlinear optics in integrated TiO_2 waveguides. By measuring the spectral broadening of femtosecond pulses in TiO_2, we quantify the nonlinear index of anatase TiO_2 around 1565 and 794 nm. In addition, we explore stimulated Raman scattering and third-harmonic generation in our waveguides. With this first demonstration of an integrated nonlinear optical device in TiO_2, we conclude that TiO_2 is a viable and promising material for all-optical applications.

Contents

Citations to previously published work

Parts of this dissertation cover research reported in the following articles:

1. C. C. Evans and E. Mazur, "Nanophotonics: Linear and nonlinear optics at the nanoscale", in *Nano-Optics for Enhancing Light-Matter Interactions on a Molecular Scale: Plasmonics, Photonic Materials and Sub-Wavelength Resolution*, edited by B. Di Bartolo and J. Collins (Springer London, Limited, 2012).

2. C. C. Evans, J. D. B. Bradley, E. A. Martí-Panameño, and E. Mazur, "Mixed two- and three-photon absorption in bulk rutile (TiO_2) around 800 nm," *Optics Express*, **20** (3), 3118-3128, 2012.

3. C. C. Evans, K. Shtyrkova, J. D. B. Bradley, O. Reshef, E. Ippen, and E. Mazur, "Spectral broadening in anatase titanium dioxide waveguides at telecommunication and near-visible wavelengths," *Optics Express*, **21** (15), 18582-18591, 2013.

4. J. D. B. Bradley, C. C. Evans, J. T. Choy, O. Reshef, P. B. Deotare, F. Parsy, K. C. Phillips, M. Lončar, and E. Mazur, "Submicrometer-wide amorphous and polycrystalline anatase TiO_2 waveguides for microphotonic devices," *Optics Express*, **20** (21), 23821-23831, 2012.

5. J. T. Choy, J. D. B. Bradley, P. B. Deotare, I. B. Burgess, C. C. Evans, E. Mazur, and M. Lončar, "Integrated TiO_2 resonators for visible photonics," *Optics Letters*, **37** (4), 539-541, 2012.

Acknowledgments

> "Listen Lad, I've built this kingdom up from nothin'. When I started here, all there was was swamp. Everyone said I was daft to build a castle on a swamp, but I built it all the same, *just to show 'em!* It sank into the swamp, so... I built a second one... that sank into the swamp... so I built a third one... That burned down, fell over, then sank into the swamp, *but the fourth one STAYED UP!* And that's what you're going to get, Lad, the strongest castle in these islands."
>
> *The King of the Swamp Castle*, Monty Python and the Holy Grail

Success in research and in life often requires failure, however, I have been very lucky to have a network of people who have helped me navigate and persevere through these pitfalls to find success and fulfilment in science. I am very thankful for countless people who helped me find my way to graduate school and the many more that helped me get through it.

Getting to graduate school has been a long journey that was only possible thanks to many amazing mentors. Early on, my uncle Steve encouraged creativity and inquiry through lively debate. Equally inspiring was my uncle Charlie, who possessed unbounded knowledge and had the patience to explain population inversion to a curious 10 year old. At the end of high school before I headed off to pursue a music career, my math teacher, Mr. Kaczowka, reminded me to "keep up with calculus". I had many mentors when I was learning to become a recording engineering, including Mark Wessel, Carl Beatty, Will Sandalls, and Jesse Henderson. They helped me develop the confidence, independence, eyes and ears for detail, and the "whatever it takes" attitude that has stayed with me throughout graduate school. When I began repairing audio equipment, Bill Gitt and Burt Price helped me develop trouble-shooting skills and introduced me to "The Art of Electronics", which later enticed me to study electrical engineering at the University of Massachusetts, Lowell. I am

deeply indebted to my physics professors David Pullen, Kunnat Sebastian, Robert Giles, and Albert Altman at UMass Lowell for reawakening the passion for physics that I had forgotten about since high school. The focus and follow-through I learned in music, powered by my revitalized excitement for physics, lead me to pursue a PhD at Harvard, thanks to all of my mentors along the way.

I would like to thank Eric Mazur for giving me such a wonderful opportunity to work in his group. Eric has given me the freedom and responsibility to plan and execute my research that, with his encouragement and respect, has developed my skill and self-confidence as a researcher. Eric's elegance for presentations has allowed me to study the "magic" he brings to what could be a dry scientific talk. Eric has also been a great friend outside of the lab. We have shared many adventures from mountain biking and hiking to cross-country skiing, and we managed to squeeze in the occasional squash game into our busy schedules. As I go forth and explore new directions, I realize and appreciate how much Eric has helped me grow both as a scientist and as a person.

My adjustment to the research and lifestyle at Harvard was made easier by all of the senior students and postdocs. First, I want to thank Jonathan Bradley for the dedication, and push that made this work successful. I am truly grateful for his guidance and his friendship. Many senior students reminded me to focus on the bigger picture: Sam Chung (for giving me "the speech"), Tina Shih (for reminding me that "reviewers will just get lost in too many details"), Eric Diebold (for his "go big or go home" attitude), and Paul Peng (my Photonics West "roomie", who demonstrates the value of keeping an open mind). Additionally, Rafael Gattass, Geoff Svacha, Mark

Winkler, Prakriti Tayalia, and Jessica Watkins provided a warm welcome and were exemplary role models. I would also like to thank the many postdocs within the Mazur Group: Julie Schell (for conversations that "go a little too far"), Laura Tucker (for reminding me of my music beginnings), Jin Suntivich (for the amazing scientific discussions), and Valeria Nuzzo (for telling me to "just graduate").

I feel I could not have made it through without the support and friendship of every member of the Mazur Group. I would like to thank all of my peers including Jason Dowd (for switching projects), Kevin Vora (for all the help figuring out various optical toys), and Renee Sher (my go-to person for advice). I have had a lot of fun learning what it means to be a graduate student from such a great group of mentors and peers. I also greatly appreciate the younger students and visitors who have made life in the lab fun: Sally Kang ("um ma!"), Yu-Ting Lin (for the occasional help writing text messages), Michael Moebius (for being a good sport, "Mickey"), Kasey Phillips (for all the writing help and for organizing impromptu group activities), Phil Munoz (for making the Mazur Group men look classy), Kelly Miller ("Squaaasssh!!"), Ben Franta (for all the adventures), Orad Reshef (for singing about his dislike for e-beam), Sarah Greisse-Nascimento (for the colorful nickname), Guoliang Deng (for all the spicy food), Nabiha Saklayen (for bringing an upbeat attitude to the lab), Fauzy Wan (for all the squash), Erwin Marti (mi amigo), Markus Pollnau (for the music in "The Marsala Room"), Virginia Casas (for being on top of all the details), and Sebastien Courvoisier (for making the office sound like an airport). I will truly treasure all of the memories, from Erice to hiking, skiing, mountain biking, canoeing, and squash. I am honored to say the Mazur Group has been my family throughout

graduate school. I could not ask to be surrounded by a better group of people.

This research would not be possible without the extended nanophotonics team. I owe the silica nanowire team a great amount of thanks as their work directly inspired this research: Limin Tong, Rafael Gattass, Geoff Svacha, and Jason Dowd. It has been an honor to collaborate with so many great professors: Marko Loncar, Markus Pollnau, Erwin Marti, Erich Ippen, Anming Hu, Tobias Voss, and Hamed Majedi. I want to thank all of the students and postdocs who helped pioneer this work (Jennifer Choy, Jonathan Bradley, Parag Deotare, Ruwan Senaratne, Kasey Phillips, and Ian Burgess) and everyone else who helped realize its potential (Francois Parsy, Orad Reshef, Katia Shtyrkova, and Michael Moebius). I would also like to recognize all of the undergraduate students who have supported my research over the years: Lili Jiang, Grisel Rivera Batista, Stephanie Swartz, Vivek Thacker, and Cavanaugh Welch. These last few months have been a fun and dynamic time for research, thanks to the unique makeup of our extended subgroup. Orad's creativity and passion to realize actual devices has allowed him to persevere, even when banished to the cleanroom. Michael's curiosity, versatility, and camaraderie have helped me see the forest through the trees. Katia's skill, excitement, and unbounded dedication to "getting it right" reminds me of my favorite recording sessions that were so electrifying, the energy kept us working well into the next morning. Although she has just joined, working with Sarah has been fantastic and I am excited to see where her fresh perspective, dependability, and eagerness to learn will take her. Finally, I would like to say that I am thrilled for the next generation of the nanophotonics team and wish them continued success.

Lastly, and most importantly, I would like to thank my family. I am very fortunate to have parents who are so supportive of all the different directions I have taken. I am also extremely grateful for my wife, Lesley. She has been an amazing partner whose support and understanding has allowed me to follow my passions. I have always believed life is not a straight line. My winding journey to graduate school is a testament to this belief, and has only been possible and enjoyable thanks to a near countless number of people, for whom I am deeply indebted.

Christopher C. Evans

Cambridge, Massachusetts

September, 2013

Acknowledgements of Financial Support

The research described in this thesis was supported by the National Science Foundation under contracts ECCS-0901469 and ECCS-1201976, by the MRSEC Program of the National Science Foundation under contract DMR-0819762, with additional funding from the Harvard Quantum Optics Center.

To my family.

Chapter 1

Introduction

As the information age progresses, our demand for telecommunications bandwidth and computing power continues to skyrocket. By 2020, the demand for single-channel bandwidth is predicted to exceed 1 Tb/s [1]. Such high bitrates will require processing ultrafast optical signals. One potential solution is to use all-optical processing to avoid the speed limitations imposed by electron transport times in conventional optoelectronic devices. An ideal photonic material should enable ultrafast optical signal processing from the interconnect band (800–900 nm) to telecommunications bands (1300–1600 nm). Additionally, integration of such a material will enable a compact, low-cost, mass-producible solution that can be further integrated with other electronic and photonic components, all on a chip. To achieve these goals, we seek to push the boundaries of ultrafast devices by developing a new integrated photonics medium: titanium dioxide (TiO_2).

While promising all-optical devices have been demonstrated using current materials [2–5], most nonlinear photonic materials suffer from a variety of limiting fac-

tors [6]. These limitations include: high materials cost (III-V semiconductors), poor stability (polymers), large device size due to low nonlinearity and low refractive index contrast (various glasses), high linear absorption (plasmonic materials), high multi-photon absorption (silicon [7]), and low maximum operating intensities (chalcogenide glasses [8]). In addition, nearly all of these technologies address the 1.5-µm telecommunications band exclusively and neglect wavelengths around 1300 nm as well as the interconnect band (800–900 nm). We see an imminent need for a novel integrated material that overcomes many of these limits and bridges the gap between these communication bands.

Ultrafast all-optical processing demands a near-instantaneous material response. For bit rates greater than 1 Tb/s, this is currently only achievable with passive, non-resonant nonlinearities such the electronic Kerr effect. Therefore, the goal is to maximize the Kerr nonlinearity while minimizing parasitic two-photon absorption. Given that the onset of two-photon absorption occurs at $2\hbar\omega = E_g$ [9] and the nonlinearity in semiconductors scales at E_g^{-4} [10], the solution is simple: choose a material with a bandgap energy that is just over twice the single photon energy. For operation from 800–1600 nm, these scaling rules suggests a bandgap energy of 3.1 eV.

Titanium dioxide's band gap of 3.1 eV provides transparency throughout the visible spectrum and ultrafast all-optical capabilities for wavelengths greater than 800 nm. It has a high nonlinear refractive index that is 30 times silica, with vanishing two-photon absorption around 800 nm [11]. Its high linear refractive index (2.4–2.8) enables dense on-chip integration of nanophotonic waveguides, adaptable waveguide dispersion, and high confinement. This high confinement produces effective nonlin-

earities up to 100,000 times that found in standard silica fiber. By exploiting the ultrafast nonlinear Kerr effect in TiO_2, our devices can achieve theoretical bitrates in excess of 1 Tb/s. In addition, TiO_2 is inexpensive, abundant, and nontoxic. By using deposited TiO_2 and conventional fabrication procedures, we present a scalable technology that is readily integrated into electronic or other photonic systems. These properties make TiO_2 an excellent candidate material for all-optical processing.

In this thesis, we explore and develop integrated TiO_2 devices for nonlinear optical applications. We first gain insight into the nonlinear properties of TiO_2 by studying the bulk material near its half-bandgap (800 nm). Next, we develop and characterize thin films of TiO_2. Using these films, we form waveguides and then demonstrate several linear optical building-block devices. Finally, we characterize the nonlinear optical properties of integrated TiO_2 waveguides and compare with our bulk measurements. By developing and exploring this novel photonic material, we demonstrate that TiO_2 is a promising material platform for integrated nonlinear optics at wavelengths ranging from the interconnect band (800–900 nm) to the telecommunication band (1300–1600 nm).

1.1 Organization of the dissertation

We introduce TiO_2 by first studying the bulk material, then we optimize thin-films to serve as a preform for devices, and lastly, we develop and explore integrated nanowire devices.

Chapter 2 serves as an basic introduction to linear and nonlinear optics of bulk materials. This lays the foundation for all the work covered in this thesis. We discuss

how to evaluate a potential nonlinear optical material using nonlinear coefficients. Next, we show the additional control that nanoscale structure can have for nonlinear optical applications. To demonstrate these principles, we summarize previous work using silica nanowires.

Chapter 3 explores the nonlinear properties of bulk rutile TiO_2 around its half-bandgap (800 nm) using the Z-scan technique. We first describe the experimental and analytical methods, then present two studies. The first study measures nonlinear refraction, then the second quantifies mixed two- and three-photon absorption.

Chapter 4 summarizes a series of deposition studies to develop high-quality thin films suitable for device fabrication. This results in two varieties of TiO_2 films, depending on the deposition temperature. Lower temperature results in amorphous TiO_2; at higher temperature, we obtain polycrystalline anatase.

Chapter 5 uses these thin films to fabricate waveguides. Using these waveguides, we explore their linear optical properties. Lastly, we form them into basic devices including bends, directional couplers, and racetrack resonators.

Chapter 6 reports on the nonlinear properties of polycrystalline anatase waveguides. Nonlinear effects include spectral broadening, stimulated Raman scattering, and third-harmonic generation.

Chapter 7 concludes this thesis and presents an outlook for the future of TiO_2 photonics.

Appendix A describes a theoretical model we developed to extract mixed two- and three-photon absorption coefficients from open-aperture Z-scan measurements.

Appendix B presents a preliminary study of photodarkening of amorphous TiO_2

thin films using femtosecond pulses around 800 nm.

Appendix C presents the nonlinear Sagnac interferometer as a promising device for all-optical modulation, switching, and logic. In this section, we present the basic theory of nonlinear Sagnac interferometers. We conclude with simulation results using theoretically and experimentally obtained parameters for TiO_2 and present key milestones necessary to achieve full modulation in a Sagnac interferometer.

Chapter 2

Linear and nonlinear optics

Light propagation in sub-wavelength waveguides enables tight confinement over long propagation lengths to enhance nonlinear optical interactions. Not only can sub-wavelength waveguides compress light spatially, they also provide a tunable means to control the spreading of light pulses in time, producing significant effects even for small pulse energies. By exploring linear and nonlinear light propagation, first for free-space conditions, then for sub-wavelength guided conditions, we demonstrate how sub-wavelength structure can enhance nonlinear optics at the nanoscale.

2.1 Linear optics

We begin by developing a fundamental understanding of light propagation in materials that we will build upon as we cover linear and nonlinear light propagation in nanoscale structures. We introduce plane-wave propagation in bulk materials and develop a simple model to explain the frequency dependence of the dielectric function. We

observe how this frequency dependence affects optical pulse propagation. With this foundation, we will later explore nonlinear optics in TiO_2.

2.1.1 Plane waves

Throughout this chapter, we will develop and use several different wave equations. Each wave equation makes assumptions to localize energy both in time, using pulses, and in space, using waveguides. The first wave equation assumes *plane waves at a single frequency* (continuous wave). To localize in time, an optical pulse requires the interference of multiple frequencies. Therefore, we model a pulse as a single frequency modulated by an envelope function using the *slowly varying envelope approximation* (SVEA). We use waveguides to confine light spatially by taking advantage of sustained propagating solutions of Maxwell's equations, known as modes. Light guided within a mode propagates in an analogous way to plane waves using the *guided-wave equation*. Finally, we will augment this equation using the SVEA to form a fourth wave equation to describe pulses in waveguides. Strong light-matter interactions create a nonlinear polarization that we must include. We will introduce the physics of nonlinear optics in the simplest way possible, using plane waves. Lastly, we will modify the pulsed waveguide equation to include third-order nonlinear optical effects to form the Nonlinear Schroedinger Equation (NLSE).

Wave equation for plane waves

We start with Maxwell's equations in a linear, homogeneous material with no free charges or currents:

$$\begin{array}{llll} (i) & \vec{\nabla}\cdot\vec{E}=0 & (iii) & \vec{\nabla}\times\vec{E}=-\frac{\partial\vec{B}}{\partial t} \\ (ii) & \vec{\nabla}\cdot\vec{B}=0 & (iv) & \vec{\nabla}\times\vec{B}=\frac{\mu_r\varepsilon_r}{c^2}\frac{\partial\vec{E}}{\partial t}. \end{array} \tag{2.1}$$

In this set of coupled differential equations, the vectors $\vec{E}$ and $\vec{B}$ are the electric and magnetic fields, ε_r and μ_r are the relative electric permittivity and the relative magnetic permeability and we define $c \equiv 1/\sqrt{\varepsilon_0\mu_0}$, which is the speed of light in vacuum. If we take the curl of equation (2.1) (iii) and substitute equations (i) and (iv), the wave equation is commonly derived as [12]:

$$\nabla^2\vec{E}-\frac{\mu_r\varepsilon_r}{c^2}\frac{\partial^2\vec{E}}{\partial t^2}=0. \tag{2.2}$$

To gain physical insight into this equation, we define $k^2/\omega^2 \equiv \mu_r\varepsilon_r/c^2$ and solve this differential equation in one dimension for $\vec{E}\,(z,t)$:

$$\vec{E}\,(z,t)=\frac{1}{2}\left[\vec{E}_0e^{i(kz-\omega t)}+c.c.\right]=\mathrm{Re}\left[\vec{E}_0e^{i(kz-\omega t)}\right], \tag{2.3}$$

where $\vec{E}_0$ is the complex electric field vector, z is the position, t is the time and *c.c.* denotes the complex conjugate of the previous term, insuring the field is a real quantity. The last expression uses phasor notation, which is mathematically more compact. Consequently, we will use phasor notation occasionally and leave it to the reader to take the real part.

Velocity of plane waves in a material

The first question one might ask is: what is the speed of this wave? For a fixed location, the time between crests is $T = 2\pi/\omega = 1/f$, where f is the frequency and the quantity $\omega = 2\pi f$ is the angular frequency. In a similar way, the spacing between crests is given by the wavelength in the material, $\lambda_{mat} = 2\pi/k$, and we refer to $k = 2\pi/\lambda_{mat}$ as the wavevector. In three dimensions, k is a vector that points in the direction of the phase velocity; however, we will use it as a scalar for one dimension. This wavelength in the material λ_{mat} should not be confused with the wavelength in vacuum λ_0. For most materials we can approximate $\mu_r \approx 1$ [12]. We also allow the relative permittivity ε_r to be frequency dependent using $\varepsilon_r(\omega)$. We determine the speed of the wave v by observing how long it takes a single crest to propagate one wavelength:

$$v = \frac{\lambda_{mat}}{T} = \lambda_{mat} f = \frac{\omega}{k} = \frac{c}{\sqrt{\varepsilon_r(\omega)}} \equiv \frac{c}{n(\omega)}. \tag{2.4}$$

Here, we define the index of refraction as $n(\omega) \equiv ck(\omega)/\omega$. If ε_r and μ_r are unity (their values in vacuum), the velocity is the speed of light in vacuum c. We refer to the velocity at which the crests and the troughs of the wave propagate as the *phase velocity*, to distinguish it from the pulse or group velocity.

Propagation losses

We have defined the refractive index in terms of the square root of the dielectric function. What happens if the dielectric function is complex? A complex dielectric constant causes k to be complex and we must consider the consequences of a complex index of refraction, $\tilde{n}(\omega)$. Therefore, we must further define the index of refraction

as:

$$n(\omega) \equiv \mathrm{Re}\left[\frac{ck(\omega)}{\omega}\right] = \mathrm{Re}\left[\sqrt{\varepsilon_r(\omega)}\right]. \tag{2.5}$$

Considering a complex wavevector for a single frequency given by $\tilde{k} = k' + ik''$, we get immediate physical insight by observing the propagation of a plane wave in a medium with a complex wavevector:

$$\vec{E}(z,t) = \frac{1}{2}\left[\vec{E}_0 e^{i[(k'+ik'')z-\omega t]} + c.c.\right] = \frac{1}{2}\left[\vec{E}_0 e^{-k''z} e^{i(k'z-\omega t)} + c.c.\right]. \tag{2.6}$$

We see that k'' exponentially attenuates the wave as it propagates.

We rarely measure the electric field directly and instead measure the time-averaged power. For a plane wave, the time-averaged power per unit area is the intensity or irradiance I defined by:

$$I = \frac{c\varepsilon_0 n}{2}\left|\vec{E}(z,t)\right|^2. \tag{2.7}$$

Writing equation (2.6) in terms of intensity, the expression becomes:

$$I = \frac{1}{2}c\varepsilon_0 n\left|\vec{E}_0\right|^2 e^{-2k''z}, \tag{2.8}$$

and the imaginary part of the wavevector k'' is responsible for intensity attenuation. Attenuation is important because high intensities are critical for efficient nonlinear interactions, thus, attenuation is a limiting factor. We use this expression to define the attenuation coefficient given by $\alpha = 2k''$, having units of inverse length. When the attenuation is due to absorption, we refer to α as the absorption coefficient. In a similar manner, if we allow the index of refraction to become complex, we define $\tilde{n} \equiv n + i\kappa$ and this new term κ is known as the extinction coefficient $\kappa(\omega) \equiv ck''(\omega)/\omega$.

In the optical engineering literature, losses are usually notated in units of decibels per length, and it is convenient to relate this convention to the absorption coefficient. For a distance L, the intensity decreases from I_0 to $I(L)$ and the loss is given by [13]:

$$\text{loss in dB} = -10\log_{10}\left(\frac{I\left(L\right)}{I_0}\right) = -10\log_{10}\left(\frac{I_0 e^{-\alpha L}}{I_0}\right) = 10\left(\alpha L\right)\log_{10}\left(e\right) \approx 4.34\alpha L. \tag{2.9}$$

Using this equation and assuming the losses are due to absorption, we can relate all of these quantities:

$$\begin{aligned} \kappa\left(\omega\right)\left[\text{unitless}\right] &= k''\left(\omega\right)\tfrac{c}{\omega}\left[k'' \text{ in } \text{m}^{-1}\right] \\ &= \tfrac{\alpha(\omega)}{2}\tfrac{c}{\omega}\left[\alpha \text{ in } \text{m}^{-1}\right] \approx \tfrac{\text{loss}}{8.68}\tfrac{c}{\omega}\left[\text{loss in dB/m}\right]. \end{aligned} \tag{2.10}$$

Although we have assumed that the loss of light is due to absorption, any source of attenuation, such as absorption and scattering from inhomogeneities within the materials, limits nonlinear interactions. Therefore, we should use the inclusive definition of α (the attenuation coefficient) when analyzing nonlinear devices.

2.1.2 Dielectric function

The frequency-dependent dielectric function produces a frequency-dependent wavevector that is important for pulse propagation. To understand the origins of the frequency dependent dielectric function, we will develop a simple model here.

Drude-Lorentz Model

We classically model the interaction between an electromagnetic wave and electrons bound to their respective ion-cores using the Drude-Lorentz model. By modeling the

electron-ion interaction as a one-dimensional simple harmonic oscillator, we explore the features of the dielectric function. The binding force between an electron and its ion is given by:

$$F_{binding} = -m{\omega_0}^2 x, \tag{2.11}$$

where m is the mass of the electron, ω_0 is the resonant frequency of the electron-nucleus system, and x is the displacement of the electron. While in motion, the electron is also subject to a damping force with strength proportional to a constant γ, resisting its movement. The damping force is given by:

$$F_{damping} = -m\gamma \frac{dx}{dt}. \tag{2.12}$$

Lastly, a steady oscillating electric field, using equation (2.3) with $z = 0$, provides the driving force given by:

$$F_{driving} = -eE = -eE_0 e^{-i\omega t}, \tag{2.13}$$

proportional to the charge of the electron e. The equation of motion thus becomes:

$$m\frac{d^2x}{dt^2} + m\gamma\frac{dx}{dt} + m{\omega_0}^2 x = -eE_0 e^{-i\omega t}, \tag{2.14}$$

whose solution is:

$$x\left(t\right) = x_0 e^{-i\omega t}, \qquad x_0 \equiv -\left(\frac{e}{m}\right)\frac{1}{({\omega_0}^2 - \omega^2) - i\gamma\omega}E_0. \tag{2.15}$$

The oscillating electron creates a dipole moment given by:

$$p\left(t\right) = -ex\left(t\right) = \left(\frac{e^2}{m}\right)\frac{1}{({\omega_0}^2 - \omega^2) - i\gamma\omega}E_0 e^{-i\omega t}. \tag{2.16}$$

In a bulk material, we have N of these dipoles per unit volume and we must express the dipole moment as a vector:

$$\vec{P}(t) = \frac{Ne^2}{m}\frac{1}{({\omega_0}^2 - \omega^2) - i\gamma\omega}\vec{E}(t) \equiv \varepsilon_0\chi_e\vec{E}(t). \tag{2.17}$$

From the polarization, with the definitions for the susceptibility $\vec{P}(t) \equiv \varepsilon_0\chi_e\vec{E}(t)$ and the relative dielectric function $\varepsilon_r(\omega) \equiv 1 + \chi_e$, we solve for the relative dielectric function:

$$\varepsilon_r(\omega) = 1 + \frac{Ne^2}{m\varepsilon_0}\frac{1}{({\omega_0}^2 - \omega^2) - i\gamma\omega}. \tag{2.18}$$

Dielectric function for a single resonance

We realize that the relative dielectric function is a complex quantity $\varepsilon_r(\omega) = {\varepsilon_r}'(\omega) + i{\varepsilon_r}''(\omega)$. For a single resonance, we separate equation (2.18) into real and imaginary parts:

$${\varepsilon_r}'(\omega) + i{\varepsilon_r}''(\omega) = \left(1 + \frac{Ne^2}{m\varepsilon_0}\frac{({\omega_0}^2 - \omega^2)}{({\omega_0}^2 - \omega^2)^2 + \gamma^2\omega^2}\right) + i\left(\frac{Ne^2}{m\varepsilon_0}\frac{\gamma\omega}{({\omega_0}^2 - \omega^2)^2 + \gamma^2\omega^2}\right). \tag{2.19}$$

Plotting the displacement of the electron x as a function of frequency ω in Figure 2.1 (left, solid line), we see that the amplitude on-resonance is largest. The phase shift (dashed line) is initially in-phase for frequencies below resonance and lags behind at higher frequencies. This results in a complex dielectric function which has a strong imaginary component ${\varepsilon_r}''(\omega)$ on resonance (Figure 2.1, right, dashed line). Observing the real component ${\varepsilon_r}'(\omega)$, the bound charges keep up with the driving field and the wave propagates more slowly, corresponding to a higher refractive index. At resonance, energy is transferred to the bound charges and the wave is attenuated.

Above the resonance, the bound charges cannot keep up and the dielectric acts like a vacuum.

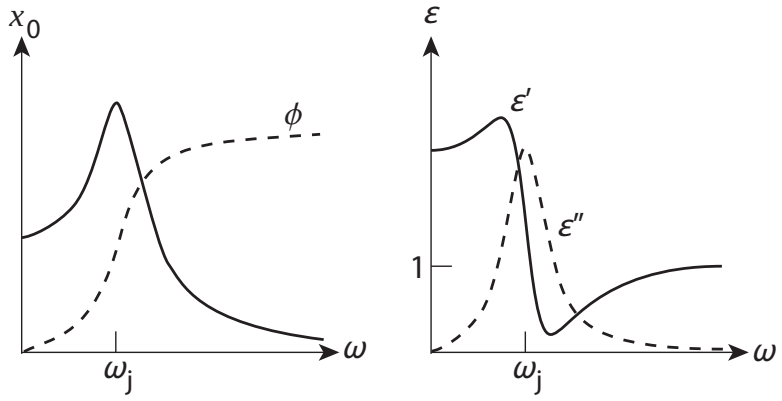

Figure 2.1: The displacement amplitude x_0 and phase ϕ versus frequency for the Drude-Lorentz model (left). The complex frequency-dependent dielectric function for a single resonance (right).

Multiple resonances

In a bulk material, the electric field becomes a vector and we sum over all dipoles, creating a material polarization given by:

$$\vec{P}(t) = \left(\frac{Ne^2}{m}\right) \sum_j \frac{f_j}{({\omega_j}^2 - \omega^2) - i\gamma_j\omega} \vec{E}_0(t) \equiv \varepsilon_0 \chi_e \vec{E}(t) \,. \tag{2.20}$$

Here, we sum over the individual electrons for each molecule of the bulk material. The subscript j corresponds to a single resonant frequency ω_j with a damping coefficient γ_j, of which there are f_j electrons per molecule and there are N molecules per unit volume. This model is most quantitatively accurate in the dilute gas limit [12]; however, it provides a qualitative insight into solid materials. Using this polarization,

the complex relative dielectric function is given by:

$$\varepsilon_r(\omega) = 1 + \left(\frac{Ne^2}{\varepsilon_0 m}\right) \sum_j \frac{f_j}{({\omega_j}^2 - \omega^2) - i\gamma_j \omega}. \tag{2.21}$$

We can extend the dielectric function to include other resonances, as shown in Figure 2.2. At very high frequencies, the dielectric acts like a vacuum. At ultraviolet and visible frequencies, electronic resonances play a dominant role. Lastly, for low frequencies, the driving fields are slow enough to access both ionic and dipolar resonances.

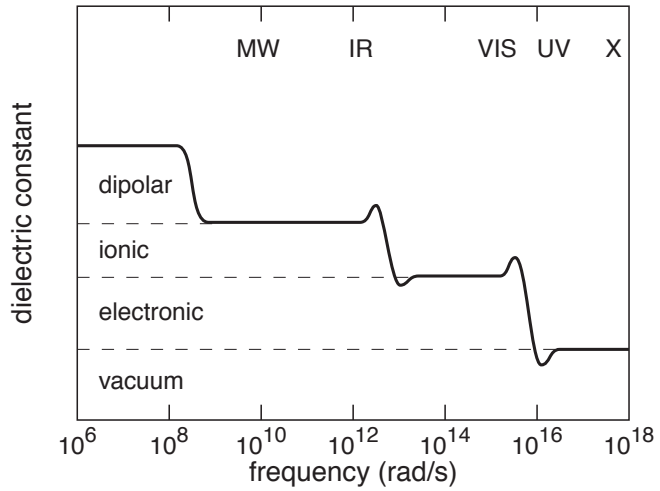

Figure 2.2: Schematic illustration of the various contributions to the dielectric constant across the electromagnetic spectrum.

Metals

Now, let us consider the case where the binding energy is very weak, as in the case of a metal. Here, we have $F_{binding} \approx 0$. The equation of motion reduces to:

$$m\frac{d^2x}{dt^2} + m\gamma\frac{dx}{dt} = -eE_0 e^{-i\omega t}, \tag{2.22}$$

which has a solution of:

$$x(t) = \left(\frac{e}{m}\right) \frac{1}{\omega^2 + i\gamma\omega} E_0 e^{-i\omega t}. \tag{2.23}$$

Metals are known for their conductivity. In the low frequency limit, where $\omega \ll \gamma$, the generated current J is proportional to the velocity, charge, and number of electrons per unit volume, given by:

$$J = -Ne\frac{dx}{dt} = \frac{Ne^2}{m}\frac{1}{\gamma - i\omega}E(t) \approx \frac{Ne^2}{m\gamma}E(t) \equiv \sigma E(t). \tag{2.24}$$

From this expression, we readily defined the conductivity σ. In the high frequency limit $\omega \gg \gamma$ we find that:

$$J = \frac{Ne^2}{m}\frac{1}{\gamma - i\omega}E(t) \approx -i\frac{Ne^2}{m\omega}E(t) \equiv \sigma E(t), \tag{2.25}$$

and that the conductivity σ is complex and that J is out of phase with $E(t)$.

At optical frequencies, if the frequency is large relative to the damping ($\omega \gg \gamma$) we can approximate $\gamma \approx 0$, and we obtain the free electron model:

$$\varepsilon(\omega) = 1 - \frac{Ne^2}{m\varepsilon_0}\frac{1}{\omega^2} \equiv 1 - \frac{{\omega_p}^2}{\omega^2}. \tag{2.26}$$

Here, we define the plasma frequency as $\omega_p \equiv Ne^2/(m\varepsilon_0)$. For a typical metal, having 10^{22} electrons/cm^3, this density corresponds to a plasma frequency of 6×10^{15} rad/s or a vacuum wavelength of 330 nm. When the frequency of light is above the plasma frequency, ${\varepsilon_r}'' = 0$ and the metal is transparent. At the plasma frequency, the real part of the dielectric function becomes zero. Below the plasma frequency, the dielectric function is completely imaginary; the wave does not propagate and is reflected instead. Therefore, the metal acts as a high-pass filter and can be used as a mirror.

2.1.3 Pulse propagation

Short optical pulses are a key tool for nonlinear optical research as they can achieve high intensities even with small pulse energies and low average powers. However, pulsed transmission requires multiple frequencies propagating coherently together, as shown in Figure 2.3 (left). The frequency-dependent phase velocity causes the pulse envelope to propagate at its own velocity and can lead to temporal pulse spreading during propagation shown in Figure 2.3 (right). In this section, we will address these issues and develop the mathematical framework to handle pulses.

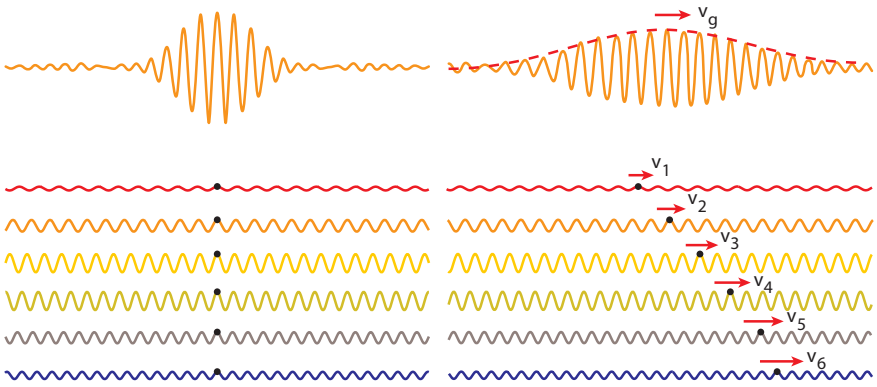

Figure 2.3: A pulse is made up of many frequencies (left) that propagate with their own phase velocities yet travel together at one group velocity. If the group velocity is frequency dependent, this can lead to temporal pulse spreading (right).

Phase versus group velocity

To understand how a pulse propagates, let us begin with a simple model (two continuous waves of differing angular frequencies and wavevectors) and explore what happens

when they propagate together. The two propagating waves are given by:

$$y_1 = A\sin\left(k_1 z - \omega_1 t\right) \text{ and } y_2 = A\sin\left(k_2 z - \omega_2 t\right), \tag{2.27}$$

where A is the amplitude of the waves (identical values here), k_1 and k_2 are the wave vectors, and ω_1 and ω_2 are the frequencies for the first and second waves (respectively). Each wave has a speed, or phase velocity, given by:

$$v_1 = \frac{\omega_1}{k_1} = f_1\lambda_1 \text{ and } v_2 = \frac{\omega_2}{k_2} = f_2\lambda_2. \tag{2.28}$$

If we superimpose these waves by adding, then apply the trigonometric identity:

$$\sin\alpha + \sin\beta = 2\cos\left(\frac{\alpha-\beta}{2}\right)\sin\left(\frac{\alpha+\beta}{2}\right), \tag{2.29}$$

we arrive at the following result:

$$y \equiv y_1 + y_2 = 2A\cos\left[\frac{1}{2}\left(z\left(k_1-k_2\right) - t\left(\omega_1-\omega_2\right)\right)\right]\sin\left[\frac{k_1+k_2}{2}z - \frac{\omega_1+\omega_2}{2}t\right]. \tag{2.30}$$

We can simplify this expression using the following definitions:

$$\begin{aligned} \Delta k \equiv k_1 - k_2 \quad &\text{and} \quad \Delta\omega \equiv \omega_1 - \omega_2, \\ k \equiv \tfrac{k_1+k_2}{2} \quad &\text{and} \quad \omega \equiv \tfrac{\omega_1+\omega_2}{2}, \end{aligned} \tag{2.31}$$

to show:

$$y = 2A\cos\left[\frac{1}{2}\left(z\Delta k - t\Delta\omega\right)\right]\sin\left(kz - \omega t\right). \tag{2.32}$$

This expression takes the form of a fast oscillating term (the sine function) modulated slowly by the cosine function. To visualize this behavior, we set $t = 0$ and plot equation (2.32) in Figure 2.4. We see the beating between these two frequencies forms the basis of a simple pulse or group. We call the cosine function the *envelope*, and the fast oscillatory part the *carrier*.

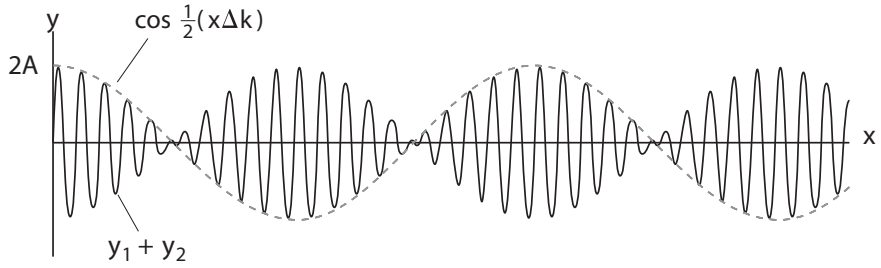

Figure 2.4: Two waves interfere, forming a simple pulse train whereby a carrier wave is modulated by a slowly varying envelope $\cos(z\Delta k/2)$.

Observing equation (2.32), we see two relevant velocities. The velocity of the carrier wave from the sine term is:

$$v_p = \frac{\omega}{k} = f\lambda. \tag{2.33}$$

We refer to this velocity as the *phase velocity*. Similarly, the envelope has a velocity given by:

$$v_g = \frac{\Delta\omega}{\Delta k} \rightarrow \frac{d\omega}{dk}, \tag{2.34}$$

which we refer to as the *group velocity*. If we consider the case of no dispersion, the phase velocities of the two waves are the same $v_p = \frac{\omega_1}{k_1} = \frac{\omega_2}{k_2}$ and we find that:

$$\begin{aligned} v_g &= \tfrac{\Delta\omega}{\Delta k} = \tfrac{\omega_1-\omega_2}{k_1-k_2} = \tfrac{\omega_1/(k_1k_2)-\omega_2/(k_1k_2)}{1/k_2-1/k_1} \\ &= \tfrac{v_p/k_2-v_p/k_1}{1/k_2-1/k_1} = v_p\tfrac{1/k_2-1/k_1}{1/k_2-1/k_1} = v_p \ , \end{aligned} \tag{2.35}$$

and therefore the group velocity and the phase velocity are identical. There are several categories of linear dispersion as shown in Table 2.1.

If we consider a single optical element, such as a mirror, lens, or length of fiber, the group velocity will cause a fixed time-delay for the pulse, known as the *group delay*. The group delay can deviate substantially from the delay caused by the phase

Table 2.1: Types of linear dispersion

$\frac{dn}{d\omega} > 0$	normal dispersion	$v_g < v_p$
$\frac{dn}{d\omega} = 0$	no dispersion	$v_g = v_p$
$\frac{dn}{d\omega} < 0$	anomalous dispersion	$v_g > v_p$

velocity (inversely dependent on the index) in a dispersive media. The difference between the phase and group velocity within a single optical element will cause an offset between the absolute phase of the carrier and the envelope of the pulse, known as the *carrier-envelope offset*.

Gaussian pulse

In our simple model, we have only considered two propagating waves. As we add more waves in between these initial waves, the envelope is no longer defined by a simple cosine function and the pulses can separate in time, as shown in Figure 2.3. To describe such a pulse, we use the slowly-varying envelope approximation (in phasor notation):

$$\vec{E}(z,t) = A(z,t)\, e^{i(kz-\omega_0 t)}\hat{x}. \tag{2.36}$$

Here, $A(z,t)$ is the envelope function and $\exp(i(kz-\omega_0 t))$ is the carrier. A Gaussian is a common shape for an ultrashort pulse, given by:

$$\begin{aligned} \vec{E}(z,t) &= \vec{E}_0 \exp\left(-\tfrac{1}{2}\left(\tfrac{t}{\tau}\right)^2\right) e^{i(kz-\omega_0 t)} \\ &= \vec{E}_0 \exp\left(-2\ln(2)\left(\tfrac{t}{\tau_{\mathrm{FWHM}}}\right)^2\right) e^{i(kz-\omega_0 t)}, \end{aligned} \tag{2.37}$$

Here, $\vec{E}_0$ is the amplitude of the electric field, t is time and both τ and τ_{FWHM} reflect the pulse duration. Additionally, ω_0 and k are the angular frequency and wavevector

of the carrier wave (respectively).

We can measure the pulse duration in several ways by applying different clipping levels ($1/e$,$1/e^2$, full-width at half maximum) and calculating these in terms of either the electric field or the power. Using equation (2.37), we define two definitions for the pulse duration with respect to the time-averaged power:

$$P(t) = P_p \exp\left(-(t/\tau)^2\right) = P_p \exp\left(-4\ln(2)\,(t/\tau_{\mathrm{FWHM}})^2\right). \tag{2.38}$$

Here, $P(t)$ is the power as a function of time t, and P_p is the peak power. In the first pulse-duration definition, τ is the duration from the peak to the $1/e$-clipping level and is often used for its mathematical simplicity. Experimentally, we use the full-width at half-maximum duration, related to τ using $\tau_{\mathrm{FWHM}} = 2\sqrt{\ln 2}\tau$.

A Gaussian pulse is very convenient because the spectrum also takes the shape of a Gaussian. A pulse is as short as possible if the spectral phase is frequency-independent. We refer to such a pulse as being *transform limited* and we use the time-bandwidth product: $\tau\Delta\nu \approx 0.44$ (for a Gaussian). Alternatively, we can write this expression in terms of wavelength to show: $\tau \approx 0.44\lambda^2/(c\Delta\lambda)$. Thus, the transform limited pulse duration is inversely dependent on the spectral width. For example, a transform limited 100-fs pulse has a spectral width of $\Delta\lambda \approx 9.4$ nm at 800 nm and a width of $\Delta\lambda \approx 35.3$ at 1550 nm.

2.1.4 Temporal pulse broadening

We observed how a frequency-dependent propagation constant gives rise to phase velocity and group velocity. If we continue to expand the propagation constant in a

Taylor series, we see:

$$\begin{aligned} k(\omega) &= k_0 + \left.\frac{dk}{d\omega}\right|_{\omega_0}(\omega-\omega_0) + \left.\frac{1}{2}\frac{d^2k}{d\omega^2}\right|_{\omega_0}(\omega-\omega_0)^2 + \dots \\ &= k_0 + k'(\omega-\omega_0) + \tfrac{1}{2}k''(\omega-\omega_0)^2 + \dots . \end{aligned} \tag{2.39}$$

Of these coefficients, we recall that k_0 and k' are related to the phase and group velocities, respectively. We find that higher order dispersion, beginning with k'', begins to change the shape of the pulse, reducing the peak intensity, and is therefore a critical factor for many nonlinear experiments.

Group velocity dispersion

There is a simple way to think about the spreading of a pulse as it propagates in a material. Consider a transform limited pulse of light, consisting of a spectrum of colors. If we cut the spectrum in half, we will have a higher-energy "blue" pulse and a lower-energy "red" pulse. If we propagate these partial pulses in a media with only linear dispersion (k' is constant and $k''=0$), both will propagate with the same group velocity, and we can recombine the blue and red pulses to obtain the original pulse duration. If the medium has higher order dispersion, $k'' \neq 0$ and the group velocity changes as a function of frequency, causing the red and blue pulses to separate in time as they propagate. When we recombine them, there will be a delay between the red and blue pulses, and their combination will be of longer duration than the original pulse. This fixed delay is known as the *group delay dispersion* (GDD). An optical element, such as a fixed length of fiber or a microscope objective, will have a fixed amount of GDD.

If we care about the pulse duration as we propagate, we require the GDD per

unit length, which is known as the *group velocity dispersion* (GVD). We define the group velocity dispersion in a material as:

$$\text{GVD} = \frac{\partial}{\partial\omega}\left(\frac{1}{v_g}\right) = \frac{\partial}{\partial\omega}\left(\frac{\partial k}{\partial\omega}\right) = \frac{\partial^2 k}{\partial\omega^2}, \tag{2.40}$$

GVD has units of time squared per length (often fs^2/mm).

We can clarify the difference between GDD and GVD by considering an experiment that consists of several optics (mirrors, lenses, etc.) leading up to a nonlinear pulse propagation experiment (for example, a fiber or a photonic chip). Each optical element before the fiber adds a fixed amount of GDD, broadening the pulse. However, we must consider the interplay between the nonlinearity and dispersion as the pulse propagates within the fiber and therefore, we consider the fiber's GVD.

Just as we have normal and anomalous dispersion previously, the group velocity dispersion can be normal or anomalous. Here, we consider positive values of the GVD as normal and negative values as anomalous. This labeling convention is because most materials at visible wavelengths show normal GVD. For example, the GVD of silica is normal (positive) in the visible, reaches zero around 1.3 µm, and becomes anomalous (negative) for longer wavelengths, such as 1.5 µm.

To make things slightly more confusing, the optical engineering community takes the derivative of the refractive index with respect to the wavelength, producing another term, known as the *dispersion parameter* D given by:

$$D = -\frac{\lambda}{c}\frac{d^2 n}{d\lambda^2} = -\frac{2\pi c}{\lambda^2} GVD = -\frac{2\pi c}{\lambda^2}\frac{\partial^2 k}{\partial\omega^2}. \tag{2.41}$$

The dispersion parameter has units of time per length squared, often specified in ps/nm/km. These units are convenient when we estimate strong pulse broadening.

It is important to note that the sign of the dispersion parameter is opposite to that of GVD, and thus, a material with anomalous dispersion has a *positive* dispersion parameter. These are often used interchangeably, so one should avoid saying "positive" and "negative" dispersion and instead use "normal" and "anomalous" dispersion.

Dispersive pulse broadening

To observe dispersive broadening, we can consider the Gaussian pulse from equation (2.37) and apply the effects of group velocity dispersion given by k''. To simplify the analysis, we assume $k_0 = 0$ and $k' = 0$, both of which will not broaden our pulse, as we have shown. We take the Fourier transform of equation (2.37):

$$E\left(z=0,\omega\right) = \frac{1}{\sqrt{2\pi}}\int_{-\infty}^{\infty} E_0 e^{\frac{-t^2}{2\tau^2}} e^{-i\omega_0 t} e^{i\omega t} dt = E_0 \tau e^{\frac{-\tau^2(\omega_0-\omega)^2}{2}}. \tag{2.42}$$

From here, we can add the spectral phase and take the inverse Fourier transform:

$$\begin{aligned} E\left(z=L,t\right) &= \tfrac{1}{\sqrt{2\pi}}\textstyle\int_{-\infty}^{\infty} E_0 \tau e^{\frac{-\tau^2(\omega_0-\omega)^2}{2}} e^{-i\frac{k''}{2}(\omega-\omega_0)^2 L} e^{-i\omega t} d\omega \\ &= \tfrac{\tau E_0}{\sqrt{\tau^2+ik''L}} e^{\frac{-t^2}{2\tau^2\left(1+\left(\frac{k''L}{\tau^2}\right)^2\right)}} e^{i\frac{k''Lt^2}{2\left((k''L)^2+\tau^4\right)}} e^{-i\omega_0 t}. \end{aligned} \tag{2.43}$$

We notice that the amplitude changes as the pulse broadens and there is additional phase from the propagation. We also observe that the middle term closely resembles the form of equation (2.42) if we let:

$$\tau' = \tau\sqrt{1+\left(\frac{k''L}{\tau^2}\right)^2}, \tag{2.44}$$

thus, the pulse broadens in time by $\sqrt{1+\left(k''L/\tau^2\right)^2}$. We can write this expression in terms of the full-width at half-maximum to show:

$$\tau'_{\mathrm{FWHM}} = \tau_{\mathrm{FWHM}}\sqrt{1+\left(4\ln 2\frac{GVD}{{\tau_{\mathrm{FWHM}}}^2}d\right)^2} \approx 4\ln 2\frac{GVD}{\tau_{\mathrm{FWHM}}}d, \tag{2.45}$$

as it propagates through a distance d. This approximation is valid for strong dispersive broadening. For silica fiber at 800 nm, GVD = 36 fs^2/mm, which corresponds to a dispersion parameter D of -106 ps/nm/km. Consider a 100 fs pulse at 800 nm; after propagating through 1 m of silica fiber, it will have a duration of 1 ps. As the broadening is very strong, we see that using the dispersion parameter is convenient to estimate the pulse duration. For this situation, a 100-fs pulse at 800 nm has a spectral bandwidth of $\Delta\lambda \approx 9.4$ nm, thus $\Delta\tau \approx |-106 \text{ ps/nm/km}| \, (9.4 \text{ nm} \times 1 \text{ m}) = 996$ fs, which is approximately correct. However, this expression is invalid for small broadening, for example, from a 10-cm length of fiber. Recall that a short pulse has a wide bandwidth and is therefore more susceptible to dispersive broadening than a longer pulse with a reduced bandwidth. This phenomenon creates the counter-intuitive effect where a narrowed spectrum can produce a shorter pulse for a given amount of dispersion.

Group velocity dispersion compensation

To facilitate strong nonlinear interactions with low pulse energies, we require very short pulses. As each optical element adds dispersion, potentially broadening the pulse, we address the practical concern of pulse compression here. As the change in pulse duration is a linear effect, we can counteract an amount of normal GDD with an equal amount of anomalous GDD to recover the original pulse duration. With sufficient GDD, we can pre-compensate additional optics to form the shortest pulse somewhere later in the optical path. For visible and most NIR optical elements, the dispersion is normal. To compensate, we can use a device that has tunable anomalous

GDD known as a pulse compressor.

Tunable anomalous group delay dispersion can be achieved using both gratings and prisms, as shown in Figure 2.5 (top and bottom, respectively). These configurations consist of four elements (gratings or prisms) such that the first two provide half of the intended group delay dispersion starting with a collimated beam and ending with parallel, spatially dispersed colors. The second pair provides the second half of the GDD and reforms the collimated beam. Very often, we use a single grating or prism pair with a mirror that reflects the spatially dispersed colors backward to "fold" the compressor onto itself. This folding-mirror is angled slightly so that the compressed, retroreflected beam can be diverted by another mirror that is initially missed by the incoming beam

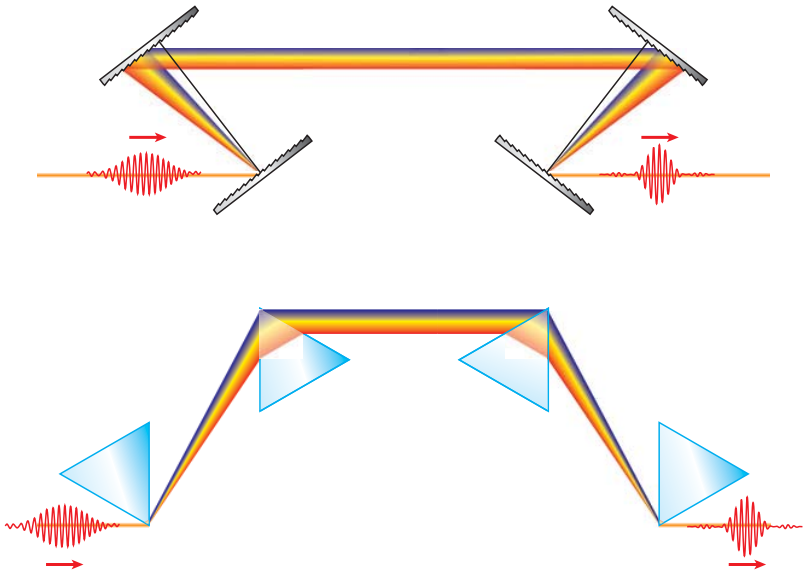

Figure 2.5: Schematic of a two types of pulse compressors: a grating compressor (top) and a prism compressor (bottom).

To determine the GDD through a grating or prism pair, we determine the

wavelength-dependent path length and the resulting phase through a single pair. From here, we calculate $d^2\varphi/d\omega^2$. For the case of a grating pair, the total GDD is [14]:

$$\frac{d^2\varphi}{d\omega^2} = -\frac{(1/\omega^2)\,(\lambda/\Lambda)\,(2\pi L/\Lambda)}{\left[1-(\sin\theta_i - \lambda/\Lambda)^2\right]^{3/2}}. \tag{2.46}$$

Here, ω is the angular frequency, λ is the wavelength, Λ is the spatial period, θ_i is the angle of incidence of the incoming light, and L is the separation of the gratings. We tune the amount of dispersion compensation by changing the separation of the gratings, L.

For the case of a prism pair, the situation is more complicated because of the additional material dispersion within the prism itself. We find the following approximation is useful for small amount of material dispersion when the prism pair is cut and aligned to the Brewster angle (for maximum efficiency) [15]:

$$\frac{d^2\varphi}{d\omega^2} \approx \frac{\lambda^3}{2\pi c^2}\left[-8L\left(\frac{dn}{d\lambda}\right)^2 + 8\left(\frac{d^2n}{d\lambda^2}\right)\left(D_{1/e^2}\right)\right]. \tag{2.47}$$

Here, L is the separation of the prisms, D_{1/e^2} is the beam diameter (at the $1/e^2$ clipping level), n is the index of refraction, and c is the speed of light. The first term provides tunable anomalous dispersion and depends on the prism material and the separation of the prisms (similar to gratings). The second term is very often normal and depends on the propagation length in the prism material.

For a fixed separation L, the amount of dispersion compensation obtained using gratings is very large compared to prisms, making for shorter separation distances and potentially smaller footprints. For example, to compensate 1000 fs^2 around 800 nm, fused silica prisms require a separation of 77 cm and SF10 glass prisms require 21 cm [15]. A grating compressor with 600 grooves/mm and a 13° angle requires

only 2.8 mm of separation to achieve the same dispersion compensation. Although, gratings compressors can correct for very strong dispersion, they typically have high amounts of loss and cannot be used for all applications, such as intra-cavity dispersion compensation for a femtosecond laser.

2.2 Nonlinear optics

The strong electric fields achievable in a laser can drive the motion of electrons and atoms to create a *nonlinear polarization*. This nonlinear polarization gives rise to many effects, from the generation of new frequencies to light-by-light modulation. In this section, we will explore these effects and establish a foundation to later explore all-optical devices.

2.2.1 Nonlinear polarization

For weak electric fields, the polarization depends linearly on the material susceptibility (in SI units):

$$\vec{P} = \varepsilon_0 \chi \vec{E}. \tag{2.48}$$

For stronger electric fields, we expand equation (2.48):

$$P = \varepsilon_0 \left(\chi^{(1)} E + \chi^{(2)} E^2 + \chi^{(3)} E^3 + ... \right), \tag{2.49}$$

to produce a series of polarizations:

$$P = P^{(1)} + P^{(2)} + P^{(3)} + ..., \tag{2.50}$$

where $P^{(1)} \equiv \varepsilon_0 \chi^{(1)} E$ is the linear polarization, $P^{(2)} = \varepsilon_0 \chi^{(2)} E^2$ is the second-order nonlinear polarization, and so on. Although we have written this polarization in

terms of scalars, the electric field is a vector quantity and therefore $\chi^{(1)}$ is a second rank tensor (with 9 elements), $\chi^{(2)}$ is a third rank tensor (27 elements), and $\chi^{(3)}$ is a fourth rank tensor (81 elements), to which we often apply symmetry arguments to isolate unique, non-zero terms [16].

These nonlinear polarization terms act as a driving field in the wave equation, forming the nonlinear wave equation:

$$\nabla^2 \vec{E} - \frac{n^2}{c^2}\frac{\partial^2 \vec{E}}{\partial t^2} = \frac{1}{\varepsilon_0 c^2}\frac{\partial^2 \vec{P}^{\mathrm{NL}}}{\partial t^2}. \tag{2.51}$$

Here, n is the linear index of refraction and P^{NL} is the nonlinear polarization (excluding the linear term from equation (2.50) contained within n). This driving term acts as a source of new propagating waves.

Second-order nonlinear polarization

The second order nonlinear polarization is responsible for several effects involving three photons. For example, two photons can combine to make a third photon. If the two initial photons are of the same (different) frequency, this effect is second harmonic generation (sum-frequency generation). Alternatively, one photon can split to make two photons through difference frequency generation.

Not all bulk crystals exhibit second-order nonlinearities. Let us consider the centrosymmetric case where a crystal has inversion symmetry. For the second order polarization, we find that:

$$\vec{P}^{(2)} = \varepsilon_0 \chi^{(2)} \vec{E}\vec{E}. \tag{2.52}$$

If we invert the sign of the fields, we expect the same polarization, only with an

opposite sign, therefore:

$$-\vec{P}^{(2)} = \varepsilon_0 \chi^{(2)} \left(-\vec{E}\right)\left(-\vec{E}\right) = \varepsilon_0 \chi^{(2)} \vec{E}\vec{E}. \tag{2.53}$$

Both equations cannot be simultaneously true in a centrosymmetric material unless $\chi^{(2)}$ vanishes. Therefore, materials possessing inversion symmetry do not exhibit second-order nonlinearities within the bulk material. Only a handful of materials, typically crystals, are non-centrosymmetric and exhibit $\chi^{(2)}$ nonlinearities. Meanwhile, most materials have inversion symmetry including many crystals such as TiO_2, amorphous materials such as glasses, as well as liquids and gases. However, inversion symmetry is broken at an interface, leading to second-order nonlinearities even for materials with bulk inversion symmetry [17, 18].

Now, let us consider second-harmonic generation in a non-centrosymmetric crystal. Here, we have an electric field given by:

$$\vec{E}\left(\vec{r},t\right) = \frac{1}{2}\left(E\left(\vec{r},t\right)e^{-i\omega_0 t} + \text{c.c.},\right)\hat{x}, \tag{2.54}$$

where we consider a single polarization in the x-direction. We use the slowly varying envelope approximation through the use of the scalar field $E\left(\vec{r},t\right)$, which we will refer to simply as E. The nonlinear polarization is given by:

$$\vec{P}^{\text{NL}}\left(\vec{r},t\right) = \frac{1}{2}\left(P^{\text{NL}}\left(\vec{r},t\right)e^{-i\omega_{\text{NL}} t} + \text{c.c.}\right)\hat{x}, \tag{2.55}$$

which produces a second-order polarization:

$$\vec{P}^{(2)} = \varepsilon_0 \chi^{(2)} \vec{E}\vec{E} = \varepsilon_0 \chi^{(2)} \left[\frac{EE^*}{2} + \frac{1}{2}\left(\frac{E^2}{2}e^{-i2\omega_0 t} + c.c.\right)\right]\hat{x}\hat{x}. \tag{2.56}$$

From this expression, we see two terms. The first is at zero frequency, and is not responsible for generating a propagating wave as it vanishes when operated on by the

time-derivative in the wave equation. The next term is at twice the initial frequency, known as the *second harmonic*. We can solve this expression for the slowly varying amplitude of the nonlinear polarization and the frequency to show:

$$P^{(2)}_{2\omega_0} = \frac{\varepsilon_0 \chi^{(2)} E^2}{2} \quad \text{and} \quad \omega_{\text{NL}} = 2\omega_0. \tag{2.57}$$

The process of generating second-harmonic signal efficiently requires additional considerations, known as phase matching, which is often achieved using birefringent crystals [19]. In a similar way, a field consisting of two different frequencies can generate terms at the second harmonic of each frequency, as well as for their summation and difference.

Third-order nonlinear polarization

The majority of materials are centrosymmetric and therefore, the first non-zero nonlinear polarization is usually the third-order polarization. Writing this polarization out, we find:

$$\vec{P}^{(3)}(t) = \varepsilon_0 \chi^{(3)} \vec{E}\vec{E}\vec{E} = \varepsilon_0 \chi^{(3)} \left[\frac{1}{2} \left(\frac{E^3}{4} e^{-i3\omega_0 t} + c.c. \right) + \frac{1}{2} \left(\frac{3}{4} |E|^2 E e^{-i\omega_0 t} + c.c. \right) \right] \hat{x}\hat{x}\hat{x}. \tag{2.58}$$

Two terms emerge, leading to distinct physical processes. As before, the slowly varying envelope amplitude and nonlinear frequency for the first term is:

$$P^{(3)}_{3\omega_0} = \frac{\varepsilon_0 \chi^{(3)} E^3}{4} \quad \text{and} \quad \omega_{\text{NL}} = 3\omega_0, \tag{2.59}$$

respectively. This term is responsible for third harmonic generation. This process is often not efficient unless we use phase-matching techniques.

Meanwhile, the second term is extremely relevant, as the polarization occurs at the original frequency. The slowly varying amplitude and nonlinear frequency are:

$$P_{\omega_0}^{(3)} = \frac{3\varepsilon_0 \chi^{(3)} |E|^2 E}{4} \quad \text{and} \quad \omega_{\text{NL}} = \omega_0. \tag{2.60}$$

This effect leads to a nonlinear index of refraction and is extremely important for devices. The nonlinear index is perhaps the most frequently observed nonlinearity. Not only do all materials exhibit third-order nonlinearities, but also, phase-matching is automatically satisfied as the polarization is *at the original frequency*. Therefore, we can observe this nonlinear effect without the specialized configurations required of other nonlinearities, such as second- and third-harmonic generation.

Anharmonic oscillator model

In the same way that we used the Drude-Lorentz model to gain physical insight into the linear dielectric function, we can use the classical anharmonic oscillator model to explore electronic nonlinearities. We base this nonlinear model on the same principles as before, but replace the binding force with an altered, nonlinear force. Just as the binding force for the Drude model is proportional to an electron's displacement from its equilibrium position (x), the second-order polarization requires a term proportional to x^2. For the (more applicable) third-order case, the binding force is:

$$F_{\text{binding}} = -m{\omega_0}^2 x + mbx^3, \tag{2.61}$$

where we have introduced a force term proportional to x^3 with a phenomenological proportionality constant of b. Typically, b is on the order of ω_0^2/d^2, where d is on the

order of the Bohr radius [16]. The equation of motion becomes:

$$m\frac{d^2x}{dt^2} + m\gamma\frac{dx}{dt} + m{\omega_0}^2 x - mbx^3 = -eE_0e^{-i\omega t}. \tag{2.62}$$

We proceed in much the same way as before, which we will not show here. For the case of self-phase modulation, we arrive at [16]:

$$\chi^{(3)} = \frac{Nbe^4}{\varepsilon_0 m^3 D(\omega)^3 D\left(-\omega\right)}, \tag{2.63}$$

where $D\left(\omega\right) = \omega_0^2 - \omega^2 - i\gamma\omega$. This expression takes a very similar form as χ_e from equation (2.18), with additional factors of e^2 and m^{-2}, along with multiple degenerate resonances given by $D(\omega)$. We can approximate this expression if we are far from resonance using:

$$\chi^{(3)} \approx \frac{Ne^4}{\varepsilon_0 m^3 \omega_0^6 d^2}. \tag{2.64}$$

2.2.2 Nonlinear index of refraction

The third-order nonlinear polarization gives rise to a nonlinear index of refraction that we use to make all-optical devices. An intensity-dependent index leads to self-phase modulation (SPM) for coherent waves and cross-phase modulation for non-coherent waves. In addition, by allowing $\chi^{(3)}$ to take on complex values, we discover a new source of *nonlinear absorption*, analogous to the linear absorption caused by a complex $\chi^{(1)}$.

Intensity-dependent refractive index

If we take the slowly varying envelope amplitudes for the linear polarization $P^{(1)} = \varepsilon_0 \chi^{(1)} E$ and add this new term, we can write an effective linear susceptibility:

$$P^{(1)} + P^{(3)}_{\omega_0} = \varepsilon_0 \chi^{(1)} E + \frac{3\varepsilon_0 \chi^{(3)} |E|^2}{4} E = \varepsilon_0 \left(\chi^{(1)} + \frac{3\chi^{(3)}}{4} |E|^2 \right) E = \varepsilon_0 \chi^{(1)}_{eff} E. \quad (2.65)$$

This effective susceptibility creates an effective index of refraction:

$$n = \sqrt{\mathrm{Re}\,(\varepsilon)} = \sqrt{\mathrm{Re}\left(1 + \chi^{(1)}_{eff}\right)} = \sqrt{1 + \mathrm{Re}\,(\chi^{(1)}) + \frac{3\mathrm{Re}\,(\chi^{(3)})}{4} |E|^2}, \quad (2.66)$$

which we can simplify by expanding around small $|E|^2$:

$$n \approx \sqrt{1 + \mathrm{Re}\,(\chi^{(1)})} + \frac{3\mathrm{Re}\left(\chi^{(3)}\right)}{8\sqrt{1 + \mathrm{Re}\,(\chi^{(1)})}} |E|^2 = n + \frac{3}{8n} \mathrm{Re}\left(\chi^{(3)}\right) |E|^2 = n + \bar{n}_2 |E|^2. \quad (2.67)$$

This derivation produces our first definition of the nonlinear refractive index (in terms of $|E|^2$):

$$\bar{n}_2 = \frac{3}{8n_0} \mathrm{Re}\left(\chi^{(3)}\right). \quad (2.68)$$

In terms of the intensity, equation (2.67) becomes:

$$n = n_0 + n_2 I = n_0 + \frac{3}{4n_0^2 \varepsilon_0 c} \mathrm{Re}\left[\chi^{(3)}\right] I. \quad (2.69)$$

The nonlinear index is often referred to as the *Kerr effect*. For a single wave propagating in a Kerr-medium, the wave's intensity modulates the index of refraction, which modulates the phase of the wave as it propagates. We refer to this process as *self-phase modulation*. A similar effect occurs across different, non-coherent waves, known as *cross-phase modulation* [16]. We note that n_2 can be either positive or negative, depending on the origin of the nonlinearity (electronic polarization, molecular

orientation, thermal, etc.). For the electronic, non-resonant nonlinear polarization in silica, n_2 is positive and therefore, we will assume a positive value of n_2. For silica, the nonlinear index of refraction is 2.2–3.4 $\times 10^{-20}$ m^2/W [20, 21].

We have used SI units during this derivation, thus $\chi^{(3)}$ is in units of m^2/V^2. Often $\chi^{(3)}$ is given in electrostatic units (cm^3/erg, or simply esu). Meanwhile, the nonlinear index is typically quoted in units of cm^2/W. The conversion is [16]:

$$n_2 \left(\frac{cm^2}{W} \right) = \frac{12\pi^2}{n_0^2 c} 10^7 \chi^{(3)}_{esu}. \tag{2.70}$$

Two-photon absorption

Using a complex valued $\chi^{(3)}$, we see that the third-order nonlinear polarization implies a nonlinear extinction coefficient, given by:

$$\kappa = \kappa_0 + \kappa_2 I = \kappa_0 + \frac{3}{4n_0^2 \varepsilon_0 c} \mathrm{Im}\left[\chi^{(3)}\right] I. \tag{2.71}$$

Using $\alpha = 2\omega_0 \kappa / c$, we can write this expression as the nonlinear absorption:

$$\alpha(I) = \alpha_0 + \alpha_2 I = \kappa_0 + \frac{3\omega_0}{2n_0^2 \varepsilon_0 c^2} \mathrm{Im}\left[\chi^{(3)}\right] I. \tag{2.72}$$

The new term is responsible for two-photon absorption and has units of length per power. For two-photon absorption to occur, the total energy of both photons must be large enough to promote an electron from the valence to the conduction band, and therefore $\chi^{(3)}$ must necessarily be frequency dependent. For degenerate (same frequency) two-photon absorption, the single-photon energy must be at least half of the band-gap energy.

We note that two-photon absorption is a *third-order process* and not a second-order process. We can see this distinction by observing equation (2.58), whereby

the imaginary third-order nonlinear polarization produces a wave at the original frequency. This out-of-phase wave adds destructively with the original wave, resulting in attenuation.

Nonlinear index scaling

Understanding how n_2 scales with bandgap energy helps us select candidate materials for all-optical applications. To understand how n_2 scales, we consider a direct-bandgap semiconductor with bandgap energy of E_g and photon energies less than E_g. Sheik-Bahae *et al.* developed a simple model for an instantaneous nonlinearity which neglects one-photon processes to describe the scaling of two-photon absorption and the nonlinear index [10, 22]. We find that, under these approximations, two-photon absorption has the form:

$$\alpha_2 = \frac{K\sqrt{E_p}}{n_0^2 E_g^3} F_2\left(2\hbar\omega/E_g\right), \tag{2.73}$$

where K is an empirical constant found to be 3.1×10^3 when E_p and E_g are in eV and n_2 is in units of cm^2/W, and $E_p = 21$ eV. Here, we use the universal function:

$$F_2\left(2x\right) = \frac{(2x-1)^{3/2}}{(2x)^5} \quad \text{for} \quad 2x > 1. \tag{2.74}$$

We can related this expression to n_2 using a nonlinear version of the Kramers-Kronig relation to show:

$$n_2 = K\frac{\hbar c\sqrt{E_p}}{2n_0^2 E_g^4} G_2\left(\hbar\omega/E_g\right), \tag{2.75}$$

where:

$$G_2\left(x\right) = \frac{-2 + 6x - 3x^2 - x^3 - \frac{3}{4}x^4 - \frac{3}{4}x^5 + 2(1-2x)^{3/2}\Theta\left(1-2x\right)}{64x^6}, \tag{2.76}$$

with $\Theta(y)$ being the Heaviside step function.

We plot equations (2.73) and (2.75) in Figure 2.6 and observe several key features [10,22]. First, we find that two-photon absorption does not occur for photon energies below $E_g/2$, which means that we can avoid the effects of two-photon absorption by operating at sufficiently long wavelengths. Second, we find that n_2 is relatively flat for small photon energies, then reaches a maximum around $\hbar\omega/E_g \approx 0.54$, reaches zero around $\hbar\omega/E_g \approx 0.69$, and goes negative for higher photon energies. From equation (2.75), we also see that n_2 scales as E_g^{-4}. The strong bandgap scaling suggests that, for a given wavelength of operation λ, a ideal material (having negligible two-photon absorption and maximal n_2) should have a bandgap energy of $E_g \geq 2hc/\lambda$.

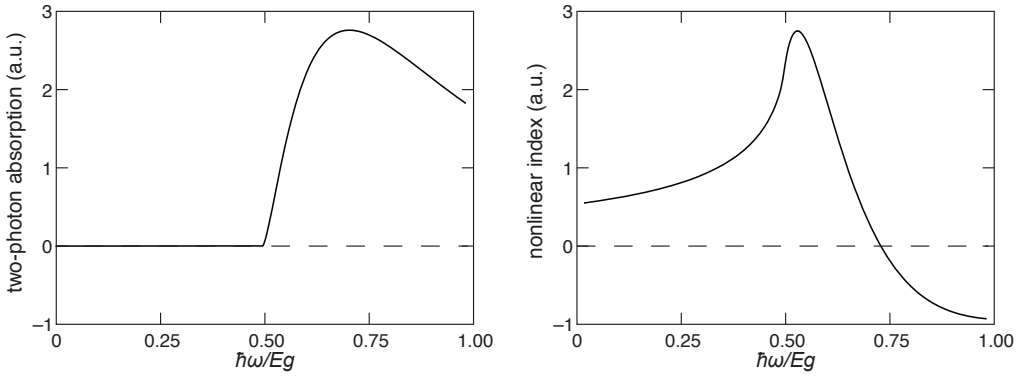

Figure 2.6: Frequency dependence of the two-photon absorption coefficient (left) and the nonlinear index of refraction (right).

2.2.3 Self-phase modulation effects

In this section, we look at how self-phase modulation gives rise to several effects that we can use in devices. Applying self-phase modulation in the spatial domain leads to self-focusing; and in the time domain, this effect is responsible for spectral broaden-

ing, supercontinuum generation, and four-wave mixing. These processes require high intensities to be efficient; therefore, all sources of loss are important for materials and devices. With losses in mind, we explore the nonlinear figures of merit to assess current and future materials for third-order nonlinear optical applications.

Nonlinear phase

Understanding the accumulation of nonlinear phase is essential, as it forms the basis for many all-optical devices. Starting with equation (2.3), we realize that as the wave propagates, it accumulates a phase given by $\varphi = kL$, where L is the distance traveled. Adding the nonlinear index we see:

$$\varphi = k\left(I\right)L = \frac{2\pi}{\lambda}\left(n + n_2 I\right)L = \frac{2\pi n L}{\lambda} + \frac{2\pi n_2 L}{\lambda} I = \varphi_L + \varphi_{NL}. \tag{2.77}$$

The intensity alters the phase accumulated by a factor of:

$$\phi_{NL} = \frac{2\pi n_2 L}{\lambda} I, \tag{2.78}$$

through a process known as self-phase modulation (SPM). For a plane wave at a single frequency, the wave gains a fixed phase change per unit distance. As we will show in Appendix C, we can use this nonlinear phase to modulate nonlinear interferometers.

Self-focusing

If we make the intensity non-uniform in space or in time, these gradients results in self-focusing or spectral-broadening, respectively. To demonstrate the effects of a spatial non-uniformity, let us consider a Gaussian beam profile passing through a thin, flat, nonlinear-material. At the center of the beam, the intensity is higher than

at the edges, therefore the center accumulates a larger amount of nonlinear phase. For a material with a positive nonlinear index, the distribution of nonlinear phase shifts is analogous to a positive lens and causes the wave to focus. The Z-scan technique uses this intensity-dependent lens to measure the nonlinearity of bulk samples [23, 24].

Spectral broadening

If we make the intensity non-uniform in time using a pulse, self-phase modulation broadens the pulse's spectrum. Consider a pulse at a fixed location in space that has an intensity that changes in time, $I(t)$. Using equation (2.77), we can take a derivative with respect to time, to find a change in frequency given by:

$$\Delta\omega = -\frac{d\varphi}{dt} = -\frac{2\pi}{\lambda} L n_2 \frac{dI\,(t)}{dt}. \tag{2.79}$$

For the case of a Gaussian pulse, we remember that equation (2.38) can be converted to intensity by dividing by an area and replacing $P_p \rightarrow I_0$. With equation (2.79), we find the frequency shift for a Gaussian pulse is:

$$\Delta\omega = \frac{2\pi}{\lambda} L n_2 \frac{8\ln(2)}{\tau^2} t I\,(t)\,. \tag{2.80}$$

From this equation, we realize that $I(t)$ is always positive and $tI(t)$ goes from negative to positive. At a fixed position, negative time is the front of the pulse and therefore, the front of the pulse experiences a negative frequency shift, creating longer, "red" wavelengths in the front. Oppositely, the back end of the pulse (positive time values) is frequency shifted positively and the wavelengths appear "blue-shifted". These are new frequencies that are not present in the original pulse. Alternatively, one can picture this process as the peak of a pulse traveling with a slower phase velocity and

therefore, the carrier wave "stretches out" in the front and "bunches up" in the back, creating red and blue wavelengths in the front and back, respectively.

Group velocity dispersive effects are extremely important in a real system. For a positive nonlinearity and normal GVD, both effects cause a "red" wave-packet to move toward the front of the pulse and a "blue" wave-packet to the back, reducing the intensity, leading to a limited amount of spectral broadening. If GVD is low, the broadening can be very strong, forming a continuum of wavelengths, known as supercontinuum or "white light" generation. In the case of anomalous GVD, the effects of self-phase modulation and GVD are opposite and can lead to a situation where the two effects balance one another, creating stable packets of light, known as *solitons*.

Nonlinear figures of merit

Material losses limit the performance of SPM-based all-optical switches. Switches made using nonlinear interferometers, for example, require a specified total nonlinear phase for full modulation [25–27]. Total losses (both intrinsic and from fabrication) limit the maximum amount of nonlinear phase by attenuating the wave as it propagates, making full modulation impossible for certain materials [25]. We quantify these limitations using dimensionless parameters known as the nonlinear figures of merit.

To proceed, we ask: for a given material, what is the maximum amount of nonlinear phase that the wave can accumulate? Let us consider the simplest case of a monochromatic plane-wave experiencing both linear and nonlinear attenuation. Our

first step must be to determine the intensity as a function of distance using:

$$\frac{dI(z)}{dz} = -\left[\alpha_0 + \alpha_2 I(z)\right] I(z). \tag{2.81}$$

This differential equation has a solution of the form:

$$I(z) = I_0 e^{-\alpha_0 z}\left[1 + I_0\alpha_2\left(\frac{1-e^{-\alpha_0 z}}{\alpha_0}\right)\right]^{-1}. \tag{2.82}$$

The total nonlinear phase accumulated over a distance L is therefore:

$$\text{total } \varphi_{NL} = \int_0^L \frac{2\pi n_2}{\lambda} I(z)\, dz = 2\pi\left(\frac{n_2}{\alpha_2\lambda}\right)\ln\left[1 + I_0\alpha_2\left(\frac{1-e^{-\alpha_0 L}}{\alpha_0}\right)\right]. \tag{2.83}$$

From this expression, we define the effective length for plane-waves and in waveguides as [24]:

$$L_{\text{eff}} = \frac{1-e^{-\alpha_0 L}}{\alpha_0}. \tag{2.84}$$

Taking $L \to \infty$, the effective length becomes $1/\alpha_0$ and the maximum nonlinear phase is given by:

$$\max \varphi_{\text{NL}} = 2\pi\left(\frac{n_2}{\alpha_2\lambda}\right)\ln\left[1 + \left(\frac{n_2}{\alpha_2\lambda}\right)^{-1}\left(\frac{n_2 I_0}{\alpha_0\lambda}\right)\right]. \tag{2.85}$$

From this result, we can define two figures [6, 27]:

$$W \equiv \left(\tfrac{n_2 I_0}{\alpha_0\lambda}\right) \quad \text{and} \quad T^{-1} \equiv \left(\tfrac{n_2}{\alpha_2\lambda}\right), \tag{2.86}$$

and we can rewrite equation (2.85) as:

$$\max \varphi_{\text{NL}} = 2\pi T^{-1}\ln\left[1 + TW\right]. \tag{2.87}$$

The W and T^{-1} figures of merit are associated with linear losses and two-photon absorption, respectively.

Now, let us look at the simplest case, where we have only linear losses, by taking the limit of equation (2.87) as $T^{-1} \to \infty$. The maximum nonlinear phase amounts to $2\pi W$, and if we require max $\varphi_{\mathrm{NL}} > 2\pi$, we require that $W > 1$. This result suggests the need for a minimum operating intensity: for a given attenuation coefficient α_0 we require an intensity of $I_0 > \alpha_0\lambda/n_2$. The damage threshold of the material or additional nonlinear effects (particularly two- and three-photon absorption) pose limits for all-optical switching. Alternatively, for a given operating intensity, we must achieve total losses (absorption and scattering) of $\alpha_0 < n_2 I_0/\lambda$.

Usually, we are only interested in materials with no intrinsic linear absorption and therefore, two-photon absorption and imperfections from the fabrication are limiting factors. For strong two-photon absorption, T^{-1} is small, and the wave is strongly absorbed at the start of propagation. After the intensity quickly drops, we will continue to accumulate nonlinear phase at a reduced rate, requiring very large devices for full modulation. For a fixed value of T^{-1}, we can determine the required value of max $\varphi_{\mathrm{NL}} > 2\pi$:

$$W_{\mathrm{req}} > \frac{\left(e^T - 1\right)}{T} = 1 + \frac{1}{2}T + \frac{1}{6}T^2 + ... \tag{2.88}$$

For reasonable values of W_{req} (near unity), we use the following guidelines [6, 27]:

$$W = \left(\tfrac{n_2 I_0}{\alpha_0 \lambda}\right) > 1 \quad \text{and} \quad T^{-1} = \left(\tfrac{n_2}{\alpha_2 \lambda}\right) > 1. \tag{2.89}$$

These two figures of merit are a simple and effective way to evaluate a nonlinear material. Although the intrinsic nonlinearity of silica fiber is relatively low, it is a fantastic nonlinear material, having exceptionally low loss and low two-photon absorption. These factors become much more critical in new materials systems with high nonlinearity and serve as a check for applications. For example, silicon has a

very strong intrinsic nonlinearity, 200–300 times silica glass [7]. However, this high nonlinearity is accompanied by strong two-photon absorption, and thus the T^{-1} figure of merit is below unity for all telecommunications wavelengths and is only above unity for wavelengths longer than 1800 nm [7]. Although low figures of merit make ultrafast interferometric switches impractical in silicon, other effects are used for switching [28].

2.3 Nonlinear optics at the nanoscale

In this section, we will explore sub-wavelength waveguides both theoretically and experimentally and use these later to enhance nonlinear interactions. To motivate the use of waveguides for nonlinear optics, we observe that the total accumulated nonlinear phase depends on the intensity and the effective length in equation (2.83). We can reach high intensities by focusing a laser using a lens; however, the beam will quickly diverge, leading to few accumulated nonlinearities. Considering a Gaussian beam, the peak intensity is $I_0 = 2P_0/(\pi w_0^2)$, where P_0 is the power, and w_0 is the beam waist. For a focused beam, the divergence limits the length of nonlinear phase accumulation. If the effective length for a Gaussian beam is given by the Rayleigh distance $z_R = \pi w_0^2/\lambda$, the intensity-length product for a focused beam is [20]:

$$I_0 z_R = \left(\frac{2P_0}{\pi w_0^2}\right)\left(\frac{\pi w_0^2}{\lambda}\right) = \frac{2P_0}{\lambda}. \tag{2.90}$$

The intensity is inversely proportional to the square of the spot size, w_0; meanwhile, the focused spot will diverge based on the Rayleigh distance, which is directly proportional to the square of the spot size. These combined effects lead to a situation whereby tight focusing, alone, does not change the accumulated nonlinearity. We can

achieve much stronger nonlinear interactions if we can counteract the divergence by keeping the wave confined as it propagates. Such confinement is precisely what we achieve using a waveguide. If the waveguide has a loss of α_0, using equation (2.84), the intensity-length product is [20]:

$$I_0 L_{\text{eff}} = \left(\frac{2P_0}{\pi w_0^2}\right)\left(\frac{1-e^{-\alpha_0 L}}{\alpha_0}\right) \approx \frac{2P_0}{\pi w_0^2 \alpha_0}. \tag{2.91}$$

The maximum intensity-length product (for a waveguide of infinite length) depends completely on the loss of the waveguide and is far greater than for a focused beam. This ability to accumulate a large amount of nonlinear phase in a waveguide is an essential tool for nonlinear optics. In addition, we see that the nonlinear interaction scales inversely with the area. Therefore, the highest nonlinear interactions will occur for waveguides with the smallest effective area and thus, by employing nano-scale waveguides, we can achieve very large nonlinear interactions efficiently.

2.3.1 Waveguides

Waveguides use multiple reflections to confine light signals into discrete channels, known as modes. By considering geometrical arguments, we will first develop an intuitive understanding of the guiding condition using reflections from metallic mirrors. Similarly, we will use total internal reflection to form waveguides in dielectric materials. By observing the wavelength-dependence of the guiding condition, we will demonstrate how waveguides can alter the effective propagation constant and use it to engineer the effective dispersion within a waveguide. Lastly, we will observe the field distributions within waveguides, which will enable us to create enhanced nonlinearities using sub-wavelength structure.

Metal mirror waveguide

We will start by considering the simplest waveguide formed by two parallel metallic mirrors. Considering the geometry of Figure 2.7 (left), we see that for the wave to sustain itself, the phase accumulated from multiple bounces must add constructively with the original wave. Each bounce off a metal mirror adds a phase shift of π. Therefore, the total phase from the path length and from each bounce, must be an integer multiple of 2π. From the geometry in Figure 2.7, this condition is [29]:

$$\begin{aligned} \tfrac{2\pi}{\lambda_0}\left(AC - AB\right) - 2\pi &= \tfrac{2\pi}{\lambda_0}\left(AC - AC\cos\left(2\theta\right)\right) - 2\pi \\ &= \tfrac{2\pi}{\lambda_0} 2d\sin\theta - 2\pi = 2\pi m', \end{aligned} \tag{2.92}$$

where m' is an integer (starting from zero). Simplifying this expression and using $m = m' + 1$, we obtain:

$$2d\sin\theta = m\lambda_0 \quad m = 1,\, 2,\, ... \tag{2.93}$$

Therefore, we have a discrete number of propagating solutions, as shown in Figure 2.7 (right). Each solution is known as a *mode* and acts like a channel for an electromagnetic wave. The number of guided modes for a single polarization is given by:

$$M \doteq \frac{2d}{\lambda_0}. \tag{2.94}$$

We find that no guiding can occur when the distance becomes less than half of the wavelength.

Depending on the orientation of the electric field, two unique waves can propagate. If the electric field of the wave is transverse to the plane of the mirror, we find the *transverse-electric* polarization (TE) and there is no electric field in the direction of

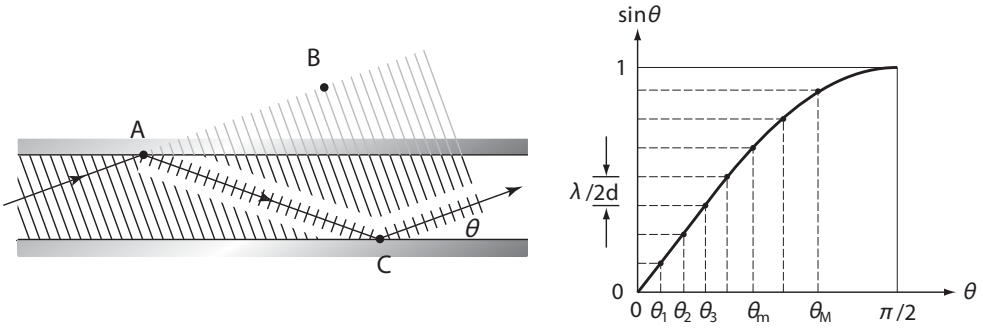

Figure 2.7: A metallic mirror waveguide showing the periodicity condition requirement (left) and a graphical method to determine the solutions to equation (2.93) (right).

propagation. Swapping the electric and magnetic fields results in *transverse-magnetic* polarization (TM). These will become important when we consider dielectric waveguides, as the boundary conditions are slightly different for TE- versus TM-waves.

In the case of a metal mirror waveguide, this condition is identical for both the TE and TM polarizations, and therefore the total number of supported modes is twice this value. Alternatively, we can write down an equation for the cutoff frequency (the lowest frequency that is still guided), by setting $\sin\theta = 1$ and $m = 1$, then solving for the frequency to show:

$$\omega_c = \frac{\pi c}{d}. \tag{2.95}$$

Planar dielectric guiding

Alternatively, we can form a waveguide using dielectric materials. This case is very similar to the two-mirror case, except the wave is guided using total internal reflection. Therefore, we require a high index material surrounded on the top and bottom by lower index materials. The relative index difference is related to the index contrast

and determines parameters including the number of modes, the phase and group velocities, GVD and the confinement.

For total internal reflection, the angle between the wavevector and the normal to the interface must be greater than the critical angle. The critical angle is given by $\sin\theta_c = n_2/n_1$, where n_1 is the index in the guiding layer and n_2 is the cladding index. We should note that our current waveguide discussion uses the *complimentary angle*. In our present notation, waves will be totally internally reflected if $\theta < (\pi/2 - \theta_c)$. Using these conditions, we modify equation (2.92) by scaling the length by the index of the guiding layer, n_1, and we replace the phase-shift upon reflection, previously π, with a new material- and polarization-dependent phase-shift, φ:

$$\frac{2\pi}{\lambda_0} n_1 \left(2d\sin\theta\right) - 2\varphi = 2\pi m'. \tag{2.96}$$

If we use the convention that $\lambda = \lambda_0/n_1$, the condition becomes [29]:

$$\frac{2\pi}{\lambda} 2d\sin\theta - 2\varphi = 2\pi m. \tag{2.97}$$

The phase change depends on the materials (through θ_c) and on the polarization [30]:

$$\varphi_{\mathrm{TE}} = 2\tan^{-1}\left(\sqrt{\tfrac{\cos^2\theta_c}{\sin^2\theta} - 1}\right), \quad \text{and} \tag{2.98}$$

$$\varphi_{\mathrm{TM}} = 2\tan^{-1}\left(\csc^2\theta_c\sqrt{\frac{\cos^2\theta_c}{\sin^2\theta} - 1}\right), \tag{2.99}$$

for TE- and TM-polarizations, respectively. Using these expressions, we determine the guiding condition to be:

$$\tan\left[\tfrac{\pi d}{\lambda}\sin\theta_{\mathrm{TE}} - \tfrac{m\pi}{2}\right] = \sqrt{\tfrac{\sin^2(\pi/2-\theta_c)}{\sin^2\theta_{\mathrm{TE}}} - 1}, \quad \text{and} \tag{2.100}$$

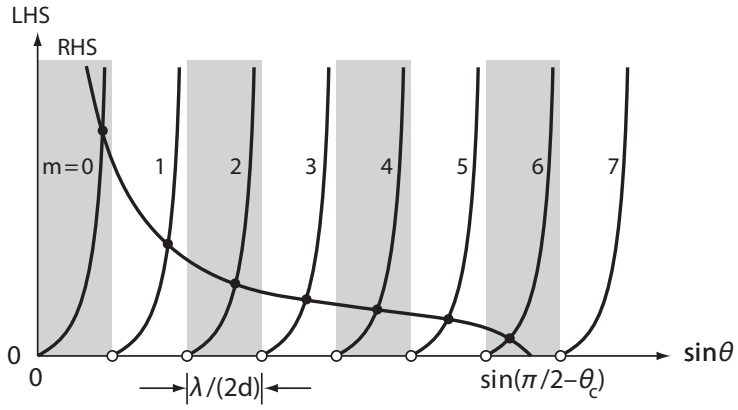

Figure 2.8: Graphical solutions to the waveguiding condition from equation (2.101).

$$\tan\left[\frac{\pi d}{\lambda}\sin\theta_{\mathrm{TM}} - \frac{m\pi}{2}\right] = \csc^2\theta_c\sqrt{\frac{\sin^2\left(\pi/2-\theta_c\right)}{\sin^2\theta_{\mathrm{TM}}} - 1}. \tag{2.101}$$

To find the modes graphically, we can plot both the left- and right-hand sides in terms of $\sin\theta$, the solutions occur whenever the two curves intersect, as shown in Figure 2.8.

In addition, we can calculate the number of modes by determining the number of crossings. We realize that the left-hand side is periodic in $\sin\theta$ and we can expect a solution for each period until the right hand side goes to zero. Considering both even and odd values of m, the function has a periodicity of $\lambda/\left(2d\right)$ in terms of $\sin\theta$. We find that the right-hand side goes to zero when $\sin\theta = \sin\left(\pi/2-\theta_c\right)$. Therefore, the number of modes, M, for TE-polarization is given by:

$$M \doteq \frac{\sin\left(\pi/2-\theta_c\right)}{\lambda/\left(2d\right)}. \tag{2.102}$$

Note that we must round up in this case. Alternatively, we can write this expression in terms of the refractive indices use by using:

$$\sin\left(\pi/2-\theta_c\right) = \cos\theta_c = \sqrt{1-\sin^2\theta_c} = \sqrt{1-n_2^2/n_1^2} = \frac{\sqrt{n_1^2-n_2^2}}{n_1}, \tag{2.103}$$

to show:

$$M \doteq \frac{2d}{\lambda n_1}\sqrt{n_1^2 - n_2^2} = \frac{2d}{\lambda_0}\sqrt{n_1^2 - n_2^2}, \tag{2.104}$$

for TE-polarization [29]. (Note the substitution of the free-space wavelength.) This expression is not correct if we consider an asymmetric waveguide with a different upper and lower cladding. Similarly, we have a cutoff frequency of [29]:

$$\omega_c = \frac{\pi c}{d}\frac{1}{\sqrt{n_1^2 - n_2^2}}, \tag{2.105}$$

above which multiple modes of one polarization will propagate.

Multiple modes in a waveguide can make designing and fabricating devices difficult. Although modes are linearly independent, small perturbations in real systems can couple multiple modes to one another. Therefore, we often try to make waveguides *single-mode*. We consider a waveguide single-mode if it only supports a single guided mode for a particular polarization (TE or TM). We can obtain single-mode operation by adjusting the waveguide materials and geometry, as shown in equations (2.94) and (2.104).

Comparing the single-mode condition for mirror versus dielectric guiding, we find that using 600-nm light, the single-mode thickness d for mirror guiding is in the range from 300–600 nm, below which, no modes are supported. On the other hand, for fused silica, we find single-mode guiding for thicknesses less than 283 nm, with no minimum thickness, in contrast to the mirror guided case. If we reduce the index contrast between the core and the cladding, we can increase the size of the waveguide, as is done for standard silica fiber.

Propagation constants

A guided wave will propagate at a different speed due to the multiple bounces it must undergo. Therefore, it no longer makes sense to use the wavevector k to describe the rate of phase propagation and we define a new constant $\beta = 2\pi n_{\text{eff}}/\lambda_0$ known as the propagation constant. The wave travels in an analogous manner to a plane wave, however k is replaced by β and the wave propagates with an effective index of n_{eff}. We can illustrate the propagation constant by consider the mirror waveguide shown in Figure 2.9. We see that [29]:

$$\beta^2 = k^2 - k_y^2 = k^2\left(1 - \sin^2\theta_m\right) = k^2\left(1 - \frac{m^2\lambda_0^2}{4d^2}\right) = k^2 - \frac{m^2\pi^2}{d^2}, \tag{2.106}$$

then we write this expression in terms of the cutoff frequency to obtain:

$$\beta_m = \frac{\omega}{c}\sqrt{1 - m^2\frac{\omega_c^2}{\omega^2}} = \frac{\omega}{c}\cos\theta_m. \tag{2.107}$$

The propagation constant for a mirror waveguide is less than the free-space propagation constant, implying that the phase velocity is greater than the speed of light. We determine the group velocity for a mirror waveguide using:

$$v_g = \left[\frac{d\beta_m}{d\omega}\right]^{-1} = c\sqrt{1 - m^2\frac{\omega_c^2}{\omega^2}} = c\cos\theta_m, \tag{2.108}$$

showing that the group velocity is still slower than the speed of light. Similarly, we calculate the GVD for a mirror waveguide using:

$$\text{GVD} = \frac{d^2\beta_m}{d\omega^2} = -\left(\frac{m^2\omega}{c}\right)\left(\frac{\omega_c}{\omega^2 - m^2\omega_c^2}\right)^2\sqrt{1 - \left(\frac{m\omega_c}{\omega}\right)^2}. \tag{2.109}$$

This simple model provides two critical insights. First, we find that the dispersion for a metal waveguide is always negative (anomalous), contrary to many dielectric

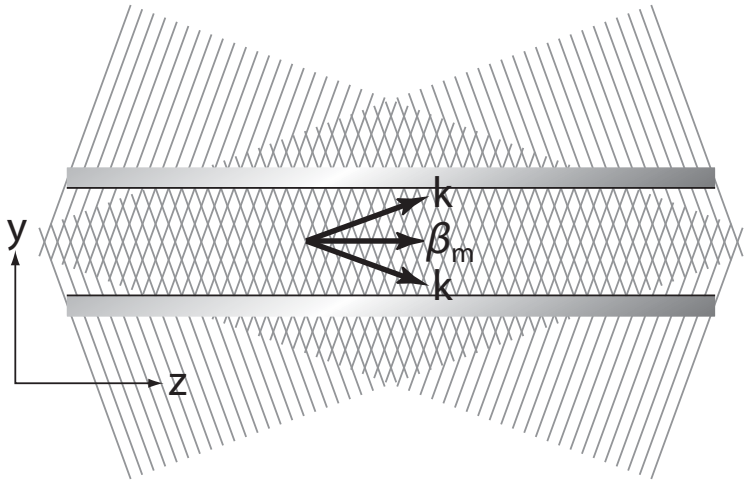

Figure 2.9: Propagation constant for a metallic mirror waveguide.

materials. Secondly, we find that the GVD depends heavily on the cutoff frequency of the waveguide $\omega_c = \pi c/d$ and becomes very strong as we approach the cutoff frequency. Therefore, the GVD is heavily dependent on the waveguide geometry. Thus, by changing the mirror separation d, we have the ability to tune the GVD, which we have seen is a critical parameter for pulse propagation.

In a similar way, we determine the propagation constant for a dielectric waveguide starting with:

$$2d\sqrt{\frac{\omega^2}{c_1^2} - \beta^2} = 2\varphi_r + 2\pi m, \tag{2.110}$$

with integer values of m. Similar to the mirror waveguide, we can use this condition to derive the group velocity for a dielectric waveguide. The derivation is rather mathematical and is of limited use in the present context. Therefore, we refer the

reader to the derivation presented in [29], and present the result here:

$$v_g = \frac{d\cot\theta + \Delta z}{n_1 d\csc\theta/c + \Delta\tau}. \tag{2.111}$$

Here, n_1 is the refractive index of the core, θ is the angle associated with the planar mode. In addition, we have introduced Δz, which corresponds to the additional distance that the wave propagates along the boundary in the form of an evanescent wave for each round trip. This additional propagation takes a time $\Delta\tau$. We can relate this result to our previous result, if we have no evanescent field by setting $\Delta z = \Delta\tau = 0$. Equation (2.111) reduces to equation $v_g = (c/n_1)\cos\theta$, which is identical to (2.108), with the addition of a dielectric between the two mirrors.

Just as for a metal mirror waveguide, the group velocity depends on the thickness of the dielectric waveguide. The dielectric's intrinsic GVD alters the total GVD, which is sometimes approximated as the sum of the material dispersion and the waveguide dispersion [31, 32]. We must also consider the penetration of the evanescent wave into the cladding. Because of these considerations, and the complications of a two-dimensional waveguide cross-section, we often use numerical simulations.

As many materials display normal GVD at optical frequencies, we are often interested in reducing the amount of normal dispersion by introducing anomalous waveguide dispersion. For this case, we see two general design considerations. First, we should design our waveguides with dimensions that are comparable to the wavelength of interest (near cutoff). Second, we should use core and cladding materials with high index-contrasts to reduce the penetration of the evanescent field and better approximate the strong anomalous dispersion found in the mirror waveguide.

Waveguide equation

Light propagates differently in a waveguide than it does in free-space; however, it is similar to plane wave propagation. To reflect this similarity, we can rewrite the wave equation and look for solutions that take the same form as plane waves. We use a spatially varying dielectric constant $\varepsilon_r(x,y)$ that is infinite in the z-direction. We start with the equation for the time-harmonic vector and scalar potentials in a source-free, non-magnetic, non-uniform, dielectric medium [14]:

$$\nabla^2\vec{A} + \omega^2\frac{\varepsilon_r}{c^2}\vec{A} = -i\frac{\omega}{c^2}\nabla\varepsilon_r\Phi. \tag{2.112}$$

The electric field is determined by $\vec{E} = -i\omega\vec{A} - \nabla\Phi$. We see that the right hand side of equation (2.112) couples the vector and scalar potential. If we assume that $\nabla\varepsilon_r$ is small and set it to zero, we can obtain:

$$\nabla^2\vec{A} + \frac{\omega^2}{c^2}\varepsilon_r\vec{A} = 0. \tag{2.113}$$

We can look for solutions that resemble plane waves of the form:

$$\vec{A} = \vec{y}F(x,y)\,e^{-i\beta z}, \tag{2.114}$$

where we assume that all the of z dependence is in $e^{-i\beta z}$, and therefore $F(x,y)$ is the modal distribution, which describes the spatial profile of the mode. After substitution, the differential equation for $F(x,y)$ is:

$$\nabla_T^2 F + \left(-\beta^2 + \frac{\omega^2}{c^2}\varepsilon_r(x,y)\right)F = 0, \tag{2.115}$$

where ∇_T^2 is the Laplacian in the transverse spatial direction. This equation has the same form as the time-dependent Schrodinger equation for a two-dimensional

potential well with a potential of $-\omega^2\mu_0\varepsilon(x,y)$. Therefore, this equation's solutions are completely analogous to those for a quantum well and, as we've seen previously, requires specific values of the propagation constant β.

Waveguide field distributions

For the case of a metallic mirror waveguide, the electric field must necessarily be zero at the metallic boundary. However, for the case of dielectric waveguides, the field extends beyond the boundary as a decaying *evanescent* field. Solving equation (2.115), a TE mode has an internal field given by [29]:

$$F_m(y) \propto \begin{cases} \cos\left(2\pi\frac{\sin\theta_m}{\lambda}y\right), & m = 0,\ 2,\ 4,\ ... \\ \sin\left(2\pi\frac{\sin\theta_m}{\lambda}y\right), & m = 1,\ 3,\ 5,\ ... \end{cases} \qquad -\frac{d}{2} \leqslant y \leqslant \frac{d}{2}, \tag{2.116}$$

with $\lambda = \lambda_0/n_1$. Outside of the waveguide core, the evanescent field is given by:

$$F_m(y) \propto \begin{cases} \exp\left[-\left(n_2k_0\sqrt{\frac{\cos^2\theta_m}{\cos^2(\pi/2-\theta_c)}-1}\right)y\right], & y > d/2 \\ \exp\left[\left(n_2k_0\sqrt{\frac{\cos^2\theta_m}{\cos^2(\pi/2-\theta_c)}-1}\right)y\right], & y < -d/2 \end{cases} \tag{2.117}$$

.

We see the evanescent field decays into the surrounding medium, as shown in equation (2.117). The higher order modes, having larger angles θ_m, will extend further into the cladding [29].

Just as for quantum wells, there are analogous oscillatory solutions for waveguides, as shown in Figure 2.10. For mirror waveguides, the modes resemble an infinite quantum well, with the wave going to zero at the boundaries (Figure 2.10, left). Alternatively, we see that waves guided by a dielectric extend beyond the boundaries and propagate in the form of an evanescent wave, analogous to a finite quantum well (Figure 2.10, right).

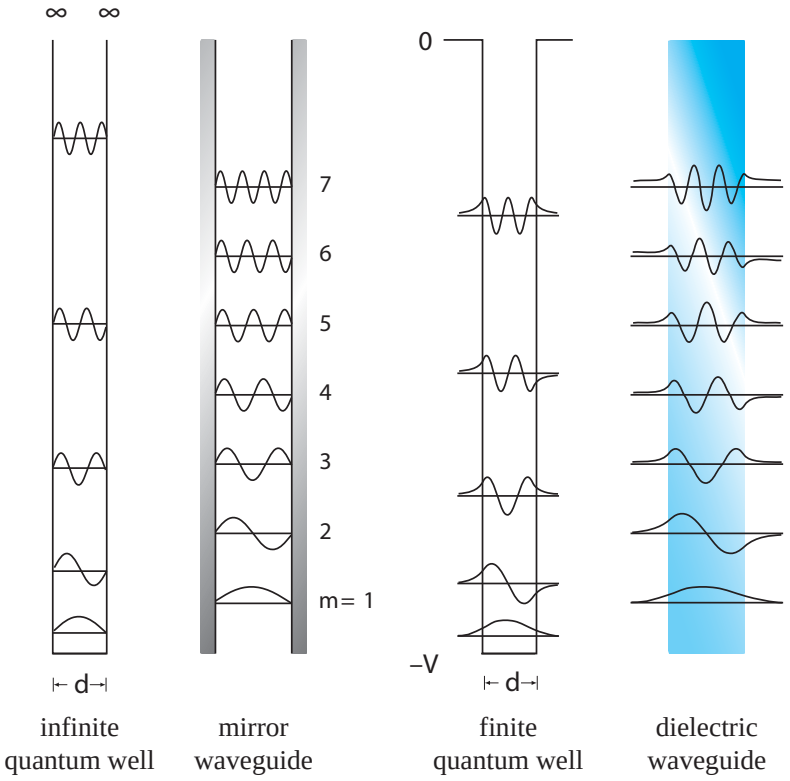

Figure 2.10: The spatial-distribution for the wave functions of a quantum well have the same form as a guided electromagnetic wave. Here, we see the several wave function for an infinite quantum well (far left), a mirror waveguide (middle left), a finite potential quantum well (middle right), and a dielectric waveguide (far right).

We have only dealt with planar waveguides so far, for simplicity. We can confine the wave in the other transverse dimension as well, which enables us to concentrate light strongly in two-dimensions. Adding an additional degree of freedom leads to many different type of waveguides including cylindrical waveguides, such as fibers, as well as rectangular waveguides such as channel, strip, and ridge waveguides [13].

2.3.2 Nonlinear pulse propagation

The generalized nonlinear Schroedinger equation (NLSE) is the workhorse of nonlinear fiber and integrated optics. It adds a third-order nonlinear response to the waveguide equation and describes the temporal evolution of a pulse in a nonlinear waveguide. Although we will discuss the simplest version here, we can extend this model to include wide-bandwidth pulses, a delayed nonlinearity, and two-photon absorption.

Nonlinear Schroedinger equation

To develop the nonlinear Schroedinger equation, we will follow the derivation by Agrawal [20]. Let us consider the wave equation in terms of the linear and nonlinear polarization in the time domain:

$$\nabla^2 \vec{E} - \frac{1}{c^2}\frac{\partial^2 \vec{E}}{\partial t^2} = \mu_0 \frac{\partial^2 \vec{P}_L}{\partial t^2} + \mu_0 \frac{\partial^2 \vec{P}_{NL}}{\partial t^2}. \tag{2.118}$$

Our strategy for simplifying this differential equation starts by including the nonlinear polarization into an effective dielectric constant $\varepsilon_{\text{eff}}(\omega)$. Next, we use separation of variables to isolate a transverse-wave equation from the propagation equation, as we did when analyzing the modes in a waveguide. We incorporate the nonlinear polarization by solving the transverse equation and using the nonlinear part of $\varepsilon_{\text{eff}}(\omega)$

as a perturbation. The lowest order perturbation alters the propagation constant, while keeping the distribution of the mode intact. We apply the resulting linear and nonlinear propagation constants to the propagation equation to arrive at the NLSE, which describes the temporal evolution of a pulse in a nonlinear waveguide.

As we have seen in previously, the effects of dispersion are easiest to handle in the frequency domain. For clarity, we will denote variables in frequency domain using a tilde above. Therefore, we take the Fourier transform of equation (2.118), to show:

$$\nabla^2 \tilde{E} - \varepsilon_{\text{eff}}(\omega) k_0^2 \tilde{E} = 0, \tag{2.119}$$

and we define an effective relative dielectric constant in the frequency domain:

$$\varepsilon_{\text{eff}}(\omega) = 1 + \tilde{\chi}_{xx}^{(1)}(\omega) + \varepsilon_{\text{NL}}. \tag{2.120}$$

Although not explicitly stated, the effective dielectric constant varies in the transverse direction to form the waveguide. By combining both the linear and nonlinear terms into an effective dielectric constant, we simplify the analysis.

Next, we combine the slowly varying amplitude approximation from equation (2.36) with the modal distribution from equation (2.114) in the time domain:

$$\vec{E} = F(x,y) A(z,t) \exp(i\beta_0 z - \omega_0 t) \hat{x}. \tag{2.121}$$

Here, we have a carrier wave given by $\exp(i\beta_0 z - \omega_0 t)$ that is slowly modulated by an envelope function, $A(z,t)$. Taking the Fourier transform of this expression, we substitute:

$$\tilde{E} = F(x,y) \tilde{A}(z, \omega - \omega_0) \exp(i\beta_0 z), \tag{2.122}$$

into (2.119). Now, we perform a separation of variables to show:

$$\frac{\partial^2 F}{\partial x^2} + \frac{\partial^2 F}{\partial y^2} + \left[\varepsilon_{\text{eff}}(\omega) k_0^2 - \tilde{\beta}(\omega)^2\right] F = 0, \tag{2.123}$$

and:

$$2i\beta_0 \frac{\partial \tilde{A}}{\partial z} + \left(\tilde{\beta}^2(\omega) - \beta_0^2\right)\tilde{A} = 0. \tag{2.124}$$

We have used the slowly varying amplitude approximation and assumed the term $\partial^2\tilde{A}/\partial z^2$ is negligible compared to $\beta(\omega)\left(\partial\tilde{A}/\partial z\right)$. Equation (2.123) closely resembles (2.115), determines the modal distribution $F(x,y)$ and the propagation constant $\tilde{\beta}(\omega)$, and includes the nonlinear dielectric constant $\varepsilon_{\text{eff}}(\omega)$.

We incorporate the nonlinearity by using first-order perturbation theory. We replace ε with n^2 and approximate $\varepsilon = (n+\Delta n)^2 \approx n^2 + 2n\Delta n$. Next, we use:

$$\Delta n = n_2|E|^2 + \frac{i\alpha}{2k_0}, \tag{2.125}$$

where n_2 is the nonlinear index of refraction and α is the attenuation coefficient. Using perturbation theory results in a modal distribution $F(x,y)$ that is unaffected by the nonlinearity, to first order. Meanwhile, the nonlinearity comes into play through a perturbation of the propagation constant:

$$\tilde{\beta}(\omega) = \beta(\omega) + \Delta\beta(\omega), \tag{2.126}$$

where:

$$\Delta\beta(\omega) = \frac{\omega^2 n(\omega)}{c^2\beta(\omega)} \frac{\int\int_{-\infty}^{\infty} \Delta n(\omega)\,|F(x,y)|^2 dxdy}{\int\int_{-\infty}^{\infty} |F(x,y)|^2 dxdy}, \tag{2.127}$$

This expression is completely analogous to self-phase modulation using a nonlinear wavevector k from equation (2.77), except applied to the propagation constant. This situation is slightly more complicated because we must consider the modal distribution. However, we can use the waveguide geometry, through $F(x,y)$, to increase the rate of nonlinear phase accumulation.

Solving equation (2.123) and applying (2.127), we obtain the modal distribution and both the linear and nonlinear propagation constants. Now, we can apply these results to equation (2.124). To further simplify equation (2.124), we assume that the frequency-dependent propagation constant remains close to the propagation constant of the carrier wave $\tilde{\beta}(\omega) \approx \beta_0$, and we approximate $\tilde{\beta}^2(\omega) - \beta_0^2 \approx 2\beta_0\left(\tilde{\beta}(\omega) - \beta_0\right)$. Now, the Fourier transform of the slowly varying envelope $\tilde{A}(z, \omega - \omega_0)$ satisfies:

$$\frac{\partial \tilde{A}}{\partial z} = i\left[\beta(\omega) + \Delta\beta(\omega) - \beta_0\right]\tilde{A}. \tag{2.128}$$

As we are only concerned with the spectral bandwidth around the carrier frequency of the pulse, we Taylor expand the propagation constant in the frequency domain:

$$\beta(\omega) = \beta_0 + (\omega - \omega_0)\beta_1 + \frac{1}{2}(\omega - \omega_0)^2\beta_2 + \frac{1}{6}(\omega - \omega_0)^3\beta_3 + ..., \tag{2.129}$$

where $\beta_0 = \beta(\omega_0)$ is the propagation constant of the carrier wave and:

$$\beta_m \equiv \left(\frac{d^m\beta}{d\omega^m}\right)_{\omega=\omega_0}. \tag{2.130}$$

Similarly, we expand $\Delta\beta(\omega)$:

$$\Delta\beta(\omega) = \Delta\beta_0 + (\omega - \omega_0)\Delta\beta_1 + \frac{1}{2}(\omega - \omega_0)^2\Delta\beta_2 + ..., \tag{2.131}$$

using a comparable definition of $\Delta\beta_m$ to equation (2.130). Using these definitions for the propagation constant to second order in $\beta(\omega)$, and first order in $\Delta\beta(\omega)$, we take the inverse Fourier transform of equation (2.128) to arrive at:

$$\frac{\partial A}{\partial z} + \beta_1\frac{\partial A}{\partial t} + \frac{i\beta_2}{2}\frac{\partial^2 A}{\partial t^2} = i\Delta\beta_0 A. \tag{2.132}$$

We note that both the nonlinearity and the losses are contained in the $\Delta\beta_0$ term. Using the assumption that the modal distribution $F(x, y)$ does not vary considerably

over the pulse bandwidth and $\beta(\omega) \approx n(\omega)\,\omega/c$, we can write:

$$\frac{\partial A}{\partial z} + \beta_1 \frac{\partial A}{\partial t} + \frac{i\beta_2}{2}\frac{\partial^2 A}{\partial t^2} + \frac{\alpha}{2}A = i\gamma(\omega_0)\,|A|^2 A. \tag{2.133}$$

This equation is related to the nonlinear Schroedinger equation from quantum mechanics if the loss term α is zero. We have also introduced the nonlinear parameter, or *effective nonlinearity* [20]:

$$\gamma(\omega_0) = \frac{2\pi}{\lambda}\frac{\int\int_{-\infty}^{\infty} n_2(x,y)\,|F(x,y)|^4 dxdy}{\left(\int\int_{-\infty}^{\infty} |F(x,y)|^2 dxdy\right)^2}. \tag{2.134}$$

The effective nonlinearity has units of $\mathrm{W}^{-1}\mathrm{m}^{-1}$ when $|A|^2$ represents the optical power.

Equation (2.133) is approximately valid for pulses that are longer than 1 ps and does not include the effects of Raman or Brillouin scattering. Raman scattering requires the inclusion of a delayed (non-instantaneous) nonlinearity. Meanwhile, shorter pulses have a much larger bandwidth that requires several modifications. For short, large-bandwidth pulses propagating in the linear regime, $\beta(\omega)$ cannot be sufficiently modeled unless we include higher-order dispersive terms beyond β_2. Additionally, for short pulses in the nonlinear regime, the nonlinear parameter's frequency dependence must also be included, leading to an effect known as self-steepening [20]. These additional effects change the details of how a pulse evolves as it propagates; however, equation (2.133) describes many of the major features.

The NLSE is only solvable analytically under certain conditions [33]. However, an efficient method for numerically simulating the NLSE exists, which is known as the split-step Fourier method [34, 35]. The technique discretizes pulse propagation in the z-direction. We split each discrete step into two parts. We apply only the

nonlinear phase in the time domain during the first part. Subsequently, we Fourier transform and apply linear dispersion in the frequency domain, followed by second Fourier transform back to the time domain, which completes the z-step. This method is both efficient and straightforward to apply.

Effective nonlinearity

The effective nonlinearity is the nonlinear phase per distance, per power, thus, large value of γ enable smaller and more efficient devices. With the effective nonlinearity, we can rewrite equation (2.77) for the nonlinear phase within a waveguide by including the propagation constant β the effective nonlinearity $\gamma(\omega)$:

$$\varphi = \beta L + \gamma(\omega) LP = \varphi_L + \varphi_{NL}. \tag{2.135}$$

We note that γ takes both the distribution of the mode into account and a location-dependent nonlinearity. The importance of the modal distribution is critical for the high-index contrast waveguides because the only significant nonlinearity occurs within the core and not the cladding. The spatially dependent nonlinearity is also important for waveguides formed from multiple materials with different intrinsic nonlinearities.

If the field is contained within a single material, such as in optical fiber, we can write:

$$\gamma(\omega_0) = \frac{n_2(\omega_0)\,\omega_0}{cA_{\text{eff}}}, \tag{2.136}$$

where the *effective mode area* is:

$$A_{\text{eff}} = \frac{\left(\int\int_{-\infty}^{\infty} |F(x,y)|^2 dxdy\right)^2}{\int\int_{-\infty}^{\infty} |F(x,y)|^4 dxdy}. \tag{2.137}$$

Alternatively, we can write the effective area in terms of the *mode-field diameter* (MDF) d, related to the effective area by $A_{\text{eff}} = \pi(d/2)^2$.

Pulse propagation using the nonlinear wave equation

Pulse propagation within a nonlinear waveguide is considerably different from the continuous-wave case. For large nonlinear interactions, high powers are necessary. This requirement benefits from restricting the wave spatially by reducing the effective area, and controlling the spreading of the pulse in time using dispersion. Therefore, there is an interplay between the nonlinearity and the group velocity dispersion.

To get a sense of which effects are dominant, we look to equation (2.133) and determine length scales on which these relative effects become important. The length associated with group velocity dispersion is:

$$L_{\text{D}} = \frac{T_0^2}{|\beta_2|}, \tag{2.138}$$

known simply as the dispersion length. Similarly,

$$L_{\text{NL}} = \frac{1}{\gamma P_0}, \tag{2.139}$$

is known as the nonlinear length. When the physical length of the waveguide is comparable to these lengths scales, the associated effects become important.

There are four relevant combinations of these lengths scales [20]. For $L_{\text{D}} \gg L$ and $L_{\text{NL}} \gg L$, both the dispersion and the nonlinearity are minimal and the pulse passes through unaffected, ideal for transmission systems. When $L_{\text{D}} \leqslant L$ and $L_{\text{NL}} \gg L$, the pulse undergoes significant dispersive broadening, but the spectrum remains constant. If $L_{\text{D}} \gg L$ and $L_{\text{NL}} \leqslant L$, the pulse is affected primarily by the nonlinearity

and the spectrum will change via self-phase modulation. This regime is important for wide spectral broadening because the pulse remains relatively short due to the minimal dispersive broadening.

The final combination requires special attention [20]. When both $L_{\mathrm{D}} \leqslant L$ and $L_{\mathrm{NL}} \leqslant L$, the interplay between the dispersion and the nonlinearity produces dramatically different results depending on relative signs of the two effects. If both effects are positive ($n_2 > 0$ and $\beta > 0$, dispersion in the normal regime), spectral broadening can occur and even temporal pulse compression can be achieved under certain conditions [20]. If the dispersion is anomalous with $\beta < 0$ and $n_2 > 0$, stable solutions, known as solitons, can form [20, 36]. Under these conditions, the group velocity dispersion causes the red to move toward the front and blue toward the back; however, the nonlinearity causes the opposite effect and the two effects balance one another. These solutions are quantized in the sense that the shape repeats itself after a regular, fixed distance. Solitons are extremely stable because they can shed excess energy in the form of a *dispersive wave* until a stable solution is formed [37].

The lowest order (fundamental) soliton is of particular interest for communications systems because the dispersion and nonlinearity are in constant balance ($L_{\mathrm{D}} = L_{\mathrm{NL}}$) and the pulse maintains its shape as it propagates [38, 39]. In addition, the spectral phase across the pulse is flat, which has two advantages for all-optical switching [40–42]. First, a fundamental soliton is intrinsically transform-limited, leading to efficient switching. Secondly, unlike other pulses, the flat-phase guarantees that the entire pulse will undergo switching, avoiding pulse distortions.

2.3.3 Nonlinear properties of silica nanowires

We will now theoretically explore the advantages of using waveguides for nonlinear optics by exploring silica nanowires as a canonical example. This discussion will illustrate how high index-contrast sub-wavelength waveguides can achieve large effectively nonlinearities and tunable group velocity dispersion.

Effective nonlinearities

The high index contrast between silica and air enables strong light confinement, facilitating large effective nonlinearities (γ) [43]. High confinement within a waveguide, alone, does not increase γ. Instead, we must consider both the effective mode area and the distribution of the mode, as shown in equation (2.134).

To study how we can maximize γ in silica nanowires, we will first consider the how the MFD changes as we change the physical diameter (PD) of the nanowire [43]. Figure 2.11 (left) shows the MFD versus the PD. For illustration, we also plot the PD versus itself (a dashed line with a slope of unity). We see that for large diameter fibers, the MFD is smaller than the PD [43]. As we reduce the PD, the MFD becomes equal to the PD. Then the evanescent field increases rapidly, causing the MFD to become much larger than the PD. Because the nonlinearity of air is negligible, we expect the largest γ when the MFD is smallest, while remaining in the core. This crossover occurs when the MFD is equal to the PD, which corresponds to a diameter around 550 nm for 800-nm light.

From the simple structure of silica nanowires, we expect the highest effective nonlinearity when the MFD coincides with the PD. We calculate and plot the effective

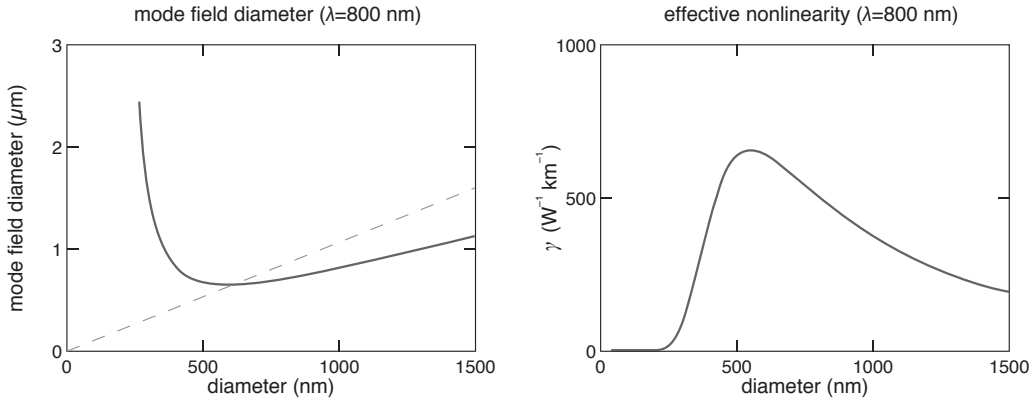

Figure 2.11: Strong nonlinear-optical interaction in silica nanowires. The mode-field diameter versus the physical diameter (left). The effective nonlinearity as a function of the physical diameter (right) [43].

nonlinearity for a silica nanowire as a function of the diameter (Figure 2.11, right) [43]. As expected, the largest nonlinearity occurs for a diameter of 550 nm for 800-nm light. The nonlinearity peaks at a value of 660 $W^{-1}km^{-1}$, which is over 300 times the effective nonlinearity of standard telecommunications fibers [20]. This result is impressive considering that we are using a material, silica, which has a comparatively low nonlinear index of refraction [44].

Group velocity dispersion

As we have seen previously, waveguide dispersion enables us to engineer the total dispersion, greatly influencing nonlinear pulse propagation. Figure 2.12 (left) shows the wavelength-dependent total dispersion for silica nanowires of varying diameters [45]. We see that the material dispersion in silica is normal for short wavelengths, reaches zero around 1300 nm, and then becomes anomalous for longer wavelengths. If we operate around 800 nm, we are restricted to normal dispersion, unless we can

counteract the normal dispersion with anomalous waveguide dispersion.

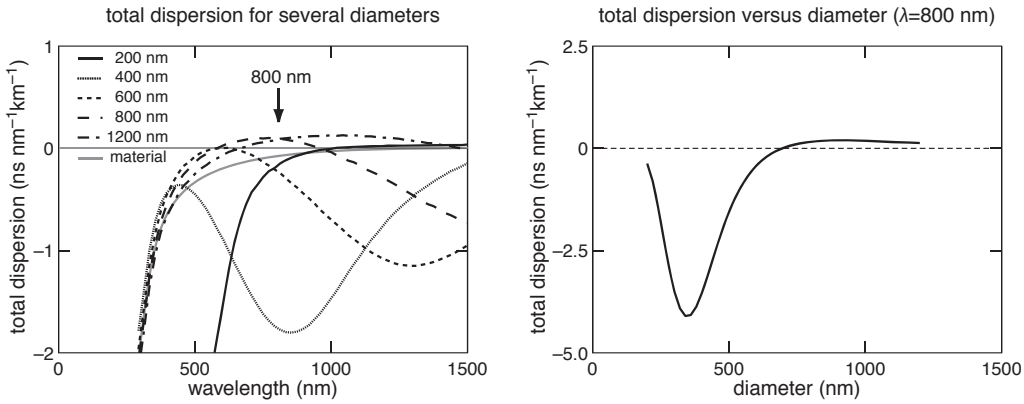

Figure 2.12: Dispersion engineering in silica nanowires. The dispersion parameter D versus wavelength for several waveguide dimensions (left). The dispersion parameter D as a function of silica nanowire dimension for 800-nm light (right) [45].

Figure 18 (right), shows the dispersion for 800-nm light as a function of nanowire diameter [45]. For diameters of 700–1200 nm, strong anomalous waveguide dispersion overcomes the material dispersion and results in anomalous total dispersion. For diameters near 700 nm, total dispersion is very low. For even smaller dimensions, the dispersion becomes extremely normal. This ability to tune the total dispersion is a key element for engineering efficient nonlinear interactions.

2.4 Summary

We have shown the advantages of using sub-wavelength dielectric waveguides for nonlinear optics. We have developed a theoretical basis for linear and nonlinear propagation of continuous-wave and pulsed optical signals in free-space, within materials, and using waveguides. We have seen how nano-scale, high-index contrast waveguides

are capable of enhancing nonlinear interactions spatially using strong confinement and temporally using tunable dispersion. Lastly, we have observed how to optimize nonlinear interactions in a real photonic system. These principles serve the basis for the proceeding chapters as we develop TiO_2 photonics.

Chapter 3

Nonlinearities in bulk rutile TiO_2

In this chapter, we study nonlinear refraction and multiphoton absorption in the bulk TiO_2 to establish a baseline that we can use when designing all-optical devices. Two-photon absorption acts as the short-wavelength limit for many all-optical applications and therefore, we investigate this around limit in TiO_2 (800 nm). The interplay between nonlinear refraction and absorption determines the usefulness of a nonlinear material for all-optical processing. The Z-scan technique can characterize both of these effects in a simple system. This chapter is divided into three section. First, we will develop the theory of the Z-scan technique. Second, we will study nonlinear refraction in bulk rutile TiO_2 using the "closed-aperture" Z-scan technique. Lastly, we will study multiphoton absorption using "open-aperture" Z-scan and evaluate TiO_2 as a candidate material for all-optical applications.

3.1 The Z-scan technique

The Z-scan technique is popular technique to characterize nonlinear refraction and absorption in bulk samples. It requires a single laser beam, can determine both magnitude and sign of the nonlinearity, and is straightforward to analyze. The experimental and analytical simplicity of the Z-scan technique makes it an efficient and powerful method to characterize bulk samples. We begin by discussing how to measure nonlinear refraction using closed-aperture Z-scan.

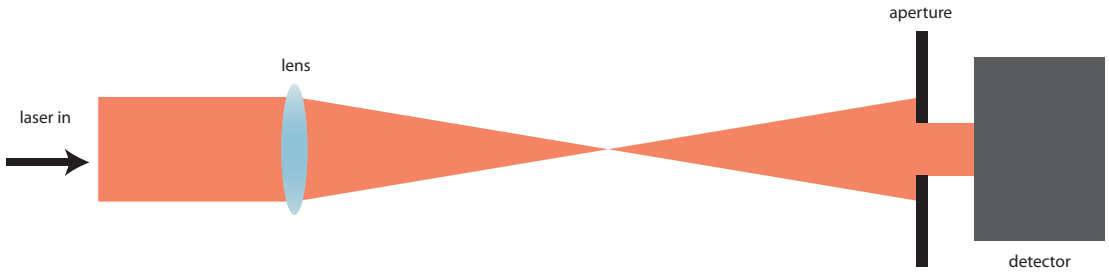

Figure 3.1: A basic closed-aperture Z-scan setup consisting of a focused beam, an aperture, and a detector.

The setup of a typical Z-scan experiment is shown in Figure 3.1. It consists of a focused Gaussian beam, an aperture, and a detector. We perform a Z-scan measurement by scanning the sample through the focus and measuring the amount of transmitted light that passes through the aperture with a photodetector (Figures 3.2 and 3.3). The location of the sample relative to the natural focus determines the intensity incident on the sample and therefore, the strength of the nonlinear lens created (self-focusing). This nonlinear lens changes the size of the beam in the far-field, resulting in more or less power seen by the detector.

We can gain intuition for the Z-scan technique if we consider a positive n_2

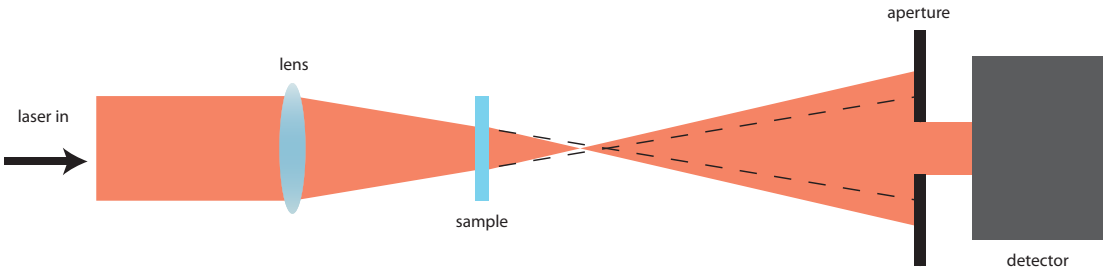

Figure 3.2: When a sample with positive n_2 is in front of the natural focus (dashed lines) the nonlinear lens causes the beam to focus closer to the source, resulting in stronger divergence at the aperture, *reducing* the signal at the detector.

material at three different sample positions. First, let us consider the case of a sample in front of the natural focus. The nonlinear index creates a positive lens and causes the beam to focus before the natural focus. This results in stronger divergence in the far field, reducing the amount of light collected by the detector (Figure 3.2). Next, we consider positioning the sample after the natural focus. The sample's nonlinear lens decreases the beam's natural divergence, resulting in more light being registered at the detector (Figure 3.3). Lastly, if the sample is far from the focus by several Rayleigh distances on either side, self-focusing is negligible, resulting in a linear material response. This linear signal provides a way to normalize the transmission for data analysis.

We form a Z-scan plot by scanning the sample through the focus and recording the amount of light that the detector collects, then normalizing to the linear signal at the edges. We show a typical Z-scan plot in Figure 3.4. For a positive n_2 material (solid line), we observe a dip before the natural focus followed by a peak after the focus. For the case of a negative n_2 material (dashed line), we observe a peak followed

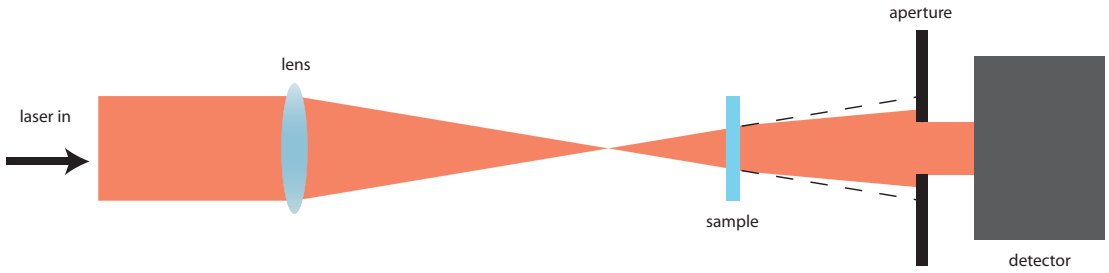

Figure 3.3: When a sample with positive n_2 is behind the natural focus (dashed lines) the nonlinear lens reduces the beam's divergence, resulting in a smaller beam at the aperture, *increasing* the signal at the detector.

by a dip. We analyze this data by determining the peak-valley transmission different (ΔT) or by fitting to a theoretical model.

Additionally, opening the aperture and collecting all of the light allows us to quantify nonlinear absorption. Hence, the nonlinear refraction measurement is known as the "closed-aperture" Z-scan technique, to distinguish it from the "open-aperture" technique used to measure nonlinear absorption. Using this simple, single-beam technique, we can quickly measure both the magnitude and sign of bulk nonlinear optical materials.

3.1.1 Closed-aperture Z-scan analysis

In this section, we show how to analyze Z-scan data by deriving expressions for the normalized transmission. For the case of third-order nonlinearities (nonlinear refraction and two-photon absorption), we follow the derivation found in several references [23, 24, 46]. Throughout this derivation, we make several assumptions. The first assumption is that the sample thickness (L) is "thin" relative to the Rayleigh distance (z_0), specifically $L \leq z_0$. For the derivation, we start with the electric-field

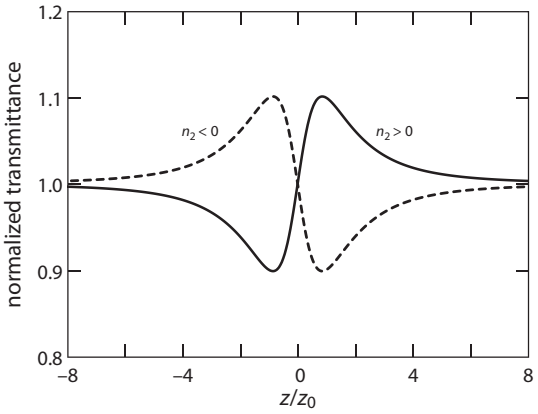

Figure 3.4: A typical Z-scan plot showing the normalized transmission versus z position for a material with $n_2 > 0$ (solid line) and $n_2 < 0$ (dashed line).

profile at the front interface within the sample $E(Z, r, t)$ and calculate the nonlinear phase and absorption accumulated during propagation through the sample, then obtain the electric field at the exit $E_e(Z, r, t)$. With this, we calculate how the exiting beam will propagate to the far field where we place an aperture $E_a(Z, r, t)$. We integrate over the aperture (r from 0 to the aperture radius r_a) and then we integrate in time to determine the amount of energy that reaches the detector. Finally, we normalize this transmission to the transmitted energy with no nonlinearities present to determine the normalized Z-scan transmission $T(Z)$.

Closed-aperture derivation

We start with a focused Gaussian beam given by:

$$E(z, r, t) = E_0(t) \frac{w_0}{w(z)} \exp\left[-\frac{r^2}{w^2(z)} + i\frac{\pi r^2}{\lambda R(z)} + i\phi\right], \tag{3.1}$$

where $E(z, r, t)$ is the complex amplitude and phase of the electric field within the front surface of the sample, z is the sample position relative to the natural focus, r is

the radial distance, t is the time, $E_0(t)$ is the on-axis time-dependent electric field, w_0 is beam waist, and with $w(z) = w_0\sqrt{1 + z^2/z_0^2}$, where $z_0 = \pi w_0^2/\lambda$ is the Rayleigh distance and $R(z) = z(1 + z_0^2/z^2)$. In addition, ϕ is a constant phase term across the beam profile and can be ignored here. We note that the power corresponding to $E(z, r, t)$ is the power before the sample, less the Fresnel reflection at the front surface.

We have previously solved equation (2.81), which describes nonlinear absorption, and determined the intensity through propagation (equation (2.82)). With this, we calculated the total nonlinear phase accumulated in equation (2.83). Rewriting the intensity equation to include spatially varying intensity (through r and the sample position z):

$$I_e(z, r, t) = \frac{I(z, r, t)\, e^{-\alpha L}}{1 + q(z, r, t)}, \tag{3.2}$$

and similarly, we rewrite the nonlinear phase equation as:

$$\Delta\phi(z, r, t) = \frac{k_0 n_2}{\alpha_2} \ln\left[1 + q(z, r, t)\right]. \tag{3.3}$$

Here $k_0 = 2\pi/\lambda_0$ is the free space propagation constant, $q(z, r, t) = \alpha_2 I(z, r, t) L_{\text{eff}}$ and L_{eff} is the effective length (equation (2.84)). We note that the on-axis phase shift is given by:

$$\Delta\Phi_0 = \Delta\phi(z, 0, t) = \frac{k_0 n_2}{\alpha_2} \ln\left[1 + q(z, 0, t)\right], \tag{3.4}$$

and, in the limit when $\alpha_2 \to 0$, this becomes:

$$\Delta\Phi_0 = k_0 n_2 I_0 L_{\text{eff}}, \tag{3.5}$$

providing an easy way to calculate n_2.

Using these expressions, the complex electric field at the exit of the sample:

$$E_e = E\left(z,r,t\right)e^{-\alpha L/2}\left(1+q\left(z,r,t\right)\right)^{\left(ik_0 n_2/\alpha_2 - 1/2\right)}. \tag{3.6}$$

For the case of a Gaussian beam and $|q(z,r,t)| < 1$, we can perform a binomial expansion around $q(z,r,t)$ to arrive at:

$$E_e(z,r,t) = E\left(z,r,t\right)e^{-\alpha L/2}\sum_{m=0}^{\infty} F_m \exp\left(2mr^2/w^2\left(z\right)\right), \tag{3.7}$$

where

$$F_m = \frac{\left(i\Delta\phi_0\left(z,r=0,t\right)\right)^m}{m!}\prod_{j=1}^{m}\left[1+i\left(j-\frac{1}{2}\right)\frac{\lambda\alpha_2}{2\pi n_2}\right]. \tag{3.8}$$

This expansion is known as the Gaussian decomposition method. Using this expression, we perform a zeroth-order Hankel transform to determine the electric field distribution at the aperture at a distance d away:

$$E_a\left(r,t\right) = E\left(z,r=0,t\right)e^{-\alpha L/2}\sum_{m=0}^{\infty} F_m \frac{w_{m0}}{w_m}\exp\left[-\frac{r^2}{w_m^2}+\frac{i\pi r^2}{\lambda R_m}+i\theta_m\right], \tag{3.9}$$

with the following parameters:

$$\begin{gathered} w_{m0}^2 = \tfrac{w^2(z)}{2m+1}, \qquad d_m = \tfrac{kw_{m0}^2}{2}, \qquad w_m^2 = w_{m0}^2\left[g^2+\tfrac{d^2}{d_m^2}\right], \\ R_m = d\Big[1-\tfrac{g}{g^2+d^2/d_m^2}\Big]^{-1}, \quad \theta_m = \tan^{-1}\left[\tfrac{g}{d/d_m}\right], \qquad g = 1+d/R\left(z\right). \end{gathered} \tag{3.10}$$

Now, if the time-dependence is due to the power at the entrance of the sample $P(t)$, we can arrive at solutions for continuous-wave and pulsed transmission. First, we integrate over the aperture:

$$T_{\mathrm{CW}}\left(z,P(t)\right) = \frac{\int_0^{r_a}\left|E_a\left(z,r,P\left(t\right),d\right)\right|^2 rdr}{\int_0^{r_a}\left|E_a(z,r,P\left(t\right),d)_{\mathrm{linear}}\right|^2 rdr}. \tag{3.11}$$

We note that the denominator is the same as the numerator, except we take the limit where n_2 and multiphoton-absorption go to zero, thus it is the ratio of the power

with and without nonlinearities. If $P(t)$ = constant, this is the solution for a laser in continuous-wave operation. To arrive at the pulsed solution, we need to integrate over time using:

$$T_{\text{pulsed}}\left(z, P(t)\right) = \frac{\int_{-\infty}^{\infty} P\left(t\right) T_{\text{CW}}\left(z, P\left(t\right)\right) dt}{\int_{-\infty}^{\infty} P\left(t\right) T_{\text{CW}}\left(z, 0\right) dt}. \tag{3.12}$$

This is the ratio of the energy with and without nonlinearities. It is essentially a weighted average of transmission functions. We note that this model does not take group velocity dispersion into account.

The distance d and the radius of the aperture r_a are related through the S parameter, which is the transmittance through the aperture. For a Gaussian beam, the S parameter is:

$$S = 1 - e^{\left(-2r_a^2/w_a^2\right)} \tag{3.13}$$

with $w_a = w_0(1 + d^2/z_0^2)^{1/2}$. In the limit where S goes to unity, we arrive at the open-aperture solution.

Closed-aperture simplifications

Although equations (3.9) and (3.11) are quite complicated, we can obtain immediate insight if we take the limit when $S \to 0$ for a very small aperture ($d \gg z_0$). This can be accomplished by taking the limit when $r \to 0$. Additionally, we assume the nonlinear phase shift $|\Delta\Phi| \ll 1$. With these simplifications, we find equation (3.11) becomes:

$$T_{\text{CW}}\left(z, \Delta\Phi_0\right) \simeq 1 + \frac{4\Delta\Phi_0 \left(\frac{z}{z_0}\right)}{\left(\frac{z^2}{z_0^2} + 9\right)\left(\frac{z^2}{z_0^2} + 1\right)}. \tag{3.14}$$

This is a relatively good approximation. For example, using a ΔT of 50% corresponds to an error of roughly 5%. Alternatively, we can find the peak and valley locations,

then look at the change in transmission to find an approximate value for the $\Delta\Phi_0$:

$$\Delta T_{p-v} \simeq 0.406\Delta\Phi_0. \tag{3.15}$$

In addition, we can calculate the peak-valley separation in the z-direction to be:

$$\Delta Z_{p-v} \simeq 1.7Z_0. \tag{3.16}$$

These expressions serve as a quick method to estimate the Rayleigh distance and calculate the nonlinear phase shift (and hence n_2) of an unknown sample. We note that for higher intensities, larger nonlinear phase shifts cause the signal to become asymmetric and consequently, all of our analysis uses the full calculation using equations (3.9), (3.11), and (3.12).

3.1.2 Open-aperture Z-scan analysis

Z-scan is a very convenient technique for measuring not only nonlinear refraction, but nonlinear absorption using a small adjustment. By opening the aperture, $S \to 1$, and we collect all of the transmitted light. Here, nonlinear absorption is strongest at the focus, appearing as a dip in the Z-scan plot. In this section, we provide a basic analytical framework for measuring both two- and three-photon absorption in bulk samples using the open-aperture Z-scan technique.

Open-aperture Z-scan with two-photon absorption

For two photon absorption, the open-aperture Z-scan derivation requires that we determine the intensity change through a sample material for an arbitrary beam waist and z location. For the simplest derivation, we assume that the beam does

not change its shape as it passes through the medium in the absence of two-photon absorption and linear losses. This simply requires that the sample is smaller than the Rayleigh distance. Using this approximation, for each point in the beam's cross section at the entrance of the material, there is a corresponding point at the exit that is determined solely by the entrance intensity, linear and nonlinear loss, and the length of the material. This also implies that our beam does not exhibit significant self focusing within the material. Once we have this expression, we integrate over the beam profile.

We begin our derivation with a Gaussian input profile:

$$I_{in}\left(z,r,P(t)\right)=\frac{2P\left(t\right)}{\pi w^{2}\left(z\right)}e^{\frac{-2r^{2}}{w^{2}(z)}}, \tag{3.17}$$

where $P(t)$ is the instantaneous power of the beam at time t, r is the radial coordinate and:

$$w\left(z\right)=w_{0}\sqrt{1+\left(\frac{z}{z_{0}}\right)^{2}}, \tag{3.18}$$

is the beam waist at sample position z, where $z=0$ is the focus. In addition, we define the Rayleigh distance as $z_0=\pi w_0^2/\lambda$. Now, we calculate the intensity at the exit of the sample $I_e(z,r,P(t))$ using equation (3.2), and integrate over the area at the exit of the sample to determine the transmitted power:

$$P_{e}\left(z,P(t)\right)=2\pi\int_{0}^{\infty}\frac{I_{in}\left(z,r,t\right)e^{-\alpha L}}{1+\alpha_{2}L_{\text{eff}}I_{in}\left(z,r,t\right)}rdr=P\left(t\right)e^{-aL}\frac{\ln\left(1+q_{0}\left(z,P(t)\right)\right)}{q_{0}\left(z,P(t)\right)}, \tag{3.19}$$

where:

$$q_{0}\left(z,P(t)\right)=\frac{2\alpha_{2}L_{\text{eff}}z_{0}}{\lambda\left(z^{2}+z_{0}^{2}\right)}P\left(t\right)=\frac{\alpha_{2}L_{\text{eff}}w_{0}^{2}}{w^{2}\left(z\right)}I_{0}\left(t\right). \tag{3.20}$$

To determine the normalized transmission, we take the limit of this expression as $\alpha_2 \to 0$:

$$P_{\text{linear}}(z,t) = P(t)\, e^{-aL}, \tag{3.21}$$

then normalize equation (3.19) using this expression to arrive at the normalized transmission:

$$T(z, P(t)) = \frac{\ln\left(1 + q_0\left(z, P(t)\right)\right)}{q_0\left(z, P(t)\right)}. \tag{3.22}$$

Equation (3.22) is a simple, closed-from expression for open-aperture Z-scan. If $P(t)$ is constant, this can be used for continuous-wave light. Most often, two-photon absorption coefficients are very small, and therefore, pulsed light is necessary to obtain measurable signal. Therefore, we integrate this equation as we have previously done in equation (3.12).

Open-aperture Z-scan with three-photon absorption

We perform an identical procedure to the two-photon absorption case to derive three-photon absorption. Now, we solve:

$$\frac{d}{dl} I(l) = -\left(\alpha_1 + \alpha_3 I^2(l)\right) I(l), \tag{3.23}$$

where l is the distance within the sample. This equation has a solution of:

$$I_e(z,r,t) = \frac{I(z,r,t)\, e^{-\alpha L}}{\sqrt{1 + 2\alpha_3 L_{\text{eff2}} I^2(z,r,t)}}, \tag{3.24}$$

where we have defined an effective length for three-photon absorption:

$$L_{\text{eff2}} \equiv \frac{1 - e^{-2\alpha L}}{2\alpha}. \tag{3.25}$$

Using equations (3.17), performing a similar integration to (3.19) and normalizing using (3.21), we arrive at the normalized transmission:

$$T\left(z, P\left(t\right)\right) = \frac{\sinh^{-1}\left(q_3\left(z, P\left(t\right)\right)\right)}{q_3\left(z, P\left(t\right)\right)}, \tag{3.26}$$

with

$$q_3\left(z, P\left(t\right)\right) = \frac{2\sqrt{2\alpha_3 L_{\text{eff2}}}}{\lambda} \frac{z_0}{z^2 + z_0^2} P\left(t\right). \tag{3.27}$$

Again, if $P(t)$ is constant, this is the continuous-wave solution for three-photon absorption and we apply similar methods we used in the two-photon case to arrive at pulsed solutions.

3.2 Nonlinear refraction in bulk rutile TiO_2

We quantify nonlinear refraction in bulk rutile (TiO_2) around 800 nm using the closed aperture Z-scan technique. By fitting our data to theoretical models, we obtain nonlinear refraction coefficients of $n_2 = 8.2 \times 10^{-19}$ for $E \perp c$ and $n_2 = 9.7 \times 10^{-19}$ for $E||c$. The strong nonlinearities observed in TiO_2 around 800 nm are promising for all-optical applications.

3.2.1 Introduction

Titanium dioxide (TiO_2) possesses a high linear and nonlinear index of refraction with minimal two-photon absorption for wavelengths longer than 800 nm, making it a promising candidate material for integrated nonlinear optics applications [11, 44]. However, such devices often contain multiple materials in close proximity, which makes isolating and studying a particular component material difficult. It is therefore

advantageous to quantify the optical nonlinearity of bulk TiO_2 to facilitate the design of integrated optical components.

TiO_2 exists in several crystalline phases rutile, anatase and brookite, thus, establishing a reference value for the nonlinear index of refraction may be difficult. These phases have similar bandgap energies (E_g) of 3.1 eV for rutile and brookite and 3.2 eV for anatase, with rutile being the most stable phase [47, 48]. Around 800 nm, their indices of refraction range from 2.52 –2.79 in rutile, to 2.48 in anatase and 2.63 in brookite [49–51]. Theoretically, the similar indices and bandgap energies should produce comparable optical nonlinearities [10, 44, 52]. Experimentally, reported values of n_2 in thin film anatase and rutile are similar when measured in the same study [53,54]. Even though all three phases should have consistent nonlinearities, their availability in bulk form is very different. Reports on the optical properties anatase are nearly restricted to powder or thin-film form and there are very few reports using brookite. Meanwhile, high-quality single-crystal rutile is commercially available. The availability and high quality of bulk rutile allow us to establish a robust value for the nonlinear index of TiO_2 that can be used as a first approximation for all-phases of TiO_2.

In this study, we quantify nonlinear refraction in bulk rutile near 800 nm using the closed-aperture Z-scan technique [23]. We fit our data to a theoretical model to determine the nonlinear index of TiO_2. These measurements, in conjunction with nonlinear absorption measurements will allow us to calculate nonlinear figures of merit for TiO_2 in Section 3.3.

Table 3.1: Measured laser parameters

λ_0	τ	t	z_0	w_0	d_0	S	M^2	max I_0
(nm)	(fs)	(mm)	(mm)	(µm)	(m)			GW/mm^2
800	50	1.00	3.2	28	0.54	0.02	< 1.06	0.43

3.2.2 Experimental

We perform closed-aperture Z-scan measurements to quantify nonlinear refraction in bulk rutile TiO_2. We measure a 1-mm-thick single-crystal rutile sample grown using the floating zone method, then cleaved along the (100) plane [55]. This cut allows us to measure both the ordinary ($E \perp c$) and extraordinary ($E || c$) axes by changing the crystal orientation. Our measured systems parameters are summarized in Table 3.1. We use a chirped-pulse amplified Ti:Sapphire system with a full-width at half-maximum (FWHM) pulse durations τ of 50 fs and energies up to 3 µJ at a repetition rate of 250 kHz, similar to that described in [23]. We optimize dispersion using a grating compressor and measure the pulse duration using frequency-resolved optical gating (FROG) [56]. We spatially filter the beam to obtain a Gaussian profile, then focus through 0.15-m focal length lens. A scanning slit detector on a single axis stage measures the caustic (beam width versus z-position), which defines the beam waist w_0 and the quality factor (M^2). A pick off mirror and a reference detector before the lens allows us account for small power fluctuations [24].

We carry out a set of closed-aperture Z-scan measurements at several different pulse energies for each orientation. Each measurement set consists of five different Z-scan curves for different incident powers. Measurements taken at low irradiances

(0.02 GW/mm^2) characterize linear signal caused by sample imperfections, which is typically less than a few percent. We use these measurements to remove the linear "background" signal from the four higher-power measurements. Additionally, we measure laser noise to be ±1–2 %. Using a reference detector reduces the system noise to less than ±0.0015 in all but the lowest energy measurements.

3.2.3 Analysis methods

We fit our data to a standard theoretical model for thin samples to extract a value of the nonlinear index of refraction (n_2, defined using $n = n_0 + n_2 I$) [23] [7]. Our system has an S parameter of 0.02, which allows us to analyze our data in the $S = 0$ limit to within 0.5%. We assume a Guassian pulse shape and perform a weighted average of continuous-wave solutions (see equation (3.12)). We note that this method implicitly neglects chromatic dispersion in the sample, which we must correct for. Our fit parameters are n_2 and the waist location (as this is not determined during measurement).

The strong material dispersion in TiO_2 reduces the peak intensity, lowering the apparent value of n_2 if not accounted for. Using $\beta_2 = 985$ fs^2/mm for $E \perp c$ and $\beta_2 = 1240$ fs^2/mm for $E||c$ for rutile around 800 nm, we calculate dispersion lengths ($\tau_{1/e}^2/\beta_2$) of 0.9 and 0.7 mm (ordinary and extraordinary, respectively), where $\tau_{1/e}$ is the pulse duration measured from the $1/e$ point. These dispersion lengths are shorter than our 1-mm sample and reduce the peak intensity by as much as 40% at the exit. We incorporate group velocity dispersion into our model by rescaling the n_2 value extracted without GVD to reflect the effects of dispersion.

We calculate the GVD correction factor by first considering the duration (FWHM) of a Gaussian pulse as it propagates:

$$\tau(z) = \tau_0 \sqrt{1 + \left(4 \ln 2 \frac{\beta_2}{\tau^2} L\right)^2}. \tag{3.28}$$

For a material with negligible higher-order dispersion, the pulse will maintain its Gaussian shape while becoming longer in duration. If there is negligible linear and nonlinear absorption, the peak intensity within the sample is the intensity at the entrance of the sample scaled by the duration:

$$I_0(z) = I_0(0) \left(1 + \left(4 \ln 2 \frac{\beta_2}{\tau^2} L\right)^2\right)^{-1/2}. \tag{3.29}$$

We calculate the nonlinear phase by integrating this expression over the sample length:

$$\begin{aligned} \Delta\Phi_0 &= k_0 n_2 I_0(0) \int_0^L \left(1 + \left(4 \ln 2 \tfrac{\beta_2}{\tau^2} l\right)^2\right)^{-1/2} dl \\ &= k_0 n_2 I_0(0) \tfrac{\tau^2}{\beta_2 4 \ln(2)} \sinh^{-1}\left(4 \ln(2) \tfrac{\beta_2}{\tau^2} L\right) \end{aligned}. \tag{3.30}$$

Our Z-scan measurement determines the nonlinear phase shift $\Delta\Phi_0$, thus, we can rescale our value of the nonlinear index of refraction without dispersion, $n_2^{\beta_2=0}$, to a value that includes dispersion, $n_2^{\beta_2\neq 0}$, using:

$$n_2^{\beta_2\neq 0} = n_2^{\beta_2=0} \frac{\beta_2 4 \ln(2) L}{\tau^2 \sinh^{-1}\left(4 \ln(2) \frac{\beta_2}{\tau^2} L\right)}. \tag{3.31}$$

This expression allows us to analyze our data using standard techniques, extracting an effective $n_2^{\beta_2=0}$, then we scale this value to determine the actual nonlinear index $n_2^{\beta_2\neq 0}$ that takes GVD into account.

3.2.4 Results and analysis

We present closed-aperture Z-scan measurements and theoretical fits for bulk rutile in Figures 3.5 and 3.6 using ordinary ($E \perp c$) and extraordinary ($E || c$) polarizations

(respectively). We attribute the increased noise in the lowest powers measured to the poor signal-to-noise ratio in the reference detector. These plots show a maximum ΔT of 58% for ($E \perp c$) and 62% for ($E||c$) when probed with the same pulse energy (as measured before the sample). The birefringence we observe in the data should be even stronger than it appears if we note that the higher index for $E||c$ ($n = 2.792$) results in a larger reflection off the front surface than for $E \perp c$ ($n = 2.52$). From this data, we see evidence of strong birefringence in the nonlinear index of refraction of rutile.

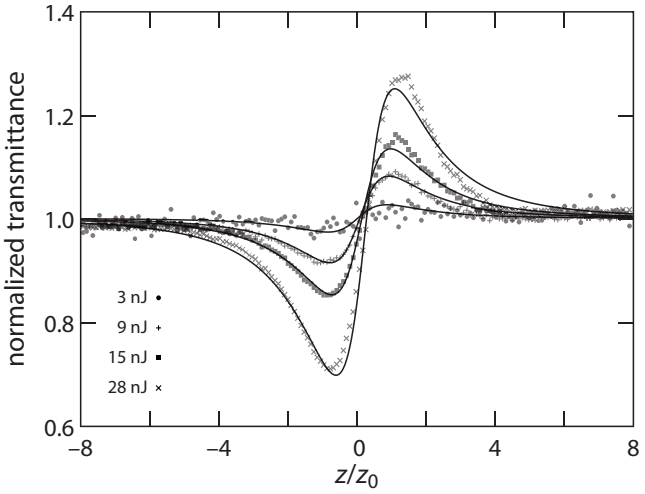

Figure 3.5: Z-scan data and theoretical fit (solid lines) for bulk rutile TiO_2 with $E \perp c$.

We find good agreement between our data and theoretical fits, shown in Figures 3.5 and 3.6. After correcting for group-velocity dispersion, we calculate $n_2 = 8.2 \times 10^{-19}$ for $E \perp c$ and $n_2 = 9.7 \times 10^{-19}$ for $E||c$. Subsequent open-aperture measurements show that nonlinear absorption accounts for $<2\%$ of the measured ΔT, therefore, we are justified neglecting multiphoton absorption and applying the dispersion correction

factors. These corrections result in a 16% and a 23% increase over the values we calculate neglecting dispersion ($E \perp c$ and $E||c$, respectively). Our analysis shows an 18% birefringence in the nonlinear index of rutile, which may have important consequences for devices made using single-crystal rutile.

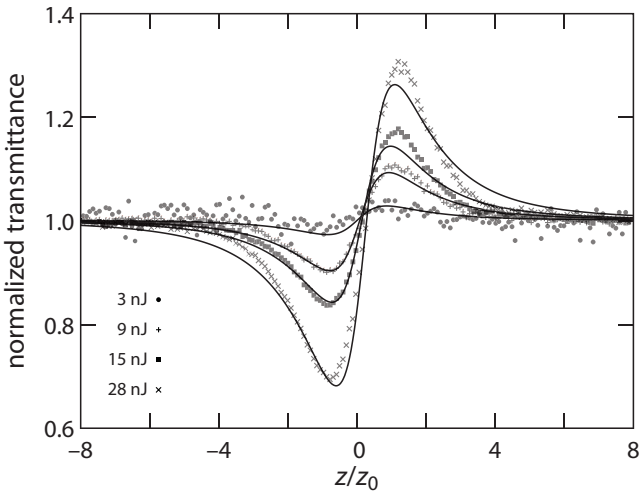

Figure 3.6: Z-scan data and theoretical fit (solid lines) for bulk rutile TiO_2 with $E||c$.

3.2.5 Discussion

We summarize reported values for bulk and thin film TiO_2 in Table 3.2, along with our measurements. Theory suggests that measurements using photon energies near or below the half-bandgap ($\hbar\omega = 1.55$ eV, 800 nm) should be in reasonably good agreement in terms of magnitude and sign [10, 52]. We find our measurements agree well with reports using 1064 nm [44,57]. The 18% birefringence in the nonlinear index may be partially attributed to the differences in the linear index, which predicts a 39% increase for $E||c$ using an empirical model [44].

Table 3.2: Reported values of n_2 in TiO_2. Daggers (†) denote effective n_2 values converted from third-harmonic measurements. Asterisks (*) denote *this work*.

form	phase	n_2 (m^2/W)	λ_0 (nm)	index	reference	notes
bulk	rutile	-1.1×10^{-17}	532	2.97	[58]	$c\|\|E$
bulk	rutile	-1.0×10^{-17}	532	2.66	[58]	$c\perp E$
bulk	rutile	9.7×10^{-19}	800	2.79	[11]	$c\|\|E^*$
bulk	rutile	8.2×10^{-19}	800	2.52	[11]	$c\perp E^*$
bulk	rutile	9.4×10^{-19}	1064	2.48	[44]	
bulk	rutile	2×10^{-18}	1064	2.48	[57]	
thin film	anatase	-6.3×10^{-17}	800	2.1	[53]	PLD
thin film	rutile	-2.7×10^{-17}	800	2.3	[53]	PLD
thin film	rutile	2.7×10^{-18}	1900	2.4	[54]	sol-gel†
thin film	anatase	1.8×10^{-18}	1900	2.29	[54]	sol-gel†
thin film	anatase	5.2×10^{-18}	800	2.32	[59]	sputtered†
nanocluster	anatase	5.2×10^{-18}	850	-	[60]	
nanoparticle	anatase	1×10^{-19}	800	-	[61]	
nanoporous	anatase	2.2×10^{-11}	1064	1.9	[62]	

While our measurements are consistent with other bulk rutile measurements, they do not agree with reported thin-film values around 800 nm in either magnitude or sign [53, 59]. This disagreement is even larger if we consider nanocluster, nanoparticle, and nanopourous thin-films of TiO_2 [60–62]. Whereas the negative values around 532 nm are consistent with theoretical models for direct-bandgap semiconductors [10, 58], the negative values observed in thin-films around 800 nm are inconsistent with theory [53]. These differences in reported n_2 values may suggests a different physical mechanism is responsible for the nonlinearities in thin films that is not present in the bulk material [62]. Alternatively, these discrepancies may simply reflect the experimental difficulty of working with thin films, which suffer from etalon effects, nonlinear background signal caused by the substrate, and are susceptible to damage [63, 64]. Our values for n_2 in bulk rutile TiO_2 agree with other reported bulk

values, which suggests that different physical mechanisms may be responsible for the nonlinearities in TiO_2 thin films.

If we can integrate single-crystal rutile into devices, future designs should consider the birefringence in n_2, either to avoid potential problems or to take advantage of this unique effect. This birefringence may produce a power-dependent polarization rotation, potentially leading to unexpected results when used in conjunction with polarization optics. Therefore, strategies to mitigate this nonlinear birefringence may be necessary. Alternatively, designs which predominantly use $E||c$ may benefit from the increased value of n_2. In addition, we may use this effect for nonlinear mode-conversion or in new phase-matching schemes. The birefringence we observe in bulk rutile may have important impacts for integrated nonlinear optical devices.

3.2.6 Nonlinear refraction summary

We quantify nonlinear refraction in bulk rutile around 800 nm using the closed-aperture Z-scan technique. We measure strong nonlinearities that are 30 and 35 times those found in silica [21]. We observe an 18% birefringence in our measured values of n_2 that correlates with the higher linear index of refraction for $E||c$. By studying bulk rutile, this study provides representative values for the nonlinear index of TiO_2. These values, in conjunction with nonlinear absorption measurements, provide a baseline to evaluate TiO_2 for integrated nonlinear optical devices.

3.3 Multiphoton absorption in bulk rutile TiO_2

The following paper appears in *Optics Express* **20** (3), 3118-3128, 2012.

Mixed two- and three-photon absorption in bulk rutile (TiO_2) around 800 nm

C. C. Evans,[1] J. D. B. Bradley,[1] E. A. Martì-Panameño,[2] and Eric Mazur[1]

[1]*School of Engineering and Applied Sciences, Harvard University, 9 Oxford Street, Cambridge, Massachusetts 02138, USA*

[2]*FCFM, Benemèrita Universidad Autònoma de Puebla, Av. San Claudio y Rio Verde, C.P. 72570, Puebla, Puebla, Mèxico*

Abstract: We observe mixed two- and three-photon absorption in bulk rutile (TiO_2) around 800 nm using the open aperture Z-scan technique. We fit the data with an extended model that includes multiphoton absorption, beam quality, and ellipticity. The extracted two- and three-photon absorption coefficients are below 1 mm/GW and 2 mm^3/GW^2, respectively. We observe negligible two-photon absorption for 813-nm light polarized along the extraordinary axis. We measure the nonlinear index of refraction and obtain two-photon nonlinear figures of merit greater than 1.1 at 774 nm and greater than 12 at 813 nm. Similarly, we obtain three-photon figures of merit that allow operational intensities up to 0.57 GW/mm^2. We conclude that rutile is a promising material for all-optical switching applications around 800 nm.

3.3.1 Introduction

Rutile (titanium dioxide) is a wide-bandgap semiconductor, advantageous for many optical applications due to its high refractive index, birefringence, and transparency for wavelengths $\geq$ 400 nm. In addition, it is naturally abundant, and highly stable.

Rutile also has a large Kerr nonlinearity ($n_2 = 9\times10^{-19}$ m^2/W) [44]. These properties make rutile a promising material for nonlinear all-optical applications such as ultrafast switching, logic [65] and wavelength conversion [66].

Even with a high Kerr nonlinearity, two- and three-photon absorption (2PA and 3PA, respectively) impose limitations for nonlinear optical devices that rely on high intensities [6]. For semiconductors, we expect 2PA (3PA) to occur for photon energies equal to or greater than the half- (third-) bandgap energy (E_g) [9, 10]. The half- (third-) bandgap energy corresponds to 800 nm (1200 nm) in rutile ($E_g = 3.101$ eV) [47]. We expect device properties to be strongly wavelength dependent around 800 nm due to the transition from pure 3PA to mixed two- and three-photon absorption.

Studies have quantified pure 2PA in bulk rutile for visible wavelengths (532–750 nm) [58, 67, 68] and 3PA for near-infrared wavelengths (1054 µm) [69]. In bulk rutile, two-photon absorption was observed via weak luminescence for pump wavelengths near 800 nm, however two-photon absorption coefficients were not reported [70]. Meanwhile, the nonlinear properties of TiO_2 films [53, 54, 71–76] and TiO_2 composites [71, 72, 74, 75, 77, 78] have been extensively investigated. Of these thin film studies, those that address pure-phase TiO_2 near 800 nm report effective two-photon absorption coefficients that vary in both magnitude and sign [53, 71, 73–76]. However, there are no reports on two-photon absorption in the bulk material using similar laser parameters for comparison. In addition, 3PA near 800 nm in bulk rutile has not been reported. Therefore, our understanding of multiphoton absorption in bulk rutile is incomplete and requires further study around 800 nm.

In this paper, we investigate multiphoton absorption near 800 nm in bulk rutile

using the open aperture Z-scan technique [23]. We develop a theoretical model to fit the experimental data and extract two- and three-photon absorption coefficients for different wavelengths and crystal orientations. Using the extracted multiphoton absorption coefficients, we discuss nonlinear absorption processes near rutile's half-bandgap and evaluate its applicability as a material for all-optical devices.

3.3.2 Experimental

We perform open-aperture Z-scan measurements using two commercially available 1-mm-thick single-crystal rutile samples grown using the floating zone method [55]. One sample is cleaved along the (001) plane and the second is cleaved along the (100) plane. The (001)-cut allows for measurements with the incident laser beam polarized along the ordinary axis of the crystal ($E \perp c$), while the (100)-cut allows for polarization along both the ordinary and extraordinary axes ($E || c$).

Our experimental setup is similar to that described in [23]. We use a chirped-pulse amplified Ti:Sapphire system with pulse durations $\tau \geq 50$ fs, energies up to 3 µJ at a repetition rate of 250 kHz. We measure the pulse duration using frequency-resolved optical gating (FROG). The beam is spatially filtered to obtain a Gaussian shape then focused through a lens with a 0.15-m focal length. A scanning slit detector on a single axis stage measures the caustic (beam width versus z-position). The caustic determines the beam waist (w_{x0}, w_{y0} in the x and y directions, respectively), quality factor (M^2) and ellipticity (w_{x0}/w_{y0}). A reference detector before the lens allows us account for small power fluctuations [24]. We adjust the central wavelengths, λ_0, of the fs-pulses by spectrally filtering the seed using a physical aperture within

Table 3.3: Measured laser parameters for measurements taken at spectrally filtered center wavelengths of 774 and 813 nm as well as unfiltered measurements at 800 nm. Here, λ_0 is the center wavelength, $2\hbar\omega$ is the two-photon energy, $\Delta\lambda$ is the measured bandwidth (full-width at half-maximum), τ is the pulse duration, $w_{0,\text{ave}}$ is the average beam waist, $z_{0,\text{ave}}$ is the average Rayleigh distance, is the beam parameter product, w_{x0}/w_{y0} is the ellipticity and $I_{0,\max}$ is maximum peak on-axis irradiance for the highest power measurement used for analysis.

λ_0 (nm)	$2\hbar\omega$ (eV)	$\Delta\lambda$ (nm)	τ (fs)	$w_{0,\text{ave}}$ (µm)	$z_{0,\text{ave}}$ (mm)	M^2	w_{x0}/w_{y0}	$I_{0,\max}$ (GW/mm^2)
774	3.20	4	290	33	4.4	< 1.13	0.78	0.21
813	3.05	10	174	36	5.0	< 1.18	0.92	0.32
800	3.10	30	50	28	3.1	< 1.06	0.95	1.04

the pulse-stretcher before the amplifier. Without filtering, the spectral width, $\Delta\lambda$ (FWHM), is 30 nm at $\lambda_0 = 800$ nm with a pulse duration of 50 fs. With filtering, we obtain narrow-band spectra centered at either 774 nm or 813 nm with spectral widths of 4 and 10 nm, respectively. Table 3.3 presents a summary of the measured laser parameters.

We carry out a set of open-aperture Z-scan measurements at the three different central wavelengths for each sample/orientation. Each measurement set consists of five different Z-scan curves for different incident powers. Measurements taken at low irradiances (< 0.06 GW/mm^2) characterize linear signal caused by sample imperfections. We use this signal to remove the linear response from the four higher-power measurements [23].

The intensity dependent attenuation coefficient is approximately given by $\alpha(I, \lambda) = \alpha_0 + \alpha_2 I + \alpha_3 I^2$, where I is the intensity, α_0 is the linear attenuation coefficient ($\alpha_0 \approx 0$

for $\lambda = 800$ nm in rutile), α_2 is the 2PA coefficient, and α_3 is the 3PA coefficient. These coefficients are wavelength dependent. We extract multiphoton absorption coefficients by numerically fitting the measured data to a theoretical model that takes into account the experimental beam and sample parameters (see Appendix A). Our mixed multiphoton absorption model has four degrees of freedom (α_2, α_3, waist position, and astigmatism). Using this model, we fit the multiple Z-scan curves taken at different peak irradiances simultaneously to extract a single value of α_2 and α_3 for a given wavelength and polarization.

3.3.3 Results and discussion

Open aperture Z-scan measurements

Here, we show open aperture Z-scan measurements of bulk rutile for different incident wavelengths and pulse durations. Figure 3.7 (left) shows a typical experimental open aperture Z-scan curve in rutile for 800-nm, 50-fs pulses with $E||c$. Figure 3.7 (right) shows the transmittance change ($\Delta T = 1 - T$, at the focus) as a function of the peak on-axis irradiance for the same sample and pulse duration (referred to here as a ΔT-plot). Figure 3.8 shows data collected using $\lambda_0 = 774$ nm and an input beam polarized with $E \perp c$ and $E||c$ (Figs. 3.8, left and right, respectively). Similarly, Figures 3.9 and 3.10 show measurements and fits for $\lambda_0 = 813$ nm and $\lambda_0 = 800$, respectively.

The primary sources of uncertainty in our Z-scan measurements are the noise of the laser and sample imperfections. We measure laser noise to be ±1–2 %. Using low intensity and by adjusting the sample position, we reduce the linear background variations caused by sample imperfections to less than 1%. To reduce the overall

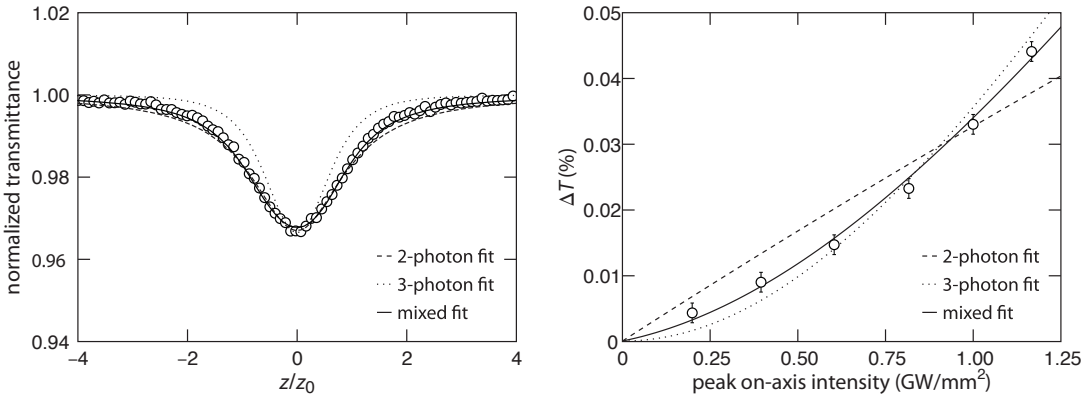

Figure 3.7: The left plot shows open-aperture Z-scan measurements of bulk rutile (open circles) using a 50-fs pulse with $\lambda_0 = 800$ nm for the extraordinary ($E||c$) polarization (peak on-axis irradiance of 0.95 GW/mm^2). Theoretical fits for pure two-photon [23], three-photon [79], and our mixed multi-photon absorption models are shown in dashed, dotted, and solid lines, respectively. The right plot shows the change in transmittance ($\Delta T = 1 - T$) at the focus as a function of peak on-axis irradiance for the same sample, wavelength, and pulse duration. Data is shown in open circles with error bars. Theoretical fits for pure two-photon, three-photon and mixed two- and three-photon absorption are shown in dashed, dotted, and solid lines, respectively.

noise, we use a reference photodiode, drift detection, temporal averaging, and background subtraction. These methods suppress the normalized transmittance variation to ± 0.0015. Consecutive scans resulted in measurements that were within this transmittance variation. To characterize the repeatability of our technique, we analyzed four measurement sets using $E \perp c$, taken over non-consecutive days for both the (001)- and (100)-cut. We could not compare these measurements on a point-for-point basis, consequently, we analyzed these measurement sets using our mixed two- and three-photon model (see section A) and determined the standard deviation of α_2 and α_3. We obtain a standard deviation of 5% for α_2 and 18% for α_3. In addition, we have tested our system using CS_2 with a 50-fs pulse at 800 nm and we obtain a 2PA coefficient of 0.06 mm/GW using standard analysis. This value falls within the range of values obtained for CS_2 in previous studies using 110-fs pulses [80, 81] and thermal methods [82, 83].

Sample damage [63] and thermal effects [82, 83] can mask electronic nonlinearities. We verified that no damage or alterations occurred to the sample by comparing low irradiance scans taken directly before and after each high intensity measurement set. We performed thermally managed Z-scan [82, 83] using our bulk rutile samples in both open- and closed-aperture configurations. By utilizing an optical chopper and fast photodiodes to resolve pulse-to-pulse transmittance changes, we did not observe cumulative (i.e. thermal) changes in the signal. Similarly, measurements taken at 10 kHz produced equivalent measurements to those taken at 250 kHz, confirming that no cumulative effects were present.

Justification and fitting of the mixed-multiphoton absorption model

To establish the optimum fitting procedure, we first fit our data with standard open-aperture Z-scan models and compare to our mixed-multiphoton absorption model. Figure 3.7 (left) presents a typical experimental Z-scan curve that is fit using a pure 2PA-model [23], a pure 3PA-model [79] and our mixed-multiphoton model (dashed, dotted, and solid lines, respectively). In Fig. 3.7 (right), we show an experimental ΔT-plot which is fit using a pure 2PA-, 3PA- and our mixed-multiphoton model (dashed, dotted, and solid lines, respectively).

Comparing a pure 2PA to a pure 3PA model, we find that fitting individual Z-scan curves appears to favor the 2PA model. However, a 2PA model predicts a very different ΔT behavior with increasing irradiance. Three-photon absorption better fits the high intensity ΔT data, yet is insufficient for low intensity data and individual Z-scan curves. We see that our mixed-multiphoton model provides an excellent fit to both Z-scan curves and ΔT-plots. These observations highlight two important points. First, neither a pure 2PA- nor a pure 3PA-model can describe the data sufficiently, necessitating a mixed-multiphoton absorption model. Second, both curve fitting and the ΔT-plot method provide complimentary information. Curve fitting is advantageous because signal away from the focus always contains the lowest order absorption, such as 2PA. However, curve fitting can mask higher order absorption and is susceptible to beam distortions. In contrast, the ΔT-plot provides a fast measure on higher order absorption processes. Yet, this method may overlook lower order absorption if sufficient low irradiance data is not included.

Quantifying mixed two- and three-photon absorption requires a balance between

the curve fitting and the ΔT-plot methods. It also requires further constraint to account for the additional fitting coefficients. Consequently, we use a more robust method whereby we fit an entire measurement set, consisting of several full Z-scan curves taken at different peak irradiances, using a single set of parameters. This technique produces equivalent results to the ΔT-plot method within the uncertainty.

We tested the optimization algorithm by using various starting points while keeping all other parameters at experimentally determined values. These variations included starting both α_2 and α_3 at zero as well as other magnitudes and signs of α_2, α_3 and the astigmatism. Other combinations, such as two- and four-photon absorption (with astigmatism) could produce reasonable fits in some, but not all cases (notably the 813-nm data set). We found that including two- and three-photon absorption in our model resulted in good fits for all experimental data while minimizing the number of fitted parameters.

We quantitatively compare the fit quality using standard 2PA [23] and 3PA [79] models to our mixed-multiphoton model. Fitting a full data set (for example, a 50 fs pulse, $E||c$) using a 2PA or 3PA model produces R^2 values of 0.974 and 0.925 for ± 4 Rayleigh distance (respectively). We fit the same data set with our mixed-multiphoton model and observe an R^2 of 0.991 (solid lines, Fig. 3.10 right). We performed a similar analysis with the 813-nm data set ($E||c$) and obtain R^2 values of 0.841, 0.944 and 0.950 (2PA, 3PA and mixed-multiphoton models, respectively). From this analysis, the R^2 correlation shows that the mixed-multiphoton model fits the data better than either a pure two- or three-photon absorption model in all cases. Therefore, we conclude that our mixed-multiphoton model is adequate for fitting our

experimental data and use this model to fit the Z-scan data in Figs. 3.8, 3.9, and 3.10 (shown in solid lines).

Two additional fitting parameters were included in the two- and three-photon absorption fitting method. We fit the beam waist location, which aligns the model to the experimental waist position. We found that fitting the astigmatism resulted in a significant improvement in fit quality that we could not achieve by other means (i.e. using additional multiphoton absorption terms or fitting the waist). However, the fit astigmatism is relatively large, ranging from 25% to 100% of the measured Rayleigh distance. We find the largest fit astigmatism using 50-fs pulses. Meanwhile, the measured astigmatism is only up to 12% of the Rayleigh distance. This discrepancy represents the largest source of uncertainty within our analysis. By including the effects of fitting with and without the astigmatism, we estimate the uncertainty to be $\pm 15\%$ in α_2 and a factor of 2 for α_3.

Two- and three-photon absorption coefficients

Table 3.4 summarizes bulk rutile two- and three-photon absorption coefficients. Overall, α_2 ranges from less than 10^{-7} mm/GW to 0.9 mm/GW ($\pm 15\%$). Comparing 774 nm to 813 nm measurements, we find that the 2PA coefficients at these two wavelengths differ considerably. At 774 nm, α_2 is 0.54 mm/GW ($E \perp c$) and 0.89 mm/GW ($E || c$). At 813 nm and $E || c$, α_2 is below the measureable limit. For $E \perp c$, we extract a value of 0.08 mm/GW. Lastly, two-photon absorption coefficients for 800 nm are between the 774 nm and 813 nm coefficients. Rutile has typical values of α_3 on the order of 1 mm^3/GW^2 as shown in Table 2. The values of α_3 at 800 nm are

0.2 mm^3/GW^2. We observe 4 to 9 times higher three-photon absorption coefficients for 774 and 813 nm wavelengths. The difference in α_3 between 774-nm and 813-nm measurements is less than a factor of two and is therefore within the experimental uncertainty (considering both orientations).

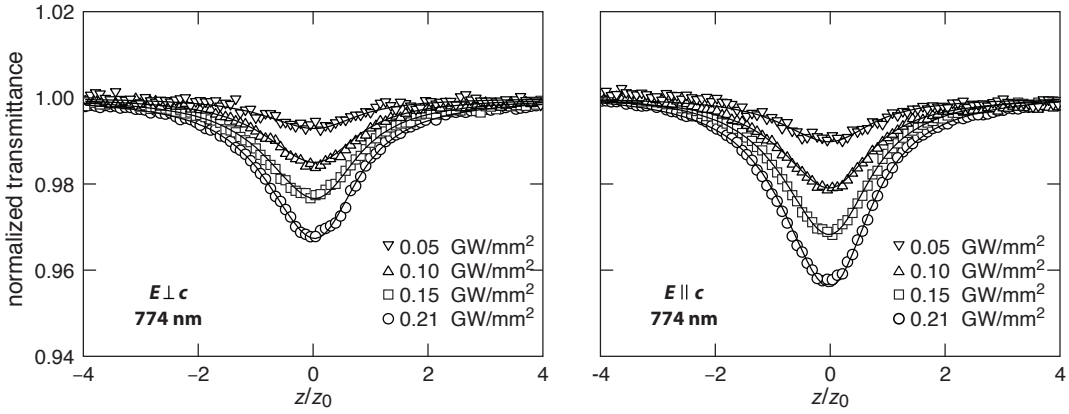

Figure 3.8: Open-aperture Z-scan measurements of bulk rutile using a 290-fs pulse with $\lambda_0 = 774$ nm for ordinary ($E \perp c$) and extraordinary ($E||c$) polarizations (left and right, respectively). Solid lines are a fit across all irradiances shown. Fit parameters are α_2, α_3, average z_0 and the astigmatism.

These values of α_2 and α_3 in bulk rutile are consistent with values obtained under similar conditions [69]. Our degenerate 2PA coefficients around 774 nm are in good agreement with other nondegenerate two-photon absorption measurements (using a 1054-nm pump and a 612-nm probe producing an effective α_2 coefficient of 1–5 mm/GW) [69]. Similarly, our values of α_3 (0.2–2 mm^3/GW^2) are within the range of measurements taken at 1054 nm (0.5 mm^3/GW^2) in the same study.

Recently, both negative and positive 2PA coefficients of significantly higher magnitude have been measured in TiO_2 thin films in the 750–830 nm range [53,71,73–75]. However, the thin films investigated vary widely in growth methods, composition, and crystalline phase, thus making it difficult to compare directly to the bulk measure-

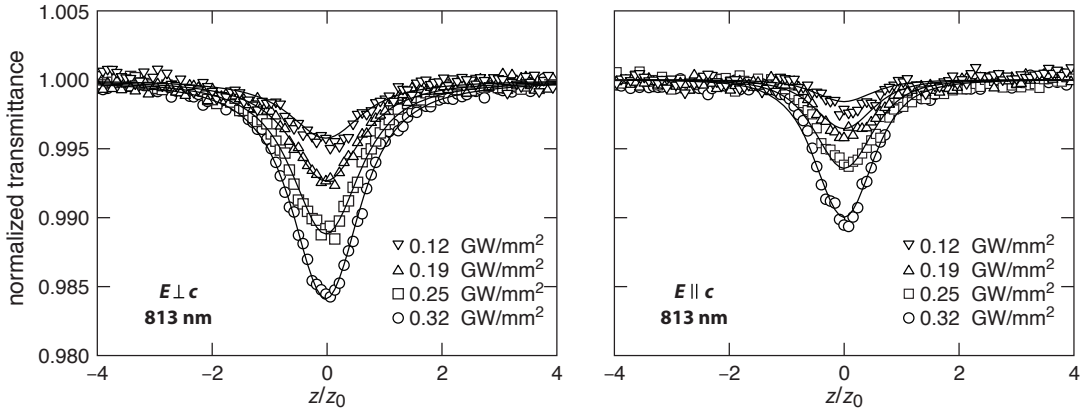

Figure 3.9: Open-aperture Z-scan measurements of bulk rutile using a 174-fs pulse with $\lambda_0 = 813$ nm for ordinary ($E \perp c$) and extraordinary ($E||c$) polarizations (left and right, respectively). Solid lines are a fit across all intensities shown. Fit parameters are α_2, α_3, average z_0 and the astigmatism.

ments reported here. Furthermore, while our values are consistent with other bulk measurements, there are inconsistencies with reported thin film values in both sign and magnitude for polycrystalline rutile [53] and anatase TiO_2 [53, 71, 74, 75]. Thin films are more challenging to measure than bulk samples, and often require intensities approaching the damage threshold to achieve sufficient signal-to-noise, which may lead to linear effects that appear as nonlinear signal [63]. Therefore, further investigation of TiO_2 thin film versus bulk nonlinearities is required.

We find that the 2PA coefficients decrease significantly between 774 and 813 nm. These wavelengths correspond to two-photon energies of $2\hbar\omega = 3.20$ eV and 3.05 eV, respectively. These two-photon energies lie on opposite sides of rutile's indirect bandgap (3.101 eV) [47]. Although we observe no effective 2PA for $E||c$ at 813 nm, we still measure a small 2PA-signal for $E \perp c$. Other studies attribute weak absorption at 3.062 eV, which is only present for $E \perp c$, to a direct forbidden bandgap [47, 70, 84]. This energy is within the two-photon bandwidth of the 813-nm pulse and is likely the

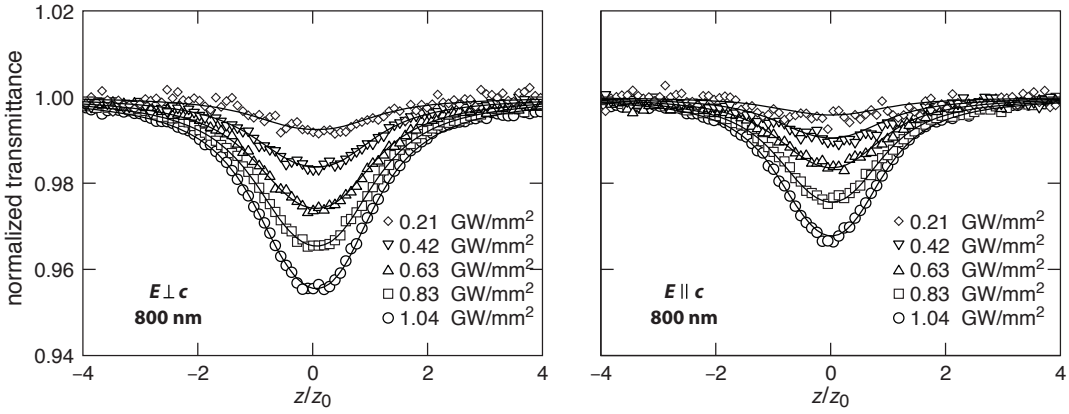

Figure 3.10: Open-aperture Z-scan measurements of bulk rutile using a 50-fs pulse with $\lambda_0 = 800$ nm for ordinary ($E \perp c$) and extraordinary ($E || c$) polarizations (left and right, respectively). Solid lines are a fit across all intensities shown. Fit parameters are α_2, α_3, average z_0 and the astigmatism.

cause of the small 2PA-signal observed. Between these two effects, the resonance at rutile's indirect bandgap is the largest source of 2PA. This analysis implies that using wavelengths further red-shifted from the two-photon resonance (longer than 800 nm) should result in reduced 2PA.

The measurements at 800 nm using a 50-fs pulse require additional interpretation. We find the 2PA coefficients using 800-nm light lie between the values obtained at 774 nm and 813 nm. As shown in Table 3.4, as the wavelength increases, α_2 decreases monotonically as it passes through the two-photon resonance at the band-edge. This behavior at 800 nm may be partially due to the pulse's extended spectrum (785–815 nm, FWHM). This bandwidth includes spectral components experiencing both higher (774 nm, $\Delta\lambda = 4$ nm) and lower (813 nm, $\Delta\lambda = 10$ nm) 2PA. This implies that the extracted values of α_2 are a convolution between the pulse spectrum and the two-photon absorption spectrum.

Table 3.4: Fitted nonlinear absorption coefficients, calculated 2PA figures of merit and maximum intensities from 3PA (using $n_2 = 7.9\times10^{-19}\text{m}^2/\text{W}$ [85]). Here, λ_0 is the center wavelength, $2\hbar\omega$ is the two-photon energy, α_2 is the 2PA coefficient, α_3 is the 3PA coefficient, $n_2/(\alpha_2\lambda)$ is the 2PA figure of merit and I_{max}^{3PA} is the maximum intensity calculated from the 3PA figure of merit, $1 < [n_2/(\alpha_3\lambda I_{\text{max}})]$ [6]. The uncertainty for measurements at 774 nm and 813 nm is ±15% for α_2 and a factor of 2 for α_3. For 800 nm, the uncertainty is ±80% for α_2 and a factor of 6 for α_3.

		ordinary polarization ($E\perp c$)				extraordinary polarization ($E\|\|c$)			
λ_0	$2\hbar\omega$	α_2	α_3	$\frac{n_2}{\alpha_2\lambda}$	I_{max}^{3PA}	α_2	α_3	$\frac{n_2}{\alpha_2\lambda}$	I_{max}^{3PA}
(nm)	(eV)	$\left(\frac{\text{mm}}{\text{GW}}\right)$	$\left(\frac{\text{mm}^3}{\text{GW}^2}\right)$		$\left(\frac{\text{GW}}{\text{mm}^2}\right)$	$\left(\frac{\text{mm}}{\text{GW}}\right)$	$\left(\frac{\text{mm}^3}{\text{GW}^2}\right)$		$\left(\frac{\text{GW}}{\text{mm}^2}\right)$
774	3.20	0.54	1.1	1.9	0.93	0.89	1.8	1.1	0.57
813	3.05	0.08	0.8	12.1	1.20	$< 10^{-7}$	0.9	$> 10^6$	1.10
800	3.10	0.15	0.2	6.6	4.90	0.09	0.2	11.0	4.90

Nonlinear figures of merit

Multiphoton absorption has important implications for nonlinear optical devices. Material performance is quantified by the nonlinear figures of merit [6]. The 2PA figure of merit (FOM) is given by $n_2/(\alpha_2\lambda)$ and the 3PA FOM is given by $n_2/(\alpha_3\lambda I_{\text{max}})$, where I_{max} is the peak operational intensity. Both FOMs should be greater than unity for all-optical applications. By setting the 3PA FOM equal to one, we calculate the intensity at which 3PA becomes a limit, given by $I_{\text{max}}^{3PA} = n_2/(\alpha_3\lambda)$. We measured the nonlinear index of refraction around 800-nm (50-fs pulse) using closed-aperture Z-scan and obtain a value of 7.9×10^{-19} m^2/W [1] using standard analysis methods [85]. Although theory predicts a resonant enhancement of the nonlinear index near the

[1] This value is without the dispersion correction in Section 3.2.3. This is more applicable for the present analysis as our nonlinear absorption model does not take dispersion into account either.

half-bandgap [10], we did not measure a significant deviation from values reported at 1064 nm [44], which may be due to dispersive broadening as explained in the previous section. Therefore, the calculated nonlinear figures of merit should be considered a lower limit. Using the nonlinear index and multiphoton absorption coefficients, we evaluate rutile as a candidate material for all-optical applications around 800 nm by calculating its nonlinear figures of merit.

Table 3.4 shows the calculated 2PA FOMs and $I_{\max}^{3PA}$ for each measurement. The 2PA FOMs at 774 nm are the lowest observed (1.9 and 1.1 for $E\perp c$ and $E||c$, respectively). At 813 nm, we obtain a FOM of 12.1 for $E\perp c$ and greater than 10^6 for $E||c$. Calculated $I_{\max}^{3PA}$ is lowest for $E||c$ using 774 nm, with a value of 0.57 GW/mm^2, and greater than 0.93 GW/mm^2 for all other measurements.

All 2PA figures of merit calculated are greater than 1.1, which implies that rutile is compatible with all-optical applications. Measurements at 813 nm show extremely large FOMs, which is favorable for devices. We observe that 2PA can be neglected at 813 nm ($E||c$) and expect similar results for $E\perp c$ at longer wavelengths [86]. These FOMs imply compatibility with popular femtosecond pulsed sources such as Ti:Sapphire and fiber lasers.

Although 2PA may be negligible for certain wavelengths, we must still avoid significant 3PA by operating below $I_{\max}^{3PA}$. For the largest 3PA measured, $I_{\max}^{3PA}$ is 0.57 GW/mm^2 ($E||c$, 774 nm). This limit is far below thin-film damage thresholds for TiO_2 [87, 88] and provides a reasonable upper limit for integrated photonic devices [89–92].

3.3.4 Conclusion

We observe mixed two- and three-photon absorption in bulk rutile around 800 nm. By fitting open aperture Z-scan data to a numeric model, we separate the effects of mixed multiphoton absorption. Two- and three-photon absorption coefficients are below 1 mm/GW and 2 mm^3/GW^2, respectively. Two-photon absorption falls below our measurement capabilities for 174-fs pulse with a central wavelength of 813 nm ($E||c$). We determine 2PA FOMs greater than 1 above and below rutile's half-bandgap. We expect superior performance for $\lambda_0 \geq 813$ nm, where the 2PA FOMs are greater than 12.1. Additionally, 3PA is sufficiently small to enable all-optical applications for intensities below 0.57 GW/mm^2. From the low two- and three-photon absorption, we conclude that rutile TiO_2 is a promising material for all-optical applications such as switching and logic near 800 nm.

3.3.5 Acknowledgements

Several people contributed to the work described in this paper. C.E. and E.M-P. conceived of the basic idea for this work. C.E., E.M-P., and J.B. planned the experiments. C.E. designed and carried out the experiments, implemented the model/fitting, and analyzed the results. E.M., E.M-P. and J.B. supervised the research and the development of the manuscript. C.E. wrote the first draft of the manuscript; all authors subsequently took part in the revision process and approved the final copy of the manuscript. Benjamin Franta, Phillip Munoz and Orad Reshef provided feedback on the manuscript throughout its development. The research described in this paper was supported by the NSF under contract ECCS-0901469. One of the authors, EM-

P, thanks CONACYT Mexico for the support through the project 120346, as well as the David Rockefeller Center for Latin American Studies and the Mazur Group for additional financial support.

Chapter 4

Optimizing TiO_2 thin films

Fabricating integrated TiO_2 optical devices requires high-quality thin films that can serve low-loss planar waveguides, additionally, these films should have similar or improved properties to bulk rutile in terms of their linear and nonlinear optical properties. Optimizing thin films, separate from fabricating nanowire devices, allows us to isolate sources of loss attributed to the deposited film. This is particularly critical for deposited materials, where there may be several sources of loss [93–96]. In this chapter, we summarize a series of thin-film studies to develop and optimize amorphous and polycrystalline (anatase phase) TiO_2 thin films using reactive radio frequency (RF) sputtering and then we compare representative films in Section 5.1.2. By developing suitable thin films, this provides us with a high-quality, well-understood starting material from which we can fabricate integrated optical devices.

4.1 Experimental

We deposited TiO_2 thin films by reactive RF magnetron sputtering using a metallic Ti target in an Ar and O_2 atmosphere. We deposited the layers on 0.5-mm-thick silicon substrates with a 2.2-µm-thick thermal oxide layer. We controlled the chamber pressure, percentage of oxygen in the chamber given by the O_2 flow rate/(Ar + O_2 flow rates), as well as the substrate temperature. In addition, we either controlled the applied power or DC substrate bias, the opposite parameter varies depending on the specific conditions within the vacuum chamber. We conducted three studies: in the first, we controlled the temperature to obtain either amorphous or anatase TiO_2, in the two remaining studies we optimized the oxygen percentage for each phase to obtain high-quality TiO_2 thin films.

4.1.1 Characterization methods

We summarize our thin-film characterization methods here.

Raman spectroscopy

The presence or absence of crystalline structure can lead to a large variation in optical properties, including losses [97]. We determine which crystalline phases are present in our deposited samples using micro Raman spectroscopy.

In Raman spectroscopy, photons are inelastically scattered by optical phonons in a material, resulting in outgoing photons of lower energy (Stokes shift) that we detect with a spectrometer. Mapping these energy shifts reveals which phonons are present within the sample. Crystalline materials have long-range order that creates sharp

Raman peaks while amorphous materials do not display discernible peaks. Using Raman spectroscopy, we quickly characterize the crystallinity of our thin films.

Ellipsometry

We determine the thickness and index of refraction of our thin films using variable-angle spectroscopic ellipsometry. Ellipsometry analyzes the outgoing polarization of light reflected from the surface of a sample. By performing a series of measurements at different wavelengths, polarization, and angles, we can fit the resulting data to a model in order to extract the thickness and optical constants of our planar sample.

We determine the index of refraction over the wavelength range of 600–1700 nm by fitting spectroscopic ellipsometry data to a Sellmeier model, given by:

$$n^2(\lambda) = 1 + \frac{B_1\lambda^2}{\lambda^2 - C_1} + \frac{B_2\lambda^2}{\lambda^2 - C_2} + \frac{B_3\lambda^2}{\lambda^2 - C_3}. \tag{4.1}$$

Here, λ is the wavelength (in µm) and the B_n's and C_n's are fitting coefficients. This relation provides us with the refractive index across a wide wavelength range that we can use to quantify dispersion in our nanowire devices.

Prism coupling

Prism coupling is a complimentary technique to spectroscopic ellipsometry that, in addition to estimating index and thickness, allows us to measure planar optical propagation losses [98]. In prism coupling, we press a prism against the film under test, forming a point of close contact. Next, we shine laser through the prism to this contact point. Now, we rotate the prism-film system causing light to encounter the prism-film interface at different angles. If the angle corresponds to an angle asso-

ciated with a waveguide mode, the light is coupled into the film and appears as a "streak" along the surface of the film (see Figure 4.1). A primary detector collects uncoupled, deflected light (i.e. at angles that do not correspond to modes). During an angular scan, dips in the primary detector's signal correspond to planar modes. If we detect two modes, we may calculate both the film index and thickness, otherwise we calculate a single parameter (index or thickness) using an assumed value for other parameter.

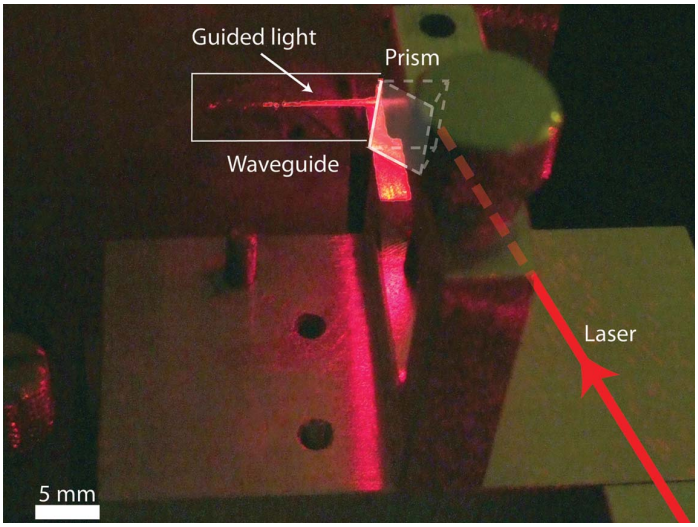

Figure 4.1: Prism coupling loss measurements.

The advantage of prism coupling over ellipsometry is the ability to determine planar waveguiding losses by measuring the streak of propagating light that occurs when coupling into a mode. Prism coupling allows us to directly and non-destructively measure planar waveguiding losses. We measure losses by scanning a secondary detector along the streak of propagation. Assuming the scattered light is proportional to the light within the waveguide, we extract loss values by fitting to an exponential function. In general, a short streak should be visible for a proper measurement

(we use an IR-viewer or an InGaAs camera for IR measurement). If no streak is observable, the propagation losses are usually greater than the measureable limit (30 dB/cm). To determine which films are guiding, we use 826-nm light and observe the streak with an IR-viewer. This wavelength typically propagates with lower losses than visible light. Additionally, these asymmetric (air-TiO_2-silica) waveguides have a long-wavelength cutoff that scales with the film thickness. Therefore, using 826-nm allows us to measure thinner films than for telecommunications wavelengths, reducing the required deposition time. Prism coupling is a simple and fast method to determine the optical quality of a deposited film, and is therefore a key component for thin-film deposition optimization.

4.2 Results and discussion

4.2.1 The effects of deposition temperature on film crystallinity

We studied the effects of the substrate temperature on the index and crystallinity of the TiO_2 thin films. Starting with the deposition parameters shown in Table 4.1, we varied the temperature from 20–400° C. We present a plot of the refractive index ($\lambda = 826$ nm) versus deposition temperature in Figure 4.2. We see a sharp increase in the index around 200°C.

Figure 4.3 shows Raman spectra (with an excitation wavelength of 633 nm) measured for films deposited at ambient temperature (20 °C) and 350 °C. Both spectra show peaks centered around 300 cm^{-1} and 520 cm^{-1} attributed to the Si substrate. The films deposited at 300 °C or above show an additional peak at 144 cm^{-1},

Table 4.1: Deposition parameters for TiO_2 temperature dependence study.

temperature* (°C)	power (W)	DC bias (V)	pressure (mTorr)	O_2 flow (% of total)	time (min)
20–400*	not controlled	300	2	10	90

consistent with the anatase phase of TiO_2 [99]. The films deposited at ambient temperature show no discernible peaks associated with the known crystalline phases of TiO_2. Therefore, we expect those layers to be primarily amorphous. We represent the depositions with discernible anatase peaks as filled circles in Figure 4.2.

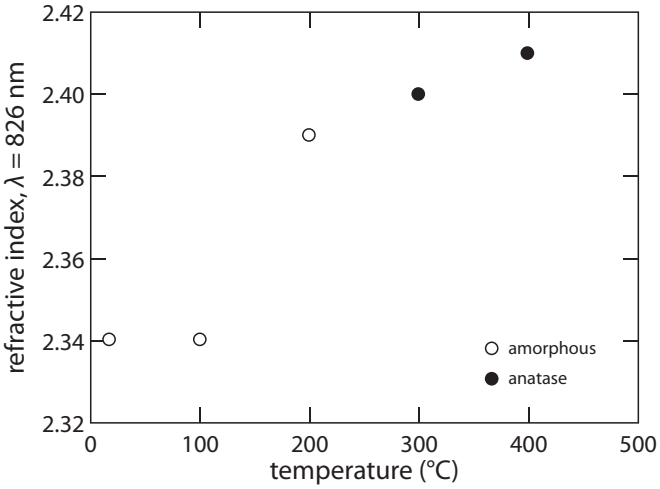

Figure 4.2: The effects of the substrate temperature on the refractive index of TiO_2 films.

This deposition study shows that temperatures of 300°C and above facilitates the crystallization of TiO_2 into the anatase phase. This transition temperature is consistent with other reports [100]. Additionally, the higher index of refraction is correlated to the crystallinity. Using the deposition temperature, we are able to control the crystallinity of our films to produce anatase or amorphous TiO_2. From

this point forward, we separate our deposition studies by substrate temperature to optimize these two varieties of TiO_2.

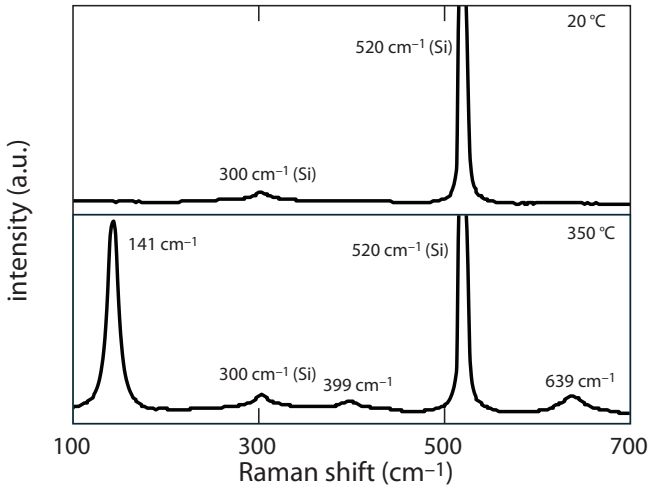

Figure 4.3: Raman spectroscopy of TiO_2 thin films deposited at two substrate temperatures. The film deposited at ambient temperature (top) displays only peaks attributed to the silicon substrate. The film deposited at 300 °C (bottom) shows peaks associated with the anatase crystalline phase of TiO_2.

4.2.2 Optimizing amorphous TiO_2 films

We optimized our amorphous TiO_2 films by controlling the oxygen flow rate, then study its effects on refractive index, deposition rate, and optical propagation losses. Our deposition parameters are summarized in Table 4.2. Figure 4.4 (left) shows the refractive index versus O_2 flow rate and Figure 4.4 (right) shows the deposition rate versus O_2 flow rate. We observed wave guiding (for $\lambda = 826$ nm) only in the film deposited with an O_2 flow rate of 10 % (notated with filled circles).

We see three interesting features in this data. First, we observe that an increased O_2 flow rate greatly reduced the deposition rate. Second, the refractive index is very

Table 4.2: Deposition parameters for amorphous TiO_2 oxygen flow-rate optimization.

temperature (°C)	power (W)	DC bias (V)	pressure (mTorr)	O_2 flow (% of total)	time (min)
20	200	power dependent	2	2 –20	90

similar for all films with O_2 flow rates from 5–20%. Lastly, only film deposited at a 10% O_2 flow rate exhibited guiding. The film deposited at an O_2 flow rate of 20% was 40-nm thick and was therefore too thin to support a guided mode due to the asymmetrical waveguide formed by the silica-TiO_2-air stack. A longer deposition at this flow rate may also produce high-quality TiO_2 films, however the deposition rate is very slow, making proper optimization a time-consuming and costly process. The 10% O_2 process is also very consistent, for example, over 20 separate depositions using this process, the average index around 826 nm was 2.356±.024. Although further optimization may be possible, our results using a 10% O_2 flow rate are sufficient for many of the first devices in TiO_2.

The films deposited with a 10% O_2 flow rate have a high refractive index and exhibit low loss. The index typically varies between 2.29–2.40 between 632 –1550 nm. The Sellmeier equation for this amorphous TiO_2 recipe is:

$$n^2(\lambda) = 1 + \frac{3.3977\lambda^2}{\lambda^2 - 0.045576} + \frac{0.76661\lambda^2}{\lambda^2 - 0.062507}, \tag{4.2}$$

where λ is the wavelength in µm. This film has relatively strong material dispersion of −2300 ps/nm/km around 800 nm. The dispersion reduces to −260 ps/nm/km around 1550 nm, which is lower than silicon around 1550 nm (−900 ps/nm/km).

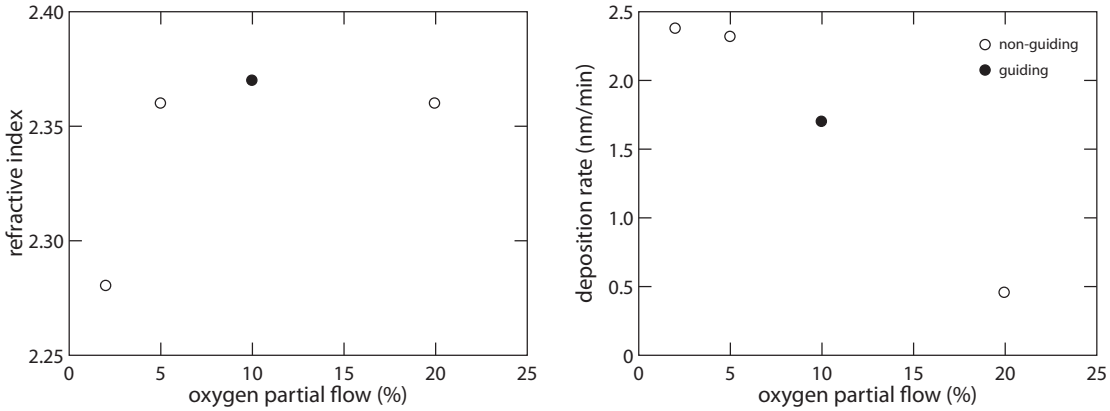

Figure 4.4: Refractive index (left) and deposition rate (right) versus O_2 flow rate for TiO_2 films deposited at 20 °C. Filled circles indicate that guiding was observed using a wavelength of 826 nm.

We show the wavelength-dependent losses of a 250-nm thick film in Figure 4.5. Shorter wavelengths have higher losses that decrease and reach a constant value of 0.4 dB/cm from 1310–1550 nm. The sharp increase in losses at short wavelengths is consistent with theoretical models that consider surface scattering alone [98].

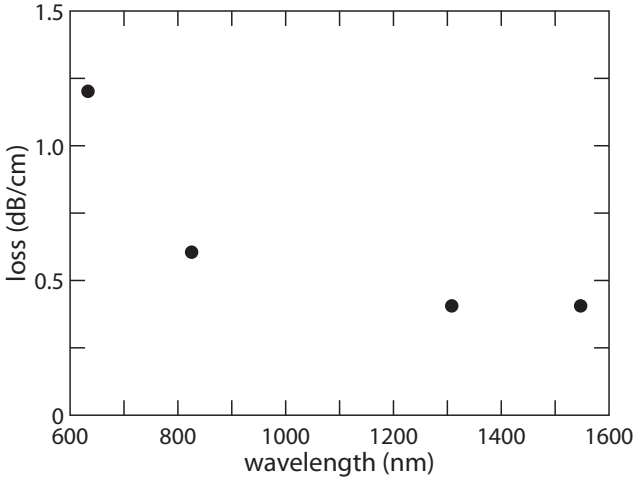

Figure 4.5: Wavelength dependent planar waveguiding losses in a 250-nm thick amorphous TiO_2 film.

4.2.3 Optimizing anatase TiO_2 films

We performed a series of depositions to optimize the O_2 flow rate using temperatures greater than 200 °C with parameters presented in Table 4.3. We show the index and deposition rate as a function of O_2 flow rate in Figure 4.6 (left and right, respectively).

Table 4.3: Deposition parameters for amorphous TiO_2 oxygen flow-rate optimization.

temperature (°C)	power (W)	DC bias (V)	pressure (mTorr)	O_2 flow (% of total)	time (hours)
200–350	130–200	power dependent	2	10–33	1.5–36

There is considerable variability in the quality of the deposited films. Aside from one film, only films deposited with O_2 flow rates of 33% guided around 826 nm. Of the three guiding films with an O_2 flow rate of 33%, the 77-nm thick film displayed losses of 4.5 dB/cm, meanwhile 100-nm and 250-nm thick films had losses of 15 and 20 dB/cm, respectively.

We were unable to extend the low loss achieved in the thinnest film to thicker films. Therefore, the low losses in the 77-nm thick film are likely due to weak confinement, allowing the wave to travel predominantly in the low-loss SiO_2 undercladding. Additionally, we observe an increased loss of 21 dB/cm for oxygen flow rates of 27% (100-nm thick).

Although additional optimization may be possible, we have focused predominantly on an O_2 flow rate of 33%. We note that the deposition rate of anatase is highly dependent on the O_2 flow rate. Unfortunately, a flow rate of 33% results in exceptionally long deposition times (for example, the 250-nm film was deposited for

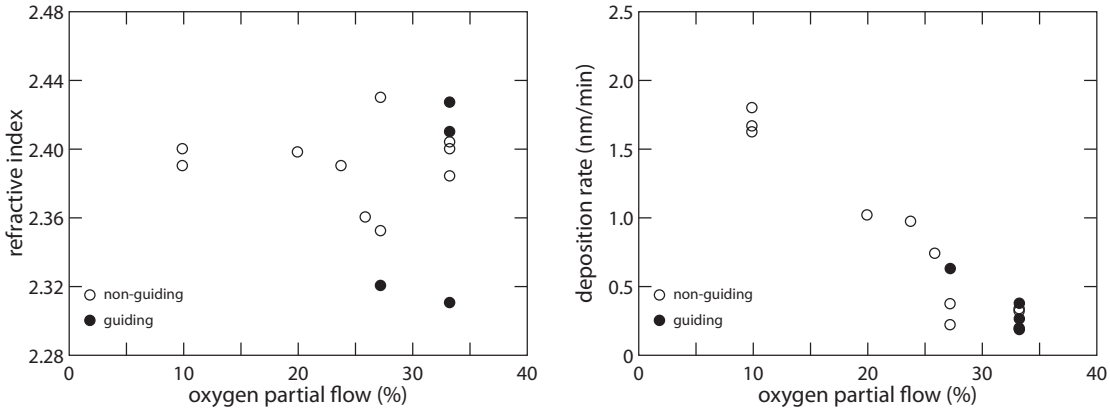

Figure 4.6: Refractive index (left) and deposition rate (right) versus O_2 flow rate for TiO_2 films deposited at 350 °C (films deposited at 10% O_2 flow rate had a substrate temperature between 200–300 °C). Filled circles indicate that guiding was observed with using a wavelength of 826 nm.

over 23 hours). The narrow window and slow deposition rates dramatically affect our ability to conduct a proper study.

Anatase films deposited with a substrate temperature of 350 °C and an oxygen flow rate of 33% exhibit higher indices of refraction than our amorphous films. The index of refraction ranges from 2.41–2.52 between 632 –1550 nm. The Sellmeier equation for a typical film is given here:

$$n^2(\lambda) = 1 + \frac{3.3973\lambda^2}{\lambda^2 - 0.0392} + \frac{1.3204\lambda^2}{\lambda^2 - 0.062776}. \tag{4.3}$$

Although the index is higher in anatase than amorphous TiO_2, the group velocity dispersion is experimentally identical in both films. The higher index in anatase enables slightly stronger dispersion engineering for integrated nonlinear optical devices.

We present the wavelength dependent losses for a 250-nm thick anatase film in Figure 4.7. We notice that the losses are very high for visible wavelengths and drastically decrease to 4.2 dB/cm around 1550 nm. Although these longer wavelengths

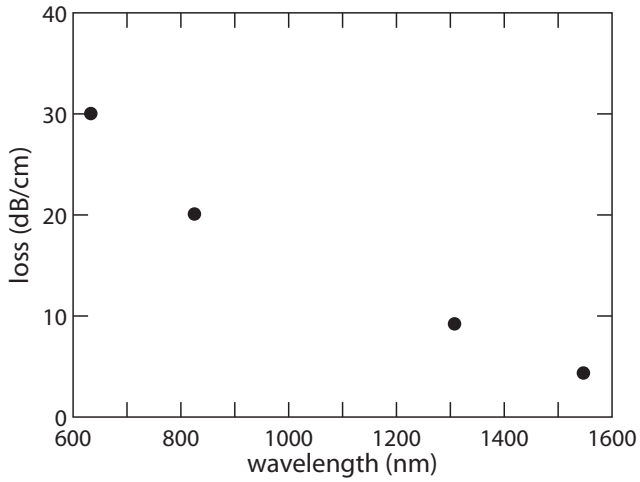

Figure 4.7: Wavelength dependent planar waveguiding losses in a 250-nm thick anatase TiO_2 film.

have increasingly lower losses, they do not appear to reach a constant value as we observed in the amorphous film. The dominant loss mechanism may be due to the poly-crystallinity of our films, which is apparent in Figure 5.2b and after channel waveguide etching in Figure 5.3b. From this trend, we expect significantly improved performance for mid-infrared wavelengths.

4.3 Conclusion

We have deposited two varieties of TiO_2 planar waveguides with typical propagation losses at 826 nm of 0.6 dB/cm (amorphous thin films) and 20 dB/cm (anatase thin films). The losses are as low as 0.4 and 4.2 dB/cm around 1550 nm (amorphous and anatase, respectively). The low losses and high refractive index confirm that these TiO_2 films are useful for integrated nanophotonic devices. Although the anatase phase

is slightly higher in index, the losses in our amorphous TiO_2 films are significantly lower. Based on these results, amorphous TiO_2 appears to have a distinct advantage for linear optical applications.

Chapter 5

Linear optical properties of integrated TiO_2 waveguides and devices

In this chapter, we present two papers that explore the linear optical properties of integrated TiO_2 waveguides and devices. The first paper presents additional details on representative amorphous and polycrystalline-anatase TiO_2 not included in Chapter 4, then develops linear waveguides, bends, and directional couplers. The second paper presents integrated optical resonators for visible wavelengths. These linear devices serve as the basis for more complex linear and nonlinear devices.

5.1 Linear waveguides

The following paper appears in *Optics Express* **20**, 23821-23831, 2012.

Submicrometer-wide amorphous and polycrystalline anatase TiO_2 waveguides for microphotonic devices

J. D. B. Bradley, C. C. Evans, J. T. Choy, O. Reshef, P. B. Deotare,

F. Parsy, K. C. Phillips, M. Lončar, and E. Mazur

School of Engineering and Applied Sciences, Harvard University,

9 Oxford Street, Cambridge, Massachusetts 02138, USA

Abstract: We demonstrate amorphous and polycrystalline anatase TiO_2 thin films and submicrometer-wide waveguides with promising optical properties for microphotonic devices. We deposit both amorphous and polycrystalline anatase TiO_2 using reactive sputtering and define waveguides using electron-beam lithography and reactive ion etching. For the amorphous TiO_2, we obtain propagation losses of 0.12 ± 0.02 dB/mm at 633 nm and 0.04 ± 0.01 dB/mm at 1550 nm in thin films and 2.6 ± 0.5 dB/mm at 633 nm and 0.4 ± 0.2 dB/mm at 1550 nm in waveguides. Using single-mode amorphous TiO_2 waveguides, we characterize microphotonic features including microbends and optical couplers. We show transmission of 780-nm light through microbends having radii down to 2 µm and variable signal splitting in microphotonic couplers with coupling lengths of 10 µm.

5.1.1 Introduction

The development of nanoscale optical waveguides with low losses has led to miniature, efficient photonic devices for applications in the fields of communications, computing, metrology, and sensing [101–108]. Nanoscale waveguides strongly confine light by

utilizing high-refractive-index-contrast materials, resulting in high optical intensities for efficient nonlinear light-matter interactions [109–111], small bending radii, and microscale device footprints [112, 113]. Furthermore, controlling nanoscale features enables one to engineer critical waveguide properties, such as the number of supported modes, the strength of signal coupling between adjacent waveguides, effective nonlinearity, and waveguide dispersion [43, 114].

Standard nanoscale waveguide materials, such as silica and silicon, have limitations despite their low cost and compatibility with current photonic and electronic platforms. Fiber-based silica nanowires have limited scalability due to labor-intensive assembly [112]. Meanwhile silicon, a scalable material with mature fabrication processes, offers transparency only at wavelengths above 1.1 µm. Limited transparency inhibits its use in emerging applications such as quantum photonics, where promising single-photon sources emit at visible wavelengths [115]. Silicon also exhibits strong two-photon absorption at telecommunications wavelengths, which leads to free-carrier absorption and prohibits many nonlinear devices [7, 92, 111]. Therefore, we require complimentary nanoscale waveguide materials to meet the demands of future visible and near infrared linear and nonlinear microphotonic systems.

Recently titanium dioxide (TiO_2) has attracted attention as a prospective photonic material [116–122]. Amorphous and polycrystalline TiO_2 thin films can be deposited at low temperatures (< 650 K) using conventional, scalable methods [97], allowing for straightforward integration with other on-chip devices [123]. TiO_2 has a high refractive index ($n \approx 2.4$), which allows for high-refractive-index-contrast waveguides and strong light confinement. Due to its large bandgap ($E_g = 3.1$ eV), TiO_2 is

transparent over a broad wavelength range that includes the visible and near-infrared. In addition, TiO_2 is a promising nonlinear photonic material, having a high nonlinearity ($\geq$ 25 times higher than silica) [11, 44, 53] and low two-photon absorption for wavelengths above 800 nm [11]. This combination of properties puts TiO_2 into a similar class as silicon nitride; however, TiO_2 exhibits both a higher linear refractive index (2.4 for TiO_2 versus 2.0 for silicon nitride at 800 nm) and nonlinear refractive index (9×10^{-19} m^2/W for bulk rutile TiO_2 versus 2.4×10^{-19} m^2/W for silicon nitride) [44, 124].

Amorphous TiO_2 waveguides on oxidized silicon [119,121] and waveguides formed in single-crystal rutile [120, 122] have been demonstrated. The reported amorphous waveguide structures were limited to large dimensions ($>$ 1 µm) [119] or only investigated for visible-wavelength operation [121]. For practical on-chip devices, such waveguides must have submicrometer dimensions to support single-mode operation. Small dimensions are also necessary for flexibility in the design of basic features such as waveguide bends and optical couplers on the microscale. In addition, anatase microphotonic waveguides have not been developed, despite having a higher reported nonlinearity [53] and requiring lower fabrication temperatures than crystalline rutile waveguides.

In this paper, we report on TiO_2 strip waveguides with submicrometer dimensions and promising optical properties for on-chip photonic devices. We fabricate both amorphous and polycrystalline anatase TiO_2 thin films and compare their structural and optical properties. We then fabricate strip waveguides and measure their propagation losses at visible and near-infrared wavelengths. Finally, we investigate

Table 5.1: Reactive RF sputtering parameters applied to deposit 0.25-µm-thick amorphous and polycrystalline anatase TiO_2 films.

deposition parameter	amorphous TiO_2	anatase TiO_2
temperature (K)	290	625
pressure (mTorr)	2	2
Ar flow (sccm)	40	40
O_2 flow (sccm)	4.4	20
RF power (W)	158	200
time (min.)	300	1390

microphotonic features to assess the prospective application of TiO_2 waveguides in photonic devices.

5.1.2 TiO_2 thin films

Thin-film deposition

We deposit TiO_2 thin films on oxidized silicon substrates (3-µm-thick SiO_2) using reactive radio frequency (RF) magnetron sputtering. We prepare 0.25-µm-thick TiO_2 films under the conditions summarized in Table 5.1. Films deposited at a substrate temperature of 290 K and 625 K yield amorphous and anatase TiO_2 thin-films, respectively [97]. We select optimal O_2 flow rates and RF powers to obtain stoichiometric, highly transparent TiO_2 thin films [118].

Thin-film characterization

We determine the crystalline structure of the TiO_2 thin films using Raman spectroscopy. To avoid background signal from the silicon substrate, we measure Raman spectra of thin films deposited on glass substrates using identical deposition param-

eters, as shown in Figure 5.1 (we observe similar spectra for the films deposited on oxidized silicon substrates, with additional silicon peaks at 300 and 519 cm^{-1}). For films deposited at 290 K, we observe no Raman peaks (Figure 5.1, left) which indicates that the TiO_2 phase is predominantly amorphous. Meanwhile, films deposited at 625 K display a strong peak at 144 cm^{-1}, and additional peaks at 194, 399, 514 and 639 cm^{-1} (Figure 5.1, right). We do not observe any of the peaks near 447, 612, or 826 cm^{-1} associated with the Raman spectrum of rutile (which also includes a relatively weak peak around 143 cm^{-1}) [125]. The observed Raman peaks closely match those measured at 144, 197, 399, 516, and 639 cm^{-1} in anatase single crystals [99], indicating that the TiO_2 phase is primarily anatase.

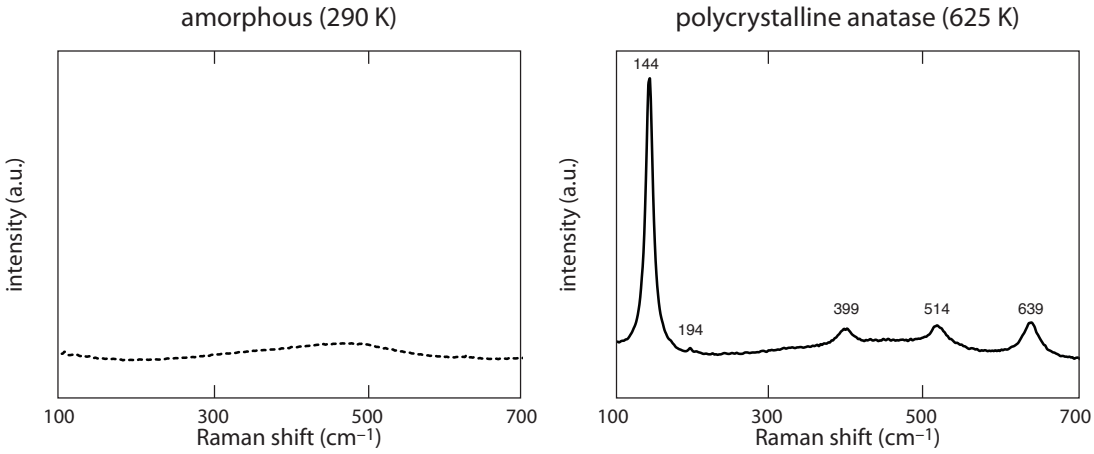

Figure 5.1: Raman spectra of TiO_2 thin-films deposited by reactive RF magnetron sputtering at 290 K (left) and 625 K (right). The film deposited at 290 K has no measurable Raman peaks, indicating an amorphous structure, while the film deposited at 625 K shows peaks at 144, 194, 399, 514, and 639 cm^{-1}, which correspond to the anatase crystalline phase of TiO_2.

In order to compare the surface morphology of the thin films, we use scanning electron microscopy (SEM) and atomic force microscopy (AFM). Scanning electron micrographs of the surface of the films (Figures 5.2a and b) show that the amorphous

structure is granular, while the anatase film consists of densely packed nanocrystals. AFM scanning images, obtained in non-contact alternating current mode with a 9-nm-radius cantilever tip, reveal root mean square (RMS) roughness of 0.4 and 2.7 nm for the amorphous and anatase films, respectively (Figures 5.2c and d).

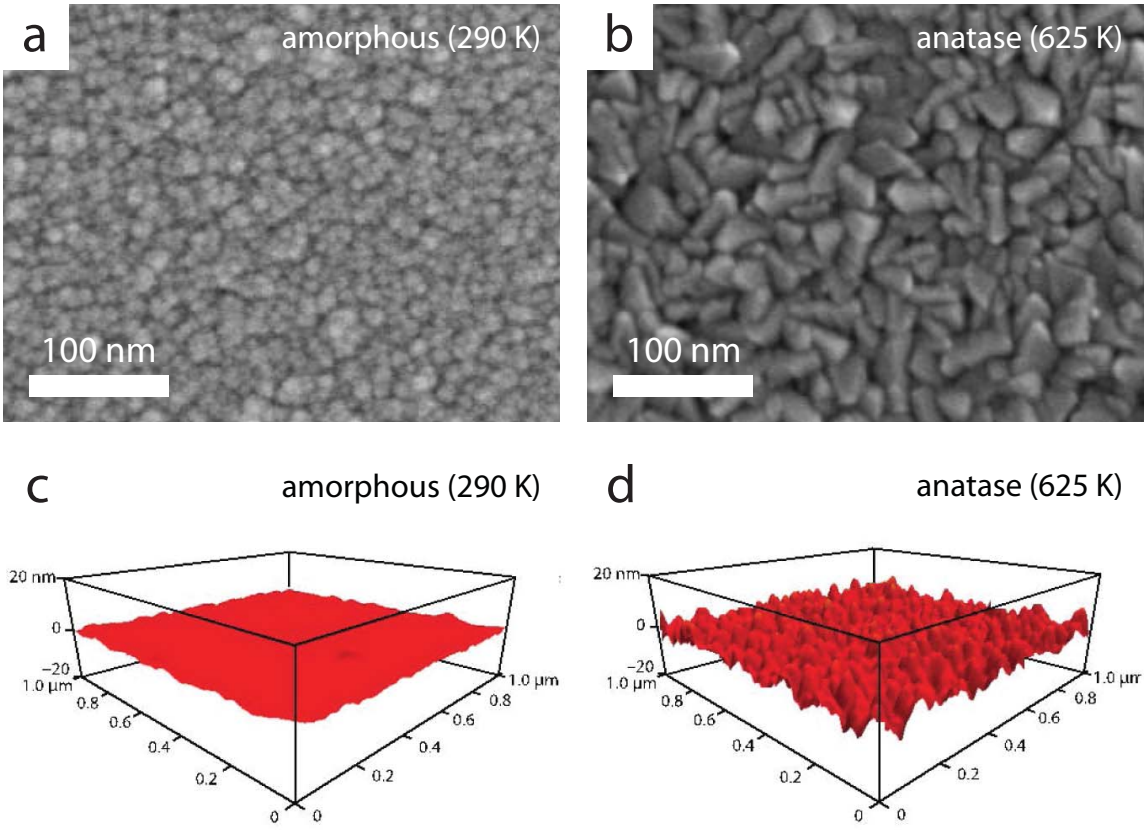

Figure 5.2: Surface morphology of TiO_2 thin films: SEM images of (a) amorphous and (b) polycrystalline anatase thin-film surfaces; and AFM surface scans of (c) amorphous and (d) polycrystalline anatase thin-films showing RMS roughness of 0.4 and 2.7 nm, respectively.

We measure the optical properties of both TiO_2 films in the visible and near-infrared spectrum using a variable angle prism coupling system [98]. Table 5.2 summarizes the refractive indices of the TiO_2 films at 633, 826, 1310 and 1550 nm measured using transverse-electric (TE) polarized light. Both films have refractive indices of

Table 5.2: Refractive indices and propagation losses of TiO_2 thin films. The films are 0.25 µm thick, consisting of amorphous and polycrystalline anatase TiO_2 on oxidized silicon substrates. Both indices and losses are determined by prism coupling using TE-polarization. We estimate an uncertainty of ±0.002 for the refractive index measurements and ±20% for the loss measurements.

	Amorphous TiO_2		Anatase TiO_2	
wavelength (nm)	refractive index	propagation loss (dB/mm)	refractive index	Propagation loss (dB/mm)
633	2.426	0.12	2.486	> 2.0
826	2.372	0.06	2.427	2.0
1310	2.323	0.04	2.375	0.91
1550	2.315	0.04	2.366	0.42

around 2.4 at 826 nm, with the anatase film having a slightly higher refractive index. Measurements using transverse-magnetic (TM) polarized light at 826 nm reveal a slight birefringence for both films, the TM indices being 0.006 and 0.012 higher in the amorphous and anatase films, respectively. Table 5.2 also shows the thin-film propagation losses measured by scanning a fiber along the coupled planar waveguide mode normal to the surface of the film. Using a germanium detector, we collect scattered light versus position and fit the data to an exponential curve. The anatase films exhibit losses ranging from > 2.0 dB/mm at 633 nm (beyond the measurable limit of the prism coupling system) to 0.42 ±0.08 dB/mm at 1550 nm. The amorphous TiO_2 thin-film propagation losses are significantly lower and are less wavelength-dependent, varying from 0.12 ±0.02 dB/mm at 633 nm to 0.04 ±0.01 dB/mm at 1550 nm.

5.1.3 Submicrometer-wide TiO_2 waveguides

Waveguide fabrication

We apply standard top-down fabrication methods to define submicrometer-wide waveguides in our amorphous and anatase TiO_2 thin films. First, we expose the waveguide pattern into a 300-nm-thick positive electron-beam (e-beam) resist layer (ZEP) on top of the TiO_2 film using a 100-keV electron-beam lithography system. The applied e-beam parameters include a 300 × 300 µm write window, a beam current of 100 pA, and a dose of 400 µC/cm^2. After developing the exposed resist, we deposit a 50-nm-thick chromium film by e-beam evaporation and perform metal lift-off to form a metal etch mask. We then transfer the metal pattern into the TiO_2 film using electron cyclotron resonance reactive ion etching. The etch parameters include a CF_4 and H_2 gas mixture in a ratio of 4:1, a microwave power of 300 W, a substrate power of 150 W, and a chamber pressure of 5 mTorr. Using surface profilometry, we find that the etch rates of the amorphous and anatase films are approximately 50 and 60 nm/min, respectively. After etching, we remove the remaining metal mask using Cr-etchant, and apply a 1.6-µm-thick fluoropolymer top-cladding layer ($n = 1.39$). Finally, we cleave the chips to prepare waveguide end-facets.

Figures 5.3a and 5.3b show scanning electron micrographs of the resulting amorphous and anatase TiO_2 waveguides (without top-cladding), respectively. Both types of waveguides have relatively smooth, uniform sidewalls with slopes of approximately 75°. The cross-section of the anatase TiO_2 waveguide facet reveals the TiO_2 core to consist of close-packed vertical nanocrystalline columns (Figure 5.3b).

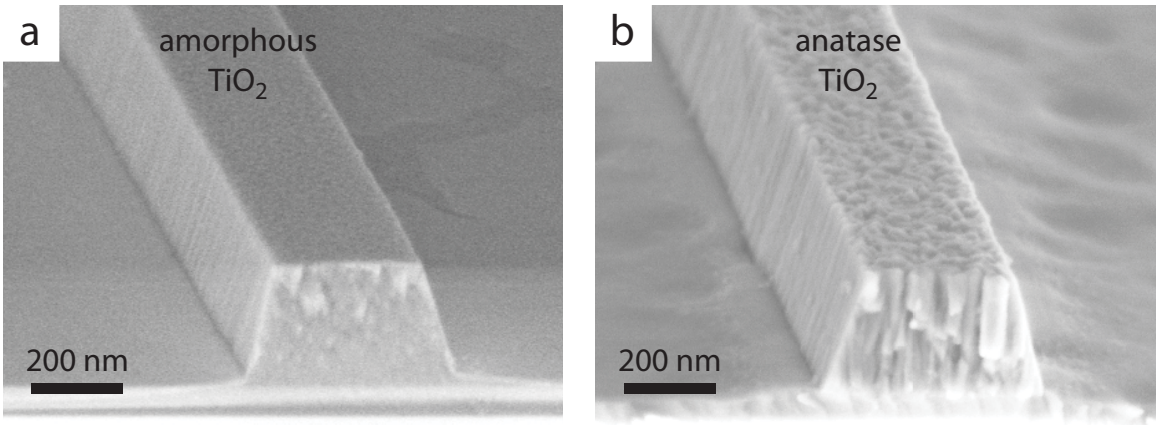

Figure 5.3: SEM images of 0.3-µm-wide (a) amorphous and (b) polycrystalline anatase TiO_2 waveguides fabricated on oxidized silicon wafers using e-beam lithography and reactive ion etching.

Waveguide characterization

We investigate light transmission in 5-mm-long S-shaped waveguides with widths of 0.2, 0.3, 0.4, and 0.5 µm. The selected waveguide dimensions support guided modes in the wavelength range 633–1550 nm. We chose a minimum bend radius of 60 µm to avoid significant bend-induced losses. Using a commercial finite-difference eigenmode solver, we determine that all waveguides are multimode at 633 nm, single-mode at 780 nm for widths of ≤ 0.3 µm (amorphous) and 0.2 µm (anatase), and single-mode at 1550 nm for widths of ≥ 0.4 µm. Widths below 0.4 µm do not support a guided mode at 1550 nm.

We measure the optical propagation losses of the TiO_2 strip waveguides at 633, 780 and 1550 nm using the top-view camera method [126]. Light from a 633-nm HeNe, 780-nm diode, or a 1550-nm diode laser source is aligned and focused onto the input facets of the waveguides using an objective lens (633 and 780 nm) or lensed fiber (1550 nm) mounted on a piezoelectric-motor-controlled XYZ stage. We adjust

the polarization of the incident light using a half-wave plate and a polarizer prior to the objective lens (633 and 780 nm) and a paddle-based polarization controller before the lensed fiber (1550 nm). We capture images using microscope-mounted CMOS (633 and 780 nm) and InGaAs (1550 nm) cameras and determine the transmission through the TiO_2 waveguides by analyzing the relative intensity of scattered light along the waveguides in the resulting images.

In Figure 5.4 we show representative top-view camera images of visible and infrared light propagation in our amorphous (Figures 5.4a, c and e) and polycrystalline anatase (Figures 5.4b, d and f) waveguides. The propagation loss data corresponding to the representative images is shown in Figures 5.5a and b. Table 5.3 summarizes the propagation-loss data measured for different waveguide widths. The amorphous losses are considerably lower than the anatase losses at 633 and 780 nm. The uncertainty in the fit for the InGaAs camera measurements is rather high ($\pm$50%) due to the large relative background intensities in the images. Therefore, we measure similar losses at 1550 nm in both types of TiO_2 waveguide within the experimental uncertainty.

5.1.4 TiO_2 microphotonic features

Design and fabrication of microphotonic features

As a proof of principle, we investigate microphotonic features at 780 nm, near TiO_2's half-bandgap and where nonlinear optical devices are feasible in bulk rutile TiO_2 [11]. We base our devices on a 0.3-µm-wide amorphous TiO_2 waveguide, which supports a single, well-confined TE-mode and has lower losses than similar anatase waveguides around 800 nm. To investigate waveguide bending losses, we fabricate waveguides

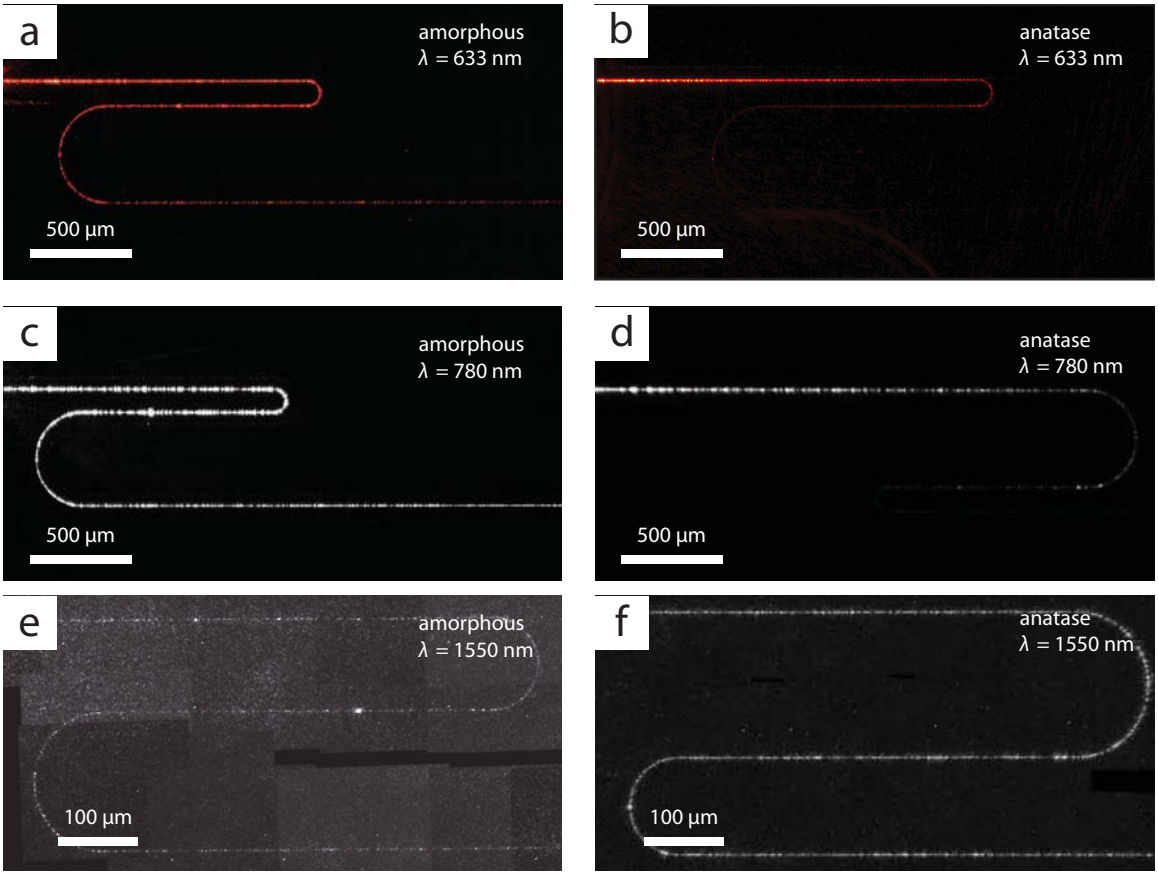

Figure 5.4: Top-view CMOS (633 nm and 780 nm) and InGaAs (1550 nm) camera images showing light propagation at different wavelengths λ in amorphous and polycrystalline anatase TiO_2 waveguides. The waveguides are 0.2-µm wide (a–d) and 0.5-µm wide (e and f).

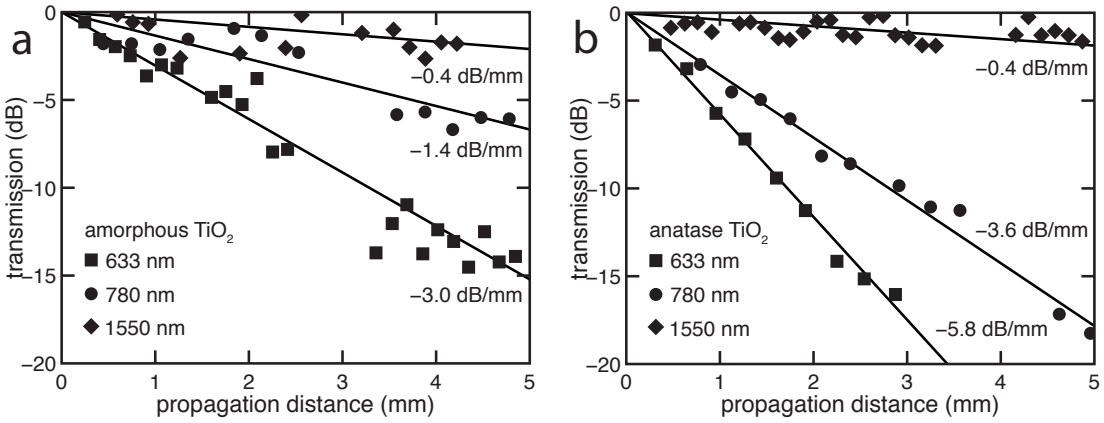

Figure 5.5: Propagation losses of (a) amorphous and (b) polycrystalline anatase TiO_2 strip waveguides measured using the top-view camera method. The input light is TE-polarized and the waveguide widths are 0.2 µm (633 and 780 nm) and 0.5 µm (1550 nm).

Table 5.3: Propagation losses in amorphous and anatase TiO_2 waveguides. Measurements are performed using the top-view camera method (TE-polarization). The uncertainty is ±20%, ±20%, and ±50% for the 633-, 780-, and 1550-nm measurements, respectively.

		propagation loss (dB/mm)	
wavelength (nm)	waveguide width (µm)	amorphous TiO_2	anatase TiO_2
633	0.2	3.0	5.8
	0.3	2.9	4.8
	0.4	2.6	6.1
	0.5	3.2	4.8
780	0.2	1.4	3.5
	0.3	2.2	3.5
	0.4	1.4	3.1
	0.5	0.9	3.8
1550	0.4	0.5	0.3
	0.5	0.4	0.4

with multiple bends having radii of 1–20 µm. In addition, we fabricate optical couplers consisting of two waveguides with adiabatic sine-bends into and out of a parallel coupling region. The spacing of the coupling region is 0.2 µm and its length, L, varies from 0 to 4 µm. We measure the transmission characteristics of the bends and optical couplers using the top-view camera method.

Micro-bends

Figure 5.6 summarizes the measurements and characterization of the TiO_2 microbends. Figure 5.6a shows the simulated electric field profile of the fundamental 780-nm TE mode confined by the amorphous-TiO_2 waveguide. In Figure 5.6b, we display a top-view SEM image of a representative TiO_2 waveguide with micro-bends having radii r of 5 µm prior to cladding layer deposition. In Figure 5.6c, we show camera images of light transmission through cladded micro-bend features with $r = 20$ µm (top), 10 µm (middle) and 5 µm (bottom). Figure 5.6d displays the measured transmission for varying r. The plot shows a minimal change in transmission as r is decreased to a value of 3 µm. At $r = 2$ µm we observe a change in transmission of -9 dB that corresponds to an added loss of < 1 dB/90° bend. For $r = 1$ µm, the transmission is below the measurable limit (-40 dB).

Optical-couplers

Figure 5.7a displays an SEM image of an optical-coupler (prior to cladding deposition) with a parallel interaction length $L = 4$ µm. Figure 5.7b shows optical images of light transmission in couplers with $L = 0$ µm (top), $L = 2$ µm (middle) and $L = 4$ µm (bottom). By measuring the scattered intensity in each output branch of the coupler

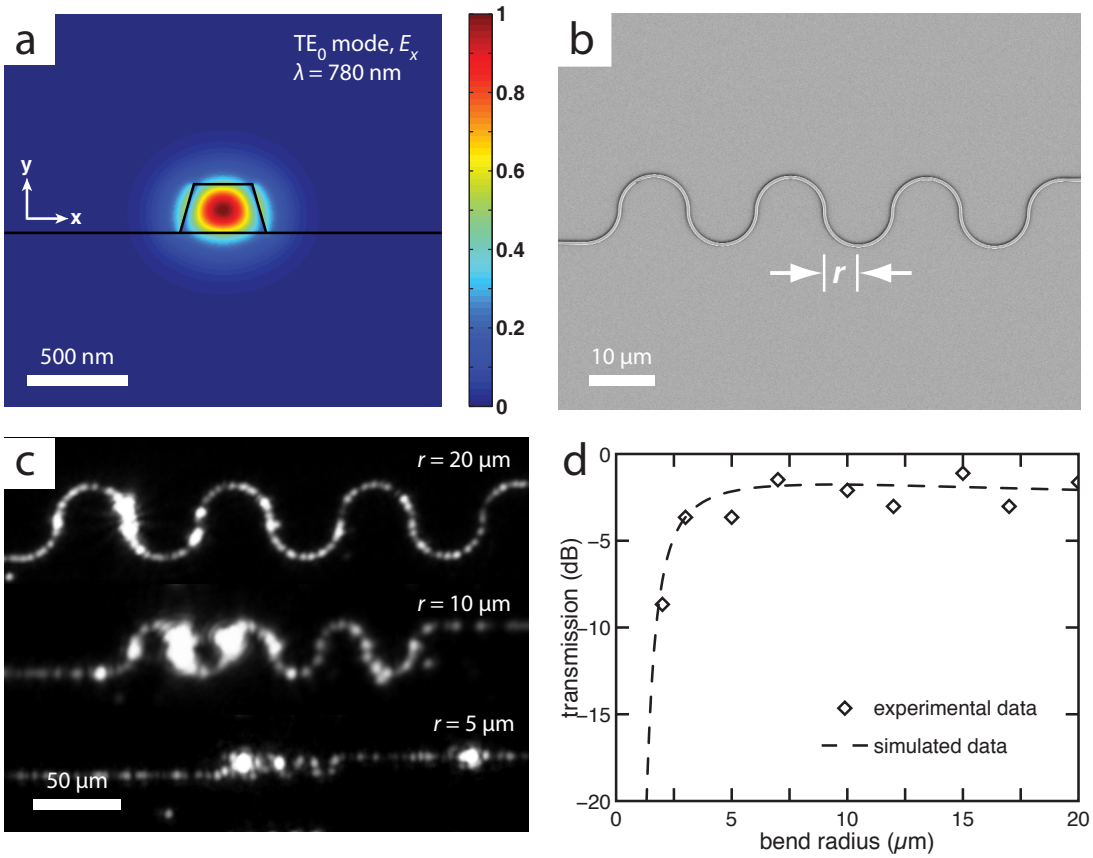

Figure 5.6: Calculated TE-like field profile of the fundamental 780-nm mode in a straight 0.25 µm × 0.3 µm amorphous TiO_2 waveguide; (b) SEM top-view image of a bend-transmission test-feature consisting of a 0.25 µm × 0.3 µm amorphous TiO_2 waveguide with fourteen consecutive 90° bends with a radius r of 5 µm; (c) CMOS camera images showing light transmission through test features with $r = 20$ µm (top), $r = 10$ µm (middle), and $r = 5$ µm (bottom); (d) measured and simulated transmission for varying bend radii.

(I_{upper} and I_{lower}) we determine splitting ratios $I_{upper}/(I_{upper} + I_{lower})$ of 0.3, 0.6, and 0.9, respectively.

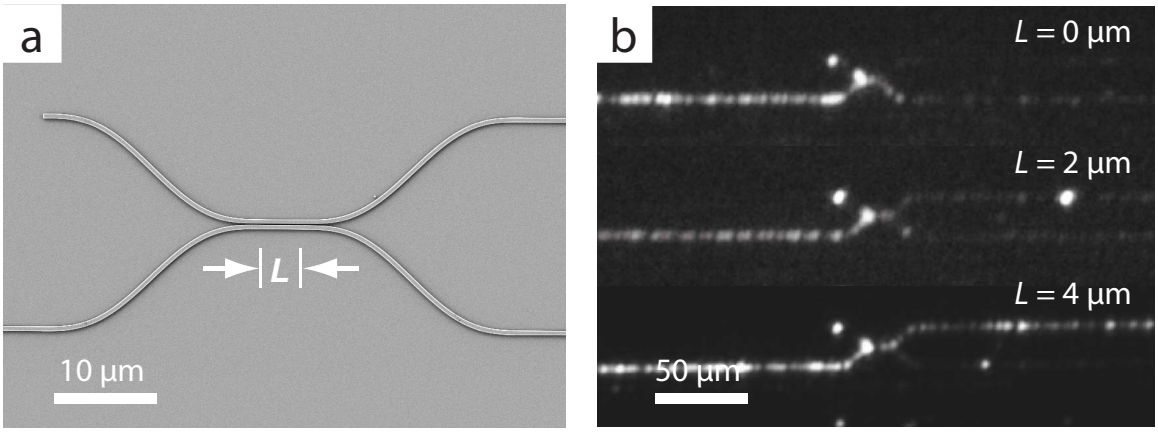

Figure 5.7: TiO_2 microphotonic couplers: (a) SEM image of a TiO_2 optical-coupler with adiabatic input/output transitions and a parallel interaction region with a waveguide spacing of 0.2 µm and length, L, of 4 µm; (b) CMOS images showing splitting ratios (light transferred to the upper waveguide divided by the total transmitted intensity) of 0.3 (top), 0.6 (middle), and 0.9 (bottom) for $L = 0$, 2 and 4 µm, respectively (780-nm light, TE polarization).

5.1.5 Discussion

We show that by adjusting substrate temperature, oxygen flow rate and RF sputtering power, we can deposit waveguide-quality amorphous and polycrystalline-anatase TiO_2 thin films. At visible and near-infrared wavelengths, our amorphous TiO_2 thin films exhibit significantly lower propagation losses. The difference in propagation loss is most evident in the visible. In the 0.25-µm-thick films prepared for this study, we observe a pronounced visible streak of light across tens of mm in the amorphous film, but observe no measureable 633-nm-light propagation in the polycrystalline film. We partially attribute the difference in loss to the larger surface roughness in the anatase thin film. Despite having higher thin-film losses, the anatase phase

of TiO_2 offers potential advantages for microphotonic devices in terms of greater thermal stability [127], higher refractive index, and higher nonlinearity [53]. Reduced nanocrystal size and smoother surfaces may lead to lower losses in the polycrystalline films.

We also demonstrate a suitable method for fabricating submicrometer-wide strip waveguides using both types of TiO_2 thin film. The amorphous TiO_2 strip waveguides have lower propagation losses at 633 and 780 nm than the anatase waveguides. As with the thin films, the difference is most significant at 633 nm, where we have recently demonstrated amorphous TiO_2 microring resonators for visible-light systems [121]. In both amorphous and polycrystalline waveguides, we measure losses on the order of 0.3–.5 dB/mm at 1550 nm, which are comparable to those initially reported in other high-refractive-index-contrast photonic waveguides [94, 102, 128]. The comparable losses at 1550 nm can be explained by the reduced influence of surface and edge roughness, and the low optical confinement within the TiO_2 core ($< 40\%$) whereby the majority of light propagates in the low-loss cladding layers.

The measured strip-waveguide propagation losses are sufficiently low for microphotonic devices requiring µm and mm waveguide lengths. However, we observe significantly higher propagation losses in our TiO_2 strip waveguides compared to the unstructured planar films, as is typical in high-refractive-index-contrast waveguides [129]. Moreover, the waveguide losses exhibit greater wavelength dependence than the thin film losses based on the relative values measured at 633 and 1550 nm. Several mechanisms may introduce additional losses in our strip waveguides, including radiation of higher-order modes, scattering due to core-cladding interfacial

roughness, and e-beam write-field stitching errors [129, 130]. Each loss mechanism theoretically scales inversely with wavelength, consistent with observation. We may reduce waveguide losses towards the thin-film values using alternative waveguide geometries [131], complimentary fabrication methods [132], or specialized e-beam writing strategies [133].

By investigating amorphous TiO_2 microphotonic features, we show that light is transmitted through waveguide bends with radii down to 2 µm and demonstrate TiO_2 optical couplers. To gain insight into the loss mechanisms of the investigated bend structures, we compare the simulated transmission properties of TiO_2 microphotonic bends with our experimental results. In Figure 5.6d we show the calculated transmission through micro-bends as a function of bend radius. The total calculated loss includes the losses due to modal overlap mismatch at the interface between straight and bent waveguides and between 90°-bends of opposite direction, radiation losses from the 90°-bends, and the experimental propagation loss of 2 ± 0.4 dB/mm measured in 300-nm-wide amorphous TiO_2 waveguides. We observe a good agreement between the calculated and experimental data. In the calculated data, the primary contribution to the total loss is the modal overlap mismatch at the interfaces, and not radiative loss due to the bend itself. For example, we calculate a bend-bend transition loss of 0.75 dB compared with a radiation loss of 0.01 dB for a 90° bend with $r = 2$ µm. For micro-bends with $r \leq 2$ µm, the transmission can be improved by incorporating adiabatic transitions. We also expect that comparably small bend radii are feasible in anatase waveguides due to their similar dimensions and refractive indices. These results, combined with the high optical confinement in TiO_2 waveguides,

demonstrate that TiO_2 devices can be densely integrated on photonic chips.

To compare our optical-coupler measurements to the theoretical splitting ratios, we calculate the coupling distance by solving for the even and odd TE-polarized modes in the investigated structures. We calculate effective indices of 1.919 and 1.885, respectively, for which coupled-mode theory predicts a 100% coupling length of 12 µm. This value is consistent with the experimentally observed coupling ratios and lengths when we account for the additional effective coupling length introduced by the adiabatic input and output regions (6 µm). We measure a splitting-ratio of approximately 90% for an effective length of 10 µm. Our data shows that we can achieve strong coupling over short lengths, allowing for small footprints for devices such as ring resonators.

5.1.6 Conclusion

In conclusion, we have fabricated amorphous and polycrystalline anatase TiO_2 thin films and strip waveguides with submicrometer widths. We observe light propagation over mm-length scales at 633 and 780 nm, and measure losses of 0.4 ± 0.2 dB/mm in amorphous and anatase strip-waveguides at 1550 nm. The consistency between simulated and experimental micro-bend and optical-coupler results suggest that realizing complex micro-scale TiO_2 photonic devices can be achieved using the techniques reported here. These results demonstrate TiO_2 to be a novel and promising platform for visible to infrared microphotonic devices.

Acknowledgements

Several people contributed to the work described in this paper. All authors provided contributions to the basic ideas described in this work. JDBB, CCE., JTC, OR, PBD, FP, and KCP designed and carried out the experiments, and analyzed the results. ML and EM supervised the research and the development of the manuscript. JDBB. wrote the first draft of the manuscript; all authors subsequently took part in the revision process and approved the final copy of the manuscript. Rafael Gattass and Ruwan Senaratne contributed to the preliminary research and Laura Tucker and Phillip Munoz provided feedback on the manuscript throughout its development. The devices were fabricated at the Center for Nanoscale Systems at Harvard University. The research described in this paper was supported by the National Science Foundation under contract ECCS-0901469, the Harvard Quantum Optics Center, and the Fonds de recherche du Québec - Nature et technologies. JTC and PBD were partially supported by the Center for Excitonics, an Energy Frontier Research Center funded by the U.S. Department of Energy, Office of Science, Office of Basic Energy Sciences under Award Number DE-SC0001088.

5.2 Racetrack resonators for visible photonics

The following paper appears in *Optics Letters* **37** (4), 539-541, 2012.

Integrated TiO_2 resonators for visible photonics

J. T. Choy, J. D. B. Bradley, P. B. Deotare, I. B. Burgess, C. C. Evans, E. Mazur, and M. Lončar

School of Engineering and Applied Sciences, Harvard University,

9 Oxford Street, Cambridge, Massachusetts 02138, USA

Abstract: We demonstrate waveguide-coupled titanium dioxide (TiO_2) racetrack resonators with loaded quality factors of 2.2×10^4 for the visible wavelengths. The structures were fabricated in sputtered TiO_2 thin films on oxidized silicon substrates using standard top-down nanofabrication techniques, and passively probed in transmission measurements using a tunable red laser.

Optical microresonators are ubiquitous components in optical telecommunication systems and provide a compact means for studying cavity quantum electrodynamics [134]. The integration of microresonators into classical and quantum networks relies on materials that support high-quality optical components on a chip-scale [135,136]. In the growing field of quantum photonics, quantum emitters [137–139] operate primarily in the visible wavelengths. Therefore, the development of a chip-scale platform for the visible is a critical step toward the realization of quantum communication networks, and can be beneficial to classical applications, such as light generation and on-chip sensing. While gallium phosphide [140], silicon nitride [136, 141, 142], silicon dioxide [143], and diamond [144] are all promising materials, certain challenges remain, including intrinsic luminescence [141], difficulty of generating thin membranes with low optical loss [145], poor refractive index contrast with the sur-

rounding medium [143], and low tolerance for fabrication imperfections due to inherently small characteristic lengths.

Titanium dioxide (TiO_2) can be added to the family of viable integrated visible photonics platforms. It is a widebandgap semiconductor (with a bandgap energy between 3 –3.5 eV, depending on the crystalline phase [146]) with a moderately high index for the visible wavelengths ($n \approx 2.4$) and a wide transparency window from the near UV to the IR. It is also naturally abundant and is compatible with a host of conventional growth techniques. While the optical properties of TiO_2 have been exploited in three-dimensional photonic crystals [147], gratings [117], and waveguides [119, 148], planar resonator structures in this material had yet to be demonstrated. Here we show scalable and integrable TiO_2 racetrack resonators, having loaded quality factors (Q) of the order of 10^4 with efficient coupling to a feeding waveguide.

Amorphous TiO_2 thin films of thickness 170 nm have been deposited on oxidized silicon substrates using RF sputtering of a Ti target in an O_2/Ar environment [148]. Prism coupling experiments [148] indicated that the deposited films have propagation losses as low as 2 dB/cm. These losses suggest that the material-limited Q for optical cavities is around 5×10^5. We used racetrack resonators since they allow for controllable coupling to a waveguide via the coupling length. The fabricated parameters were designed to minimize bending losses (by making bending radii $R = 30$ µm). Additionally, the waveguide-resonator separation g and coupling length L were chosen to ensure efficient transfer of light signal between the cavity and waveguide. To optimize the coupling, we set $g = 130$ nm and waveguide width $w = 250$ nm, and calculated the coupling efficiency as a function of L, using the difference between the effective

indices of the even (n_e) and odd (n_o) eigenmodes of the coupled structure [149]. For the range of wavelengths between 630 and 640 nm, $L = 15$ µm provides near critical coupling for transverse electric (TE) polarized light.

We realized the designed structures using conventional top-down fabrication techniques, which include electron beam lithography on a positive electron beam resist (ZEP 520A), electron beam evaporation and liftoff of a chromium mask layer, and reactive ion etching in a CF_4/H_2 environment. The recipe has an etch rate of approximately 60 nm/min and leads to slightly slanted sidewalls with an angle of 75° [148]. The mask was subsequently removed by an etchant and polymer pads (SU-8 2002, with cross sections 3 µm × 3 µm) were written using electron beam lithography [150]. These pads overlap with the ends of the TiO_2 waveguides and extend to the edges of the chip (Figure 5.8 a). The edges of the polymer waveguides were then cleaved to facilitate in- and out-coupling of light. The input and output facets are offset from one another to avoid direct scattering of uncoupled light into the collection fiber. The devices have surfaces with a roughness of around 10 nm and gaps of approximately 130 nm in the coupling regions Figure 5.8 b–d).

We simulated the mode profiles of the fabricated devices (insets of Figure 5.8 b) using the finite element method (FEM). From Figure 5.8, the waveguides have an etch depth of 150 nm and a width of 250 nm on their top facets. These dimensions support one fundamental mode in each of the TE and transverse magnetic (TM) polarizations with respective effective indices of 1.80 and 1.61 at a wavelength of 630 nm. The pedestal layer, which resulted from non-uniformity in our etching process, is roughly 20 nm thick and can be beneficial for waveguide-resonator coupling [136].

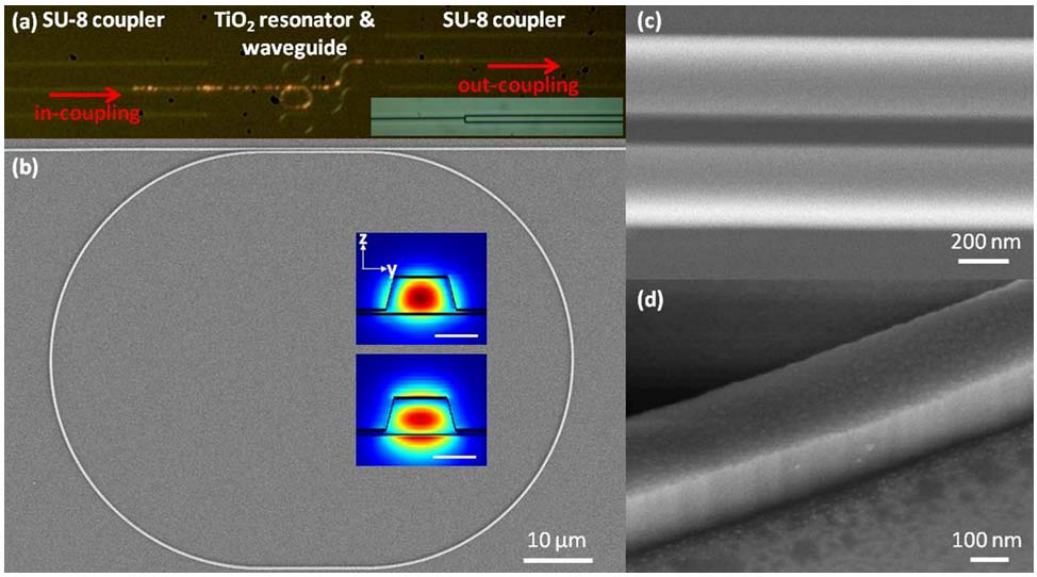

Figure 5.8: (a) Optical image of a set of TiO_2 waveguide-racetrack devices integrated with polymer pads. Inset: overlapping region between the TiO_2 waveguide and polymer pad. SEM images of (b) a TiO_2 waveguide-resonator, (c) its coupling region, and (d) etch profile taken at a 45° tilt. Insets: cross sections of the fabricated waveguide-resonator with simulated electric field profiles of the TE (top) and TM (bottom) modes. Propagation is in the x direction. Scalebar = 200 nm.

In our structure, this layer improves coupling into the TM-polarized modes, so that the simulated coupling efficiencies are around 90% for both TE- and TM-polarized light.

The resonators were characterized by transmission measurements using a tunable red laser with a scanning range of 634.4–639.6 nm. The output of the laser was coupled to a single mode, tapered lens fiber that was rotated such that the input signal into the sample was polarized along either the TE or TM direction. Light with a spot size of 0.8 µm in diameter was focused onto the facet of the polymer pad by the tapered lens fiber and transmitted into the waveguide-resonator device. The output was coupled through a polymer pad on the opposite end of the chip and collected by another tapered lens fiber that was connected to a high-speed silicon detector. For this experiment, the coupling loss from the fiber to the TiO_2 waveguide is roughly 14.5 dB at each end. This loss can be reduced by polishing the facets and optimizing the geometry of the TiO_2 waveguide to reduce light reflections that arise from the refractive index mismatch.

The resonator transmission spectra are shown in Figure 5.9. All spectra shown here have not been normalized. The transmission spectra have periodically spaced dips corresponding to whispering gallery modes with either the TE (Figure 5.9 a) or TM (Figure 5.9 b) polarization. The small dips observed in (Figure 5.9 b) are due to imperfect polarization filtering of TE-polarized signals. The loaded quality factors ($Q_{\text{loaded}} = \lambda/\Delta\lambda$, where λ is the cavity resonance wavelength and $\Delta\lambda$ is the linewidth of the resonance) were extracted by fitting the transmission dips to the Fano model [151]. The model is necessary due to interference between the transmitted sig-

nals and partially reflecting elements in the waveguides, leading to asymmetries in the cavity line shapes [151]. The fits yielded linewidths as narrow as 0.028 nm and 0.11 nm for the TE and TM polarizations (respectively) near $\lambda = 635$ nm, corresponding to respective Q values of 2.2×10^4 and 5.6×10^3. The observed transmission drops are as large as 96%, indicating that the resonators are nearly critically coupled. The

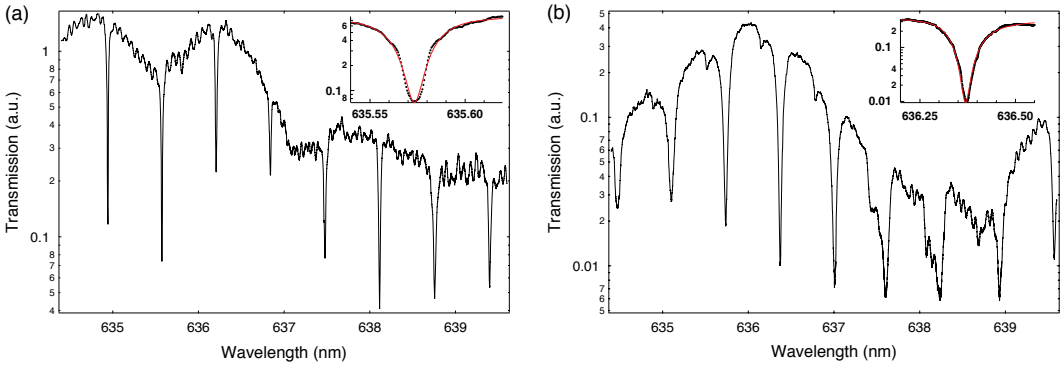

Figure 5.9: (a) TE-polarized transmission as a function of wavelength for a racetrack resonator with $R = 30$ µm and $L = 15$ µm. Inset: cavity mode at 635.57 nm, along with a fit to the Fano model (red). The fitted line-width is 0.028 nm, corresponding to a Q of 22400. (b) TM-polarized transmission as a function of wavelength for the same resonator. Inset: cavity mode at 636.36 nm, with a fitted line-width of 0.11 nm and corresponding Q of 5629.

transmission properties of a waveguide-coupled racetrack resonator have been well-described elsewhere [149, 152]. The free spectral range (FSR) between consecutive modes in the system is described by FSR $\approx \frac{\lambda^2}{2n_g(\pi R+L)}$, where n_g is the group index and takes into account dispersion in the structure. We used the Sellmeier coefficients obtained from spectroscopic ellipsometry measurements on our TiO_2 films to determine the wavelength-dependent index (n_{mat}). The first-order effective index (n_{eff}) and group index (n_g) were then computed [153] and are shown in Figure 5.10. In the visible wavelengths, n_g in TiO_2 waveguides can be significantly larger than n_{eff}

(a difference of approximately 57% for the TE mode and 70% for the TM mode). The greater difference observed in the TM polarization is due to larger waveguide dispersion, which can be estimated by calculation of the group index $n_{g,w}$ of the given waveguide without considering the wavelength-dependence in n_{mat}. The large discrepancy between n_g and n_{eff} can thus be attributed to both waveguide and material dispersion, although the contribution from the latter decreases with increasing wavelengths, as indicated by the diminishing difference between the group index with and without material dispersion (n_g and $n_{g,w}$, respectively). Dispersion must therefore be considered when designing optical components in TiO_2 and can be exploited to generate small FSRs without significantly increasing the device footprint. The calculated n_g values are in good agreement with the experimentally obtained value, in which an FSR of 0.64 nm (Figure 5.9 a) corresponds to a group index of 2.92 in the 635 to 640 nm range in the TE polarization.

Finally, the propagation loss in a critically coupled resonator can be estimated using $\alpha_r = \frac{\pi n_g}{\lambda Q_{\text{loaded}}}$ [154]. Based on a TE-polarized mode with a Q of 22400 and transmission drop of 92% (inset of Figure 5.9 a), the corresponding propagation loss is 28 dB/cm. The deviation from the planar loss value can be attributed to scattering losses from surface roughness introduced by the fabrication process, which might be reduced by using a top-cladding material.

We have demonstrated planar resonators in TiO_2 thin films for visible light operation with efficient coupling to waveguides for delivering light on- and off-chip. The methods and devices shown here could help advance the TiO_2 material platform toward integration with active emitters for novel and integrated classical and non-

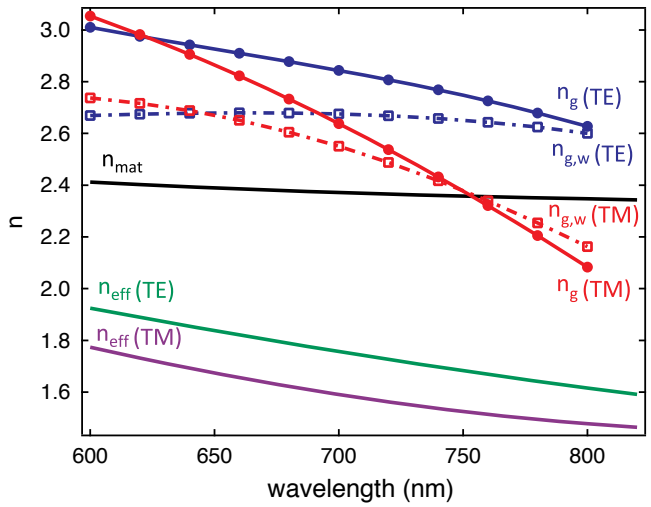

Figure 5.10: Calculated effective (n_{eff}) and group (n_g) indices as a function of wavelength for the TE- and TM-polarized waveguide modes. Contributions to the difference between n_{eff} and n_g include dispersions in the material (n_{mat}) and waveguide, which can be inferred by calculating n_g using a fixed n_{mat} of 2.4 ($n_{g,w}$).

classical light sources and on-chip sensing.

The research described in this paper was supported by the National Science Foundation (NSF) under contract ECCS-0901469 and based upon work supported as part of the Center for Excitonics, an Energy Frontier Research Center funded by the U.S. Department of Energy, Office of Science, Office of Basic Energy Sciences under award DE-SC0001088. The devices were fabricated at CNS at Harvard University. We thank Q. Quan, B. Hausmann, M. McCutcheon, M. Khan, F. Parsy, L. Xie, G. Akselrod, V. Bulovic, M. Pollnau, R. Jensen, L. Marshall, and M. Bawendi for useful discussions and help with the project. J. Choy acknowledges support from NSF GRFP.

Chapter 6

Nonlinear properties of TiO_2 waveguides

In this chapter, we present two studies on the nonlinear optical properties of integrated polycrystalline-anatase TiO_2 waveguides. The first paper describe spectral broadening of femtosecond pulses which allows us to quantify nonlinear refraction, multiphoton absorption, and stimulated Raman scattering. In the following section, we present a preliminary results on third-harmonic generation in similar waveguides. These simple wavelength conversion devices demonstrate TiO_2's potential for more complex integrated nonlinear devices.

6.1 Spectral broadening

The following paper in appears in *Optics Express* **21** (15), 18582-18591, 2013.

Spectral broadening in anatase titanium dioxide waveguides at telecommunication and near-visible wavelengths

C. C. Evans,[1] K. Shtyrkova,[2] J. D. B. Bradley,[1,2] O. Reshef,[1]

E. Ippen,[2] and E. Mazur[1]

[1]*School of Engineering and Applied Sciences, Harvard University,*

9 Oxford Street, Cambridge, Massachusetts 02138, USA

[2]*Department of Electrical Engineering and Computer Science, Massachusetts Institute of Technology, 77 Massachusetts Avenue, Cambridge, Massachusetts 02139, USA*

Abstract: We observe spectral broadening of femtosecond pulses in single-mode anatase-titanium dioxide (TiO_2) waveguides at telecommunication and near-visible wavelengths (1565 and 794 nm). By fitting our data to nonlinear pulse propagation simulations, we quantify nonlinear optical parameters around 1565 nm. Our fitting yields a nonlinear refractive index of 0.16×10^{-18} m^2/W, no two-photon absorption, and stimulated Raman scattering from the 144 cm^{-1} Raman line of anatase with a gain coefficient of 6.6×10^{-12} m/W. Additionally, we report on asymmetric spectral broadening around 794 nm. The wide wavelength applicability and negligible two-photon absorption of TiO_2 make it a promising material for integrated photonics.

6.1.1 Introduction

Integrated nonlinear optical devices have enabled many applications for traditional telecommunication wavelengths (1300–1600 nm), ranging from all-optical switches,

wavelength converters, amplifiers and lasers, to applications in metrology and quantum information [66, 89, 103, 155–161]. However, few materials are optimal for the unique features of the near-visible window (NVIS, 800–1300 nm). Devices with NVIS compatibility could link and process signals between different communications bands throughout the full communications octave (800–1600 nm) and exploit efficient sources for optical interconnects [162, 163]. Additionally, such devices would open up applications in biology (exploiting the low water absorption in the NVIS) [164–167] and integrated quantum optics (utilizing inexpensive, high-performance silicon single-photon detectors) [168]. Despite their promise, nonlinear optical applications for NVIS wavelengths are almost completely unexplored due to insufficient integrated materials.

Material properties dictate the operating wavelength for optimal performance in all-optical devices. An ideal nonlinear optical material will achieve a maximum effective nonlinearity while minimizing two-photon absorption (2PA) and have a high refractive index to enable strong dispersion engineering for all wavelengths of interest. The nonlinear index of refraction (n_2) depends on the bandgap energy (E_g) and scales as E_g^{-4}, strongly favoring narrow-bandgap materials [10,52,169]. This bandgap-dependence explains silicon's high nonlinearity ($E_g = 1.1$ eV, $n_2 = 4\text{–}6 \times 10^{-18}$ m^2/W [170, 171]). However, strong 2PA in silicon at telecommunication wavelengths limits many all-optical devices [27, 92]. Many materials such as chalcogenide glass [108], AlGaAs [172, 173] and GaInP [174] have excellent nonlinear optical properties for the 1300–1600 nm telecommunication band, yet are limited by 2PA in the NVIS window. For maximum performance at a given operating wavelength, the scaling rules suggest

avoiding this limit by selecting a material with bandgap energy of slightly more than twice the single-photon energy. Using these guidelines, we should achieve maximum performance in the NVIS window using a material with a bandgap energy of 3.1 eV.

Titanium dioxide's (TiO_2) unique balance of large optical nonlinearity and wide wavelength compatibility makes it optimal for NVIS operation. TiO_2 exists in several crystalline phases including rutile ($E_g = 3.1$ eV), anatase ($E_g = 3.2$ eV), and brookite ($E_g = 3.1$ eV) making it ideal for wavelengths near 800 nm [47, 48]. The nonlinear index of bulk and thin-film TiO_2 typically ranges from 0.8–3 $\times 10^{-18}$ m^2/W in the NVIS window [11, 44, 54, 57, 60], which is an order of magnitude greater than the nonlinear index of silica fiber (2.48×10^{-20} m^2/W [21]). However, values obtained from thin-films measurements have been reported as large as 5×10^{-17} m^2/W [59], and as small as 1×10^{-19} m^2/W [61] and -6×10^{-17} m^2/W [53]. Although there are no reported nonlinearity measurements of bulk anatase, for thin films the value of n_2 for anatase is very similar to that for rutile [53, 54]. The visible transparency and minimal 2PA near 800 nm make TiO_2 most comparable to silicon nitride [103]. However, TiO_2 has a reported Kerr nonlinearity that is over three-times greater than silicon nitride, it possesses a greater refractive index (2.4 versus 2.0), and it can be deposited at low temperatures (< 400 °C), allowing for back-end integration with silicon microphotonic devices [11,121,148]. Even though TiO_2 is well suited for NVIS applications, integrated nonlinear optical devices in TiO_2 remain undeveloped and unexplored.

In this study, we demonstrate and characterize nonlinear pulse propagation in recently developed anatase TiO_2 waveguides [148]. We observe nonlinear spectral

broadening of femtosecond pulses with central wavelengths (λ_0) of 1565 and 794 nm, spanning the communications octave. We fit our measurements to simulations to quantify nonlinear optical parameters and we discuss potential applications for this new material platform. This study represents the first demonstration of optical nonlinearities in integrated TiO_2 devices.

6.1.2 Experimental Procedure

We investigate waveguides of various dimensions to ensure strongly confined single-mode operation at widely spaced wavelengths. We fabricate polycrystalline anatase strip-waveguides on silicon substrates with SiO_2 lower cladding and fluoropolymer top cladding using previously reported methods [148]. The waveguides reported here are 250-nm high, have top-widths of 900 and 200 nm, and are 9 and 6 mm long for measurements at 1565 and 794 nm, respectively. Figure 6.1(a) shows a typical cross section of a polycrystalline anatase waveguide before applying the top cladding, making evident both the polycrystallinity of the anatase material and the 75° side-wall angle. Figures 1(b) and 1(c), show simulated optical intensity profiles for the waveguides (at 1565 nm and 794 nm, respectively). Our fabricated waveguides are single-mode and strongly confine the light at each wavelength of interest, facilitating measurement and parameter extraction.

We observe nonlinear pulse propagation by comparing the input versus output spectra of pulses propagating within our waveguides as a function of the input pulse energy. Our measurements are taken with two laser systems: an optical parametric oscillator tuned to 1565 nm and a Ti:Sapphire oscillator centered at 794 nm. We

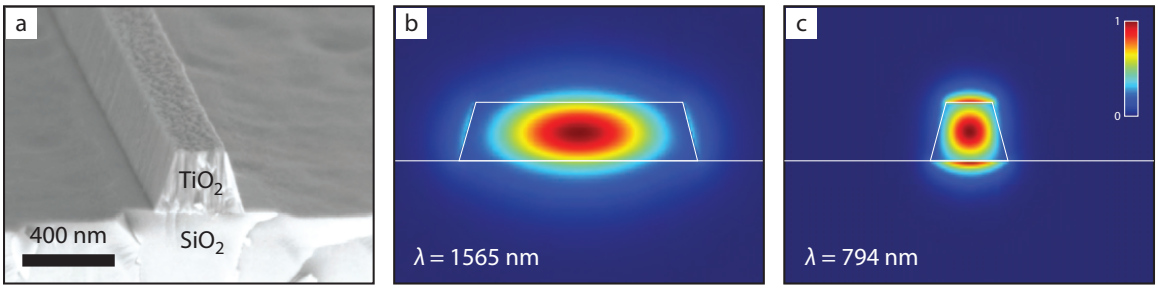

Figure 6.1: Scanning electron micrograph of a 200-nm wide polycrystalline-anatase TiO_2 waveguide, prior to top cladding (a). The waveguide is trapezoidal in shape and the TiO_2 grains are columnar in appearance. We show simulated mode-profiles of the fundamental TM and TE-like modes around 1565 and 794 nm (b and c, respectively), showing strong confinement in our single-mode waveguides.

present the laser parameters in Table 6.1. A half-wave plate followed by a polarizer controls the pulse energy and polarization. We couple into and out of the waveguides using 0.85 numerical aperture objectives. We measure the output spectra by focusing into a single-mode fiber coupled to an optical spectrum analyzer for 1565 nm and multimode fiber coupled to spectrometer for 794 nm. The shape of the recorded spectra does not change with fiber coupling efficiency, which insures that spectral broadening only occurs within the TiO_2 chips and not within the fibers. Amplitude and phase modulation from a multiphoton intrapulse interference phase scan (MIIPS) system controls the spectrum of the 794 nm pulse and provides a transform-limited duration at the input facet [175]. Even with this correction, we could not form a perfect Gaussian spectral profile. No dispersion compensation was applied for the 1565-nm measurements. The optical propagation losses are 8 and 45 dB/cm measured using the top-view method with coupling efficiencies of -9 and -12 dB/facet calculated from insertion loss measurements (1565 and 794 nm, respectively) [148]. Low-energy spectra are experimentally identical to the input spectra. These low-energy spectra

Table 6.1: Laser parameters used for measurement.

λ_0 (nm)	repetition rate (MHz)	pulse duration (fs)	max average power (mW)	polarization (TE/TM)
1565	80	170	387	TE
794	11	85	18.4	TM

serve as the seed spectra for nonlinear pulse propagation simulation from which we extract nonlinear coefficients.

6.1.3 Numerical simulation

We quantify the nonlinear optical parameters of anatase TiO_2 by fitting nonlinear pulse propagation simulations to the experimental data. Our simulation solves the generalized nonlinear Schrödinger equation using the slowly varying envelope approximation $A(z,t)$ in the retarded frame, given by:

$$\begin{array}{c} \frac{\partial A(z,t)}{\partial z} + \frac{1}{2}\alpha_1 A\left(z,t\right) + \alpha_2 \frac{A^2(z,t)}{A_{\text{eff}}} + \alpha_3 \left(\frac{A^2(z,t)}{A_{\text{eff}}}\right)^2 + \frac{i\beta_2}{2}\frac{\partial^2 A(z,t)}{\partial t^2} - \frac{\beta_3}{6}\frac{\partial^3 A(z,t)}{\partial t^3} \\ = i\gamma\left(1 + \frac{i}{\omega_0}\frac{\partial}{\partial t}\right)\left(A\left(z,t\right)\int_{-\infty}^{\infty} R\left(t'\right)\left|A\left(z,t-t'\right)\right|^2 dt'\right) \end{array}, \qquad (6.1)$$

using the split-step Fourier-transform method [20]. We model linear effects including loss (α_1) and dispersion (β_2 and β_3, where β_2 is the group velocity dispersion). We model nonlinear effects including self-phase modulation (γ), self-steepening, two- and three-photon absorption (α_2 and α_3, respectively), and stimulated Raman scattering (through the temporal nonlinear response function $R(t)$). Simulations with and without self-steepening (due to the $\frac{i}{\omega_0}\frac{\partial}{\partial t}$ term) are very similar. In addition, A_{eff} is the effective area for nonlinear absorption. We obtain a noiseless starting spectrum by fitting analytical functions (sech^2 for 1565 nm and a summation of Gaussians for 794 nm) to the measured low-energy spectrum. For each central wavelength, we

calculate linear waveguide parameters that determine light-matter interactions such as the effective area and chromatic dispersion. We extract the nonlinear coefficients by minimizing the mean squared error between simulated and measured data while leaving linear parameters fixed. The values extracted represent a single model that applies to all of the measured data at one wavelength.

Simulating the mode structure of the waveguides allows us to calculate the number of modes and linear waveguide parameters. We determine the energy distributions, $F(x, y)$, and propagation constants within the waveguide (shown in Figs. 1(b) and 1(c), 1565 and 794 nm, respectively) using a finite-difference eigenmode solver. The 900-nm waveguide only supports a TE mode for $\lambda_0 = 1565$ nm and the 200-nm waveguide supports fundamental TE-like and TM-like modes for $\lambda_0 = 794$ nm, simplifying pulse propagation simulation. Having identified the number and distributions of the modes, we calculate the effective nonlinearity and chromatic dispersion.

The strength of the nonlinear interaction is given by the effective nonlinearity γ, which we calculate from the energy distribution using [20]:

$$\gamma = \frac{2\pi}{\lambda} \frac{\int \int_{-\infty}^{\infty} n_2 (x, y) |F (x, y)|^4 dxdy}{\left(\int \int_{-\infty}^{\infty} |F (x, y)|^2 dxdy \right)^2}. \tag{6.2}$$

Using $n_2 = 3 \times 10^{-20}$ m^2/W for both silica and the fluoropolymer top cladding and γ determined during fitting, we solve this equation for n_2 in the TiO_2 core. The nonlinearity attributed to the cladding is 10 % for 1565 nm and less than 1 % for 794 nm. Assuming no nonlinear absorption in the cladding, we use a similar expression to calculate effective nonlinear absorption areas, A_{eff}, of 0.43 and 0.16 µm^2 for 1565 nm and 794 nm, respectively [20].

Our model includes the waveguide's group velocity dispersion (GVD), which

determines the temporal pulse spreading. GVD reduces the observed nonlinearity for positive (normal) values and leads to complex soliton phenomena for negative (anomalous) values. We calculate the GVD by evaluating the wavelength-dependent propagation constant. We observe lower GVD for the TM mode around 794 nm and therefore conduct all analysis and measurements using TM polarization. The GVD is 1450 and 1480 fs^2/mm, corresponding to dispersion parameters $D = -1120$ and -4420 ps/nm/km around 1565 and 794 nm, respectively. The GVD for both waveguides is normal, which enables deterministic broadening and simplifies parameter extraction.

In addition to dispersion and self-phase modulation, the pulse may experience stimulated Raman scattering (SRS), causing photons to scatter inelastically during propagation. It is necessary to add this effect to our simulation because of the strong Raman peaks observed in anatase TiO_2 [99]. The shift (Ω_R), bandwidth (Γ_R), and peak Raman gain (g_R) are characteristic of the waveguide material [20, 176]. In anatase, we expect the 144-cm^{-1} Raman line to be the dominant source of SRS [99]. The simulation includes SRS as the sum of an instantaneous and a delayed nonlinearity in the temporal nonlinear response function:

$$R(t) = (1 - f_R)\,\delta(t) + f_R h_R(t)\,, \tag{6.3}$$

where $R(t)$ is the nonlinear response as a function of time, f_R is the fractional strength of the delayed response, $\delta(t)$ is the Dirac delta function, and $h_R(t)$ is the delayed Raman response function[1]. The Raman gain (g_R) is related to f_R through $f_R =$

[1]We note that the instantaneous and Raman response are physically different processes. Therefore, the fractional strength is a consequence of grouping both parameters into a single nonlinear response function.

$g_R\Gamma_R/(n_2 k_0 \Omega_R)$, where k_0 is the free-space wavevector. We model the Raman response as a Lorentzian using [177]:

$$h_R(t) = \frac{\tau_1^2 + \tau_2^2}{\tau_1 \tau_2^2} \exp(-t/\tau_2) \sin(t/\tau_1). \tag{6.4}$$

The parameters τ_1 and τ_2 relate to the frequency shift, $\Omega_R/(2\pi)$, and width, Γ_R/π, of the Raman gain spectrum through $\tau_1 = 1/(\Omega^2 - \Gamma_R^2)^{1/2}$ and $\tau_2 = 1/\Gamma_R$ [20, 176, 178]. By including SRS, this simulation models all linear and nonlinear optical effects expected in our measurements, except for the wavelength-dependence of 2PA, which only occurs near the half-bandgap (775 nm), and third-harmonic generation.

6.1.4 Experimental and simulation results

Figure 6.2 shows measured and simulated spectra for a 900-nm wide anatase TiO_2 waveguide using a 170-fs pulse at $\lambda_0 = 1565$ nm. We present the extracted nonlinear parameters in Table 6.2. Comparing the lowest and highest energies, we observe broadening by a factor of 3.8, measured -15 dB below the peak. We observe a reasonably good fit for pulse energies up to 229 pJ, while the modulation of the peak at 443 pJ is stronger experimentally than in our simulations.

We observe two distinct features in the 1565-nm data. First, we see a rounding of the central peak for energies of 172–229 pJ (corresponding to a $^3/_4$- π nonlinear phase shift in the simulation) followed by an M-shaped oscillatory structure for 443 pJ. This structure corresponds to a π phase shift in the simulation and is a result of self-phase modulation. Second, we observe an additional asymmetric peak around 1600 nm for a pulse energy of 120 pJ. This peak corresponds to an energy difference of 140 cm^{-1} from the 1565 nm peak and is similar to the 144 cm^{-1} Raman shift in anatase [99].

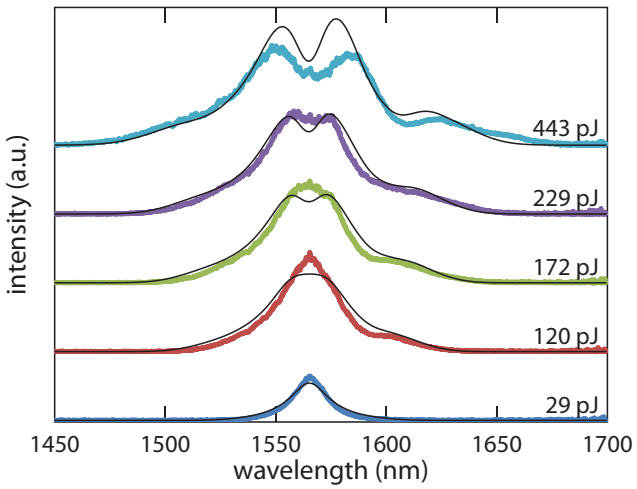

Figure 6.2: Measured (thick) and simulated (thin) spectral broadening for a 900-nm wide polycrystalline-anatase TiO_2 waveguide at $\lambda_0 = 1565$ nm at incident energies from 29 pJ to 443 pJ. As the energy is increased, oscillatory features appear in the central peak and a secondary peak around 1600 nm emerges for energies greater than 120 pJ.

Therefore, we fix τ_1 to 37 fs to correspond to 144 cm^{-1}. Additionally, the peak red shifts with higher pulse energies, an effect which becomes strongly pronounced at 443 pJ. Setting f_R to zero in the simulation turns off SRS and removes the asymmetric peak while retaining the dominant features in the central peak.

Figure 6.3 shows measured and simulated spectra for a 200-nm wide anatase TiO_2 waveguide using a 85-fs pulse ($\lambda_0 = 794$ nm) with the simulation parameters shown in Table 6.2. We were unable to reliably fit all Raman parameters. Consequently, we fix τ_1 to reported bulk values, then fit τ_2 and f_R [99]. The pulse spectrum broadens by a maximum factor of 3.2 for a 56-pJ pulse. Both the output energy and broadening factor saturate at high pulse energy. Turning off 2PA in the simulation removes this saturation. The oscillatory structure that appears in the 794-nm data

Table 6.2: Nonlinear optical parameters determined from fitting simulation to experimental data (Figs. 2 and 3). We estimate an uncertainty of ± 20% for 1565 nm. Parameters around 794 nm should be considered order of magnitude estimates. Parameters with asterisks were not fit.

λ_0 (nm)	γ ($W^{-1}m^{-1}$)	n_2 (m^2/W)	α_2 (m/W)	τ_1 (fs)	τ_2 (ps)	f_R
1565	1.5	0.16×10^{-18}	0	37*	1.4	0.18
794	79	1.6×10^{-18}	7×10^{-12}	37*	0.4	0.64

is more chaotic than the 1565-nm data set. We observe an asymmetry whereby the central peak appears red-shifted; this is much stronger than for 1565 nm. Setting f_R to zero removes the asymmetry in the simulation. The maximum phase shift observed in the simulation is 1.1π. Although the spectral broadening is relatively strong around 794 nm, we are unable to model all the features in the data accurately.

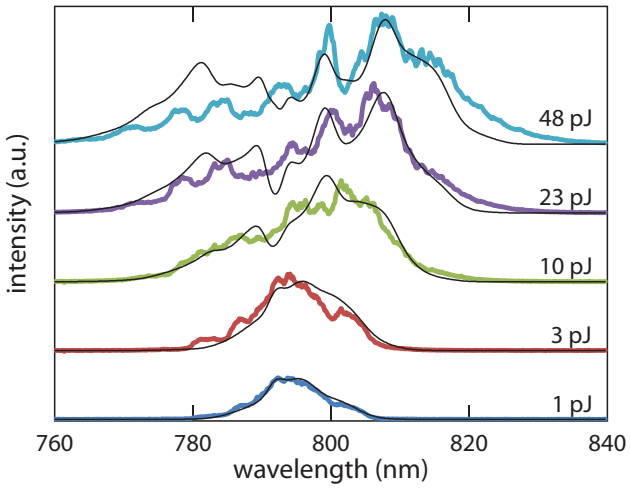

Figure 6.3: Measured (thick) and simulated (thin) spectral broadening for a 200-nm wide polycrystalline anatase TiO_2 waveguide at incident energies from 1 pJ to 48 pJ. The data show a strong red-shifted asymmetry with increasing energy at $\lambda_0 = 794$ nm.

6.1.5 Discussion

Designing nonlinear optical devices in anatase TiO_2 requires that we understand the distinct features in this new material platform, from nonlinear refraction and absorption to stimulated Raman scattering. We will first focus on the 1565-nm data set, as it has low noise and displays simple features that we can readily model, and then we comment on the 794-nm data set. The largest source of uncertainty is the measured loss (±50%) [148]. Performing a fit using these extremes corresponds to a maximum uncertainty of ±20% for all parameters. The quality of the 1565-nm data set enables reliable parameter extraction that we can use to assess TiO_2's applicability to all-optical devices.

Telecommunication wavelengths

Understanding the interplay between nonlinear refraction and absorption in TiO_2 is critical for all-optical devices. Our value of n_2 around 1565 nm (0.16×10^{-18} m^2/W) is an order of magnitude lower than typical values for TiO_2 ($0.8–3 \times 10^{-18}$ m^2/W [11,44,54,57,60]). The decreased value of n_2 at telecommunication wavelengths is consistent with theoretical models [10, 52]. In our simulation, we neither expected nor included 2PA at 1565 nm. A small amount of three-photon absorption ($\alpha_3 = 0.1$ mm^3/GW^2) was included in the model to account for output saturation. We observe a similar trend when using continuous-wave excitation at similar average powers; therefore, this effect may be the result of thermal coupling drift. Our measured value of n_2 is lower in anatase (0.16×10^{-18} m^2/W) than for silicon nitride (0.24×10^{-18} m^2/W, 1550 nm) [124]. However, the higher linear refractive index of TiO_2 (2.4

in TiO_2 versus 2.0 in silicon nitride) results in stronger confinement and leads to effective nonlinearities (γ) 1.1 times stronger in TiO_2 than in silicon nitride [43]. Our measurement around 1565 nm shows strong effective nonlinearities that are unaffected by 2PA, making TiO_2 a promising material for applications at telecommunication wavelengths.

A high nonlinearity enables maximal nonlinear phase accumulation in devices, however physical effects, such as loss and dispersion, limit the achievable phase shift. The π phase-shift we observe (443-pJ, 1565 nm) is sufficient for distributed feedback gratings, and a 2π phase-shift (needed for a nonlinear Mach-Zehnder interferometer) is achievable with nJ pulses [27]. To reduce this energy requirement, we identify the strongest effects by comparing the length scales at which different effects become relevant. Using the peak power P_0, pulse duration T_0, group velocity dispersion β_2, and the loss α_1, we calculate a minimum nonlinear length $(\gamma P_0)^{-1}$ of 0.27 mm (443 pJ, 1565 nm), a loss length α_1^{-1} of 5.4 mm, and a dispersion length $T_0^2/|\beta_2|$ of 19 mm. For this 9-mm device, linear loss is the dominant parasitic effect. This loss may be the result of the deposited material's polycrystallinity and sidewall roughness, as seen in Fig. 6.1(a). Therefore, future research should focus on reducing linear propagation losses. Low-loss TiO_2 waveguides would benefit from dispersion engineering to enable applications such as all-optical switching, four-wave mixing, and supercontinuum generation.

In addition to balancing nonlinear refraction and absorption, SRS is an important effect for all-optical devices. SRS appears as a secondary peak in the 1565-nm data, causing a pronounced asymmetry that we must model when simulating devices.

If we perform a second fitting that includes τ_1, we extract a τ_1 value of 33 fs, which corresponds to a Stokes shift of 161 cm^{-1} ($\Omega_R/(2\pi) = 4.8$ THz), which is close to the 144-cm^{-1} line in the spontaneous Raman spectrum and observed in other studies [61]. This energy shift is smaller than silica (402 cm^{-1}, $\tau_1 = 12.2$ fs) [177] and silicon (520 cm^{-1}, $\tau_1 = 10.2$ fs) [171]. SRS becomes relevant when our pulse bandwidth spans the Raman energy shift and thus, should be included when modeling short pulses (< 200 fs) in anatase.

The bandwidth and strength of SRS opens up additional applications for TiO_2. Anatase's crystallinity results in a measured response time of $\tau_2 = 1.4$ ps, which is similar to other reported values (1 ps) [61]. This response time corresponds to a bandwidth ($\Gamma_R/\pi = 230$ GHz) that is much narrower than amorphous silica (10 THz) and comparable to other crystalline materials such as silicon (105 GHz). Additionally, our extracted value of the Raman fraction, $f_R = 0.18$, is consistent with silica ($f_R = 0.18$) [177] and larger than silicon ($f_R = 0.0664$) [171]. The strength of f_R leads to peak Raman gain coefficients of 6.6×10^{-12} m/W, which is 130 times that of silica (5×10^{-14} m/W) and an order of magnitude lower than silicon (2×10^{-10} m/W) [171]. Unlike silicon, the extended transparency of anatase allows Raman amplification throughout the NVIS spectrum, and the narrow shift reduces problems associated with pulse walk-off. The high gain and narrow bandwidth of SRS in anatase may enable ps-pulse and continuous-wave Raman amplifiers, extending into the visible and NVIS windows.

Near-visible wavelengths

Our 794-nm studies provide the first observation of spectral broadening in TiO_2 waveguides in the NVIS window. Our value of n_2 around 794 nm agrees well with most literature values for the nonlinear index of bulk and thin-film TiO_2 [11, 44, 54, 57, 60]. In addition, the wavelength-independent 2PA (7×10^{-12} m/W) is of the same order of magnitude as that measured in bulk rutile and may pose a limit for all-optical devices around 800 nm [11, 27]. As was the case with the 1565-nm data set, thermal coupling drift may be the source of the apparent 2PA. Although 2PA may be present, we expect that operating at longer wavelengths (*i.e.*, 850 nm) will eliminate 2PA.

The complex structure and additional un-modeled nonlinear effects increase the uncertainty in our analysis around 794 nm compared to 1565 nm. The intricacies around 794 nm may be a result of the input pulse's structure. The delayed Raman effect attempts to model the asymmetry in the simulation, resulting in an extremely high Raman fraction (0.64), which may be unphysical. This asymmetry may be partially attributed to wavelength-dependent 2PA, which we did not model. This effect is significant in rutile TiO_2 around its half-bandgap (800 nm) [11]. The expected 2PA edge of anatase (775 nm) should not affect the majority of our data, however, a linear absorption (Urbach) tail may extend the linear and nonlinear absorption to lower energies [179]. Alternatively, the crystalline phase may have partially transformed to rutile during fabrication, leading to stronger 2PA for wavelengths shorter than 800 nm. In addition, uncertainties in the input pulse's shape may affect our analysis. We expect that including wavelength-dependent 2PA would reduce the delayed Raman fraction to values similar to those around 1565 nm. The lower quality of the

794-nm data and un-modeled physical processes imply that our analysis should only be considered an order of magnitude estimate, warranting further study in the NVIS spectrum.

6.1.6 Conclusion

We observe and quantify spectral broadening in polycrystalline anatase TiO_2 waveguides at two wavelengths ranging from NVIS to telecommunication wavelengths. Using pulse energies of tens to hundreds of pJ, we observe broadening factors greater than 3. Around 1565 nm, the strong effective nonlinearity and the absence of two-photon absorption can facilitate ultrafast, non-resonant all-optical switching applications. Additionally, the small energy shift and high Raman gain of SRS may enable efficient devices such as Raman amplifiers and lasers. The first spectral broadening measurements in the NVIS spectrum show a nonlinearity that agrees well with bulk TiO_2 values. Finally, as we expect little 2PA, we are unable to accurately quantify 2PA in our devices. Based on these first nonlinear results in TiO_2 waveguides, we show that TiO_2 is a promising material for future integrated nonlinear photonics applications throughout the communications octave.

Acknowledgements

Several people contributed to the work described in this paper. C.E. and J.B. conceived of the basic idea for this work. C.E. performed measurements near 800 nm and C.E. and K.S. performed measurements near 1565 nm. C.E. performed the simulations and fitting. J.B. fabricated the waveguides. O.R. aided in the fabrication

and the mode simulations. E.M. and E.I. supervised the research and the development of the manuscript. The authors would like to thank Markus Pollnau, Erwin Martí-Panameño, and Ruwan Seneratne for help developing the basis for this work. C.E. wrote the first draft of the manuscript; all authors subsequently took part in the revision process and approved the final copy of the manuscript. Kasey Phillips and Sarah Griesse-Nascimento provided feedback on the manuscript throughout its development. Nonlinear pulse propagation simulations were performed using RP Photonics Fiber Power software. The research described in this paper was supported by the National Science Foundation under contracts ECCS-0901469 and ECCS-1201976, by the MRSEC Program of the National Science Foundation under DMR-0819762, and by AFOSR under FA9550-12-1-0499. C.E. acknowledges support from the Harvard Quantum Optics Center. The authors acknowledge the use of facilities in the Center for Nanoscale Systems, which is supported by the National Science FoundationâĂŹs National Nanotechnology Infrastructure Network.

6.2 Third-harmonic generation

In this section, we explore the nature of green light generated in polycrystalline TiO_2 waveguides when pumped with femtosecond pulses around 1565 nm, as shown in Figure 6.4. Although the pump's central wavelength is 1565 nm (FWHM of 17 nm), we observe strong green light at a wavelength of 534 nm (FWHM of 1 nm), which is substantially offset from the energy shifted pump's central wavelength. This light generation could be a parametric (instantaneous) or a non-parametric (using an electronic state) process. To understand the nature of green-light generation in our TiO_2

waveguides, we present the results to two preliminary experiments, from which we infer that the process is third-harmonic generation (THG) and we show evidence of phase-matching using a higher-order mode at signal wavelengths.

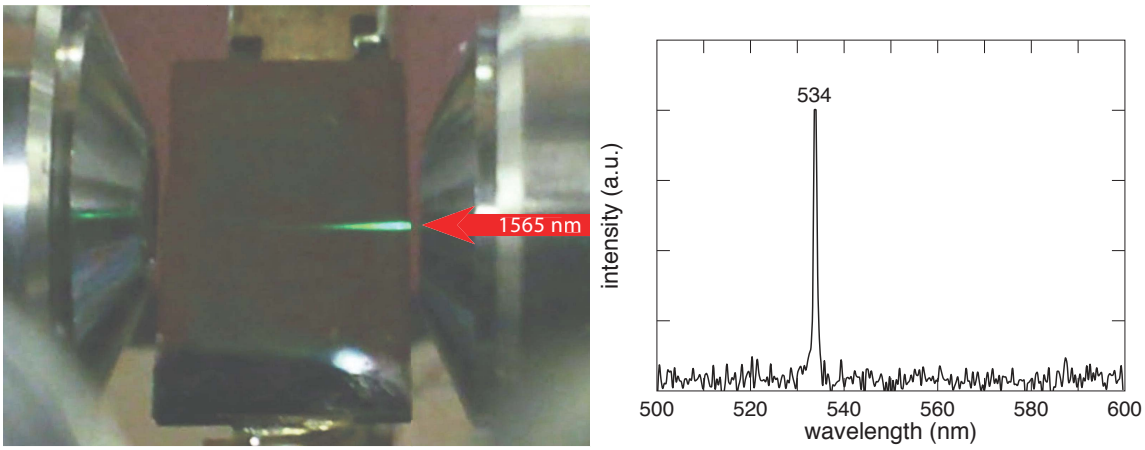

Figure 6.4: Green light generation in a polycrystalline anatase TiO_2 waveguide using a 1565 nm pump: optical image (left) and corresponding visible spectrum (right). We see a shift from the expected third-harmonic value predicted considering energy conservation alone (517.7 nm).

6.2.1 Third-harmonic generation in multimode waveguides

Converting three pump photons to one signal photon using THG is often not efficient unless both energy and momentum are conserved. For the degenerate case (three identical pump photons), energy conservation requires:

$$3\hbar\omega_p = \hbar\omega_s, \tag{6.5}$$

where, $\hbar\omega_p$ is the pump photon energy and $\hbar\omega_s$ is the signal photon energy. To make this process efficient, we must conserve momentum by minimizing the phase-mismatch. Neglecting self-phase modulation, this expression is given by:

$$\Delta\beta = \beta_s - 3\beta_p. \tag{6.6}$$

Here, β_p is the pump photon momentum in the waveguide and β_s is the signal photon momentum. In terms of physical parameters, this simply states that the pump and signal effective refractive indices should match: $n_p(\lambda_p) = n_s(\lambda_p/3)$. If photon momenta (phase) are not matched during propagation, photons will cycle between pump and signal periodically, resulting in periodic conversion and minimal efficiency. Therefore, finding a way to minimize this phase-mismatch is the central problem for THG.

The technical challenge is to circumvent the material dispersion to achieve phase-matching conditions for efficient THG. Typical material dispersion at visible and near-infrared wavelengths results in higher indices at shorter signal wavelengths. To equalize these indices, we use various phase-matching schemes. For the case of second harmonic generation, using polarized light with birefringent crystals provides a simple means to minimize phase-mismatch [16, 180]. For THG, the wide wavelength difference makes phase matching difficult using birefringence alone. Recently, an alternative technique has been developed to phase-match within a multi-mode waveguide.

Multi-mode waveguides provide a novel means to phase-match between the widely separated pump and signal wavelengths [181, 182]. In a single-mode dielectric waveguide (such as a low-index-contrast fiber), waveguide dispersion in the fundamental mode cannot overcome the strong material dispersion at such widely spaced wavelengths. Meanwhile, in a high-index-contrast waveguide, higher order modes (HOMs) have very strong waveguide dispersion that can result in much lower effective indices than the fundamental mode. This allows us to pump the fundamental

mode in the infrared and efficiently generate THG signal a phase-matched HOM. This multimode (MM) phase-matching scheme provides a new way to generate THG signal utilizing the strong and sustained nonlinearities in nanowires devices.

To understand how we can apply MM phase-matching to a real system, we show the dispersion for two typical waveguide modes in Figure 6.5. The x-axis on the bottom corresponds to the pump wavelength and the x-axis on the top corresponds to the energy-matched signal wavelength. The crossing point for these two modes indicates the phase-matched wavelength for this pair of modes: $n_p(\lambda_p) = n_s(\lambda_p/3)$. The difference in the group velocities, related to the relative slopes of the dispersion curves, determines the phase-matching bandwidth. In the limit where we can neglect self-phase modulation, the spectral width of the peak is given by $\Delta\omega \approx 2\pi(|{v_s}^{-1} - {v_p}^{-1}|\, z)^{-1}$, where v_s and v_p are the group velocities at the signal and pump wavelengths (respectively) and z is the distance in the waveguide [181, 182]. This expression shows a decrease in the spectral width for larger group-velocity mismatches and longer distances. For the waveguides modes considered here, the bandwidth is typically 1 nm ($z = 0.5$ mm). For comparison, we can observe the energy scaled pump (ESP) spectrum, $\lambda_p/3$, which provides an idea of the expected THG spectrum if phase-matching is not considered. We find that the pump spectrum is typically 10–20 nm in the infrared (with $\lambda_p/3$ from 3–7 nm in the visible), thus, the phase-matched THG spectrum is significantly narrower. The bandwidth may also display an offset from the central peak around $\lambda_p/3$. If we consider that spectral broadening can increase the available pump spectrum for THG, this may further increase this offset. From this analysis, phase-matched THG should appear stronger than non-phase matched THG,

it should also be significantly narrower than the ESP spectrum, and we should observe that the THG peak may be offset from the ESP-peak.

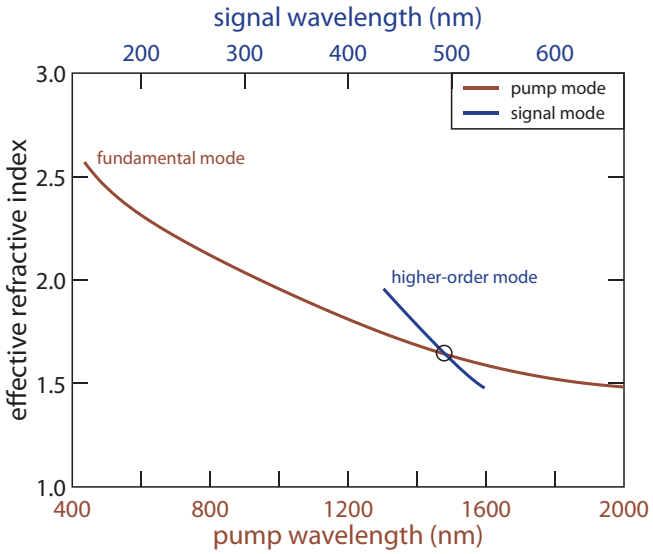

Figure 6.5: Phase-matching between the fundamental and a higher-order waveguide mode. By overlaying the two dispersion plots to show energy conservation ($3\lambda_p = \lambda_2$), the phase-matched wavelength is shown by the crossing point. This wavelength results in the highest third-harmonic conversion efficiency.

In this section, we explore phase-matched THG in polycrystalline anatase TiO_2 waveguides. We conduct two experiments, first to observe different waveguide geometries at a fixed pump wavelength, and second, to measure THG signal in a single waveguide as a function of pump wavelength. These preliminary experiments suggest that we are achieving THG using a MM phase-matching scheme. We conclude this section with a discussion on future experiments and potential applications for THG in this new material platform.

6.2.2 Experimental

In our first experiment, we observe visible-light generation for a series of differently sized TiO_2 waveguides using a fixed pump wavelength. We utilize the TiO_2 strip-waveguides fabricated as described in [148]. These polycrystalline TiO_2 waveguides are 250-nm thick and 600, 700, 800, and 900-nm wide, have a sidewall angle of 75°, and have an SiO_2 under-cladding and a fluoropolymer top-cladding. We utilize a setup identical to the optical parametric oscillator described in [183], except we tune to a central wavelength of 1550 nm (180 fs pulse duration, 360 mW average power) and excite the fundamental transverse-electric mode. No dispersion compensation was applied. For each waveguide, we pump using the full laser power and collect the generated visible light using a multimode fiber placed in close proximity to the waveguide. We adjust the fiber placement to maximize signal and then record each spectrum using a spectrometer. Because the coupling, chip, and fiber placement varies for each measurement, the visible signal strength only qualitatively indicates efficiency.

In the second experiment, we observe a single-waveguide as a function of pump wavelength. We fabricate a 250-nm thick, 280-nm wide waveguide, similar to the previous waveguides, however, we apply a 4-µm thick cladding of SiO_2 using chemical vapor deposition. This choice of cladding extends the cutoff condition past 1560 nm and allows us to confirm that our observed signal is not the result of the fluoropolymer cladding. We observe visible light generated for central pump wavelength from 1440–1560 nm using 20 mW of average power. Over this tuning range, our pump laser bandwidth varies from 10–31 nm, which corresponds to transform limited durations

between 110–310 fs.

6.2.3 Results

We present the visible spectra generated in polycrystalline anatase TiO_2 waveguides for a fixed pump wavelength of 1550 nm with design widths of 600, 700, 800, and 900 nm in Figure 6.6. In Figure 6.6 d, we show the spectra for two different physical waveguides, both designed to be 900 nm wide, on the same chip to show the effects of small fabrication variations. For reference, we plot the ESP spectrum ($\lambda_p/3$), which approximately corresponds to the expected third-harmonic spectrum, neglecting phase-matching. For the 600, 700, and 800-nm wide waveguides (Figure 6.6 a–c), the recorded spectra resemble the ESP spectrum. The amount is signal is very low and close to the noise floor of the spectrometer. On visual inspect, visible light is generated only near the waveguide facets. Meanwhile, the waveguides designed to be 900-nm wide show a streak of green light, similar to Figure 6.4. The visible peaks around 521.8 and 526.8 nm are strong and do not resemble the ESP spectrum in terms of central wavelength (516.7 nm) or width (6.9 nm). We note that both third-harmonic spectra fall within the ESP spectrum. Additionally, reducing the average power from 330 to 200 mW does change the third-harmonic spectrum. This data shows that strong visible signal is only generated in the 900-nm wide waveguide and appears to be sensitive to fabrication variations.

In Figure 6.7, we show THG wavelengths in a 280-nm wide waveguide as a function of pump wavelength. We plot each visible signal spectrum as an intensity plot (vertically) at each central pump wavelength. For reference, we plot the energy con-

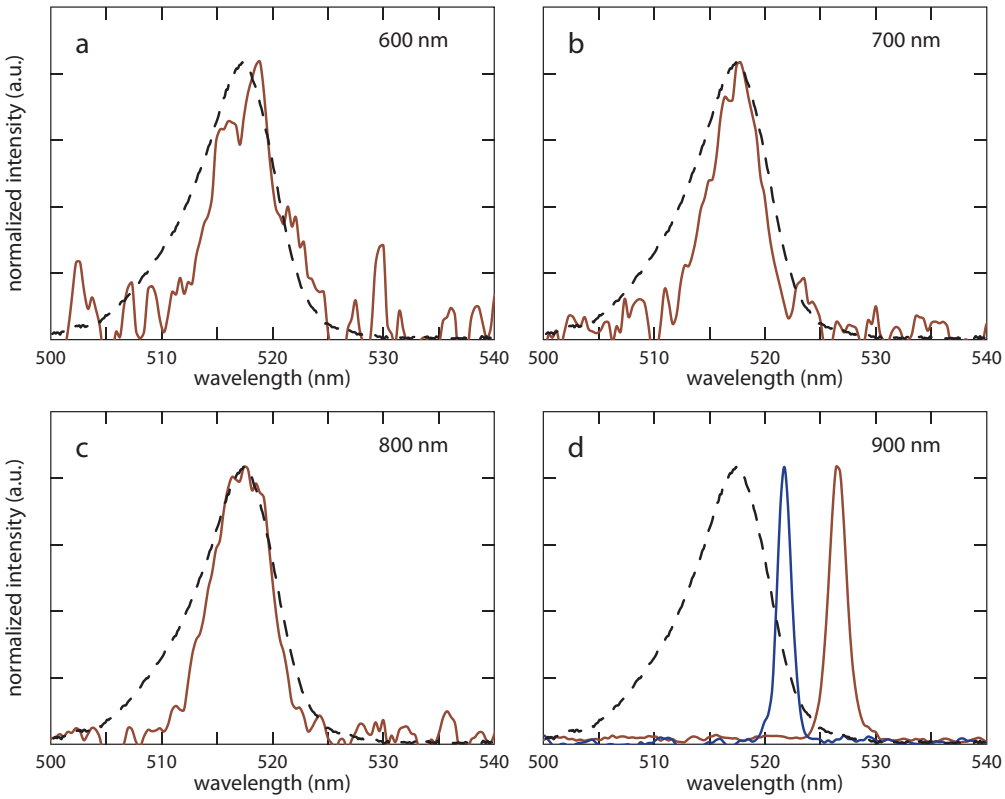

Figure 6.6: Visible spectra for different waveguide dimensions (with two similar 900-nm wide waveguides). For reference, we show the ESP spectrum ($\lambda_p/3$) as a dashed line. Waveguide widths from 600–800 nm have low signal (observable here via the poor SNR) and approximately follow the ESP spectrum. Meanwhile, the 900-nm wide waveguides generate strong, narrow-bandwidth signal that is offset from the central ESP wavelength and appears to be sensitive to small fabrication variations.

servation line ($\lambda_s = \lambda_p/3$) and place yellow dots corresponding to the peak locations in each signal spectrum.

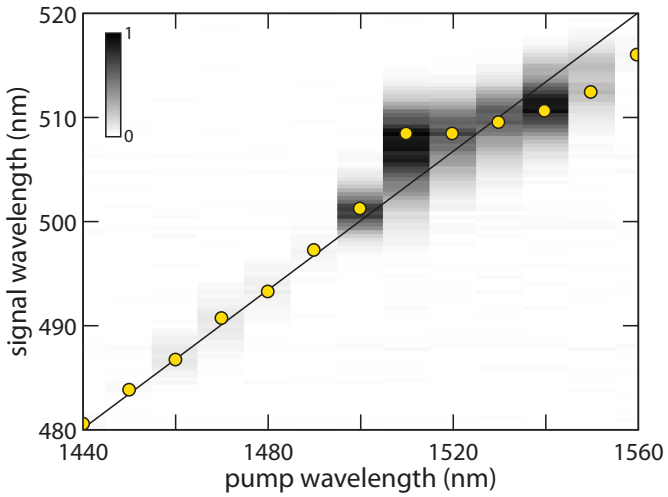

Figure 6.7: Visible spectra as a function of pump wavelength for a 300-nm wide waveguide. For each central pump wavelength, we show the corresponding visible spectrum vertically, as an intensity plot, and we mark the peak wavelength with a yellow circle. For reference, the energy-conservation line ($\lambda_s = \lambda_p/3$) is shown as a solid line. Between 1440 and 1490 nm, the signal is weak and follows the energy-conservation line. Around 1520 nm, the visible signal around 509 nm is much stronger and varies little with pump wavelength, signifying phase-matched third-harmonic generation.

Our swept-wavelength measurement plot shows three key features. First, we see that the signal peaks closely follow the energy conservation line for wavelengths shorter than 1500 nm. Second, we see very strong signal between 1500 nm and 1550 nm. Lastly, the strong signal we observe is shifted away from the energy conservation line. The visible-wavelength peaks shift 4 nm around 509 nm for pump wavelengths of 1510–1560 nm. Meanwhile, energy conservation predicts this shift should be over 13 nm. The strength, width, and offset of the visible spectrum is consistent with efficient THG using a MM phase-matching scheme.

6.2.4 Discussion

In the first experiment, we observe that changing waveguide dimensions produces two distinct phenomena, which we broadly categorize as phase-matched and non-phase-matched. First, we see weak, broad signal that follows the ESP spectrum for waveguide widths between 600–800 nm. This is consistent with non-phase-matched third-harmonic generation near the facet. Second, for the 900-nm wide waveguide, we observe strong, narrow signal that is within the ESP bandwidth of the pump, but does not follow the central ESP wavelength. The peak around 526.8 nm is shifted near the edge of the ESP's bandwidth, however, we expect that this peak falls within a spectrally broadened ESP spectrum. The increased efficiency, bandwidth, and wavelength offset we observe in the 900-nm wide waveguide suggests that only this waveguide achieves MM phase-matching around 1550 nm.

Comparing our data with simulation allows us to understand and ultimately control MM phase-matching in TiO_2 waveguides. We calculate the total dispersion for all guided modes from 400 nm to the cutoff condition using a finite-difference eigenmode solver. For each pair of modes, we calculate the phase-matching wavelength, if it exists. Additionally, these asymmetrical waveguide geometries do not support pure TE or TM modes, and instead support hybrid modes (this is particularly the case for higher order modes). To quantify the polarization, we report the TE-fraction of the mode, given by:

$$\mathrm{TE-fraction} = \frac{\int |E_x|^2 dxdy}{\int \left(|E_x|^2 + |E_y|^2\right) dxdy}. \tag{6.7}$$

MM phase-matching only occurs when pumping the fundamental transverse-electric-like (TE-like) and transverse-magnetic-like (TM-like) modes. We show the

nearest three phase-matched wavelengths around 1550 nm for a pump in the fundamental TE-like mode in Table 6.3. Additionally, we report the TE-fraction calculated around our starting wavelength of 400 nm for these hybrid modes.

Table 6.3: Phase-matching wavelengths between the fundamental TE-like mode and several higher-order modes in 250-nm thick waveguides with widths between 600 and 900 nm. We present the TE-fraction, calculated around 400 nm, to quantify the polarization of these hybrid modes.

	600 nm			700 nm		
pump (nm)	1517.6	1591.4	1614.0	1499.1	1599.9	1652.2
signal (nm)	505.9	530.5	538.0	499.7	533.3	550.7
TE-fract.	0.969	0.044	0.063	0.928	0.016	0.984
	800 nm			900 nm		
pump (nm)	1564.4	1590.8	1594.1	1555.5	1564.2	1648.9
signal (nm)	521.5	530.3	531.4	518.5	521.4	549.6
TE-fract.	0.016	0.075	0.076	0.879	0.057	0.033

Our simulation results provide key insights for THG in terms of polarization and waveguide fabrication. The small, broad signal we observe for the 600 and 700-nm waveguides is consistent with the absence of phase-matching wavelengths within the pulse bandwidth. Meanwhile, the 800 and 900-nm wide waveguides have phase-matching wavelengths within the bandwidth of the pump. The 800-nm wide waveguide is phase-matched around 521.5 nm, however its TE-fraction is low, indicating the signal mode is cross-polarized with the pump. Similar to second-harmonic generation, we expect the tensor element responsible for co-polarized THG to be larger than the cross-polarization term [16]. Therefore, the absence of measurable signal may simply reflect the lower efficiency. If this is the case, the strongest signal should be for the 900-nm wide waveguide around 518.5 nm. The additional offset we observe may be

due to variations in the dimensions or material dispersion between the simulated and fabricated devices. We estimate that a width increase of 20 nm (2.2%) will shift the 518.5 nm signal to the 521.8 nm we observe experimentally, similarly a width increase of 47 nm (5.2%) will shift this further to 526.5 nm. These variations are close to our typical fabrication tolerance (5%). Using simulation as a guide, we see that both the polarization and specific waveguide dimensions determine the efficiency phase-matching wavelengths for THG in TiO_2 waveguides.

Our swept pump data using a single-waveguide shows that efficient THG depends most strongly on waveguide dimensions. We see two major features that show both phase-matched and non-phase-matched conditions within the same waveguide. First, for pump wavelengths between 1510–1550 nm, we observe strong signal that we attribute to phase-matching. The shift away from the nominal energy conservation line for pump wavelengths between 1510–1550 nm suggests a visible phase-matched wavelength of 509 nm. There is a slight tilt in the signal around this 509-nm signal that corresponds to pump's central wavelength. The abrupt shift in wavelength (slightly shifted from the nominal energy conservation line) and strong signal around 1500 nm may be due to an additional phase-matched pump wavelength. Second, the weak signal we observe from 1440–1490 nm closely follows the scaled pump's central wavelength, which is consistent with non-phase-matched THG. Longer transform-limited pulse durations at shorter wavelengths and uncompensated dispersion may play a role in the decreased efficiency. We expect that tuning over a wider range should produce additional phase-matched wavelengths. The signal strengths and offsets demonstrate MM phase-matching within this TiO_2 waveguide.

Our preliminary data suggests the process we observe is parametric THG, thus enabling ultrafast applications. Parametric (instantaneous) processes often require phase-matching to be efficient and are polarization dependent, as we have observed experimentally. A non-parametric process adds many complications. For example, this may be multiphoton absorption followed by fluorescence from a mid-gap state. In this case, we would expect geometry-independent signals at visible wavelengths, contrary to our experiments. Additionally, we would require an electronic state for fluorescence to occur either in TiO_2 or in the cladding material, which we do not expect. Also, the measurement using a silica cladding rules out the fluorescence from the fluoropolymer cladding. Further experiments to explore the ultrafast dynamics of this process, such as pump-probe, should determine the true nature of the THG we observe. Our evidence favors a parametric over a non-parametric process, which may enable ultrafast frequency conversion between telecommunications and visible wavelengths.

These results open up many future experiments, applications, and challenges for THG in TiO_2 waveguides. Two-key experiments should be further investigated: quantifying THG efficiency and resolving multiple phase-matched wavelengths within the same waveguide. These first experiment provide a basis for comparison to other integrated materials and will establishes a stronger link between theory and experiment. As for applications, our THG device provides a means to convert telecommunication to visible wavelengths. The narrow bandwidth may enable selective THG from a wavelength-multiplexed source. Additionally, the sensitivity to waveguide geometry suggests thermal tuning is possible. Future work should focus on increasing the

reliability and efficiency of both generating and extracting THG signal. The geometry sensitivity demands tight fabrication tolerances for predictable phase-matched wavelengths. Additionally, efficient extraction of the HOM signal is more challenging than from fundamental modes. Our preliminary results provide a basis for future experiments and applications utilizing the high efficiency and wavelength specificity of THG in TiO_2 waveguides.

6.2.5 Conclusion

We observe THG in polycrystalline anatase TiO_2 waveguides and show that this process is phase-matched utilizing higher-order waveguide modes. We observe that phase-matched THG has increased efficiency, a narrow bandwidth, and can have a wavelength that is offset from the wavelength expected from the central pump wavelength. Tuning the pump reveals that phase-matching wavelengths are highly dependent on the waveguide's geometry. Our demonstration of THG in TiO_2 waveguides shows new applications for this exciting material.

Chapter 7

Conclusions and outlook

We have explored and developed titanium dioxide for integrated nonlinear optical devices. We have quantified the optical nonlinearities of bulk rutile TiO_2 around 800 nm, which represents the material's wavelength limit for many all-optical devices. We have presented a series of studies to produce high-quality thin films of TiO_2 suitable for planar integrated photonics. Using these films, we have fabricated linear waveguides and devices, demonstrating many of the building blocks of more complex integrated photonic circuits. Lastly, we have explored, observed, and quantified the first nonlinear optics in TiO_2. Having presented the foundation for titanium dioxide integrated optical circuits, we now summarize the major conclusions and suggest directions of future research.

Our study of the nonlinear optical properties of bulk TiO_2 around 800 nm shows the onset of two-photon absorption and reveals birefringence in both the nonlinear index and multiphoton absorption coefficients. Our measurements demonstrate that two-photon absorption can be avoided in rutile TiO_2 by operating at wavelengths as

short as 813 nm. This is promising for all-optical applications utilizing near-visible wavelengths, particularly around 850 nm, where two-photon absorption should be negligible. The low two-photon absorption enables ultra-wide bandwidth devices that could operate from 800–1600 nm. To support such work, extending bulk measurements to telecommunications wavelengths is both an important and straightforward study that will serve as the foundation for advanced devices operating throughout the telecommunications octave (800–1600 nm).

In Chapter 4, we developed high-index optical-quality thin films in both amorphous and anatase TiO_2 using reactive sputtering. Of these varieties, amorphous TiO_2 has superior losses, particularly for visible wavelengths, and can be deposited at a higher rate than anatase. The lower losses are likely due to the small grain size and low surface roughness. Meanwhile, polycrystalline anatase films have a higher index, yet they exhibit much higher losses. We cannot explain these losses using surface roughness alone and therefore, we believe scattering from the crystallites (being comparable to the wavelength) is likely responsible. Even with these increased losses, they are reasonable when compared to other polycrystalline materials such as silicon [94–96, 154].

To develop the higher-quality thin films necessary for many devices, there are two paths forward: optimize current thin-film deposition methods or explore alternative thin-film sources. Both the amorphous and anatase films can be optimized to further reduce the losses by exploring the large deposition parameter space. Although amorphous TiO_2 is considerably more consistent, there was some unexplained variability in both film varieties, resulting in a handful of very high-loss films, even with

well-established recipes. We have seen improved results from careful wafer handling and cleaning procedures, as well as pre-depositions to "season" the chamber, which avoids contamination from previous depositions. Target depletion during long depositions causes the DC bias voltage to change when using fixed power, and complete depletion results in the deposition of copper from the target holder. Careful target control or a series of short deposition may improve results. Improving the losses of deposited films is an ideal solution that is flexible and scalable, however, the parameter space is large and so far, we can only achieve high-quality TiO_2 within a narrow parameter range.

In addition to optimizing the deposition, we recommend exploring alternative sources of TiO_2 thin films. For deposited films, electron-beam evaporation has produced some reasonable films, however the results were inconsistent. We anticipate that atomic layer deposition (ALD) should achieve excellent quality films, however, none of our ALD-deposited films guide. Lastly, we expect single-crystal films should permit extremely low-loss devices, similar to the benefits of using silicon-on-insulator wafers versus deposited polycrystalline silicon [94–96]. Single-crystal anatase or rutile may be achievable using epitaxial growth methods on a lattice-matched substrate. Alternatively, bulk rutile can be adhered to a substrate, then ground to a thickness of several microns followed by chemical mechanical polishing to produce single-crystal films. Improving film quality may increase the cost per device, however a high-quality starting material may be necessary to create devices that can exploit the unique features of TiO_2.

In Chapter 5, we demonstrated and evaluated waveguides and devices in TiO_2

using visible to telecommunications wavelengths. These devices can serve as the building blocks for integrated linear and nonlinear optical devices. For linear-optical devices, we found that amorphous TiO_2 outperforms polycrystalline anatase. Similar to thin films, reducing losses in TiO_2 waveguides is necessary for devices, particularly resonators and nonlinear interferometers. In addition to higher-quality thin films, refining structuring methods may reduce losses. Even with these challenges, there are many opportunities to demonstrate new or even well-known devices in this new material.

In Chapter 6, we explored the first nonlinear optics in anatase TiO_2 waveguides. We observed spectral broadening at wavelengths of 1565 and 794 nm, then extracted values for n_2 nonlinearities of approximately 5 and 50 times silica, respectively. From the shape of the broadened spectra around 1565 nm, we observed a delayed Raman nonlinearity that we attribute to the 144 cm^{-1} Raman line. From this, we estimated a Raman gain coefficient that is two orders of magnitude greater than silica fiber. These first nonlinear measurements are promising for TiO_2 and demonstrate a strong nonlinearity over an extended range.

There are several directions for future nonlinear studies and devices. First, a careful study of the nonlinearity of polycrystalline anatase TiO_2 may shed light on the difference in n_2 between 1565 and 794 nm. For devices, we find that losses are the dominant parasitic effect for both wavelengths studies. Once we reduce the losses, dispersion engineering will become more effective for telecommunications wavelengths (1300–1600 nm), enabling devices that utilize four-wave mixing and soliton propagation. Additionally, increasing the coupling efficiency will be necessary to make energy

efficient devices. Lastly, the Raman effect is an interesting phenomenon in TiO_2 waveguides that we may be exploit for such devices as Raman amplifiers and lasers. The small energy shift from the Raman line should also avoid many of the problems of pulse-walk off, leading to more efficient devices.

For nonlinear applications near 800 nm, the material's group velocity dispersion is very strong and normal in both bulk and thin films (–3000 ps/nm/km). This prohibits efficient four-wave mixing and soliton propagation (due to $n_2 > 0$ for near-visible wavelengths) without dispersion engineering. Our preliminary studies suggest that we cannot compensate this strong dispersion around 800 nm using nanowire dispersion engineering alone. Dispersion engineering may be possible using photon crystals, adding complimentary materials with anomalous dispersion, or utilizing higher-order modes for their unique dispersion properties.

We presented our preliminary work on photodarkening in amorphous TiO_2 in Appendix B. Whereas the linear losses of amorphous TiO_2 are superior to anatase, we have observed photodarkening of amorphous TiO_2 when films and waveguides were exposed to femtosecond light pulses around 800 nm. Understanding and avoiding photodarkening will be necessary for integrated nonlinear optical devices in amorphous TiO_2. This preliminary work suggests that the onset of photodarkening may be related to multiphoton absorption. This implies that for telecommunications wavelengths, multiphoton absorption will be a higher order process (*i.e.* four-photon instead of two-photon absorption), which may result in a higher threshold for photodarkening, allowing for measurement. Additionally, the long-term stability of amorphous films should be carefully investigated. If photodarkening can be mitigated,

nonlinear optical devices in amorphous TiO_2 would benefit from the low propagation losses.

Although there are many ways to improve upon current TiO_2 technology, perhaps the most captivating future applications will exploit the unique properties of TiO_2 in terms of its bandwidth, near-visible compatibility, and its chemical properties. The high bandwidth of TiO_2 should allow for nonlinear optical processing between widely-spaced communications bands. For example, a signal in the interconnect band around 850 nm could control a telecommunications signal around 1550 nm, all within a single chip. Many single and entangled-photon sources as well as high-efficiency photon counters operate at visible and near-visible wavelengths. Thus, the extended transparency of TiO_2 may be well suited for quantum information applications. Alternatively, the low-absorption of water for near-visible wavelengths is excellent for biological applications. Thus, TiO_2's extended wavelength compatibility and nontoxicity may also enable biophotonic applications such as chemical sensors. Lastly, TiO_2 is a very well-known photocatalyst [184, 185]. Current applications of bulk and nanoparticle TiO_2 include photo-induced water splitting and the decomposition of organic materials. The high-surface area and strong light confinement in nanostructured TiO_2 waveguides may facilitate light-controlled surface chemical reactions or self-cleaning devices. We expect further research will identify additional applications that exploit the distinctive features of TiO_2.

The work presented in this thesis lays much of the foundation for TiO_2 photonics. Although there are many ways to explore and refine the devices presented here for all-optical processing applications, TiO_2 may also enable novel applications at the

interface between the fields of integrated photonics, biology, and chemistry. We hope that future research will unlock the breadth of applications possible in this new and exciting field of titanium dioxide photonics.

Appendix A

Z-scan model for mixed two- and three- photon absorption

Several reports of modeling multiphoton absorption using the Z-scan method exist in the literature [23, 79, 186–189]. Models including single nonlinear absorption mechanisms such as pure 2PA [23], higher-order nonlinear absorption [79], and mixed multiphoton absorption [186–188] have been presented. In contrast to single absorption processes, mixed multiphoton absorption is only occasionally observed [190] and measured [191–193]. Non-idealities, such as ellipticity [189] and laser beam quality [46, 194], can obscure interpretation of mixed multiphoton data by changing the shape of the Z-scan curve. For example, beam ellipticity reduces the total signal and can cause asymmetry [189]. Meanwhile, the beam quality factor, M^2, reduces the apparent Rayleigh distance by $1/M^2$ while maintaining the waist [46, 194, 195]. Mixed multiphoton absorption is particularly sensitive to such shape changes [186–188]. These effects are not included in the previous models. Thus, we develop a mixed

multiphoton absorption model that includes these non-idealities here.

We apply an open aperture Z-scan derivation using an elliptical beam, similar to that presented in Ref. [189] and highlight the differences. We start with equation (10) for an elliptical Gaussian beam from reference [189]:

$$I_{in}\left[x,y,z,P\left(t\right)\right]=\frac{2P\left(t\right)}{\pi\, w_x\left(z\right)\, w_y\left(z\right)}\exp\left[-\frac{2x^2}{w_x^2\left(z\right)}-\frac{2y^2}{w_y^2\left(z\right)}\right]. \tag{A.1}$$

Here, z is the sample position, x and y are the transverse spatial coordinates, $P(t)$ is the instantaneous power as a function of time, and $w_x(z)$ and $w_y(z)$ are the beam widths as a function of the sample position, z. We include the beam quality factor through the width as follows:

$$w_x\left(z\right)=\sqrt{{w_{x0}}^2+\left(\frac{M_x^2\lambda_0}{\pi w_{x0}}\right)^2\left(z-z_{x0}\right)^2}. \tag{A.2}$$

In this equation, w_{x0} is the beam waist, M_{x2} is the beam quality factor [195], z_{x0} is the location of the waist and λ_0 is the center wavelength. We use a similar expression in the y-direction. We define the ellipticity by w_{x0}/w_{y0} and the astigmatism by $z_{x0}z_{y0}$. We include 3PA in the attenuation coefficient, defined for a single wavelength by $\alpha(I)=\alpha_0+\alpha_2 I+\alpha_3 I^2$. Here I is the intensity, and α_0, α_2, and α_3 are the one-, two-, and three-photon absorption coefficients, respectively. Rutile is highly transparent for 800 nm, so we set α_0 to zero. We solve the following ordinary different equation using standard numerical methods along the sample length, L:

$$\frac{dI}{dz'}=-\alpha\left(I\right)I \tag{A.3}$$

Here, z' is the position inside the sample. We solve for each point in x and y at a fixed sample position (z). Then, we integrate over x and y at the entrance and

exit of the sample to calculate the transmittance (power out normalized to power in). It should be noted that by following conventional theory [23], we do not include the effects of self-phase modulation, self-focusing (e.g. filamentation), or dispersion. We model pulsed transmittance using a Gaussian shape, given by $P(t)$, integrated over time using:

$$T\left(z\right) = \frac{\int P\left(t\right)\, T\left[z, P\left(t\right)\right] dt}{\int P\left(t\right)\; dt} = \frac{E_{out}\left(z\right)}{E_{in}} \tag{A.4}$$

In this equation, $T(z)$ is the observed energy transmittance, $T[z, P(t)]$ is the instantaneous power transmittance, and E_{in} and E_{out} are the input and output energies, respectively. We take into account the reflection from the front surface. Numerical methods require that we discretize our parameters including the x- and y-position and time. Consequently, we test for the convergence of all discretization parameters. Additionally, we find excellent agreement between this model and analytical solutions for two- [23] and three-photon absorption [79].

Unless otherwise stated, we fit each data set (multiple Z-scan traces at different powers) using this model to a single set of fit parameters, keeping all others fixed to experimental values. We fit our data using the Levenberg-Marquardt method. Our fit parameters are α_2, α_3, the average z-position of the waist (z_0) and the astigmatism. From this fit, we determine a single value for α_2 and α_3 that describes the Z-scan traces for all irradiances measured.

Appendix B

Photodarkening in amorphous TiO_2 films

Our original aim in this section was to study the nonlinear properties of our optimized TiO_2 films to correlate these results with our bulk TiO_2 measurements, however during our experiments we discovered an important phenomenon: photo-induced darkening of our amorphous TiO_2 films. Compared to bulk samples, the small interaction lengths in thin films makes studying their nonlinear properties directly using the Z-scan technique challenging. This is especially the case in anatase thin films, where the slow deposition rate limits film thickness, making them unsuitable for measurement. Nonetheless, by exploiting the comparatively high deposition rate of amorphous TiO_2, we have achieved films sufficiently thick to permit nonlinear measurement.

In this section, we summarize our observations of photodarkening in amorphous TiO_2 films. First, we present standard Z-scan measurements which first revealed photodarkening. Next, we quantify the accumulation of photodarkening using time-

dependent transmission measurements. Lastly, we present two measurements of darkened TiO_2 to measure electronic and thermal nonlinearities. We will conclude with a discussion on the implications that photodarkening may have on future devices.

B.1 Standard *Z*-scan measurements

We perform standard open and closed aperture *Z*-scan measurements using TiO_2 thin films around 800 nm. The signal to background ratio for thin film measurements is approximately given by $t_{\text{film}} n_{2\text{film}} / (t_{\text{substrate}} n_{2\text{substrate}})$. This ratio must be approximately twice the signal-to-noise ratio (SNR) of the system for proper measurement (a substrate measurement must be subtracted from the measurement with the film). For an SiO_2 substrate thickness of 500 µm, a SNR of 2%, and an estimated n_2 of 8.2×10^{-19} m^2/W, we require a minimum film of approximate 1 µm. Considering this thickness criteria, the low deposition rate of anatase makes proper measurement impractical and thus, we proceed to measure a 2.2-µm thick amorphous TiO_2 film.

B.1.1 Experimental

Our measurement parameters for amorphous TiO_2 thin-films are summarized in Table B.1. Our maximum fluence of 80 mJ/cm^2 is well below the reported damage threshold for TiO_2 films (550 mJ/cm^2 at 800 nm) [87]. Damage can produce errors that can be mistaken for *Z*-scan signal that remains even for low powers [63]. Therefore, we conduct three sequential measurements to determine the stability of the sample. First, a low-power measurement provides a pre-baseline, a high-power measurement shows the nonlinear response of the sample, and a subsequent low-power measurement

provides a post-baseline. By insuring a clean area of the sample for each set of measurements, differences between the pre- and post-baseline indicate any residual changes (i.e. damage) that occur during the high-power measurement. To further study these sample changes, we take optical images and Raman spectra of the laser spots in question.

Table B.1: Z-scan laser parameters for amorphous TiO_2.

λ_0	w_0	z_0	M^2	rep-rate	τ	energy	fluence	S
nm	(µm)	(mm)		(kHz)	(fs)	(µJ)	mJ/cm^2	
800	37	2.1	1.8	10	100	1.8	80	0.016

B.1.2 Results and analysis

We present three open-aperture Z-scan measurements using amorphous TiO_2 in Figure B.1. Comparing these three Z-scan measurements, we find that the pre- and post-baselines (low powers) are very different. We find the test measurement is asymmetrical during the scan from negative to positive z values. In addition, the post-baseline closely resembles the test measurement and even achieves a more pronounced dip. Subsequent low-power measurements taken several hours later are experimentally identical to these results. Performing a similar set of measurement with a longer pulse duration (6 ps) with the same average power produces no measurable change. This trend is consistent with a nonlinear optically induced material change.

In Figure B.2, we present three closed-aperture Z-scan measurements. The signal present in the high-power scan is distinguishable from the baselines and is likely due to nonlinear refraction in the substrate. The differences between closed-

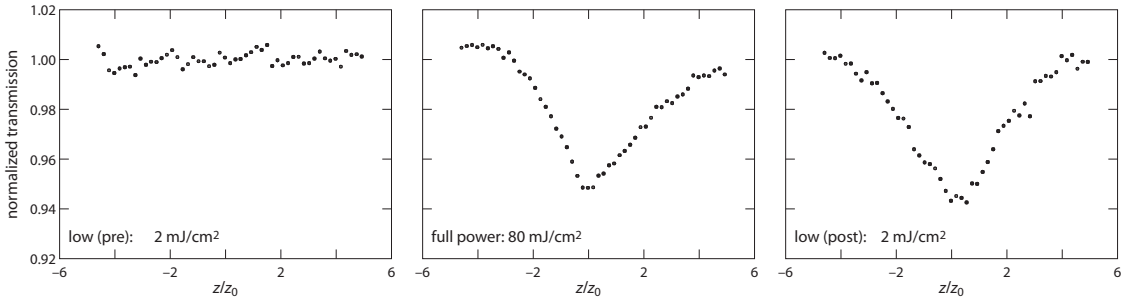

Figure B.1: Open-aperture Z-scan using a 2.2 µamorphous TiO_2 thin film. We see the low-power pre-high-power scan does not match the post-high-power scan, indicating a permanent change.

aperture pre- and post-baselines are comparable to the differences in open-aperture measurements. We note, there is an asymmetry in the post-baseline measurement, likely due to misalignment between the laser and translation directions.

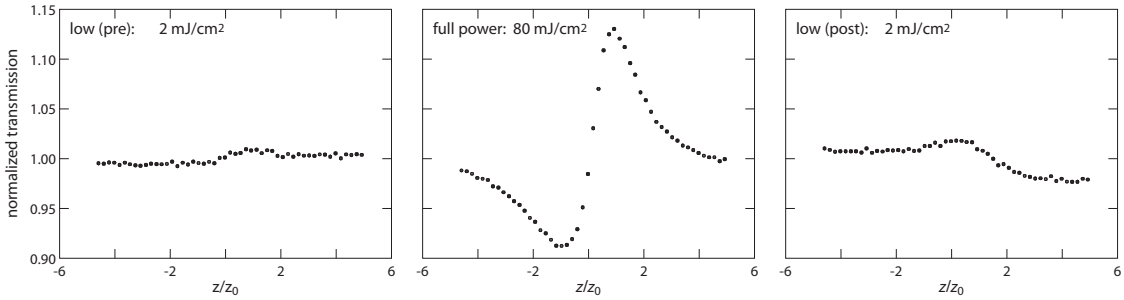

Figure B.2: Closed-aperture Z-scan using a 2.2 µamorphous TiO_2 thin film. We see the low-power pre-high-power scan does not match the post-high-power scan, indicating a permanent change.

To investigate the potential sample damage, we take optical images of the laser spots in question at a series of different fluences, shown in Figure B.3 (normal image on top, color-enhanced on bottom to show spot location). In Figure B.4, we present a Raman measurement on one of the laser spots, showing no discernible peaks. This signal is expermentally identical to measurements adjacent to, but away from the laser spot. We see that the amorphous TiO_2 film appears darker with increasing fluence

and we do not detect any significant change in crystalline phase (i.e. amorphous turning to anatase).

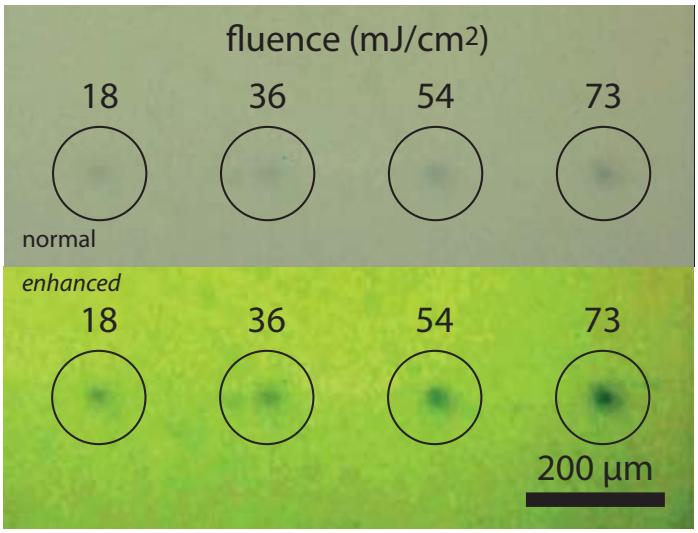

Figure B.3: Optical images of several laser-darkened spots as a function of fluence. We see that increased fluence results in stronger photodarkening. For visual clarity, we show an enhanced-contrast image on the bottom.

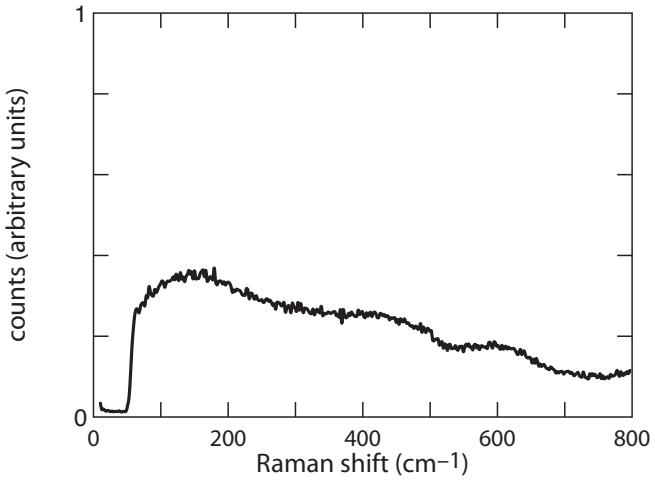

Figure B.4: Raman spectroscopy of photodarkened amorphous TiO_2 shows no discernable peaks. Measurements on and off the darkened spot are experimentally identical.

B.1.3 Discussion

The open-aperture Z-scan measurements show that as-deposited amorphous TiO_2 undergoes photodarkening. The nature of this effect is hard to discern from this data and it does not appear to be crystallization. The fluences and peak-powers used are significantly lower than reported literature values [87, 88]. However, photodarkening can still be quite significant, resulting in a 6% transmission change for a 2.2 µm film for the data shown. This transmission change corresponds to a propagation loss as high as 1200 dB/cm, therefore, understanding and mitigating photodarkening in amorphous TiO_2 is critical for devices.

The amount of photodarkening in amorphous TiO_2 is correlated with several experimental parameters. First, it is energy dependent, producing darker spots with increasing fluence. Second, it appears to be a cumulative effect, which is most evident from the post-baseline open-aperture data, which displays a deeper dip than the high-power measurement. Lastly, we only observe photodarkening when using high intensities (short pulse durations), which is consistent with a nonlinear process. Seeing how the darkening results in linear absorption of the pump, such a multiphoton process may initiate photodarkening. If this is the case, operating at longer wavelengths will increase the number of required pump photons, increasing the threshold for photodarkening. Cumulative photodarkening can drastically impact the functionality and reliability of devices and is therefore important to study.

B.2 Time-dependent photodarkening

Photodarkening in amorphous TiO_2 thin films appears to be a cumulative effect that can result in strong linear absorption. In this section, we observe the photodarkening of amorphous TiO_2 as a function of time and pulse energy to understand how this effect accumulates to determine if a parameter space exists that either avoids or stabilizes photodarkening.

B.2.1 Experiment

We quantify the rate and energy dependence of photodarkening by performing time-dependent measurement using 100-fs pulses around 800 nm at various pulse energies. We use the same laser parameters in Table B.1. We start with a clean amorphous TiO_2 sample with a thickness of 2.2 µm on a glass substrate. We record the transmission of our 800-nm laser through the sample as a function of time.

B.2.2 Results and analysis

We present the time dependent transmission in Figure B.5 for several pulse energies. We observe a stronger change in transmission for higher pulse energies and longer times. We measure a maximum transmission change of 22% in a 2.2 µm film after a total exposure time of 4000 seconds (4×10^7 shots, 73 mJ/cm^2).

The time-dependent transmission change has two distinct features, first we see a sharp decrease for within the first 500 seconds (5×10^6 shots). Second, we see a slow decline in transmission for timescales longer than 1000 second (1×10^7 shots) that does not appear to saturate over 4000 seconds. We fit each data set to an empirical

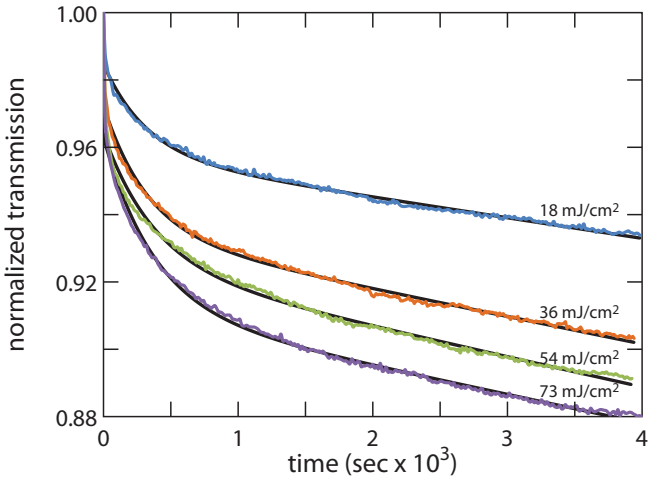

Figure B.5: Time-dependent photodarkening of amorphous TiO_2 at several fluences. We fit this to a bi-exponential function (black lines).

model that takes form of a biexponential:

$$T(t) = A_1(P)\, e^{\frac{-t}{\tau_1}} + A_1(P)\, e^{\frac{-t}{\tau_2}}, \tag{B.1}$$

as shown in Figure B.5. Using this model, we extract two time-scales for photodarkening. We find an average short time-scale of $\tau_1 = 350$ seconds (3.5×10^6 shots) and an average long timescale of $\tau_2 = 32$ hours (1×10^9 shots). For increasing pulse energies, we find $A_1(P)$ increases monotonically while $A_2(P)$ decreases monotonically. In our fitting the average $A_1(P)$ was 4% and the average $A_2(P)$ was 90%. These values should total 100%, however the uncertainty in the start time may effect this value.

B.2.3 Discussion

Photodarkening in amorphous TiO_2 around 800 nm appears to have two time-scales. The shortest time-scale is 350 seconds, which is responsible for a maximum change of 5% for the fluences considered here. Darkening attributed to this short time-scale

increases with increasing pulse energy $A_1(P)$. This is consistent with multiphoton absorption, although we cannot determine the order of the process (*i.e* two- versus three-photon absorption) from the current data. Meanwhile, the long-timescale process decreases when we increase the pulse energy $A_2(P)$.

Photodarkening may be related to a surface chemical reaction. TiO_2 is well known as a photocatalyst, however, such processes require photons which can bridge the bandgap (3.25 eV, 381 nm). Instead of the linear absorption, this may be due to nonlinear absorption (*i.e.* three-photon absorption) that initiates the surface reaction. Subsequently, the products of this reaction may linearly absorption pump photons. This strong linear absorption then would lead to local heating, which may then thermally drive this or a different chemical reaction. Future research should try to resolve which, if any, chemical reaction may be occurring at the surface of, or within the film.

Given these two processes, it is difficult to find a pulse energy that is sufficiently large enough to enable nonlinear measurement while inhibiting photodarkening under current experimental conditions. However, we do find that for long-time-scales, the photodarkening saturates, which allows us to measure nonlinearities in photodarkened TiO_2 films.

B.3 Thermal nonlinearities in photodarkened amorphous TiO_2

From the previous section, we have seen how photodarkening is a significant effect in amorphous TiO_2 that saturates with sufficient exposure. Using this stability as a guide, we now perform two sets of measurements on photodarkened amorphous TiO_2 around 800 nm, the first to measure electronic nonlinearities, the second to measure thermal nonlinearities. In the first measurement, we perform closed-aperture Z-scan with a repetition rate of 10 kHz to avoid thermal nonlinearities. By comparing samples with and without the TiO_2 film, we determine the strength of the electronic nonlinearity. For the second experiment, we perform thermally managed closed-aperture Z-scan measurements of photodarkened films using a repetition rate of 250 kHz. This chopper-technique quantifies thermal nonlinearities in our samples and allows us to resolve the effective sign of dn/dT.

B.3.1 Experiment

We perform two sets of closed-aperture Z-scan measurements using 2.2 µm-thick photodarkened amorphous TiO_2 on 0.5-mm fused silica substrates using the laser parameters listed in Table B.1. In the first measurement, use a repetition rate of 10 kHz and compare measurements with a thin film to substrate-only measurements. We guarantee our sample is sufficiently darkened and aligned with our measurement by conducting multiple Z-scan measurements until we observe reproducible results. Additionally, the reflection from the front surface changes with and without the film

alters the power within the substrate and changes the background signal. Therefore, we insure that the same energy is within the substrate by adjusting the power so that we measure the same average power after the sample.

In the second set of measurements we increase the repetition rate to 250 kHz and perform thermally managed Z-scan. Thermally managed Z-scan uses an optical chopper to provide a burst of pulses, followed by dead-time to allow the sample to reach thermal equilibrium. Our chopper has a duty cycle of 6% (4 ms on, 67 ms off). By comparing Z-scan measurements using data from the beginning and end of the window, we infer the sign and strength of the effective thermal nonlinearity. In addition, observing individual time-traces allows us to estimate the time-scale of the thermal nonlinearity.

B.3.2 Results and analysis

We present two closed aperture Z-scan measurements using a repetition rate of 10 kHz in Figure B.6. We find that adding the film does not produce a change beyond our estimated experimental uncertainty ($\pm 2\%$). We note that the largest source of uncertainty comes from matching the power with and without the thin film.

We present two thermally managed Z-scan curves for darkened amorphous TiO_2 in Figure B.7. We see at the end of the 4-ms window, the relative Z-scan signal increases, indicating a positive thermal nonlinearity (dn/dT) within the film-substrate system. This effect is quite large, resulting in a ΔT which increases from 15% to 21%.

In Figure B.8 we present time traces for pre- and post- focal positions corresponding to the minimum and maximum transmission values (respectively). Using

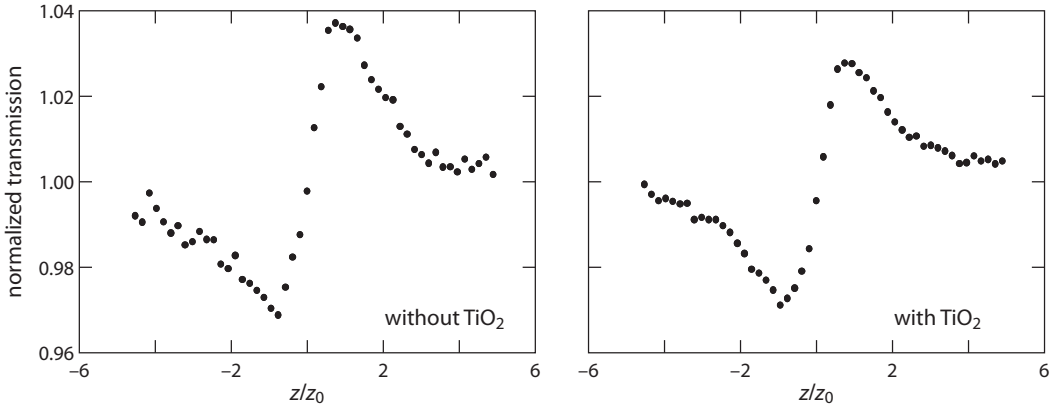

Figure B.6: Closed-aperture Z-scan of the substrate (left) and fully darkened amorphous TiO_2 and substrate (right) at a repetition rate of 10 kHz.

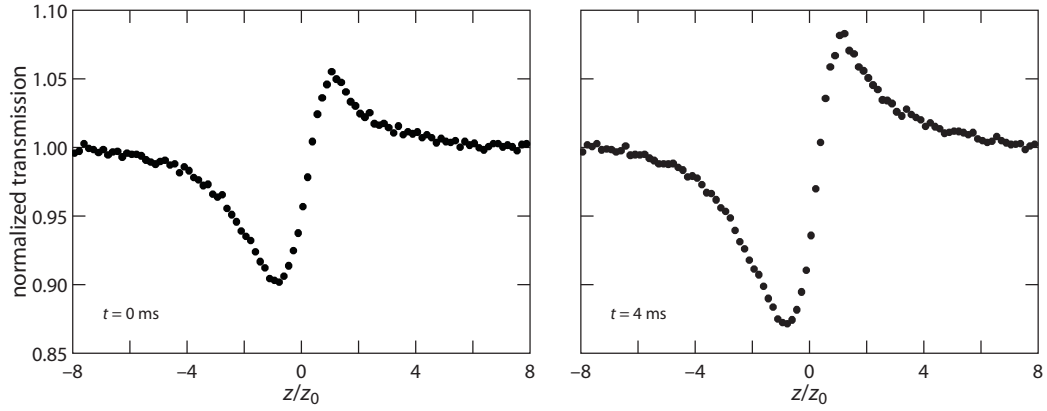

Figure B.7: Thermally managed Z-scan at the beginning ($t = 0$ms) and end ($t = 4$ms) of the chopper window. We attribute the differences between these plots to thermal nonlinearities.

this data, we fit to an exponential and find a response time of 0.6 ms in both cases.

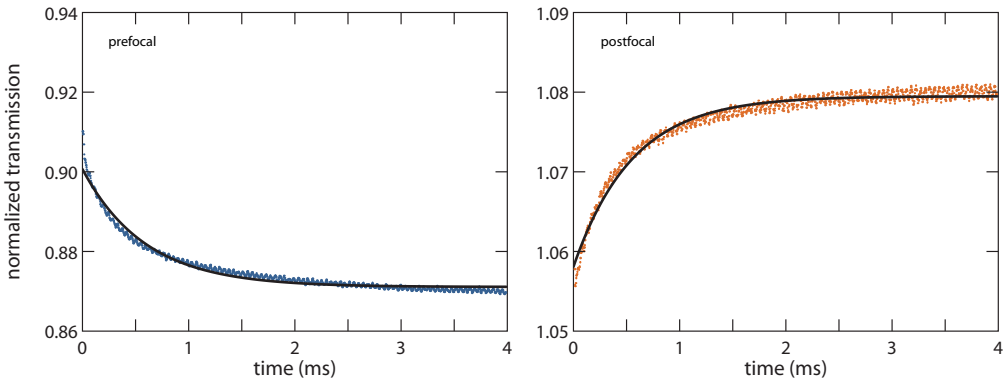

Figure B.8: Thermally managed Z-scan time-traces during open-chopper windows at z locations corresponding to the prefocal minimum (left) and the postfocal maximum (right) transmission.

B.3.3 Discussion

In this section, we look into the electron and thermal nonlinearities in thin films of amorphous TiO_2. We were unable to measure an electronic nonlinearity above the experimental uncertainty, due to power-matching considerations. To resolve the electronic nonlinearity, future experiments could utilize a dual-arm Z-scan technique [196, 197]. In this technique, two matching substrates (with and without the thin film) are measured simultaneously to remove the effects of the substrate.

Whereas we do not observe clear signal from an electronic nonlinearity, we measure a thermal nonlinearity that is both strong and positive. Given the size of the thermal signal, we do not expect that this effect is purely due to the film for two reasons. First, dn/dT is negative for bulk rutile TiO_2 [49] and positive for silica [198]. Second, the magnitude of the change is very large, which would produce a large value of dn/dT in the TiO_2 layer. Although photodarkened amorphous TiO_2 may be

sufficiently different than rutile, the sign of dn/dT suggests that either the thermal nonlinearity is positive for the film or (more likely) weak enough to be masked by the thermal nonlinearity in the silica substrate. Instead, it is reasonable that the additional absorption caused by the film is diffusing into the silica and the resulting refractive index change is purely due to the substrate.

The nonlinear signal that we observe in photodarkened amorphous TiO_2 is significant and can lead to a strong thermal effect which can either be mitigated or exploited. For many devices, photodarkening may be a mechanism for device failure both within the TiO_2 and within neighbouring components on the same chip. On the other hand, if this thermal nonliearity leads to local heating, photodarkened TiO_2 may be a component used to heat and thermally tune nearby components using an external laser.

B.4 Conclusion

In this chapter, we have presented several preliminary observation of photodarkening in amorphous TiO_2 thin-films. We find that the photodarkening is an important process, resulting in effective losses as high as 1200 dB/cm. The effect appears to be nonlinear in nature, it increases with increasing pulse energy and could not be observed with longer pulse durations of 6 ps. Darkening has two time-scales, one of only a few minutes while the other is 32 hours. There are several further experiments that can be performed to determine the source and laser parameter space for photodarkening. In particular, future work should look into the microscopic morphology of laser spots. In addition, TiO_2 is a well known photocatalyist, therefore, this phe-

nomenon may be related to a chemical reaction that occurs within the laser spot. The strength of this photodarkening severely limits potential devices using this material, although some applications may benefit. Understanding the cause of photodarkening may reveal a way to mitigate this effect, which would enable nonlinear devices that can exploit the very low propagation losses we have demonstrated in amorphous TiO_2.

Appendix C

Simulation of TiO_2-based Sagnac interferometers

Now that we have developed TiO_2 as a novel integrated material for all-optical processing, we will explore one way to enable light-by-light modulation, switching, and logics: using Sagnac interferometers. In this section, we will look at Sagnac interferometers as a prototype for all-optical modulation, switching, and logic. We will begin by developing a simple understanding of these nonlinear devices, then describe how to form them into simple all-optical logic circuits. Our analysis will be restricted to self-switching that utilizes the self-phase modulation, for simplicity. Similar results can be derived for cross-phase modulation [36]. Lastly, we will present simulation results using typical material parameters for TiO_2 and highlight how to design such devices for all-optical logic applications.

C.1 Sagnac interferometers

A Sagnac interferometer, as shown in Figure C.1, is an excellent configuration to demonstrate all-optical modulation, switching, and logic. These interferometers are perhaps the simplest nonlinear interferometer configuration achievable in a nanowire device. These symmetric, self-balancing interferometers utilize counter-propagating waves and are therefore stable, immune to temperature gradients, and easy to work with [41,199–201]. Sagnac interferometers provide a tunable balance between switching energy and device size simply by changing path lengths. These devices are non-resonant and therefore can sustain extremely high bit-rates [202]. Although we will only consider all-optical switching and logic as a final application, Sagnac interferometers are versatile, enabling operations including multiplexing and demultiplexing, switching, logic [65], and signal regeneration [203].

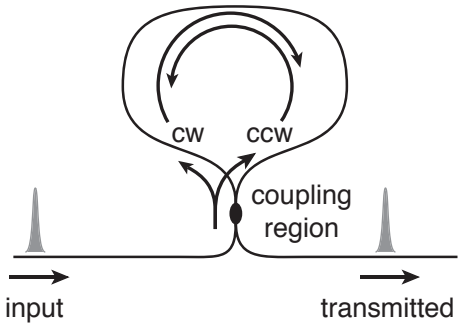

Figure C.1: Diagram of a Sagnac interferometer showing the input pulse, the coupling region, the clockwise and counter-clockwise paths as well as the transmitted pulse [204] [36].

To understand how a Sagnac interferometer works, we can consider a nonlinear interferometer using a quasi-continuous-wave pulse in an interferometer. We form

these by making a loop as shown in Figure C.1, then input light into the waveguide on the left of the loop and observe the output in the waveguide to the right.

The linear version of a Sagnac interferometer acts as a mirror [36]. A pulse enters the input in Figure C.1, and then encounters a directional coupler. A fraction of the pulse energy couples into the adjacent waveguide, adding a $\pi/2$ phase-shift, then it propagates around the loop in the counter-clockwise direction. The other fraction remains within the same waveguide (no phase-shift), and proceeds in the clockwise direction. These two pulses collect identical amounts of phase as they traverse the loop and then recombine at the directional coupler. The output is a summation of the counter-clockwise pulse and the clockwise pulse. The counter-clockwise pulse picks up a second $\pi/2$ phase-shift at the directional coupler, resulting in a total phase shift of π relative to the clockwise pulse at the output. This phase-shift results in destructive interference at the output. Meanwhile, constructive interference occurs on the input-side and the pulse is reflected back toward input, creating a mirror. For a 50-50 directional coupler, the Sagnac interferometer acts as a "perfect mirror". If the ratio is different from 50-50, part of the light will reach the output.

A Sagnac interferometer can be made nonlinear, sometimes referred to as a *nonlinear optical loop mirror* (NOLM) [42, 65, 200, 201, 205–213], by forming the loop using a nonlinear optical material. When traversing the loop, the clockwise and counter-clockwise pulses collect both linear and nonlinear phase. Both pulses collect identical linear phase. If the coupling ratio is anything other than 50-50, there will be a nonlinear phase difference between the pulses, causing power-dependent interference at the output. Just as we observe fringes in a Michelson interferometer when we

change one of the path lengths, we observe power-dependent fringes in a Sagnac interferometer. These fringes form a basic, all-optical modulator that we can extend to perform all-optical switching and logic applications. The speed of these devices is only limited by the response time of the nonlinearity, although a delay in the device will occur as the pulses propagate. For a pure electronic nonlinearity, this response is on the order of several femtoseconds [16], making such a device compatible with Tb/s operations [202].

C.2 Analysis of a Sagnac interferometer

The operation of a nonlinear Sagnac interferometer can be quite complex if we include all possible effects to correctly model pulse propagation; however, we can get a very good sense of how one works if we consider a quasi-continuous-wave pulse [36]. Essentially, we modulate a carrier wave with a square envelope, simplifying the analysis by using a continuous-wave approximation using peak-powers, (not pulse energies). For this approximation, we ignore dispersion and temporal phenomena, such as spectral broadening. For simplicity, we will also ignore cross-phase modulation between the counter-propagating pulses. This effect is negligible if the pulse durations are much shorter than the loop-propagation time. In the continuous-wave regime, cross-phase modulation is the dominant source of nonlinear phase, however the results are identical [36].

Analysis in the quasi-continuous-wave regime first requires us to determine the power that is traveling in the clockwise versus the counter-clockwise directions. We define a coupling parameter ρ that represents the fraction of the power that stays

within the input leg of the directional coupler and traverses the loop in the clockwise-direction. Thus, ρP_{in} is the clockwise power in the loop, corresponding to an electric field of magnitude $\sqrt{\rho}E_{in}$, for an input power of P_{in} and input electric field of E_{in}. Similarly, in the counter-clockwise direction, the power and electric field magnitudes are $(1-\rho)\,P_{in}$ and $\sqrt{1-\rho}E_{in}$, respectively. When we build our devices, we can change ρ within the directional coupler by adjusting the separation between the two-waveguides and/or adjusting the distance of the parallel section (described using coupled-mode theory [14]).

Now, we determine the total phase accumulated in both directions, which requires that we define the length of the loop, L. We consider three sources of phase: from the directional coupler, linear propagation, and nonlinear propagation. Within the directional coupler, the power transferred from the input pulse to the counter-clockwise pulse receives a phase shift of $\pi/2$. This phase shift occurs a second time when the counter-clockwise pulse is transferred to the output, leading to total phase shift of π for the counter-clockwise pulse only (the clockwise pulse remains in the original waveguide). Combining this phase-shift with the linear and nonlinear phase from equation (2.135), we obtain the total phase at the output for the clockwise and counter-clockwise pulses:

$$\varphi_{CW} = \varphi_L + \varphi_{CWNL} = \beta L + \gamma\left(\omega\right) L\rho P_{in}, \text{ and} \tag{C.1}$$

$$\varphi_{CCW} = \varphi_L + \varphi_{CCWNL} + \varphi_{DC} = \beta L + \gamma\left(\omega\right) L\left(1-\rho\right) P_{in} + 2\left(\pi/2\right). \tag{C.2}$$

Here, φ_{CW} is the total phase in the clockwise direction at the output, made up of a linear and a nonlinear contribution, φ_L and φ_{CWNL}, respectively. In the counter-clockwise direction, these terms are φ_{CCW}, φ_L, and φ_{CCWNL}, respectively. Addition-

ally, there is a phase shift φ_{DC} from the directional coupler in the counter-clockwise direction.

Lastly, we sum the electric fields at the output to determine the transmission. The magnitude of the electric field for the clockwise pulse becomes ρE_{in} at the output, having picked up an additional factor of $\sqrt{\rho}$ from the directional coupler. Similarly, the magnitude of the electric field for the counter-clockwise pulse is $(1-\rho)\,E_{in}$ at the output. The electric field at the output is:

$$E_{out} = \rho E_{in} e^{i\varphi_{CW}} + (1-\rho)\,E_{in} e^{i\varphi_{CCW}} = \left(\rho E_{in} e^{i\varphi_{CWNL}} - (1-\rho)\,E_{in} e^{i\varphi_{CCWNL}}\right) e^{i\varphi_L}. \tag{C.3}$$

We can solve this equation for the transmission to show:

$$T = \frac{|E_{out}|^2}{|E_{in}|^2} = 1 - 2\rho\,(1-\rho)\left\{1 + \cos\left[(1-2\rho)\,\gamma P_{in} L\right]\right\}. \tag{C.4}$$

From this equation, we see that if ρ is 0.5, the transmission is zero and therefore, we require that $\rho \neq 0.5$ to achieve modulation.

We can understand the nature of this device by plotting the output power, $P_{in}T$, as a function of the input power, as shown in Figure C.2. We also note that we can change the spacing of the fringes relative to the input power, using the coupling parameter. For small values of ρ, the fringes are closely spaced in power and the modulation is minimal. As the coupling parameter ρ approaches 0.5, the first minimum requires higher powers while the modulation increases.

Although changing the coupling parameters is straightforward experimentally, simply making longer devices is not always possible and requires that we consider both linear and nonlinear losses. Linear losses, as we have seen in previously, effectively

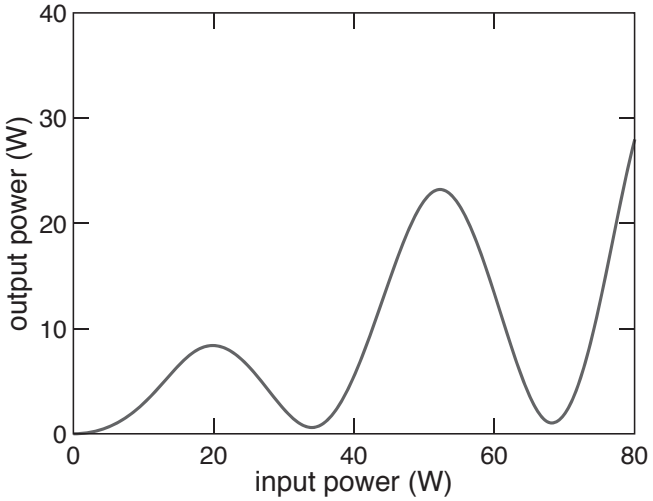

Figure C.2: Transmitted power as a function of input power for a typical nonlinear Sagnac interferometer [204] [36].

limit the amount of nonlinear phase that we can accumulate. Similarly, two-photon absorption limits the highest power that we can effectively use.

In addition to losses, a real device must include the effects of the pulse shape as well as dispersion. When moving to pulsed operation without dispersion, the phase accumulated will be different across the pulse. The non-uniform phase will cause the peak of the pulse to switch before the front and back, creating pulse distortions, and lowering the modulation. With normal dispersion, a similar effect will occur. Even with all of these complications, by exploiting nonlinear optics in nano-scale waveguides, significant modulation with minimal pulse distortion is possible using solitons, as has been shown in fiber [41].

C.3 All-optical switching

In all-optical switching devices, the power ratio between "on" and "off" states, as well as the power required for full modulation, are important design considerations. The ratio of the "off" to the "on" power is the *depth of modulation* or *extinction ratio* [13]. We can approximate the depth of modulation for our Sagnac interferometer by evaluating equation (C.4) when the argument of the cosine function is equal to π (the approximate location of the first maximum) and 2π (the approximate location of the first minimum). The extinction ratio is approximately given by:

$$\frac{P_{\max}}{P_{\min}} \approx \frac{1}{2(1-2\rho)^2}. \tag{C.5}$$

For example, we find that the extinction ratio reaches 3 dB when $\rho = 0.25$ and 17 dB when $\rho = 0.45$.

Stronger modulation requires higher input powers or longer length devices; therefore, we consider this trade-off by observing the power required to reach the first minimum, given by:

$$P_{\text{switch}} \approx \frac{2\pi}{(1-2\rho)\,L\gamma}. \tag{C.6}$$

As we approach a coupling ratio of 0.5, the required power for full switching increases as $(1-2\rho)^{-1}$. Comparing this expression to equation (C.5), as ρ approaches 0.5, the extinction ratio improves as $(1-2\rho)^{-2}$. Therefore, we can achieve a substantially increased extinction ratio for only a moderate operational power increase. In addition, we can design a longer device to offset the additional power requirements.

C.4 All-optical logic

Now we show how to form all-optical logic gates using a nonlinear Sagnac interferometer. The nonlinear optical loop mirror serves as a prototypical all-optical logic gate for future communications systems. These and similar devices have been shown using bulk fiber [65, 202, 214, 215] as well as using active nonlinear devices [203]. Our configuration begins by adding two (or more) inputs before our Sagnac interferometer, as showing in FigureC.3 (top). For each logical operation, we must define logical 1's and 0's for both the input and the output.

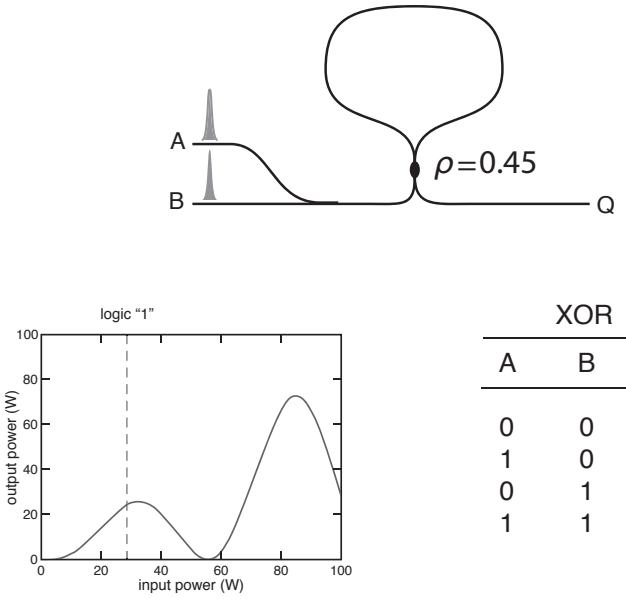

XOR

A	B	Q
0	0	0
1	0	1
0	1	1
1	1	0

Figure C.3: All-optical XOR logic gate. Physical layout (top), input versus output for the Sagnac interferometer, showing logical 0's and 1's (bottom left), truth table for the resulting XOR gate (bottom right) [204].

As a first example, we will explore an exclusive-OR gate, having the truth table shown in Figure C.3 (bottom right). We observe the power-dependent transmission plot in Figure C.3 (bottom left), using a coupling ratio of 0.45 to define our logical 1's

and 0's. On the input, a logical 1 has an input power greater of 28 W. On the output, we define a logical 1 as an output power greater than 18 W. Using the Sagnac's transmission function, we can construct the truth table. If neither A nor B is present at the input, the device produces a logical 0. If only input A or input B is present, the output is close to the first maximum, resulting in a logical 1. If both A and B are present at the input, the device produces a logical 0. This demonstrates the truth table for an XOR gate.

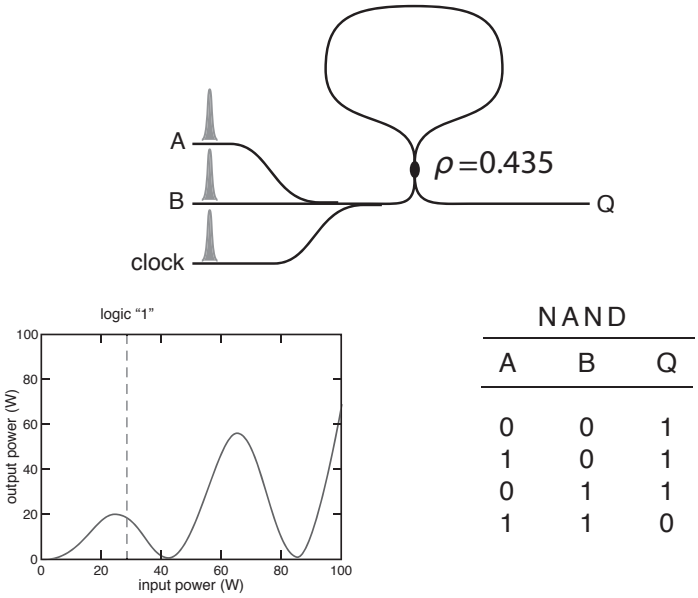

NAND

A	B	Q
0	0	1
1	0	1
0	1	1
1	1	0

Figure C.4: All-optical NAND logic gate. Physical layout (top), input versus output for the Sagnac interferometer, showing logical 0's and 1's (bottom left), truth table for the resulting NAND gate (bottom right) [204].

We can construct other gates by adjusting the coupling coefficient, and possibly adding a clock signal. We are particularly interested in constructing a "universal" logic gate. These gates can be configured together to form the entire set of Boolean logic operations. One particular universal logic gate we can construct using a Sagnac

interferometer is a NAND gate. A NAND gate has the truth table shown in Figure C.4 (bottom right). As we can see, this gate is more difficult to create than an XOR-gate because we require a logical 1 when there is no input. Therefore, we add an additional input to our Sagnac interferometer and deliver a clock pulse with every set of input pulses. By adjusting our coupling parameter to 0.435, we find that for no inputs in either A nor B, the clock pulse produces a logical 1 at the output. For an input in either A or B, the output of the device is around 15 W, constituting a logical 1 at the output. Now, if both A and B are present, the device reaches the second minimum, resulting in a logical 0. This prototypical device shows how we can construct an all-optical NAND gate and thereby create all other Boolean logic gates.

C.5 Pulse propagation in a nonlinear Sagnac interferometer

These simple continuous wave results provide a clear example of all-optical modulation in a nonlinear Sagnac interferometer. However, once we include additional effects, such as dispersion, we quickly see that full-modulation may not be possible even in a lossless loop as shown in Figure C.5. In this section, we conduct a series of simulations to determine the parameter range where good modulation is possible in a Sagnac interferometer with anomalous dispersion.

We simulate nonlinear Sagnac interferometers with different amount of loss and dispersion to understand how to balance these parameters in a real device. We utilize a nonlinear-pulse propagation simulation that includes the effects of self-phase mod-

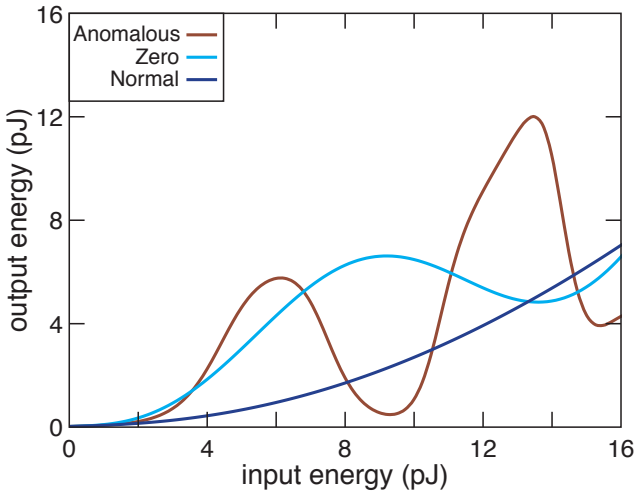

Figure C.5: Simulated Sagnac transmission for a lossless loop and different types of group-velocity dispersion. We use a 100-fs pulse around 1550 nm, a 6-cm long loop, and GVD parameters of ± 300 fs^2/mm and zero. We see that only anomalous dispersion produces significant modulation.

ulation, group-velocity dispersion and loss. To understand the most general case, we perform these simulation by comparing the physical length to normalized parameters including the dispersion length:

$$L_D = \frac{T_0^2}{|\beta_2|}, \tag{C.7}$$

the loss length:

$$L_{loss} = \frac{1}{\alpha_0}, \tag{C.8}$$

and the nonlinear length:

$$L_{NL} = \frac{1}{\gamma P_0}. \tag{C.9}$$

We quickly realize that we will be sweeping the input pulse energy, and thus the nonlinear length is not fixed. Instead, we must rescale our pulse energy. We use:

$$\Delta\phi_{NL} = 2\pi N, \tag{C.10}$$

where N is the number of 2π phase-shifts (corresponding to the minima in the continuous-wave solution). Using this expression and assuming a Gaussian pulse shape, the pulse energies used as input into our simulation are given by:

$$E_p = \frac{2\pi T_0}{\gamma L\,(1-2\rho)\,0.88} N. \tag{C.11}$$

Using these parameters, our simulation takes the input pulse and splits it coherently into two separate pulse propagation simulations (based on the coupling parameter, ρ). Each simulation is run using the nonlinear Schroedinger equation, then the pulses are combined and we calculate output energy.

We plot a series of simulations for different anomalous dispersion and loss lengths with a fixed coupling parameter ($\rho = 0.4$) in Figure C.6. The diagonal line represents the maximum transmission for the losses used in the calculation. We see improved switching using strong anomalous dispersion (short dispersion lengths) as well as for the lowest losses (long loss lengths). Additionally, we see evidence of power leakage in some of the simulations which are unable to fully modulate. Only the upper left-hand three plots show significant modulation (showing at least two maxima) due to the flat phase associated with soliton propagation.

We see two conclusions from this analysis. First, for full modulation, the dispersion length should be equal to or less than the loss length (shown by the upper left-hand plots in Figure C.6. Second, the loss length should be longer than or equal to physical length. By adhering to these guidelines in real devices, a fully modulating Sagnac is possible.

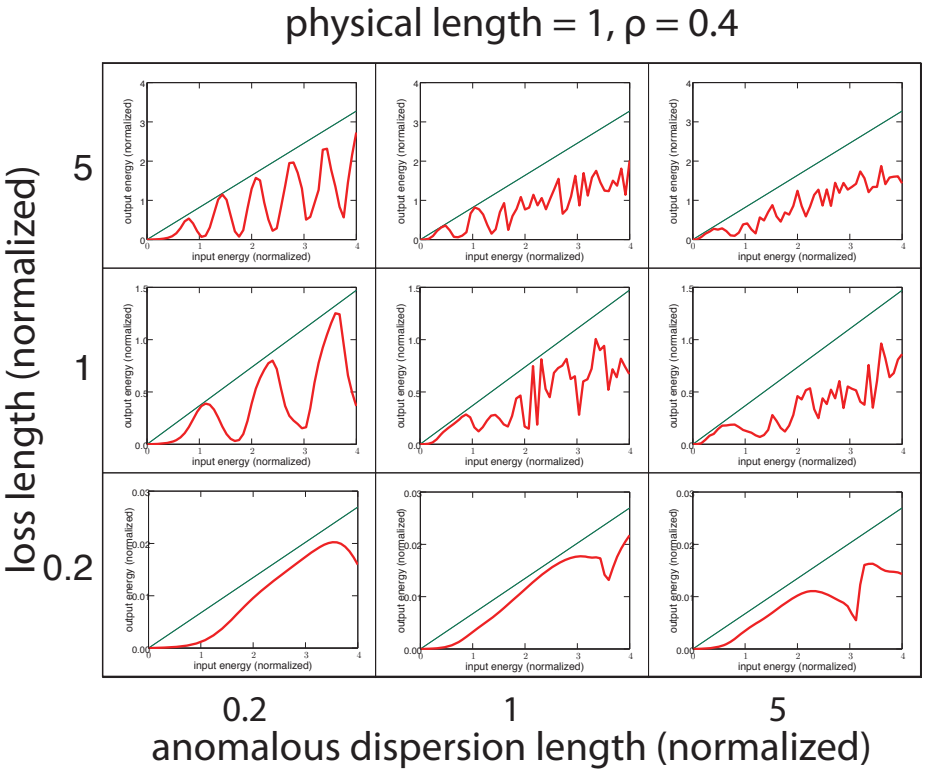

Figure C.6: Simulated Sagnac transmission for several combinations of loss lengths and anomalous dispersion lengths. We see that both reducing losses (resulting in a higher loss length) and increasing the amount of anomalous dispersion (shorter dispersion length) improves switching characteristics. We note that the noise at high pulse energies is a result of energy loss in the simulation.

C.6 All-optical switching in TiO_2 waveguides

Having developed the guidelines for full modulation in a Sagnac interferometer, we now define specific goals for future Sagnac interferometers in TiO_2 for operation around 1550 nm. Our current results show that we can achieve losses as low as 3 dB/cm, which corresponds to a loss length of 14 mm at 1550 nm. Our simulation results show that TiO_2 nanowire waveguides can attain anomalous dispersion as strong as -300 fs^2/mm (250 ps/nm/km) resulting in a loss length of 33 mm. If we assume a 100 fs pulse, this results in a dispersion length of 31 mm. Using this parameter set as a guide, we show three ways to achieve full modulation.

First, improving losses down to roughly 1 dB/cm will result in loss length of 43 mm. This will result in a functioning device, however the loop length should be roughly 4 cm. In terms of fabrication on a single chip, this length would require some variety of coiled structure. Therefore, minimizing bending losses will be an additional challenge, beyond simply reducing the waveguide losses. Although this device would fully modulate, the length of the device would be considerably large.

Second, increasing anomalous dispersion to -600 ps/nm/km would result in a dispersion length of 16 mm, thus approximately matching the loss length. Our current simulation results have exclusively explored rectangular nanowire waveguides, therefore, alternative geometries or photonic crystals may be able to achieve stronger anomalous dispersion. However, additional complications when fabricating alternative waveguide geometries can increases the losses substantially (notably in photonic crystals).

Lastly, using even shorter pulse duration (below 70 fs) would decrease the dis-

persion length to coincide with the loss length. This may seem like the simplest method to first observe all-optical switching in a TiO_2 waveguide, however, the additional bandwidth poses a new challenge. The bandwidth of a 70-fs pulse around 1550 nm is 50 nm (for a Gaussian pulse). For shorter pulses (which would enable significantly smaller devices) require even more bandwidth, therefore, common directional couplers begin to show signs of their frequency dependence.

Perhaps to best way to approach the problem of full modulation in a TiO_2 nanowire devices is to simultaneously make slight improvements using all three approaches. Reducing losses is necessary for many other applications, additionally, stronger anomalous dispersion may be well within reach, either by optimizing geometry or by pairing the device with a shorter pulsed laser. If we can make several small improvements, a fully modulating TiO_2 Sagnac interferometer may be well within reach.

C.7 Conclusion

We have explored Sagnac interferometers for all-optical modulation, switching, and logic for use with TiO_2 nanowire devices. These unique non-resonant devices show many advantages for all-optical processing in terms of speed and stability. We have developed a basic understanding of these devices using simple theory and provided examples of how to implement switching and logic devices. Lastly, we have conducted several simulation with realistic parameters to show which combination of physical parameters (loss, dispersion, and loop-length) results in full modulation and applied these principles to pinpoint the challenges for future TiO_2 devices. By further de-

veloping TiO_2, we believe that an integrated TiO_2 Sagnac interferometer can form the basic building block of an integrated all-optical logic device for ultrafast signal processing.

Bibliography

[1] R. Essiambre and R. W. Tkach, Proc. IEEE **100**, 1035 (2012).

[2] K. F. MacDonald, Z. L. Samson, M. I. Stockman, and N. I. Zheludev, Nature Photon. **3**, 55 (2009).

[3] M. Galili, J. Xu, H. C. Mulvad, L. K. Oxenlowe, A. T. Clausen, P. Jeppesen, B. Luther-Davies, S. Madden, A. Rode, D.-Y. Choi, M. Pelusi, F. Luan, and B. J. Eggleton, Opt. Express **17**, 2182 (2009).

[4] B. Corcoran, M. D. Pelusi, C. Monat, J. Li, L. O'Faolain, T. F. Krauss, and B. J. Eggleton, Opt. Lett. **36**, 1728 (2011).

[5] Y. Henry Wen, O. Kuzucu, T. Hou, M. Lipson, and A. L. Gaeta, Opt. Lett. **36**, 1413 (2011).

[6] G. I. Stegeman and W. E. Torruellas, Philos. Trans. R. Soc. London, Ser. A **354**, 745 (1996).

[7] Q. Lin, J. Zhang, G. Piredda, R. W. Boyd, P. M. Fauchet, and G. P. Agrawal, Appl. Phys. Lett. **91**, (2007).

[8] N. Hô, J. M. Laniel, R. al Vallée, and A. Villeneuve, Opt. Lett. **28**, 965 (2003).

[9] E. W. Van Stryland, M. A. Woodall, H. Vanherzeele, and M. J. Soileau, Opt. Lett. **10**, 490 (1985).

[10] M. Sheik-Bahae, D. J. Hagan, and E. W. Van Stryland, Phys. Rev. Lett. **65**, 96 (1990).

[11] C. C. Evans, J. D. B. Bradley, E. A. Martì-Panameño, and E. Mazur, Opt. Express **20**, 3118 (2012).

[12] D. J. Griffiths, *Introduction to electrodynamics*, 3rd ed. (Prentice Hall, Upper Saddler River, NJ, 1999).

[13] R. G. Hunsperger, *Integrated optics: theory and technology*, 6th ed. (Springer, New York, 2009).

[14] H. A. Haus, *Waves and fields in optoelectronics*, (Prentice-Hall, Englewood Cliffs, NJ, 1984).

[15] Newport Corporation, Application note: Prism Compressor for Ultrashort Laser Pulses, 2006.

[16] R. W. Boyd, *Nonlinear optics*, 3rd ed. (Academic Press, Boston, 2008).

[17] J. M. Chen, J. R. Bower, C. S. Wang, and C. H. Lee, Opt. Commun. **9**, 132 (1973).

[18] Y. R. Shen, Nature **337**, 519 (1989).

[19] R. W. Boyd, *Nonlinear optics*, 2nd ed. (Academic Press, San Diego, CA, 2003).

[20] G. P. Agrawal, *Nonlinear fiber optics*, 4th ed. (Elsevier / Academic Press, Boston, 2007).

[21] D. Milam, Appl. Opt. **37**, 546 (1998).

[22] M. Sheik-Bahae, D. C. Hutchings, D. J. Hagan, and E. W. Van Stryland, IEEE J. Quantum. Electron. **27**, 1296 (1991).

[23] M. Sheik-Bahae, A. A. Said, T. H. Wei, D. J. Hagan, and E. W. Van Stryland, IEEE J. Quantum. Electron. **26**, 760 (1990).

[24] E. W. Van Stryland and M. Sheik-Bahae, in *Characterization techniques and tabulations for organic nonlinear optical materials*, edited by Mark G. Kuzyk and Carl William Dirk (Marcel Dekker, New York, 1998).

[25] G. I. Stegeman, E. M. Wright, N. Finlayson, R. Zanoni, and C. T. Seaton, J. Lightwave Technol. **6**, 953 (1988).

[26] G. Stegeman and E. Wright, Opt. Quant. Electron. **22**, 95 (1990).

[27] G. I. Stegeman, Proc. SPIE **1852**, 75 (1993).

[28] V. R. Almeida, C. A. Barrios, R. R. Panepucci, M. Lipson, M. A. Foster, D. G. Ouzounov, and A. L. Gaeta, Opt. Lett. **29**, 2867 (2004).

[29] B. E. A. Saleh and M. C. Teich, *Fundamentals of photonics*, 2nd ed. (Wiley-Interscience, Hoboken, N.J., 2007), pp. xix, 1177 p.

[30] J. D. Jackson, *Classical electrodynamics*, 3rd ed. (Wiley, New York, 1999).

[31] D. Gloge, Appl. Opt. **10**, 2442 (1971).

[32] D. Marcuse, Appl. Opt. **18**, 2930 (1979).

[33] V. E. Zakharov and A. B. Shabat, Sov. Phys. JETP **34**, 62 (1972).

[34] R. H. Hardin and F. D. Tappert, SIAM Rev. Chronicle **15**, 423 (1973).

[35] R. A. Fisher and W. Bischel, Appl. Phys. Lett. **23**, 661 (1973).

[36] G. P. Agrawal, *Applications of nonlinear fiber optics*, 2nd ed. (Elsevier, Boston, 2008).

[37] R. Paschotta, *Encyclopedia of laser physics and technology* (Wiley-VCH, Weinheim, 2008).

[38] A. Hasegawa and Y. Kodama, Proc. IEEE **69**, 1145 (1981).

[39] K. J. Blow and N. J. Doran, Electron. Lett. **19**, 429 (1983).

[40] S. Trillo, S. Wabnitz, E. M. Wright, and G. I. Stegeman, Opt. Lett. **13**, 672 (1988).

[41] K. J. Blow, N. J. Doran, and B. K. Nayar, Opt. Lett. **14**, 754 (1989).

[42] M. N. Islam, E. R. Sunderman, R. H. Stolen, W. Pleibel, and J. R. Simpson, Opt. Lett. **14**, 811 (1989).

[43] M. A. Foster, K. D. Moll, and A. L. Gaeta, Opt. Express **12**, 2880 (2004).

[44] R. Adair, L. L. Chase, and S. A. Payne, Phys. Rev. B **39**, 3337 (1989).

[45] S. Leon-Saval, T. Birks, W. Wadsworth, P. St. J. Russell, and M. Mason, Opt. Express **12**, 2864 (2004).

[46] P. B. Chapple, J. Staromlynska, J. A. Hermann, T. J. McKay, and R. G. McDuff, J. Nonlinear Opt. Phys. Mater. **6**, 251 (1997).

[47] J. Pascual, J. Camassel, and H. Mathieu, Phys. Rev. B **18**, 5606 (1978).

[48] D Reyes-Coronado, G Rodríguez-Gattorno, M E Espinosa-Pesqueira, C Cab, R de Coss, and G Oskam, Nanotechnology **19**, 145605 (2008).

[49] J. Rams, A. Tejeda, and J. M. Cabrera, J. Appl. Phys. **82**, 994 (1997).

[50] Jr G. E. Jellison, L. A. Boatner, J. D. Budai, B. S. Jeong, and D. P. Norton, J. Appl. Phys. **93**, 9537 (2003).

[51] J. Li, T. Ishigaki, and X. Sun, J. Phys. Chem. C **111**, 4969 (2007).

[52] M. Dinu, IEEE J. Quantum. Electron. **39**, 1498 (2003).

[53] H. Long, A. Chen, G. Yang, Y. Li, and P. Lu, Thin Solid Films **517**, 5601 (2009).

[54] T. Hashimoto, T. Yoko, and S. Sakka, Bull. Chem. Soc. Jpn. **67**, 653 (1994).

[55] M. Higuchi, T. Hosokawa, and S. Kimura, J. Cryst. Growth **112**, 354 (1991).

[56] D. J. Kane and R. Trebino, IEEE J. Quantum. Electron. **29**, 571 (1993).

[57] S. Friberg and P. Smith, IEEE J. Quantum. Electron. **23**, 2089 (1987).

[58] Y. Watanabe, M. Ohnishi, and T. Tsuchiya, Appl. Phys. Lett. **66**, 3431 (1995).

[59] S. Kumar Das, C. Schwanke, A. Pfuch, W. Seeber, M. Bock, G. Steinmeyer, T. Elsaesser, and R. Grunwald, Opt. Express **19**, 16985 (2011).

[60] H. A. Castillo-Matadamas, R. M. Lima-García, and R. Quintero-Torres, J. Mod. Optic. **57**, 1100 (2010).

[61] E. Portuondo-Campa, A. Tortschanoff, F. van Mourik, and M. Chergui, J. Chem. Phys. **128**, (2008).

[62] V. Gayvoronsky, A. Galas, E. Shepelyavyy, T. Dittrich, V. Y. Timoshenko, S. A. Nepijko, M. S. Brodyn, and F. Koch, Appl. Phys. B **80**, 97 (2005).

[63] B. M. Patterson, W. Roc White, T. A. Robbins, and R. J. Knize, Appl. Opt. **37**, 1854 (1998).

[64] R. L. Sutherland, Appl. Opt. **33**, 5576 (1994).

[65] M. Jinno and T. Matsumoto, IEEE J. Quantum. Electron. **28**, 875 (1992).

[66] M. A. Foster, A. C. Turner, R. Salem, M. Lipson, and A. L. Gaeta, Opt. Express **15**, 12949 (2007).

[67] A. Penzkofer and W. Falkenstein, Opt. Commun. **17**, 1 (1976).

[68] H. S. Waff and K. Park, Phys. Lett. A **32**, 109 (1970).

[69] P. Sathy and A. Penzkofer, Appl. Phys. B **61**, 127 (1995).

[70] K. Watanabe, K. Inoue, and F. Minami, Phys. Rev. B **46**, 2024 (1992).

[71] D. Torres-Torres, M. Trejo-Valdez, L. Castañeda, C. Torres-Torres, L. Tamayo-Rivera, R. C. Fernández-Hernández, J. A. Reyes-Esqueda, J. Muñoz-Saldaña, R. Rangel-Rojo, and A. Oliver, Opt. Express **18**, 16406 (2010).

[72] M. Trejo-Valdez, R. Torres-Martínez, N. Peréa-López, P. Santiago-Jacinto, and C. Torres-Torres, J. Phys. Chem. C **114**, 10108 (2010).

[73] H. Long, G. Yang, A. Chen, Y. Li, and P. Lu, Opt. Commun. **282**, 1815 (2009).

[74] M. Kyoung and M. Lee, Bull. Korean Chem. Soc. **21**, 26 (2000).

[75] H. I. Elim, W. Ji, A. H. Yuwono, J. M. Xue, and J. Wang, Appl. Phys. Lett. **82**, 2691 (2003).

[76] L. Irimpan, B. Krishnan, V. P. N. Nampoori, and P. Radhakrishnan, J. Colloid Interface Sci. **324**, 99 (2008).

[77] A. H. Yuwono, B. Liu, J. Xue, J. Wang, H. I. Elim, Wei Ji, Ying Li, and T. J. White, J. Mater. Chem. **14**, 2978 (2004).

[78] Q. F. Zhou, Q. Q. Zhang, J. X. Zhang, L. Y. Zhang, and X. Yao, Mater. Lett. **31**, 39 (1997).

[79] D. S. Corrêa, L. De Boni, L. Misoguti, I. Cohanoschi, F. E. Hernandez, and C. R. Mendonça, Opt. Commun. **277**, 440 (2007).

[80] S. Couris, M. Renard, O. Faucher, B. Lavorel, R. Chaux, E. Koudoumas, and X. Michaut, Chem. Phys. Lett. **369**, 318 (2003).

[81] R. A. Ganeev, A. I. Ryasnyansky, M. Baba, M. Suzuki, N. Ishizawa, M. Turu, S. Sakakibara, and H. Kuroda, Appl. Phys. B **78**, 433 (2004).

[82] M. Falconieri and G. Salvetti, Appl. Phys. B **69**, 133 (1999).

[83] A. Gnoli, L. Razzari, and M. Righini, Opt. Express **13**, 7976 (2005).

[84] K. Watanabe and K. Inoue, Phys. Rev. B **41**, 7957 (1990).

[85] C. C. Evans, J. D. B. Bradley, F. Parsy, K. C. Phillips, R. Senaratne, E. A. Martì-Panameño, and E. Mazur, Thermally managed Z-scan measurements of titanium dioxide thin films, presented at Photonics West, San Francisco, CA, USA, 27 Jan. 2011.

[86] B. Imangholi, M. P. Hasselbeck, and M. Sheik-Bahae, Opt. Commun. **227**, 337 (2003).

[87] J. Yao, Z. Fan, Y. Jin, Y. Zhao, H. He, and J. Shao, Thin Solid Films **516**, 1237 (2008).

[88] M. Mero, J. Liu, W. Rudolph, D. Ristau, and K. Starke, Phys. Rev. B **71**, 115109 (2005).

[89] V. G. Ta'eed, N. J. Baker, L. B. Fu, K. Finsterbusch, M. R. E. Lamont, D. J. Moss, H. C. Nguyen, B. J. Eggleton, D. Y. Choi, S. Madden, and B. Luther-Davies, Opt. Express **15**, 9205 (2007).

[90] S. J. Madden, D. Y. Choi, D. A. Bulla, A. V. Rode, B. Luther-Davies, V. G. Ta'eed, M. D. Pelusi, and B. J. Eggleton, Opt. Express **15**, 14414 (2007).

[91] I. D. Rukhlenko, M. Premaratne, and G. P. Agrawal, Opt. Lett. **35**, 55 (2010).

[92] P. Koonath, D. R. Solli, and B. Jalali, Appl. Phys. Lett. **93**, 3 (2008).

[93] K. Worhoff, J. D. B. Bradley, F. Ay, D. Geskus, T. P. Blauwendraat, and M. Pollnau, IEEE J. Quantum. Electron. **45**, 454 (2009).

[94] J. S. Foresi, M. R. Black, A. M. Agarwal, and L. C. Kimerling, Appl. Phys. Lett. **68**, 2052 (1996).

[95] A. M. Agarwal, L. Liao, J. S. Foresi, M. R. Black, X. Duan, and L. C. Kimerling, J. Appl. Phys. **80**, 6120 (1996).

[96] L. Liao, D. Lim, A. Agarwal, X. Duan, K. Lee, and L. Kimerling, J. Electron. Mater. **29**, 1380 (2000).

[97] J. M. Bennett, E. Pelletier, G. Albrand, J. P. Borgogno, B. Lazarides, C. K. Carniglia, R. A. Schmell, T. H. Allen, T. Tuttle-Hart, K. H. Guenther, and A. Saxer, Appl. Opt. **28**, 3303 (1989).

[98] P. K. Tien, Appl. Opt. **10**, 2395 (1971).

[99] T. Ohsaka, F. Izumi, and Y. Fujiki, J. Raman Spectrosc. **7**, 321 (1978).

[100] M. Yamagishi, S. Kuriki, P. K. Song, and Y. Shigesato, Thin Solid Films **442**, 227 (2003).

[101] A. Villeneuve, C. C. Yang, P. G. J. Wigley, G. I. Stegeman, J. S. Aitchison, and C. N. Ironside, Appl. Phys. Lett. **61**, 147 (1992).

[102] L. Tong, R. R. Gattass, J. B. Ashcom, S. He, J. Lou, M. Shen, I. Maxwell, and E. Mazur, Nature **426**, 816 (2003).

[103] V. R. Almeida, C. A. Barrios, R. R. Panepucci, and M. Lipson, Nature **431**, 1081 (2004).

[104] M. T. Hill, H. J. S. Dorren, T. de Vries, X. J. M. Leijtens, J. Hendrik den Besten, B. Smalbrugge, Y.-S. Oei, H. Binsma, G.-D. Khoe, and M. K. Smit, Nature **432**, 206 (2004).

[105] H. Park, A. W. Fang, R. Jones, O. Cohen, O. Raday, M. N. Sysak, M. J. Paniccia, and J. E. Bowers, Opt. Express **15**, 6044 (2007).

[106] C. Koos, P. Vorreau, T. Vallaitis, P. Dumon, W. Bogaerts, R. Baets, B. Esembeson, I. Biaggio, T. Michinobu, F. Diederich, W. Freude, and J. Leuthold, Nature Photon. **3**, 216 (2009).

[107] X. Guo, M. Qiu, J. Bao, B. J. Wiley, Q. Yang, X. Zhang, Y. Ma, H. Yu, and L. Tong, Nano Lett. **9**, 4515 (2009).

[108] B. J. Eggleton, B. Luther-Davies, and K. Richardson, Nature Photon. **5**, 141 (2011).

[109] R. Espinola, J. Dadap, R. Osgood, S. McNab, and Y. Vlasov, Opt. Express **12**, 3713 (2004).

[110] R. R. Gattass, G. T. Svacha, L. M. Tong, and E. Mazur, Opt. Express **14**, 9408 (2006).

[111] R. Dekker, A. Driessen, T. Wahlbrink, C. Moormann, J. Niehusmann, and M. Först, Opt. Express **14**, 8336 (2006).

[112] L. Tong, J. Lou, R. R. Gattass, S. He, X. Chen, L. Liu, and E. Mazur, Nano Lett. **5**, 259 (2005).

[113] T. Tsuchizawa, K. Yamada, H. Fukuda, T. Watanabe, T. Jun-ichi, J. Takahashi, T. Shoji, E. Tamechika, S. Itabashi, and H. Morita, Selected Topics in IEEE J. Quantum. Electron. **11**, 232 (2005).

[114] M. A. Foster, A. C. Turner, M. Lipson, and A. L. Gaeta, Opt. Express **16**, 1300 (2008).

[115] J. T. Choy, B. J. M. Hausmann, T. M. Babinec, I. Bulu, M. Khan, P. Maletinsky, A. Yacoby, and M. Lončar, Nature Photon. **5**, 738 (2011).

[116] R. Mechiakh, F. Meriche, R. Kremer, R. Bensaha, B. Boudine, and A. Boudrioua, Opt. Mater. **30**, 645 (2007).

[117] T. Alasaarela, T. Saastamoinen, J. Hiltunen, A. Säynätjoki, A. Tervonen, P. Stenberg, M. Kuittinen, and S. Honkanen, Appl. Opt. **49**, 4321 (2010).

[118] J. D. B. Bradley, C. C. Evans, F. Parsy, K. C. Phillips, R. Senaratne, E. Marti, and E. Mazur, in *IEEE Photonics Society, 2010 23rd Annual Meeting of the* (2010), pp. 313–314.

[119] M. Furuhashi, M. Fujiwara, T. Ohshiro, M. Tsutsui, K. Matsubara, M. Taniguchi, S. Takeuchi, and T. Kawai, AIP Advances **1**, 032102 (2011).

[120] K. Abe, E. Y. M. Teraoka, T. Kita, and H. Yamada, Proc. of SPIE **7940**, 79401G–7 (2011).

[121] J. T. Choy, J. D. B. Bradley, P. B. Deotare, I. B. Burgess, C. C. Evans, E. Mazur, and M. Lončar, Opt. Lett. **37**, 539 (2012).

[122] Z.-F. Bi, L. Wang, X.-H. Liu, S.-M. Zhang, M.-M. Dong, Q.-Z. Zhao, X.-L. Wu, and K.-M. Wang, Opt. Express **20**, 6712 (2012).

[123] N. Sherwood-Droz and M. Lipson, Opt. Express **19**, 17758 (2011).

[124] K. Ikeda, R. E. Saperstein, N. Alic, and Y. Fainman, Opt. Express **16**, 12987 (2008).

[125] S. P. S. Porto, P. A. Fleury, and T. C. Damen, Phys. Rev. **154**, 522 (1967).

[126] N. Daldosso, M. Melchiorri, F. Riboli, F. Sbrana, L. Pavesi, G. Pucker, C. Kompocholis, M. Crivellari, P. Bellutti, and A. Lui, Mater. Sci. Semicond. Process. **7**, 453 (2004).

[127] N. Martin, C. Rousselot, D. Rondot, F. Palmino, and René Mercier, Thin Solid Films **300**, 113 (1997).

[128] Y. Vlasov and S. McNab, Opt. Express **12**, 1622 (2004).

[129] T. Barwicz and H. I. Smith, J. Vac. Sci. Technol., B **21**, 2892 (2003).

[130] M. Gnan, J. Vac. Sci. Technol. B **25**, 2034 (2007).

[131] S. Lardenois, D. Pascal, L. Vivien, E. Cassan, S. Laval, R. Orobtchouk, M. Heitzmann, N. Bouzaida, and L. Mollard, Opt. Lett. **28**, 1150 (2003).

[132] J. Cardenas, C. B. Poitras, J. T. Robinson, K. Preston, L. Chen, and M. Lipson, Opt. Express **17**, 4752 (2009).

[133] R. J. Bojko, J. Li, L. He, T. Baehr-Jones, M. Hochberg, and Y. Aida, J. Vac. Sci. Technol., B **29**, 06F309 (2011).

[134] K. J. Vahala, Nature **424**, 839 (2003).

[135] M. Lipson, J. Lightwave Technol. **23**, 4222 (2005).

[136] E. Shah Hosseini, S. Yegnanarayanan, A. H. Atabaki, M. Soltani, and A. Adibi, Opt. Express **17**, 14543 (2009).

[137] C. Kurtsiefer, S. Mayer, P. Zarda, and H. Weinfurter, Phys. Rev. Lett. **85**, 290 (2000).

[138] C. B. Murray, C. R. Kagan, and M. G. Bawendi, Annu. Rev. Mater. Sci. **30**, 545 (2000).

[139] B. Lounis and W. E. Moerner, Nature **407**, 491 (2000).

[140] K. Rivoire, A. Faraon, and J. Vuckovic, Appl. Phys. Lett. **93**, 063103 (2008).

[141] M. Barth, N. Nusse, J. Stingl, B. Lochel, and O. Benson, Appl. Phys. Lett. **93**, 021112 (2008).

[142] M. Khan, T. Babinec, M. W. McCutcheon, P. Deotare, and M. Lon?ar, Opt. Lett. **36**, 421 (2011).

[143] Y. Gong and J. Vuckovic, Appl. Phys. Lett. **96**, 031107 (2010).

[144] A. Faraon, P. E. Barclay, C. Santori, K.-M. C. Fu, and R. G. Beausoleil, Nature Photon. **5**, 301 (2011).

[145] C. F. Wang, R. Hanson, D. D. Awschalom, E. L. Hu, T. Feygelson, J. Yang, and J. E. Butler, Appl. Phys. Lett. **91**, 201112 (2007).

[146] S. A. Campbell, H. S. Kim, D. C. Gilmer, B. He, T. Ma, and W. L. Gladfelter, IBM J. Res. Develop. **43**, 383 (1999).

[147] G. Subramania, Y.-J. Lee, A. J. Fischer, and D. D. Koleske, Adv. Mater. **22**, 487 (2010).

[148] J. D. B. Bradley, C. C. Evans, J. T. Choy, O. Reshef, P. B. Deotare, F. Parsy, K. C. Phillips, M. Lončar, and E. Mazur, Opt. Express **20**, 23821 (2012).

[149] M. K. Chin, C. Youtsey, W. Zhao, T. Pierson, Z. Ren, S. L. Wu, L. Wang, Y. Zhao, x, G, and S. T. Ho, IEEE Photon. Technol. Lett. **11**, 1620 (1999).

[150] Q. Quan, P. B. Deotare, and M. Loncar, Appl. Phys. Lett. **96**, 203102 (2010).

[151] S. Fan, Appl. Phys. Lett. **80**, 908 (2002).

[152] L. Zhou and A. W. Poon, Opt. Express **15**, 9194 (2007).

[153] A. Guarino, G. Poberaj, D. Rezzonico, R. Degl'Innocenti, and P. Gunter, Nature Photon. **1**, 407 (2007).

[154] K. Preston, B. Schmidt, and M. Lipson, Opt. Express **15**, 17283 (2007).

[155] P. P. Absil, J. V. Hryniewicz, B. E. Little, P. S. Cho, R. A. Wilson, L. G. Joneckis, and P. T. Ho, Opt. Lett. **25**, 554 (2000).

[156] A. A. Savchenkov, A. B. Matsko, W. Liang, V. S. Ilchenko, D. Seidel, and L. Maleki, Nature Photon. **5**, 293 (2011).

[157] Y. Okawachi, K. Saha, J. S. Levy, Y. H. Wen, M. Lipson, and A. L. Gaeta, Opt. Lett. **36**, 3398 (2011).

[158] M. A. Foster, J. S. Levy, O. Kuzucu, K. Saha, M. Lipson, and A. L. Gaeta, Opt. Express **19**, 14233 (2011).

[159] O. Boyraz and B. Jalali, Opt. Express **12**, 5269 (2004).

[160] C. Xiong, L. G. Helt, A. C. Judge, G. D. Marshall, M. J. Steel, J. E. Sipe, and B. J. Eggleton, Opt. Express **18**, 16206 (2010).

[161] S. Azzini, D. Grassani, M. J. Strain, M. Sorel, L. G. Helt, J. E. Sipe, M. Liscidini, M. Galli, and D. Bajoni, Opt. Express **20**, 23100 (2012).

[162] M. Pollnau, Y. E. Romanyuk, F. Gardillou, C. N. Borca, U. Griebner, S. Rivier, and V. Petrov, Selected Topics in IEEE J. Quantum. Electron. **13**, 661 (2007).

[163] F. Koyama, J. Lightwave Technol. **24**, 4502 (2006).

[164] J. W. Hall and A. Pollard, Clin. Chem. **38**, 1623 (1992).

[165] R. W. Boyd and J. E. Heebner, Appl. Opt. **40**, 5742 (2001).

[166] H. Obrig and A. Villringer, JCBFM **23**, 1 (2003).

[167] J.-C. G. Bunzli and C. Piguet, Chem. Soc. Rev. **34**, 1048 (2005).

[168] R. H. Hadfield, Nature Photon. **3**, 696 (2009).

[169] B. S. Wherrett, J. Opt. Soc. Am. B **1**, 67 (1984).

[170] M. Dinu, F. Quochi, and H. Garcia, Appl. Phys. Lett. **82**, 2954 (2003).

[171] R. M. Osgood, N. C. Panoiu, J. I. Dadap, X. Liu, X. Chen, I. W. Hsieh, E. Dulkeith, W. M. Green, and Y. A. Vlasov, Adv. Opt. Photon. **1**, 162 (2009).

[172] J. S. Aitchison, D. C. Hutchings, J. U. Kang, G. I. Stegeman, and A. Villeneuve, IEEE J. Quantum. Electron. **33**, 341 (1997).

[173] G. A. Siviloglou, S. Suntsov, R. El-Ganainy, R. Iwanow, G. I. Stegeman, D. N. Christodoulides, R. Morandotti, D. Modotto, A. Locatelli, C. De Angelis, F. Pozzi, C. R. Stanley, and M. Sorel, Opt. Express **14**, 9377 (2006).

[174] S. Combrie, Q. V. Tran, A. De Rossi, C. Husko, and P. Colman, Appl. Phys. Lett. **95**, 221108 (2009).

[175] V. V. Lozovoy, I. Pastirk, and M. Dantus, Opt. Lett. **29**, 775 (2004).

[176] L. Yin, Ph.D. thesis, 2009.

[177] K. J. Blow and D. Wood, IEEE J. Quantum. Electron. **25**, 2665 (1989).

[178] Q. Lin, O. J. Painter, and G. P. Agrawal, Opt. Express **15**, 16604 (2007).

[179] H. Tang, F. Lévy, H. Berger, and P. E. Schmid, Phys. Rev. B **52**, 7771 (1995).

[180] Y. R. Shen, *The principles of nonlinear optics* (Wiley, New York, 1984), pp. xii, 563 p.

[181] A. M. Zheltikov, Phys. Rev. A **72**, 043812 (2005).

[182] A. Zheltikov, J. Opt. Soc. Am. B **22**, 2263 (2005).

[183] C. C. Evans, K. Shtyrkova, J. D. B. Bradley, O. Reshef, E. Ippen, and E. Mazur, Opt. Express **21**, 18582 (2013).

[184] K. Hashimoto, H. Irie, and A. Fujishima, Japanese J. Appl. Phys. Part 1 **44**, 8269 (2005).

[185] A. Fujishima, X. Zhang, and D. A. Tryk, Surf. Sci. Rep. **63**, 515 (2008).

[186] B. Gu, J. Wang, J. Chen, Y.-X. Fan, J. Ding, and H.-T. Wang, Opt. Express **13**, 9230 (2005).

[187] B. Gu, X. Q. Huang, S. Q. Tan, M. Wang, and W. Ji, Appl. Phys. B **95**, 375 (2009).

[188] J. Wang, B. Gu, X.-W. Ni, and H.-T. Wang, Opt. Laser Technol. **44**, 390 (2012).

[189] S. M. Mian, B. Taheri, and J. P. Wicksted, J. Opt. Soc. Am. B **13**, 856 (1996).

[190] M. G. Vivas, T. Shih, T. Voss, E. Mazur, and C. R. Mendonça, Opt. Express **18**, 9628 (2010).

[191] G. Boudebs, S. Cherukulappurath, M. Guignard, J. Troles, F. Smektala, and F. Sanchez, Opt. Commun. **232**, 417 (2004).

[192] M. Chattopadhyay, P. Kumbhakar, C. S. Tiwary, A. K. Mitra, U. Chatterjee, and T. Kobayashi, Opt. Lett. **34**, 3644 (2009).

[193] T. Sarma, P. K. Panda, P. T. Anusha, and S. V. Rao, Org. Lett. **13**, 188 (2010).

[194] A. Eriksson, M. Lindgren, S. Svensson, and P.-O. Arntzen, J. Opt. Soc. Am. B **15**, 810 (1998).

[195] International Organization for Standardization, *ISO 11146-1:2005 Lasers and laser-related equipment - Test methods for laser beam widths, divergence angles and beam propagation ratios* (ISO, Geneva, Switzerland, 2005).

[196] M. R. Ferdinandus, M. Reichert, T. R. Ensley, H. Hu, D. A. Fishman, S. Webster, D. J. Hagan, and E. W. Van Stryland, Opt. Mater. Express **2**, 1776 (2012).

[197] T. R. Ensley, H. Hu, A. R. Ernst, C. Fuentes-Hernandez, A. Dindar, B. Kippelen, D. J. Hagan, and E. W. Van Stryland, in *Nonlinear Refraction Measurements of Thin Films by the Dual-arm Z-scan Method*, *OSA Technical Digest (online)*,(Optical Society of America, 2013), p. NTu1B.4.

[198] M. J. Weber, *Handbook of optical materials*, *CRC Press laser and optical science and technology series* (CRC Press, Boca Raton, 2003), p. 512.

[199] K. Otsuka, Opt. Lett. **8**, 471 (1983).

[200] D. B. Mortimore, J. Lightwave Technol. **6**, 1217 (1988).

[201] N. J. Doran, D. S. Forrester, and B. K. Nayar, Electron. Lett. **25**, 267 (1989).

[202] A. Huang, N. Whitaker, H. Avramopoulos, P. French, H. Houh, and I. Chuang, Appl. Opt. **33**, 6254 (1994).

[203] D. Cotter, R. J. Manning, K. J. Blow, A. D. Ellis, A. E. Kelly, D. Nesset, I. D. Phillips, A. J. Poustie, and D. C. Rogers, Science **286**, 1523 (1999).

[204] G. Svacha, Ph.D. thesis, 2008.

[205] N. J. Doran and D. Wood, Opt. Lett. **13**, 56 (1988).

[206] K. Uchiyama, H. Takara, S. Kawanishi, T. Morioka, M. Saruwatari, and T. Kitoh, Electron. Lett. **29**, 1870 (1993).

[207] M. Asobe, T. Ohara, I. Yokohama, and T. Kaino, Electron. Lett. **32**, 1396 (1996).

[208] L. Jiun-Haw, W. Ding-An, C. Hsin-Jiun, H. Ding-Wei, S. Gurtler, C. C. Yang, K. Yean-Woei, B. C. Chen, M. C. Shih, and T. J. Chuang, IEEE Photon. Technol. Lett. **11**, 236 (1999).

[209] M. D. Pelusi, Y. Matsui, and A. Suzuki, IEEE J. Quantum. Electron. **35**, 867 (1999).

[210] A. Bogoni, M. Scaffardi, P. Ghelfi, and L. Poti, Selected Topics in IEEE J. Quantum. Electron. **10**, 1115 (2004).

[211] O. Pottiez, E. A. Kuzin, B. Ibarra-Escamilla, J. T. Camas-Anzueto, and F. Gutierrez-Zainos, Electron. Lett. **40**, 892 (2004).

[212] E. Simova, I. Golub, and M.-J. Picard, J. Opt. Soc. Am. B **22**, 1723 (2005).

[213] M. Sumetsky, Appl. Phys. Lett. **86**, 161108 (2005).

[214] M. Jinno and T. Matsumoto, Opt. Lett. **16**, 220 (1991).

[215] Y. Miyoshi, K. Ikeda, H. Tobioka, T. Inoue, S. Namiki, and K. Kitayama, Opt. Express **16**, 2570 (2008).